THE UNIVERSITY *of* EDINBURGH

Computational investigations of thermoelectric properties of lead telluride, magnesium silicide, and magnesium stannide under high pressure and anisotropic stress

Gavin Woolman

Doctor of Philosophy
The University of Edinburgh
December 19, 2021

Abstract

I present a comprehensive picture of the electrical transport properties for PbTe, Mg_2Si, and Mg_2Sn under high pressure and stress.

The electronic band structure and thermoelectric properties of *p*- and *n*-doped lead telluride, PbTe, were calculated within the framework of density functional theory, as implemented in Wien2k, and Boltzmann transport theory, as implemented in the BoltzTraP code. Thermoelectric properties were calculated as a function of hydrostatic pressure, as well as uniaxial stress along several crystal directions. Significant enhancements of the thermoelectric power factor can be obtained by using anisotropic stress, and the underlying changes in the electronic band structure are analysed. We identify two key effects in PbTe: redistribution of carriers between different carrier pockets, each of which has anisotropic transport properties; and reshaping of the carrier pockets themselves.

Individual carrier pockets of PbTe have anisotropic transport properties. Stress along [111] is shown to redistribute dopant charges between the carrier pockets. Due to this effect, compressive [111] stress improves the thermoelectric power factor along [111] of *p*-PbTe, and tensile [111] stress improves the power factor along [111] of *n*-PbTe. Compressive stress along [001], which causes an intervalley-transfer-effect, is shown to reshape the valence band of PbTe, improving the *p*-type power factor along [001].

Along with specific results for PbTe, general rules are presented for identifying other materials which could have their thermoelectric power factor increased by stress along specific directions. Guided by these rules, the thermoelectric properties of magnesium silicide and magnesium stannide under strain are presented. The same key effects, intervalley-transfer and valley-reshaping, are observed. The thermoelectric power factors of Mg_2Si, and Mg_2Sn are shown to be greatly improved by anisotropic strain.

Lay Summary of Thesis

Name of student	Gavin Armstrong Woolman
UUN	s1108127
University Email	gavin.woolman@ed.ac.uk
Degree sought	Condensed Matter Physics PHD
No. of words in the main text of thesis	60,000

A large portion of the energy we generate is lost to the environment as heat. Thermoelectric materials have the unusual property that if a temperature difference is applied across them, it induces a voltage which can power an electric device. These materials can be used to make devices that capture some of the heat that would otherwise be wasted. They can be made small to power satellites or devices in space, where compact devices are key. They can provide power for devices situated near a waste-heat source, without the need to lay miles of cables leading back to a central generator. Thermoelectric materials can be used as sensitive detectors of heat flow, as they are scalable, low-vibration, and low-noise, and because they have no moving parts, they tend to be very reliable.

Thermoelectric refrigerators, or *Peltier coolers* as they are known, are also useful. These devices are the opposite to a generator; they take electrical power and use it to create a temperature difference. Scalable to many different sizes, able to precisely control the flow of heat; they have advantages over conventional fridges in many applications. There is a profusion of applications for thermoelectric devices, motivating the development of more efficient thermoelectric materials.

The efficiency of a thermoelectric material — how much electricity it generates for a given amount of heat — depends on an intricate balance of several electrical and thermal material properties. By stressing a thermoelectric material, squeezing or stretching along one or two directions, its electronic properties

can be altered. In the manufacture of thermoelectric materials, such stresses can be induced. Understanding the effect of these stresses can help improve thermoelectric efficiency.

Although these properties are macroscopic, their origin is quantum mechanical. By studying thermoelectric materials at an atomic level, the electronic properties of the bulk material can be predicted. In this thesis, quantum-mechanical calculations are used to examine the electronic properties of three thermoelectric materials: lead telluride, magnesium silicide, and magnesium stannide.

A comprehensive picture is presented of how the electronic properties of these materials change under high pressure and stress. A key measure of the effectiveness of a thermoelectric is its so-called *power factor*, which depends on the electronic properties of the material. By stressing these materials along specific directions, their power factors can be greatly enhanced. For example, if lead telluride with a particular chemical composition at room temperature is compressed along a certain direction by just 1 % of its length, its power factor increases by 30 %.

Several qualitative rules are presented for predicting other materials which can be improved in the same way. This thesis presents a picture for understanding the effects of stress on electronic properties of thermoelectric materials, and shows that stress can be a useful tool for enhancing the efficiency of these materials.

Declaration

I declare that this thesis has been composed solely by myself and that it has not been submitted, in whole or in part, in any previous application for a degree. Except where states otherwise by reference or acknowledgment, the work presented is entirely my own.

Acknowledgements

I would like to acknowledge Harry Keen, whose mathematica code helped create several of the isosurface diagrams in this thesis.

My supervisor Ingo Loa, who gave excellent feedback and support throughout my PhD. I am a far better writer thanks to his guidance, and a better scientist because of his example.

My parents, for their help reading the chapters I sent them and their advice throughout.

And most of all my partner, Helen Price, whose enthusiasm, kindness, succour, and encouragement propelled me right to the very end.

Thank you, I couldn't have got here without you.

Contents

Chapter 1

Introduction

Sometime in the early 1790s Alessandro Volta made a circuit using his first iteration of the voltmeter: a dead frog[1,2]. He took two glasses filled with water, and laid the frog so that its legs were immersed in one glass, and its spine in the other. He took an arc of a thick iron wire, coarse and flexible, and heated one end in boiling water. After removing the hot end, without letting it cool, he immersed both ends in the glasses of water — completing the circuit. The dead frog contracted, jumped, and the first thermoelectric device was born.

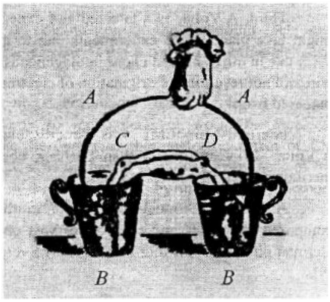

Scheme of Volta's experiment, taken from Anatychuk (2004)[1]. A - Iron Arc; B - Glasses of water; C & D - parts of the frog.

Around twenty-five years later, another physicist — Thomas Johann Seebeck — would conduct the first detailed experiments on what he would call *the thermomagnetic effect*[4]. Seebeck created a circuit from two dissimilar metals, and found that a nearby compass needle was diverted upon heating one of the junctions between the two metals.

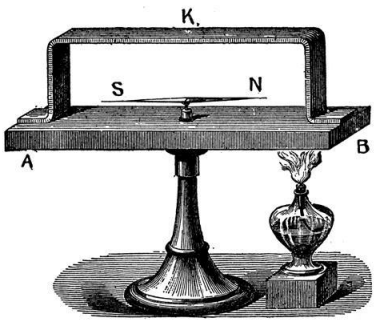

Source: Chemistryworld[3]. K is a copper wire, sitting on a block of bismuth. A & B are the two junctions, one of which is heated.

Seebeck established a link between how much the needle was diverted, and the size and direction of the temperature difference. Also important was the choice of metals, and he showed that if the same metal was chosen for both legs of the thermocouple — the compass needle did not move.

Seebeck coined his observation the *"thermomagnetic effect"*, but this name is somewhat misleading. Heating or cooling one of the junctions

was not directly magnetising the material. Instead, the temperature difference induced an electromotive potential. That potential drove a current around the circuit which, by Ampere's law, induces a magnetic field which diverted the compass.

Nevertheless, Seebeck was first to show that electrical work could be harvested from a temperature difference*, and his experiment harbingered the devices to come.

A single pair of dissimilar metals can only create very tiny currents/voltages for any reasonable temperature difference (a few hundred °C). Connecting many pairs of dissimilar metals in series can be used to increase the voltage. Such an array of thermocouples was called a *thermopile* [Fig. 1.3(b)]; the temperature analogue of the Voltaic pile, a chemical battery made by stacking dissimilar metals atop each other. Within just a few years of Seebeck's experiment, the first *thermopiles* were being created.

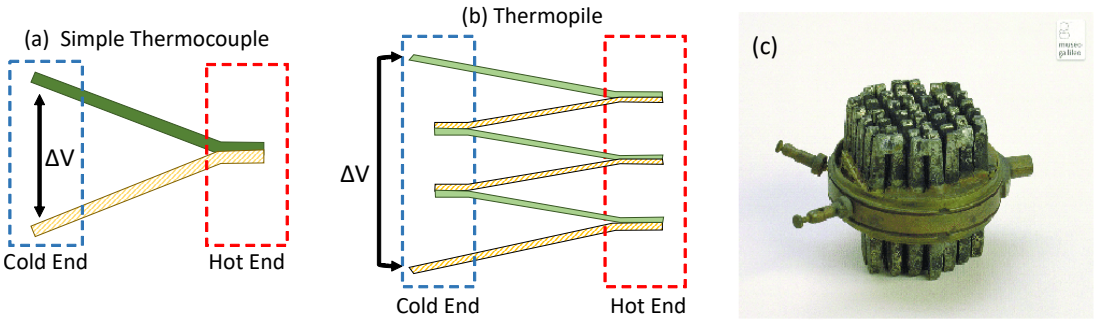

Figure 1.3 *(a) & (b): simplified diagrams of a thermocouple and thermopile respectively, (c) : early thermopile made in 1829 by Leopoldo Nobili – photograph sourced from the Museum of RetroTechnology*[5].

Figure 1.3(c) shows an early thermopile created less than a decade after Seebeck's discovery by inventor Leopoldo Nobili. It is made from an array of bismuth and antimony couples, each of which gives an output of around 12 mV per 100 °C of temperature difference. By arranging many of them in series, Nobili's device could supply a steady current for his experiments[5].

*Some sources argue that Allesandro Volta was the first to show this[1]. However, when it comes to the thermoelectric effect, his results are described far more vaguely than Seebeck's rather thorough observations.

Over time, generators with larger and larger arrays were developed. Towards the end of the 19$^{\text{th}}$ century, thermopiles were being built that could generate over 100 V, using thousands of thermocouples. The 1879 *Improved Clamond Thermopile*, one of the most efficient of its time, could burn 10 kilos of coke fuel per hour to power four electric lights[2,5].

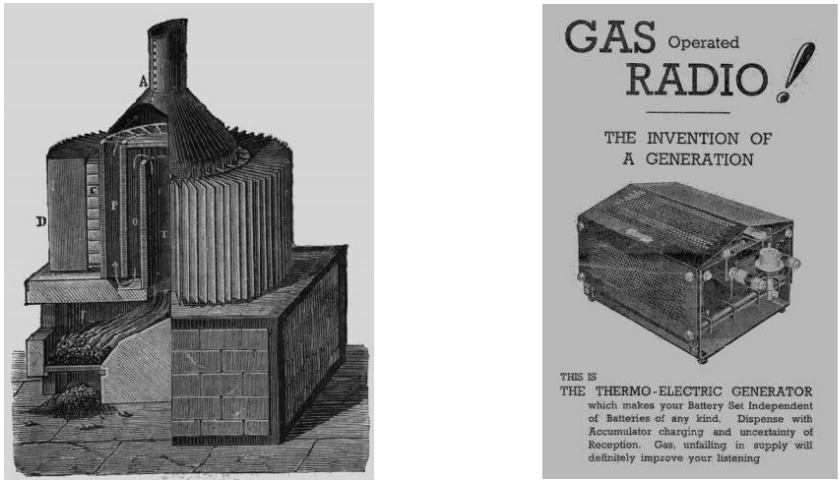

Figure 1.4 *Left: Improved Clamond Thermopile, 1879. Right: 1930s thermoelectric radio advert. Source: Museum of RetroTechnology*[5].

After the turn of the 20$^{\text{th}}$ century, *commercial* thermoelectric devices began appearing. At this point, many houses had a gas-supply, but home electricity was still very new. No longer were thermoelectrics the domain of curious physicists and engineers; there was money to be made.

Semiconductor technology, developed towards the mid-20$^{\text{th}}$ century, revolutionized thermoelectric research. For the same temperature difference, semiconductors generally induce a much larger voltage than metals, allowing more power to be generated for the same amount of heat. The first examples of thermoelectric refrigerators also appeared around this time[2]. Thermoelectric refrigerators, or *Peltier coolers* as they are known, are the opposite to a generator: they take electrical power and use it to create a temperature difference. Scalable to many different sizes, able to precisely control the flow of heat, and requiring no moving parts; Peltier coolers have advantages over conventional fridges in many applications.

Advances in nuclear technology in the mid-20$^{\text{th}}$ century inspired the creation of thermoelectric generators that can use hot radioactive material as a heat-source. These *radioisotope thermoelectric generators* (RTGs) could be compact, lightweight, reliable, and would last as long as the radioisotope remained hot. They were perfect for a rather upward thinking application: space.

The design of these generators was reminiscent of the early thermopiles, but this time the heat source was a lump of plutonium-238 rather than burning charcoal or gas. By the end of the 1960s, a thermoelectric generator made from lead telluride would be on the Moon. By the end of the 1970s, one would be on Mars.

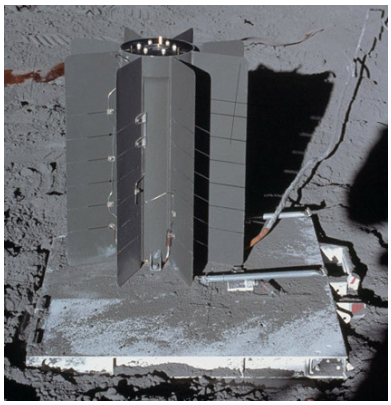

Figure 1.5 *Photograph of a lead telluride based SNAP-27 thermoelectric generator on the moon. Source: NASA* [6]

To this day, radioisotope thermoelectric generators remain a reliable power source for satellites, space probes, and applications like the Mars rover: *Curiosity*. But the demand for alternative energy sources is not limited to space.

A large portion of the energy we generate is lost to the environment as heat. Thermoelectric materials can be used to make devices which recapture some of the heat that would otherwise be wasted. They can be scaled to size and, because they have no moving parts, they tend to be very reliable. They can provide power for devices situated near a waste-heat source, without the need to lay miles of cables leading back to a central generator. Thermoelectric refrigerators are useful for applications such as sensitive detectors, as they are scalable, low-vibration, and low-noise. There is a profusion of applications for thermoelectric devices, motivating the development of more efficient thermoelectric materials.

The efficiency of a thermoelectric material is usually quantified by a measure known as the *figure of merit* ZT: the higher ZT, the more efficient the material. The figure of merit depends on several different physical properties: the square of the Seebeck coefficient S, which captures how large the generated voltage will be for a given temperature difference; the electrical conductivity σ; the absolute temperature T; and the thermal conductivity κ,

$$ZT = \frac{S^2\sigma}{\kappa}T. \tag{1.1}$$

The numerator of ZT is also called the *power factor* $\alpha = S^2\sigma$. ZT helps quantify why some materials make more efficient thermoelectric devices than others, but it also suggests an avenue to improve them: find a way to increase the power factor, or reduce the thermal conductivity. Alloying and nanostructuring are common methods to reduce the thermal conductivity, and properties like dopant concentration are often tuned to maximise the power factor. This thesis explores a different tactic: straining the crystal structure to change the electronic properties S and σ.

Initially this thesis focuses on one of the best-known thermoelectric materials: lead telluride, PbTe. Experimental studies have suggested that pressure on the scale of a GPa can improve the power factor α of lead telluride anywhere between a factor of 2 and over 100[7–9]. However, the mechanism through which pressure increases the power factor in PbTe has remained unknown.

This thesis is a computational investigation, within the framework of density functional theory and Boltzmann transport theory, of thermoelectric properties of PbTe under high pressure and non-hydrostatic stress. A comprehensive picture of how pressure and stress affect the electronic properties of PbTe will be presented, along with rules of thumb for applying this picture to other materials.

Guided by these rules, the thermoelectric properties of magnesium silicide and magnesium stannide under strain were also studied. I will show that anisotropic strain can improve the power factor of these materials, and the effect can be understood using the same picture as for lead telluride. But first, a few background chapters are presented to briefly summarize the key concepts used later.

Chapter 2

Background

2.1 The Thermoelectric Effect in Solids

This section will summarise some background ideas for the thermoelectric effect.

2.1.1 The Seebeck effect

In the canonical thermoelectric experiment, Thomas Johann Seebeck created a closed circuit from two different metals, joined in two places, with one joint heated by a flame (Fig. 2.1, left). Seebeck observed that a compass needle, placed near to the conductors, was diverted. While this is Seebeck's most famous experiment, it is not a demonstration of the rather specific effect dubbed *the Seebeck effect*.

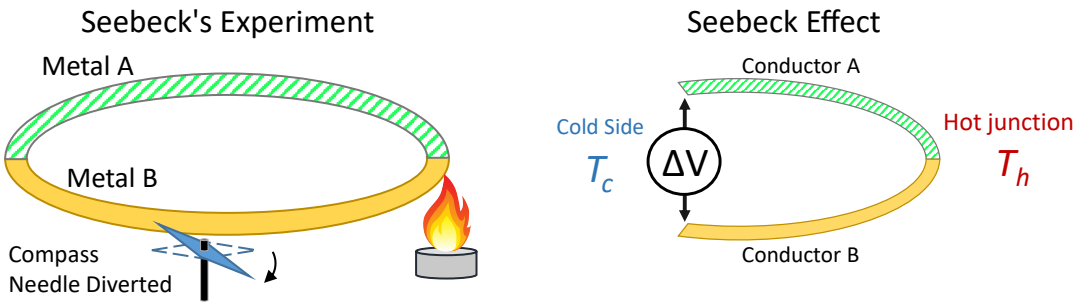

Figure 2.1 *Left: Diagram of Seebeck's "thermomagnetic effect"; Right: Diagram of what is now known as the Seebeck effect.*

To demonstrate the Seebeck effect, a slightly different experimental setup is used (Fig. 2.1, right). Two different materials A & B are connected in an open circuit, and a temperature difference is applied between the junction and the other ends

of the conductors. If a voltmeter is connected, then a potential difference can be measured. The size and direction of this voltage difference depends on the temperatures T_c and T_h, and the choice of materials A & B. This relationship between temperature difference and voltage is the Seebeck effect.

The size of the voltage depends linearly on the temperature difference, and the gradient of this relationship depends on the choice of materials A & B:

$$\Delta V = V_A - V_B = (S_B - S_A) \times (T_h - T_c)\,, \tag{2.1}$$

where $V_A - V_B$ is the voltage difference between the cold side electrodes of conductor A and B, while S_A and S_B are known as the *Seebeck coefficients* of A and B respectively. The Seebeck coefficient is a material property which depends on temperature, impurities, defects, pressure etc. Typical Seebeck coefficients range from several µV/ K for metals, to plus or minus many tens or even hundreds of µV/ K for semiconductors.

Seebeck coefficients can also be positive or negative, depending on the material involved. For p-doped semiconductors the Seebeck coefficient tends to be positive, as the direction that the holes — which carry heat — move in is the same as the direction of current. For n-doped semiconductors the Seebeck coefficient is negative, as the heat flow is opposite to the current. For metals, the Seebeck coefficient can be positive or negative, depending on the metal.

The experiment shown in Fig. 2.1(b) will only measure the relative Seebeck coefficient ($S_A - S_B$). Directly measuring an unknown Seebeck coefficient requires a known reference material (usually Platinum, Lead, Copper, or Tungsten) to be used as one of the conductors (A or B). Once the Seebeck coefficient for a material is known, then the setup shown in Fig. 2.1(b) can be used to measure the Seebeck coefficients of other materials. However, finding the initial Seebeck coefficient for the reference material requires a different method discussed later.

2.1.2 Peltier effect

A sibling to the Seebeck effect was discovered by Jean Charles Athanase Peltier in 1834. Peltier's experiment used a closed circuit made of two dissimilar metals, both at uniform temperature, with a current driven around the circuit (Fig. 2.2). The electrical current forces heat to flow from one junction to the other. Similar to the Seebeck effect — where the voltage difference depends on the temperature difference and choice of materials — in the Peltier effect the magnitude and

direction of heat flow depends on the magnitude and direction of the current, and the choice of materials. The heat current ($\dot{Q}$) and electrical current (I) are related by:

$$\dot{Q} = (\Pi_B - \Pi_A) \times I. \tag{2.2}$$

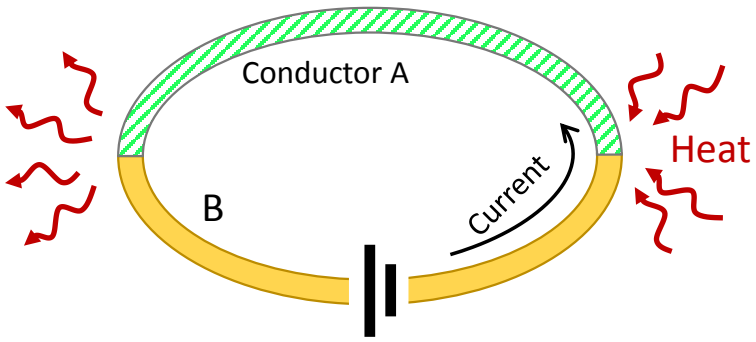

Figure 2.2 *The Peltier effect.*

Equation 2.2 is similar to the equation for the Seebeck effect 2.1, with the voltage difference replaced by heat carried each second ($\dot{Q}$), Seebeck coefficients replaced by Peltier coefficients ($\Pi_{A\&B}$), and the temperature difference replaced with an electric current (I). The Peltier coefficients quantify how much heat is carried by each charge. In a real experiment the transfer of heat could lead to a temperature difference between one junction and the other. The Pelteir effect's transfer of electrical energy into heat redistribution is the basis for *Peltier cooling*, where a circuit like that in figure 2.2 is used as a solid state refrigerator.

It is worth noting here that equations 2.1 and 2.2 are only true in the absence of a magnetic field. If a magnetic material is used, or a magnetic field is applied, then Hall, Nernst, and other effects all become overlaid, complicating the situation. But in the idealized examples just described, it is clear that the Seebeck and Peltier effects are like conjugate pairs of one another. Indeed the Peltier coefficient Π and Seebeck coefficients S are related by:

$$\Pi = TS, \tag{2.3}$$

where T is the absolute temperature. Like measuring the Seebeck coefficient, measuring the absolute Peltier coefficient requires using a known reference material as one of the two conductors. Also like the Seebeck coefficient, the Peltier coefficient is a material property, sensitive to the exact material composition.

2.1.3 Thomson effect

The Thomson effect occurs when current is driven through a closed loop made of one conductor, that has a temperature gradient across it. The electrical current redistributes heat throughout the material and with the surroundings. Figure 2.3 shows an example Thomson experiment setup. An electric current is driven through a homogenous conductor that has a temperature gradient across it. The presence of an electric current causes an asymmetric heat-current around the circuit. The heat current ($\dot{Q}$) is related to the size of the electrical current (I), and the temperature difference ($\Delta T = T_h - T_c$) across the sample:

$$\dot{Q} = -\text{ℜ}\ (I \times \Delta T)\,, \tag{2.4}$$

where ℜ is the Thomson coefficient, named after William Thomson — better known by his formal title Lord Kelvin.

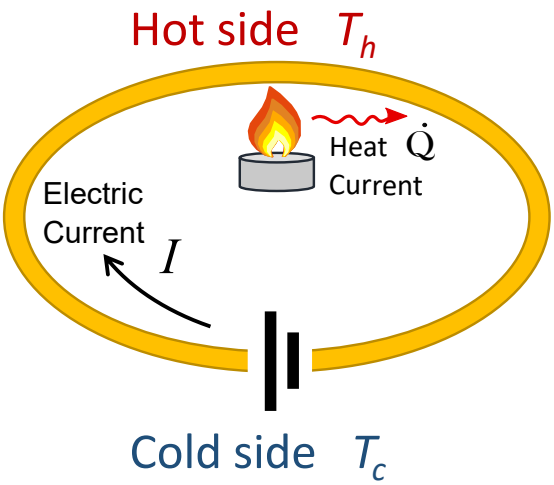

Figure 2.3 *The Thomson effect.*

The Thomson experiment setup (Fig 2.3 looks similar to the Peltier experiment setup (Fig. 2.2), where conductor A is replaced with the hot side of the loop, and conductor B is replaced by the cold side. Indeed the Thomson effect is sometimes referred to as a 'continuous Peltier effect'. In the Thomson experiment, the temperature of the sample changes continously around the circuit. Because the Peltier coefficient can change depending on the temperature of the sample, the Peltier coefficient also changes continuously around the loop. Therefore, it should be no surprise that the Thomson coefficient ℜ is intimately linked to the

temperature gradient of the Peltier (Π) and Seebeck (S) coefficients:

$$\mathfrak{K} = \frac{d\Pi}{dT} - S = T\frac{dS}{dT}. \tag{2.5}$$

Measurements of the Thomson coefficient can be used to calculate the rate of change of the Seebeck coefficient with temperature. Because of this, the absolute Seebeck coefficient S at any temperature T can be traced back to a measurement at a low temperature (T_0):

$$S\left(T\right) = \int_{T_0}^{T} \mathfrak{K}\left(t\right) \mathrm{d}t \ + S\left(T_0\right). \tag{2.6}$$

At low temperatures, the absolute Seebeck coefficient can be measured by using a superconductor as a reference material[10]. Superconductors have a Seebeck coefficient of zero, making them the perfect reference material; as long as the temperature and currents used are low enough that the material remains superconducting. Once the absolute Seebeck coefficient of a reference material, such as platinum or tungsten, has been measured at low temperatures relative to a superconductor, If a superconductor is used as a reference material, then a value of the absolute Seebeck coefficient can be obained at low temperature $S\left(T_0\right)$. This data can then be extended to room temperature and above by measuring the Thomson coefficient. Seebeck and Peltier coefficients for reference materials (such as platinum) are obtained in this way[10].

2.1.4 The Thermocouple

The Thomson, Seebeck, and Peltier experiments are designed to measure material properties, but it is easy to see that their effects could be exploited to design useful devices. The thermocouple is a common example.

A typical thermocouple circuit is shown in figure 2.4. Two dissimilar wires (A & B) are joined at a junction which is at the unknown temperature T. The other ends of each wire are held at a reference temperature T_{ref}, and connected via extension wires C to a voltmeter. If the Seebeck coefficients of wires A and B (S_A & S_B) are known, then the temperature T can be calculated using,

$$T = T_{ref} \times \frac{\Delta V}{S_A - S_B}, \tag{2.7}$$

where ΔV is the voltage difference measured. In this way an electronic signal can be used to measure a temperature.

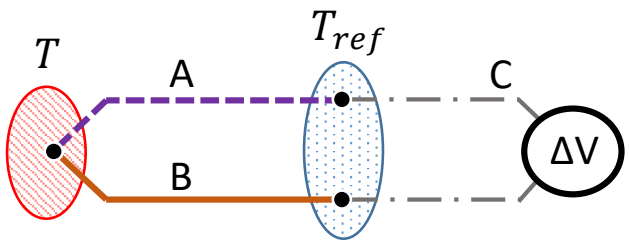

Figure 2.4 *Thermocouple circuit. A, B, and C are wires made of three different materials. T is the unknown temperature to be measured, and T_{ref} is a known reference temperature.*

2.1.5 The Thermoelectric Generator

Thermoelectric generators of electric power have been used for decades. Most satellites and space-probes are powered using one of these devices. A typical generator consists of a heat source, for example radioactive plutonium, surrounded by an array small units like those shown in figure 2.5.

Each unit consists of two legs, one made of a p-type, and the other an n-type semiconductor. The legs are connected at the top by a metallic conductor (shown in grey), which is exposed to the heat source. There are often extra layers (not shown) between the top plate and the actual heat source in order to aid heat flow and protect the device. Semiconductors are used as they tend to have large Seebeck and Peltier coefficients. P-type semiconductors have positive Seebeck coefficients, and n-type have negative. The different legs are connected in a circuit similar to the Seebeck experiment (Fig. 1.3 and 2.1). Just like in Seebeck's original experiment, a temperature difference across the unit (shown top to bottom in the figure 2.5) leads to a potential difference which drives a current.

The voltage from a single pair of $p-$ and $n-$ legs is too small for most practical applications (on the order of mV), but if many units are connected in series then a larger voltage can be obtained.

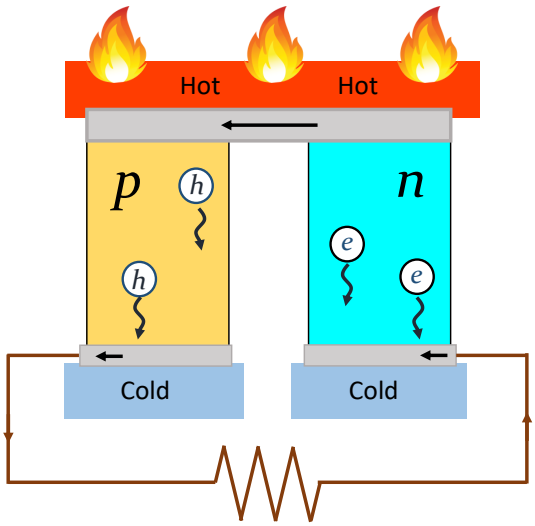

Figure 2.5 *Simplified thermoelectric generator circuit. There are two 'legs', made of one $p-$ and one $n-$doped semiconductor. Heat flow from the top to the bottom drives a current around the circuit anti-clockwise.*

How effectively a device turns heat into electricity depends on many factors, such as contact resistance between the conductor and the legs, or how effectively heat is transferred between the heat source and the top of each leg. There is

also an efficiency associated with the thermoelectric materials themselves. That efficiency is measured by the figure of merit.

2.1.6 The Thermoelectric Figure of Merit

The efficiency of a thermoelectric material is commonly quantified by the dimensionless figure of merit: ZT. It can be related to the maximum efficiency of energy conversion ($\eta_{\max}$) by a generator such as that shown in figure 2.5, where the thermoelectric material is held between a hot temperature T_h at one end, and cold temperature T_c at the other:

$$\eta_{\max} \approx \frac{T_h - T_c}{T_h} \times \frac{\sqrt{1 + ZT_{avg.}} - 1}{\sqrt{1 + ZT_{avg.}} + \frac{T_c}{T_h}}, \tag{2.8}$$

where $ZT_{avg.}$ is some kind of *'average ZT'* over the material[11]. The method for obtaining this $ZT_{avg.}$ is not uniquely defined. For most thermoelectric materials ZT varies significantly with temperature, so there is no simple way to obtain a $ZT_{avg.}$. Further discussion about how to relate a temperature dependent ZT to energy conversion efficiency can be found in the article by Kim *et al.*[11]. There is also a useful tool available for calculating it made by G. Snyder and A. Snyder[12,13]. I will not go into the detail about how this could be averaged, as it is sufficient for our purposes to know that the energy conversion efficiency $\eta_{\max}$ monotonically increases with ZT. Increasing ZT always improves the efficiency.

The figure of merit combines several material properties that need to be optimized for an efficient thermoelectric generator. It is given by:

$$ZT = \frac{\sigma S^2}{\kappa} T, \tag{2.9}$$

where σ is the electrical conductivity, S is the Seebeck coefficient, and κ is the thermal conductivity. The thermal conductivity depends both on heat carried by the electrons, and vibrations of the lattice. The numerator, specifically the Seebeck coefficient and electrical conductivity, depends on the electronic bandstructure. These terms are the focus of this thesis, and the theory behind how they are calculated is summarised in the next section.

2.2 Theory of Thermoelectricity

Various levels of theory are used in the literature on thermoelectric materials, from the most general results of the Boltzmann Transport Equation to the simple parabolic band approximation. This section will summarise some of the theory behind the thermoelectric effect, and the most common approximations.

2.2.1 The Boltzmann Transport Equation

The thermoelectric effects are all non-equilibrium effects, so some *equation of motion* is needed to describe how the distribution of electrons in both real and momentum space, change over time. The *Boltzmann transport equation* fills that role. It is a semi-classical equation that describes how an electron distribution over a combined phase space of position $\boldsymbol{r}$ and wavevector $\boldsymbol{k}$ changes with time. The phase-space distribution is quantified by using a time-dependent probability density function $f(t, \nu, b, \boldsymbol{k}, \boldsymbol{r})$. The phase-space function f is a function of both position $\boldsymbol{r}$, and wave vector $\boldsymbol{k}$. It is defined so that $f(t, \nu, b, \boldsymbol{k}, \boldsymbol{r}) \times \mathrm{d}^3\boldsymbol{r}\mathrm{d}^3\boldsymbol{k}$ is the number of spin ν electrons in the b^{th} band, at time t, in a small phase space volume $\mathrm{d}^3\boldsymbol{r}\mathrm{d}^3\boldsymbol{k}$ about the point $\boldsymbol{r}, \boldsymbol{k}$[14–16]. The dynamics of f describe how the probability density of electrons throughout phase space evolves over time. The Boltzmann transport equation for electrons is the equation of motion which governs this evolution.

To make progress, it is assumed that that f can be differentiated at least once with respect to time t, wave vector $\boldsymbol{k}$, and position $\boldsymbol{r}$. While the spin ν and band number b are important, for brevity I will drop these indices unless needed. The rate of change of the phase-space function with time $\dot{f}$ is determined through three main mechanisms: free movement; interaction with external fields; and scattering,

$$\dot{f} = \dot{f}|_{free} + \dot{f}|_{fields} + \dot{f}|_{scatt.}. \tag{2.10}$$

1. *Free movement.* If one imagines a single electron existing as a Bloch wave ψ, it will have a certain spatial density $(\psi^*\psi)$. The Bloch wave moves through space with a velocity given by $\boldsymbol{v_k} = \hbar^{-1}\partial E/\partial \boldsymbol{k}$. Thus, if the phase-space distribution has a spacial gradient $\boldsymbol{\nabla_r} f_{n,\boldsymbol{k}}$, f will change over time:

$$\dot{f}|_{free} = -\boldsymbol{v_k} \cdot \boldsymbol{\nabla_r} f. \tag{2.11}$$

Another way of considering this term is that the spacial distribution of an electron in state $(b, \boldsymbol{k})$ moves through the lattice with velocity $\boldsymbol{v_k}$ — as long as there are no other forces.

2. *External Field Interactions.* Electric ($\mathbf{E}$) and magnetic ($\mathbf{H}$) fields accelerate electrons. The Lorentz force will change the $\boldsymbol{k}$ vectors of electrons according to:

$$\hbar\dot{\boldsymbol{k}} = e\left(\mathbf{E} + \boldsymbol{v_k} \times \mathbf{H}\right). \tag{2.12}$$

Thus the occupation of different $\boldsymbol{k}$ points will change over time.

$$\dot{f}|_{\mathit{fields}} = -\frac{e}{\hbar}\left(\mathbf{E} + \boldsymbol{v}(b, \boldsymbol{k}) \times \mathbf{H}\right) \cdot \nabla_{\boldsymbol{k}} f, \tag{2.13}$$

where $\mathbf{H}$ is the magnetic field strength, $\boldsymbol{v}$ is the group velocity of state $(b, \boldsymbol{k})$, and $\mathbf{E}$ is the electric field.

3. *Scattering.* Real materials have imperfections which scatter the electrons. Even in a perfect crystal, electrons still scatter each other, or be scattered by phonons. These scattering mechanisms are responsible for equilibrating the system, and so they cannot be neglected. A scattering event will change the wave vector of an electron from $\boldsymbol{k}$ to $\boldsymbol{k'}$ or vice versa. Thus the scattering term is written as an integral over all wave vectors $\boldsymbol{k'}$ and bands b, with some transition functional $\mathfrak{P}$ which captures the probability of electrons transitioning from the state $(b, \boldsymbol{k})$ to $(b', \boldsymbol{k'})$, or vice versa:

$$\dot{f}(\boldsymbol{r}, b, \boldsymbol{k})\,|_{\mathit{scatt.}} = \sum_{b'} \int \mathrm{d}\boldsymbol{k'} \ \left[\mathfrak{P}_{in}\big(b', \boldsymbol{k'} \to b, \boldsymbol{k}\big) - \mathfrak{P}_{out}\big(b, \boldsymbol{k} \to b', \boldsymbol{k'}\big)\right]. \tag{2.14}$$

This transition functional $\mathfrak{P}$ could depend on the phase-space distribution f, the position $\boldsymbol{r}$, external fields, and the wave vectors in question. In principle, $\mathfrak{P}$ should include all possible scattering mechanisms and is a functional of the phase-space distribution itself. However, there are several simplifying assumptions that can be made about the scattering term which I shall summarise in a later section.

Putting all three processes together yields the Boltzmann Transport Equation for electrons in its most general form:

$$\dot{f}(t, b, \boldsymbol{k}, \boldsymbol{r}) = -\boldsymbol{v} \cdot \boldsymbol{\nabla}_{\boldsymbol{r}} f(t, b, \boldsymbol{k}, \boldsymbol{r}) \ \ - \frac{e}{\hbar}\left(\mathbf{E} + \boldsymbol{v} \times \mathbf{H}\right) \cdot \boldsymbol{\nabla}_{\boldsymbol{k}} f(t, b, \boldsymbol{k}, \boldsymbol{r}) \ + \ \dot{f}|_{\mathit{scatt.}}. \tag{2.15}$$

The Boltzmann Transport Equation describes how an electron distribution through phase space evolves over time. One of the key components is the scattering term, and to make the equation tenable, steps have to be taken to approximate this term.

Linearising the Boltzmann Transport Equation

One of the first steps towards simplifying the Boltzmann Transport Equation is to linearize it. The long term value of $f(t, \nu, b, \boldsymbol{k}, \boldsymbol{r})$ is the equilibrium number of particles in the phase space volume $\mathrm{d}^3\boldsymbol{k}\mathrm{d}^3\boldsymbol{r}$. This will be the Fermi-Dirac distribution for the local chemical potential $\mu(\boldsymbol{r})$ and temperature $T(\boldsymbol{r})$:

$$f_0(\nu, b, \boldsymbol{k}, \boldsymbol{r}) = \frac{1}{1 + \exp\left[\frac{1}{k_B T}\left(\varepsilon(\nu, b, \boldsymbol{k}) - \mu(\boldsymbol{r})\right)\right]}. \tag{2.16}$$

When in equilibrium, the scattering term must vanish,

$$\dot{f}_0|_{scatt.} = 0, \tag{2.17}$$

otherwise the Boltzmann transport equation would predict that, even for a completely homogeneous material with no external fields, the phase-space distribution changes over time. The scattering term is what restores the phase-space distribution f towards equilibrium.

If the electric, magnetic, and temperature fields are non-zero, the free movement, external field interaction, and scattering terms will also be non-zero. However, if the distribution f is very close to the equilibrium distribution, f can we rewritten as a sum of the equilibrium distribution f_0 and a small, time dependent perturbation δf:

$$f(t, \boldsymbol{k}, \boldsymbol{r}) = f_0(\boldsymbol{k}, \boldsymbol{r}) + \delta f(t, \boldsymbol{k}, \boldsymbol{r})\,. \tag{2.18}$$

The free movement and external field interaction terms are approximated in terms of f_0 rather than f, whilst only the lowest-order scattering term is taken. The scattering term is again written as an integral over all possible states $(b', \boldsymbol{k'})$. If $\delta f(b, \boldsymbol{k})$ is positive, then the state $(b, \boldsymbol{k})$ is more likely to be occupied than it is in equilibrium. Thus electrons are likely to transition out of that wave vector and into a different one, reducing $f(b, \boldsymbol{k})$ in the process. Similarly, if $\delta f(b', \boldsymbol{k'})$ is positive, then electrons are more likely to transition out of $(b', \boldsymbol{k'})$, potentially into $(b, \boldsymbol{k})$. The transition probability is quantified by a scattering

time between the states $(b, \boldsymbol{k})$ and $(b', \boldsymbol{k'})$ weighted by the perterbation of the phase-space distribution, δf, which captures how populated the states are relative to equilibrium:

$$\dot{f}(b, \boldsymbol{k}) \,|_{scatt.} = \sum_{b'} \oint \mathrm{d}\boldsymbol{k'} \; \frac{\delta f(b', \boldsymbol{k'})}{\tau^{b,\boldsymbol{k}}_{b',\boldsymbol{k'}}} - \frac{\delta f(b, \boldsymbol{k})}{\tau^{b',\boldsymbol{k'}}_{b,\boldsymbol{k}}}. \tag{2.19}$$

Equation 2.19 says that the rate of change of $f(b, \boldsymbol{k})$ due to scattering is the sum of scattering rates into $(b, \boldsymbol{k})$, minus the sum of scattering rates out of $(b, \boldsymbol{k})$ to some other state $(b', \boldsymbol{k'})$. According to the principle of microscopic reversibility, the term $\tau^{b',\boldsymbol{k'}}_{b,\boldsymbol{k}}$ must equal $\tau^{b,\boldsymbol{k}}_{b',\boldsymbol{k'}}$ [14,16], so equation 2.19 can be simplified to:

$$\dot{f}(b, \boldsymbol{k}) \,|_{scatt.} = \sum_{b'} \oint \mathrm{d}\boldsymbol{k'} \; \frac{\delta f(b', \boldsymbol{k'}) - \delta f(b, \boldsymbol{k})}{\tau^{b',\boldsymbol{k'}}_{b,\boldsymbol{k}}}. \tag{2.20}$$

If the scattering mechanism is known, for example there is a known scattering potential $\mathcal{H}'$, then τ could potentially be calculated using Fermi's Golden Rule. However, in most cases, calculating τ for all pairs of states $(b, \boldsymbol{k})$ and $(b', \boldsymbol{k'})$ is impractical. Most of the further simplifications summarised in this chapter will involve approximations for the scattering time function $\tau^{b',\boldsymbol{k'}}_{b,\boldsymbol{k}}$.

Adding the scattering term to the rest of the terms gives the full linearized Boltzmann transport equation:

$$\begin{aligned} \dot{\delta f}(t, \boldsymbol{k}, \boldsymbol{r}) = &-\boldsymbol{v_k} \cdot \boldsymbol{\nabla_r} f_0(\boldsymbol{k}, \boldsymbol{r}) \\ &- \frac{e}{\hbar} (\mathbf{E} + \boldsymbol{v_k} \times \mathbf{H}) \cdot \boldsymbol{\nabla_k} f_0(\boldsymbol{k}, \boldsymbol{r}) \\ &+ \sum_{b'} \int \mathrm{d}\boldsymbol{k'} \; \{\delta f\big(b', \boldsymbol{k'}\big) - \delta f(b, \boldsymbol{k})\} / \tau^{b',\boldsymbol{k'}}_{b,\boldsymbol{k}}. \end{aligned} \tag{2.21}$$

If looking for steady state solutions, the left hand side vanishes giving:

$$\begin{aligned} \boldsymbol{v}(b, \boldsymbol{k}) \cdot \boldsymbol{\nabla_r} f_0(b, \boldsymbol{k}, \boldsymbol{r}) \;\; + \;\; & \frac{e}{\hbar} (\mathbf{E} + \boldsymbol{v_k} \times \mathbf{H}) \cdot \boldsymbol{\nabla_k} f_0(\boldsymbol{k}, \boldsymbol{r}) \;\; = \\ & \sum_{b'} \int \mathrm{d}\boldsymbol{k'} \; \{\delta f\big(b', \boldsymbol{k'}\big) - \delta f(b, \boldsymbol{k})\} / \tau^{b',\boldsymbol{k'}}_{b,\boldsymbol{k}}. \end{aligned} \tag{2.22}$$

Relaxation Time Approximation

While first-principles estimates for the full electron scattering time function $\tau_{b,\boldsymbol{k}}^{b',\boldsymbol{k}'}$ are sometimes possible, for example through calculation of electron–phonon scattering terms, it is far more common to approximate this term. The Relaxation Time Approximation states that:

1. Scattering events always restore to the local equilibrium value for each state $f_0(b, \boldsymbol{k})$.
2. The scattering time which determines the rate of this restoration is independent of $f(b, \boldsymbol{k})$.

Both of these assumptions are generally appropriate when the phase-space distribution f is only a small perturbation δf from the local equilibrium phase-space distribution f_0, i.e. when using the linearized Boltzmann Transport Equation. Within the Relaxation Time Approximation the scattering term simplifies to:

$$\dot{f}(b, \boldsymbol{k}) \,|_{scatt.} = -\frac{1}{\tau(b, \boldsymbol{k})}\delta f, \tag{2.23}$$

where δf is the difference between the actual phase-space distribution f and the thermal equilibrium distribution f_0. In this equation, τ is of a more simple form that in Eq. 2.20; here it is only a function of the state $(b, \boldsymbol{k})$. Within this approximation, scattering tends the phase-space distribution towards local equilibrium on a timescale given by τ. Common further simplifications, discussed later, include making τ a function only of the energy of the state $(b, \boldsymbol{k})$, or even to set τ as a constant for all states.

2.2.2 The Thermoelectric Effect

The Boltzmann transport equation can quantitatively describe the thermoelectric effects. It leads to a series of integrals which can be used to compute transport properties such as the electrical conductivity, and Seebeck coefficient. Within the framework of linear response theory,* particle and heat currents ($\boldsymbol{j}$ and $\boldsymbol{j}^q$) are a linear response to the gradient of the local temperature field ($\boldsymbol{\nabla} T$), the gradient of the chemical potential field ($\boldsymbol{\nabla}\mu$), and the electric field ($\mathbf{E}$)[14,17–19]. This gives a tensor equation between the currents $\boldsymbol{j}$ and $\boldsymbol{j}^q$, and the fields $\boldsymbol{\nabla} T$, $\boldsymbol{\nabla}\mu$, and $\mathbf{E}$, with the coefficients $L^{\alpha\beta}$ known as the L-matrices :

*This is sometimes referred to as the *Kubo Formalism*.

$$\begin{pmatrix} \mathbf{j} \\ \mathbf{j}_q \end{pmatrix} = \begin{bmatrix} \mathbf{L}^{11} & \mathbf{L}^{12} \\ \mathbf{L}^{21} & \mathbf{L}^{22} \end{bmatrix} \begin{pmatrix} e\mathbf{E} - \boldsymbol{\nabla}\mu \\ -\boldsymbol{\nabla}T \end{pmatrix}. \tag{2.24}$$

The L-matrices quantify how gradients in temperature, chemical potential, and electrical potential fields are related to electron and thermal currents. If a material has a uniform temperature and chemical potential ($\boldsymbol{\nabla}\mu = \boldsymbol{\nabla}T = 0$), and an electric field is applied ($\mathbf{E} \neq 0$), then there will be a resulting electrical current given by

$$\mathbf{j} = \mathbf{L}^{11} e\mathbf{E}. \tag{2.25}$$

Thus, the first L-matrix is related to the electrical conductivity tensor by $e\mathbf{L}^{11} = \boldsymbol{\sigma}$. Similarly, for a material with no applied electric or chemical potential field ($\boldsymbol{\nabla}\mu = \mathbf{E} = 0$), the thermal current follows

$$\mathbf{j}^q = -\mathbf{L}^{22}\boldsymbol{\nabla}T. \tag{2.26}$$

Thus, $\mathbf{L}^{22}$ is the thermal conductivity of the electrons, usually denoted as κ. The other L-matrices $\mathbf{L}^{12}$ and $\mathbf{L}^{21}$ represent coupling terms between the electric & chemical potential fields, and the temperature field. In the Seebeck-effect experiment, no current is allowed to flow ($\boldsymbol{j} = 0$) and a temperature gradient is applied. This leads to the equation:

$$\boldsymbol{j} = \mathbf{L}^{11}(e\mathbf{E} - \boldsymbol{\nabla}\mu) - \mathbf{L}^{12}\boldsymbol{\nabla}T = 0, \tag{2.27}$$

$$\Rightarrow \quad e\mathbf{E} - \boldsymbol{\nabla}\mu = \left[\mathbf{L}^{11}\right]^{-1} \mathbf{L}^{12}\ \boldsymbol{\nabla}T. \tag{2.28}$$

Equation (2.28) describes the Seebeck effect. If a material has an applied $\boldsymbol{\nabla}T$ but no current flows, then there will be a potential difference, the magnitude of which depends on the L-matrices. The Seebeck coefficient, or thermopower, is the linear coefficient relating gradients in the temperature $\boldsymbol{\nabla}T$ and voltage $\boldsymbol{\nabla}V = -\boldsymbol{E}$;

$$\boldsymbol{\nabla}V \ = \ -\left(\frac{1}{e}\left[\mathbf{L}^{11}\right]^{-1}\mathbf{L}^{12}\right)\boldsymbol{\nabla}T \ := \ -\mathbf{S}\boldsymbol{\nabla}T, \tag{2.29}$$

$$\text{with} \qquad \mathbf{S} = \frac{1}{e}\left[\mathbf{L}^{11}\right]^{-1}\mathbf{L}^{12}, \tag{2.30}$$

where $\mathbf{S}$ is a (1,1) tensor usually given in microvolts per Kelvin. If the electrical properties of the material are isotropic, then equations (2.28) and (2.30) become scalar equations.

In the Seebeck effect no current is allowed to flow, and a temperature gradient induces a voltage difference. Equation 2.24 implies $\mathbf{j}_q$ will be non-zero, and a heat current must be maintained to keep the temperature gradient. This intuitively makes sense, as otherwise the material would equilibrate to a uniform temperature.

The Peltier Effect If an electric current $\mathbf{j}$ is driven through a material that is maintained at a uniform temperature, then a heat current will be induced. This is the Peltier effect. Substituting $\boldsymbol{\nabla} T = 0$ into equation (2.24) gives a relation for the Peltier coefficient Π:

$$\mathbf{j} = \mathbf{L}^{11}(e\mathbf{E} - \boldsymbol{\nabla}\mu) \neq 0, \tag{2.31}$$

$$e\mathbf{E} - \boldsymbol{\nabla}\mu = \left[\mathbf{L}^{11}\right]^{-1}\mathbf{j}, \tag{2.32}$$

$$\Rightarrow \quad \mathbf{j}_q = \mathbf{L}^{21}\left[\mathbf{L}^{11}\right]^{-1}\mathbf{j}, \tag{2.33}$$

$$\Rightarrow \quad \mathbf{j}_q = \Pi\mathbf{j}, \tag{2.34}$$

$$\text{with} \quad \Pi = \mathbf{L}^{21}\left[\mathbf{L}^{11}\right]^{-1} \tag{2.35}$$

Note that the equation for Π looks very similar to that for S (Eq. 2.30). Indeed, $\mathbf{L}\hat{}12$ and $\mathbf{L}\hat{}21$ differ by a scalar, as do S and Π (Eq. 2.3).

2.2.3 Computing the L-matrices

If the bandstructure of a material is known, then the L-matrices can be computed by using expressions derived from the Boltzmann transport equation. These expressions are the bridge that connects electron transport properties to the bandstructure of the material. A brief summary of how these expressions are derived is given here.

The electronic current density j_i at point $\boldsymbol{r}$ in the direction $\hat{i}$ can be written as a sum over all states $(b, \boldsymbol{k})$, weighted by the group velocity v_i and the phase-space distribution f of each state:

$$j_i(\boldsymbol{r}) = e\sum_b \oint \mathrm{d}^3\boldsymbol{k} f(b, \boldsymbol{r}, \boldsymbol{k}) \times v_i(b, \boldsymbol{k}). \tag{2.36}$$

For a crystal, the group velocity $\boldsymbol{v} = \hbar^{-1}\nabla_{\boldsymbol{k}}\varepsilon(b, \boldsymbol{k})$ is the derivative of a function which is periodic in $\boldsymbol{k}$. As a result, the integral from filled bands must vanish,

leading to the expected result that only partially filled bands contribute to the electrical current.

The thermal current density due to electrons j_i^q is given by the flow of electrons, weighted by their energy relative to the chemical potential μ[14]. Electrons with energy ε greater than μ will transfer heat in the same direction they travel, and vice versa.

$$j_i^q(\boldsymbol{r}) = \sum_b \oint \mathrm{d}^3\boldsymbol{k} \left[\varepsilon_b(\boldsymbol{k}) - \mu\right] f(b, \boldsymbol{r}, \boldsymbol{k}) v_i(b, \boldsymbol{k}). \tag{2.37}$$

Within the linearised Boltzmann Transport Equation, the relaxation time approximation, and assuming the electron-scattering-time function τ only depends on the energy of states ($\tau(b, \boldsymbol{k}) = \tau(\varepsilon(b, \boldsymbol{k}))$), the phase-space distribution function f must satisfy:

$$f(b, \boldsymbol{r}, \boldsymbol{k}) = f_0(b, \boldsymbol{r}, \boldsymbol{k}) + \tau(\varepsilon(b, \boldsymbol{k})) \left(-\frac{\partial f_{\mathrm{FD}}}{\partial \varepsilon}\right) \boldsymbol{v}(b, \boldsymbol{k}) \times \left[e\boldsymbol{E} - \boldsymbol{\nabla}\mu + \frac{\varepsilon(b, \boldsymbol{k}) - \mu}{T} \left(-\boldsymbol{\nabla} T\right)\right], \tag{2.38}$$

where $\partial f_{\mathrm{FD}}/\partial\varepsilon$ is the rate of change of the Fermi Dirac distribution for the local temperature $T(\boldsymbol{r})$ and chemical potential $\mu(\boldsymbol{r})$ at energy $\varepsilon(b, \boldsymbol{k})$, v_i is the band group velocity for state $(b, \boldsymbol{k})$ along the direction $\hat{i}$, $\boldsymbol{E}$ is the electric field, and τ is the electron-scattering time.

Solving equations (2.36)-(2.38) returns relationships for the L-matrices. It is useful to introduce an *energy-dependent conductivity tensor* $\phi(b, \boldsymbol{k})$, which essentially quantifies the contribution of each state $(b, \boldsymbol{k})$ to transport properties[20], such as the electrical conductivity. I define it here as:

$$\phi_{ij}(b, \boldsymbol{k}, \boldsymbol{r}) = \tau(b, \boldsymbol{k}) v_i(b, \boldsymbol{k}) v_j(b, \boldsymbol{k}) \left(-\frac{\partial f_{\mathrm{FD}}}{\partial \varepsilon}\right), \tag{2.39}$$

where $\partial f_{\mathrm{FD}}/\partial\varepsilon$ is the rate of change of the Fermi Dirac distribution for the local temperature $T(\boldsymbol{r})$ and chemical potential $\mu(\boldsymbol{r})$ at energy $\varepsilon(b, \boldsymbol{k})$, v_i is the i^{th} index of the band group velocity for state $(b, \boldsymbol{k})$, and τ is the electron-scattering time. The τ and $v_i v_j$ terms are related to the mobility of electrons in a state, while the $-\partial f_{\mathrm{FD}}/\partial\varepsilon$ term quantifies how populated the state $(b, \boldsymbol{k})$ is; capturing the idea that partly populated states contribute towards transport, but states which are fully populated — or completely unoccupied — do not.

The equations for the L-matrices are integrals over all states of the energy-

dependent conductivity tensor ϕ_{ij}, multiplied by some factor which may depend on the energy:

$$\mathrm{L}_{ij}^{(11)} = e \sum_b \oint \frac{\mathrm{d}^3\boldsymbol{k}}{4\pi^3} \phi_{ij}(b, \boldsymbol{k}, \boldsymbol{r}) \,, \tag{2.40}$$

$$\mathrm{L}_{ij}^{(21)} = \frac{T}{e}\mathrm{L}_{ij}^{(12)} = \sum_b \oint \frac{\mathrm{d}^3\boldsymbol{k}}{4\pi^3} \phi_{ij}(b, \boldsymbol{k}, \boldsymbol{r}) \left(\varepsilon(b, \boldsymbol{k}) - \mu\right) , \tag{2.41}$$

$$\mathrm{L}_{ij}^{(22)} = -\frac{1}{T} \sum_b \oint \frac{\mathrm{d}^3\boldsymbol{k}}{4\pi^3} \phi_{ij}(b, \boldsymbol{k}, \boldsymbol{r}) \left(\varepsilon(b, \boldsymbol{k}) - \mu\right)^2 . \tag{2.42}$$

For ease of reference I will also list the equations for the electrical conductivity σ, Seebeck S, and thermal conductivity of electrons tensors κ:

$$\sigma_{ij} = e\mathrm{L}_{ij}^{(11)}, \tag{2.43}$$

$$S_{ij} = \sum_\alpha \frac{1}{e} \left(\left[\mathrm{L}^{(11)} \right]^{-1} \right)_{i\alpha} \mathrm{L}_{\alpha j}^{(12)}, \tag{2.44}$$

$$\kappa_{ij} = \mathrm{L}_{ij}^{(22)}. \tag{2.45}$$

Using equations 2.39 – 2.42, the L-matrices can be evaluated for a given bandstructure, temperature, and chemical potential. These equations are sometimes called *the Mott formulae*. They form a bridge between the quantum mechanical bandstructure, and the macroscopic electron transport properties.

Energy Range of Importance

A key coefficient in the L-matrix integrands is the rate of change of the Fermi-Dirac distribution with energy, $-\partial f_{\mathrm{FD}}/\partial\varepsilon$. This term quantifies, to an extent, the energy-range of importance for the $\mathrm{L}^{(11)}$-matrix, and depends on the chemical potential and the temperature. At low temperatures, this function is a narrow peak around μ, which gets broader at higher temperatures. Figure 2.6(a) illustrates this factor for three different temperatures. For a sense of scale, this factor is 10 % of its' greatest value for states with energies $\pm 3.6 k_B T$ away from the chemical potential μ.

The $\mathrm{L}^{(12)}$-matrix depends on $\partial f_{\mathrm{FD}}/\partial\varepsilon \times (\varepsilon - \mu)$. Figure 2.6(b) illustrates this

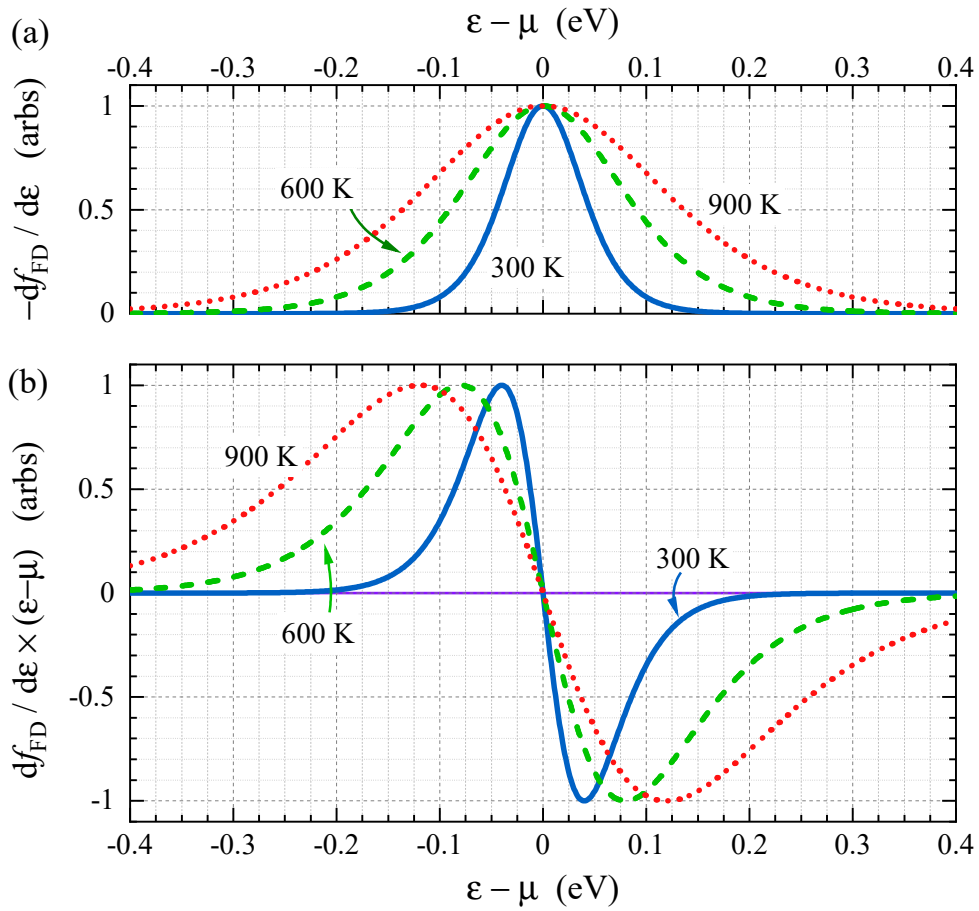

Figure 2.6 *Coefficients important to determining the energy scale of importance in the L-matrix integrals, as a function of energy varepsilon minus the chemical potential μ. (a) the rate of change of the Fermi-Dirac distribution with energy, $df_{FD}/d\varepsilon$, normalized so all three peaks are the same height. This is a factor of the $L^{(11)}$-matrix integrand (Eq. 2.40). (b) $df_{FD}/d\varepsilon$ multiplied by $\varepsilon - \mu$. This is a factor of the $L^{(12)}$-matrix integrand (Eq. 2.41).*

factor, which is an odd function around the chemical potential μ. Importantly, at this function does not decay with increasing ε as fast as the factor of the $L^{(11)}$-matrix [Fig. 2.6(a)]. This means that the $L^{(12)}$-matrix (and thus the Seebeck coefficient) are sensitive to parts of the bandstructure with different energies. As a rule of thumb, the magnitude of this factor is 10 % of its' greatest value for states $\pm 5.5 k_B T$ away from the chemical potential μ.

Equations 2.40–2.42 can be further simplified by assuming that the electron-scattering-time τ is a constant for all states contributing to transport properties, i.e. all states within several $k_B T$ of the chemical potential μ. This *constant scattering time approximation* allows τ to be factorized out from the L-matrix integrals, so the *reduced electrical conductivity* σ/τ, Seebeck coefficient, and

reduced thermal conductivity κ/τ can be calculated without the need to estimate τ.

The Hall Coefficient

Equations for the Hall coefficients $R_{\alpha\beta\gamma}$ involve a term similar to the energy-dependent conductivity tensor, here labelled $\Phi_{ijk}(b, \boldsymbol{k})$. It is most elegantly written using the Levi-Civita symbol ϵ_{ijk}:

$$\Phi_{ijk}(b, \boldsymbol{k}) = \sum_{\alpha,\beta} \tau(b, \boldsymbol{k})^2 \, \epsilon_{k\alpha\beta} v_i(b, \boldsymbol{k}) \, v_\beta(b, \boldsymbol{k}) \, M^{-1}_{j\alpha}(b, \boldsymbol{k}) \,, \tag{2.46}$$

where τ is the electron scattering time for the state in band b with wavevector $\boldsymbol{k}$; i, j, k index orthogonal basis vectors; v is the group velocity, and M^{-1} is the inverse of the effective mass tensor, defined in terms of the rate of change of the energy with respect to wavevector:

$$M^{-1}_{ij}(b, \boldsymbol{k}) = \frac{1}{\hbar^2} \frac{\partial^2 \varepsilon(b, \boldsymbol{k})}{\partial k_i \partial k_j} \tag{2.47}$$

The Hall coefficient is obtained by first integrating Φ_{ijk} over all electron states $(b, \boldsymbol{k})$ weighted by the rate of change of the Fermi-Dirac distribution with energy $\partial f_{\mathrm{FD}}/\partial \varepsilon$, and then dividing by the conductivity σ squared:

$$\Xi_{ijk} = \sum_b \oint_{BZ} \frac{d^3k}{(2\pi)^3} \Phi_{ijk}(b, \boldsymbol{k}) \,, \tag{2.48}$$

$$R_{\alpha\beta\gamma} = \sum_{ij} \left[\sigma^{-1}\right]_{i\beta} \Xi_{ij\gamma} \left[\sigma^{-1}\right]_{\alpha j} . \tag{2.49}$$

These equations quantify how the Hall coefficient is affected by different band velocities, scattering times, and the curvature of the bandstructure. Importantly, within the constant-scattering-time approximation, the Hall coefficient is independent of the scattering time τ.

2.2.4 Common Simplifications

There are several formulas derived from two common simplifications used in discussions surrounding thermoelectric materials. The results in this thesis will show that both of these simplifications do not always apply, but I include them here anyway for how they inform common understanding of what makes a good

thermoelectric material.

The Sommerfeld Expansion

A common simplification used to calculate the Seebeck coefficient is the *Sommerfeld expansion* (sometimes confusingly referred to as the *Mott formula*)[21–23]. Strictly speaking, the Sommerfeld expansion is an expansion of the L-matrix equations (Eq. 2.40–2.42) with the added assumption that the energy-dependent conductivity tensor $\phi_{ij}(\varepsilon)$ (Eq. 2.39) only varies slowly with energy over the scale of $k_B T$:

$$\left[\frac{\partial \phi_{ij}}{\partial \varepsilon}\right]_{\varepsilon=\mu} k_B T \ll \phi_{ij}(\mu) \tag{2.50}$$

Within this assumption, one can Taylor-expand the energy-dependent conductivity tensor (originally Eq. 2.39):

$$\phi_{ij}(\varepsilon) \approx \phi_{ij}(\mu) + (\varepsilon - \mu)\left[\frac{\partial \phi_{ij}}{\partial \varepsilon}\right]_{\varepsilon=\mu} + ... \tag{2.51}$$

Combined with the assumption that the scattering-time τ only depends on the energy, the Sommerfeld expansion of Eq. 2.40–2.42 allows a simplified equation for the Seebeck coefficient to be derived[16]:

$$S_{ij} = -\frac{\pi^2 k_B^2 T}{3|e|}\left[\frac{\partial \ln \phi_{ij}(\varepsilon)}{\partial \varepsilon}\right]. \tag{2.52}$$

A valuable insight this equation gives is that the sign and magnitude of the Seebeck coefficient is determined by the rate of change of ϕ with energy ε. If, for example, the density of states reduces with increasing ε, then the Seebeck coefficient will probably be positive. Conversely, in an idealized metal like the Drude model, where the band velocity and density of states increases with increasing ε, then S will be negative. Furthermore, if the velocity and density of states are constant, but the electron-scattering-time τ have a strong energy dependence, that can also affect S.

The Sommerfeld expansion is a good approximation for a metal, where the density of states and the band velocities might remain similar for most states within a few $k_B T$ of the Fermi energy. However, this approximation is entirely inappropriate for non-degenerate semiconductors — where the chemical potential μ is within a few $k_B T$ of the band edge, and thus ϕ changes rapidly on the scale of $k_B T$. If ϕ changes rapidly, Eq. 2.52 will not give an accurate result. Nevertheless,

the qualitative observation that a large rate-of-change of the density of states is correlated with a large Seebeck coefficient, often still applies to low-doped semiconductors.

Degenerate Parabolic Band

Because many of the most efficient thermoelectrics are semiconductors, a common simple model used to analyse thermoelectrics is the single parabolic band. In this case, with a constant scattering-time approximation, the electrical conductivity σ has the familiar form:

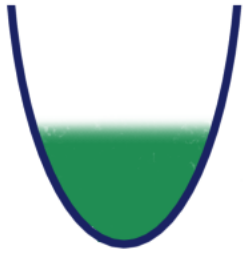

$$\sigma = \frac{ne^2\tau}{m^*}, \tag{2.53}$$

where n is the carrier density (e.g. the doping concentration of the semiconductor), τ is the electron-scattering-time, e is the fundamental charge, and m^* is the effective mass of the parabolic band.

Using the Sommerfeld expansion (Eq. 2.52) and the constant-scattering-time approximation, the Seebeck coefficient can be calculated as[21–23]:

$$S = -\frac{k_B^2}{|e|\hbar^2} m^* T \left(\frac{4\pi}{3n}\right)^{2/3}. \tag{2.54}$$

Within the parabolic band approximation, the magnitude and sign of the Seebeck coefficient is clearly determined by the effective mass m^*. A larger effective mass leads to a larger Seebeck coefficient. Furthermore, the magnitude of S reduces with increasing doping concentration n. This is commonly seen in experiment.

An important part of the thermoelectric figure of merit is the thermoelectric power factor σS^2. Combining Eq. 2.54 and 2.53 implies that increasing the doping concentration n will reduce the power factor: $\sigma S^2 \propto n^{-1/3}$. This is common for very heavily doped semiconductors (degenerate semiconductors), where one expects the Sommerfeld expansion to be valid, but it is not the case for low and intermediate dopings (usually up to $\sim 10^{20}\,\mathrm{cm}^{-3}$). Furthermore, because the Sommerfeld expansion is only valid when $\partial\phi/\partial\varepsilon \times k_B T$ is small compared to ϕ, Eq. 2.54 also breaks down at high temperatures.

Low-doped, cold, 2-parabolic band model

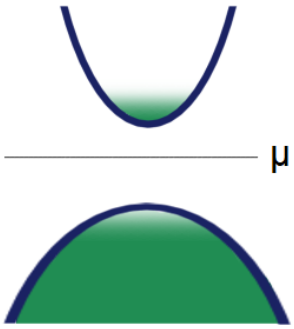

This model is a simple picture of a semiconductor made up of two parabolic bands.

For a semiconductor with a low level of doping, i.e. a non-degenerate semiconductor, the chemical potential μ lies between the energies of the conduction and valence band extrema: E_{CBM}, and E_{VBM}, respectively. In this model, the valence and conduction band edges are assumed to be parabolic and isotropic, with effective masses m_V^* and m_C^* respectively. The constant-scattering-time approximation is also assumed. Furthermore, the temperature is sufficiently low, so that $E_{\mathrm{CBM}} - \mu$ and $\mu - E_{\mathrm{VBM}} >> k_B T$.

Within these approximations, the the conductivity and Seebeck coefficient for each band can be written as follows[24]:

$$\sigma_C = \Omega \left(m_C^*\right)^{\frac{1}{2}} T^{\frac{3}{2}} e^{\frac{\mu - E_{\mathrm{CBM}}}{k_B T}} \tag{2.55}$$

$$\sigma_V = \Omega \left(m_V^*\right)^{\frac{1}{2}} T^{\frac{3}{2}} e^{\frac{E_{\mathrm{VBM}} - \mu}{k_B T}} \tag{2.56}$$

$$S_C = -\frac{k_B}{|e|}\left(\frac{E_{\mathrm{CBM}} - \mu}{k_B T} + \frac{3}{2}\right) \tag{2.57}$$

$$S_V = \frac{k_B}{|e|}\left(\frac{\mu - E_{\mathrm{VBM}}}{k_B T} + \frac{3}{2}\right), \tag{2.58}$$

where m_V^* and m_C^* are the effective masses for the valence and conduction bands, respectively; e is the electron charge; and T is the temperature. Ω is a group of constants, including the electron-scattering-time τ:

$$\Omega = 2\left(\frac{k_B}{2\pi\hbar^2}\right)^{3/2} \tau e^2. \tag{2.59}$$

The overall Seebeck coefficient of the material is given by:

$$S_{tot} = \frac{\mathrm{L}_C^{(12)} + \mathrm{L}_V^{(12)}}{\sigma_C + \sigma_V} = \frac{\sigma_C S_C + \sigma_V S_V}{\sigma_C + \sigma_V}, \tag{2.60}$$

where $\mathrm{L}_C^{(12)}$ and $\mathrm{L}_V^{(12)}$ are the $\mathrm{L}^{(12)}$ matrices calculated by only integrating over states in the conduction-bands or valence-bands, respectively; and σ_C and σ_V are the conductivities associated with the conduction and valence-bands, respectively.

The form of Eq. 2.60 leads to a distinctive trend between the overall Seebeck coefficient and the chemical potential (Fig. 2.7).

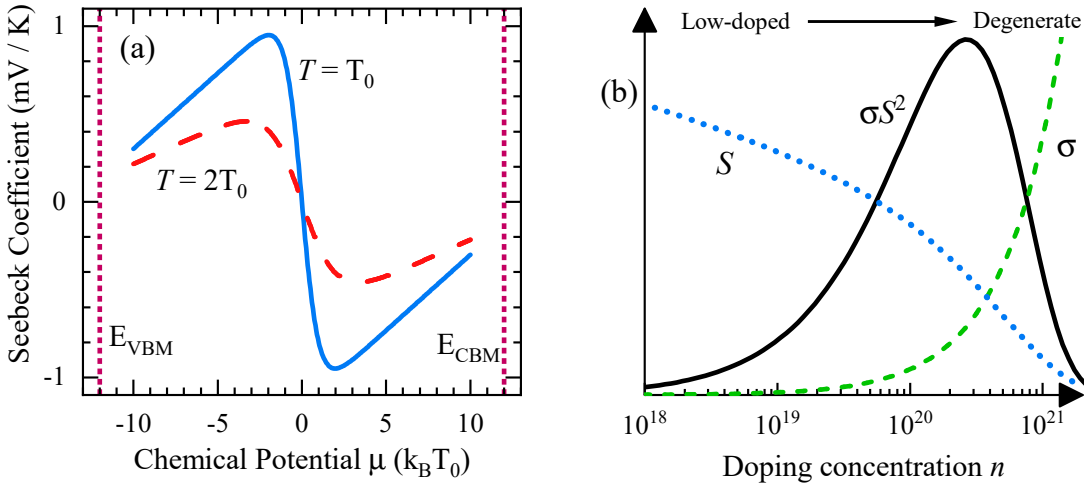

Figure 2.7 *(a) Seebeck coefficient vs chemical potential for a low-doped semiconductor at two different arbitrary temperatures: T_0 and $2T_0$. Both the valence and conduction bands are set to have equal effective masses. The valence-band maximum and conduction-band mininum have energies of -12 and $+12k_BT_0$, respectively. (b) Illustration of the dependence of electron transport properties upon doping concentration for a typical semiconductor well approximated by a parabolic band. The scales are arbitrary.*

A key fact illustrated by Fig. 2.7(a) is how, in the low-doped cold regime, the Seebeck coefficient changes with the dopant concentration n_{dop}. As the chemical potential approaches a band edge, the magnitude of the Seebeck coefficient reduces linearly with μ. However, the electrical conductivity increases exponentially with μ, because the carrier concentration is increasing (Eq. 2.55& 2.56). Indeed, in the low doped regime, the thermoelectric power-factor σS^2 increases with increasing n_{dop}.

However, equations 2.53 and 2.54 for the degenerate parabolic band imply that the power factor *reduces* with increasing n_{dop}. Indeed, as the doping concentration of a semiconductor increases, at some point a maximum value for the power factor will be reached, after which the power factor will reduce with increasing n_{dop} [Fig. 2.7(b)].

Two carrier pockets are better than one

Simplified systems can be useful to explain why some thermoelectrics have greater power-factors than others. For example: it is conventional wisdom

that semiconductors which have multiple carrier pockets can generally achieve greater power factors[21]. This can be understood through the equations for the degenerate parabolic band.

Suppose one wants to n-dope a material with concentration n electrons. If the conduction-band of that material is well described by a single parabolic band with effective-mass m^*, then it will achieve a certain Seebeck coefficient given (approximately) by Eq. 2.54. The magnitude of the Seebeck coefficient S decreases with increasing doping concentration n:

$$|S| \propto n^{-2/3} \qquad \sigma \propto n. \tag{2.61}$$

Now suppose an alternative material, the conduction-bandstructure of which consists of two separate parabolic bands, different carrier pockets A & B, each of which has the same effective-mass m^*. In this case, the n-dopant electrons are equally distributed between the two seperate bands. The total electrical conductivity can be written as a sum over contributions from each carrier pocket:

$$\sigma' = \sigma'_A + \sigma'_B = \frac{\sigma}{2} + \frac{\sigma}{2} = \sigma \tag{2.62}$$

where σ' is the new total electrical conductivity for the 2-pocket material, σ is the conductivity for the 1-pocket material, and $\sigma_A = \sigma/2$ because the conductivity is directly proportional to the carrier concentration in that pocket, $\sigma \propto n$.

On the other hand, because the Seebeck coefficient is proptional to $n^{-2/3}$, the Seebeck coefficient in the 2-pocket material S' is greater than for the 1-pocket material:

$$S' = \frac{\sigma_A S_A + \sigma_B S_B}{\sigma_A + \sigma_B} \tag{2.63}$$

$$= \frac{\frac{\sigma}{2} S (0.5)^{-2/3} + \frac{\sigma}{2} S (0.5)^{-2/3}}{\frac{\sigma}{2} + \frac{\sigma}{2}} \tag{2.64}$$

$$= S \times (0.5)^{-2/3} \approx 1.6S, \tag{2.65}$$

where S is the original Seebeck coefficient for the 1-pocket material.

Again, this assumes many things that are not valid for many thermoelectric materials , such as the parabolic band model and degenerate doping. However, in many cases the *qualitative* message, that two pockets are better than one, is helpful for understanding why changes in the bandstructure can improve thermoelectric properties.

2.3 Thermoelectric Properties of Lead Telluride

2.3.1 Introduction

The front page of the Washington Post, January 1959, shows a photo of President Eisenhower inspecting a new invention: the "Atom Battery". The article boasts "the 5-pound unit is equivalent to 1450 pounds of conventional batteries", and says it can power things from ocean buoys to satellites. In the core of the generator is radioactive polonium-210, an isotope which can give off enough heat to power the generator for around a year. Surrounding the hot core is an array of lead telluride thermoelectric devices, designed to generate power by siphoning the core's heat. Just over a decade later, a lead telluride-based generator — similar to the one shown on Eisenhower's desk — would power Apollo 12's scientific instruments on the moon.

First Atom Battery Developed by U. S.

By Edward Gamarekian
Staff Reporter

Front page story from the Washington Post 1959[25]; "President Eisenhower inspects the world's first atomic battery, displayed publicly for the first time yesterday."

Lead telluride is possibly the most prestigious thermoelectric material, and to this day remains one of the highest ZT thermoelectrics. However, there are two main drawbacks: PbTe is poisonous, and tellurium is expensive. These drawbacks hinder commercialization of PbTe devices, motivating efforts to find cheaper and safer alternative materials[26]. Despite the drawbacks, understanding why PbTe is such an effective thermoelectric material — and how it can be improved — can guide the search for new materials with a high ZT.

2.3.2 Bandstructure

The bandstructure of PbTe is part of what enables a high power factor to be achieved. PbTe is a semiconductor with a narrow band gap between ∼0.2 and 0.4 eV, depending on the temperature. Figure 2.9 shows a diagram of the Brillouin zone and the bandstructure from the *ab initio* calculations in this thesis (details in section 3.2.2). The band edges are located at the L-point of the Brillouin Zone, forming a direct band gap. For most doping concentrations and temperatures,

states outwith about 0.5 eV of the band edges will not contribute most to the transport properties. Near the band edges, the valence and conduction bands have a much steeper gradient along W–L or K–L, than they do along L–Γ. Energy isosurfaces within ∼100 meV of the valence band maxima or conduction band minima look like prolate ellipsoids, with the longest axis oriented towards the Γ point. This shows that the transport properties of each individual carrier pocket are direction-dependent, with mobility along the L–Γ direction ([111]) being much lower on average than mobility perpendicular to it. It is the cubic symmetry of PbTe — and resulting equivalence of the four carrier pockets — which makes the overall electron transport properties isotropic.

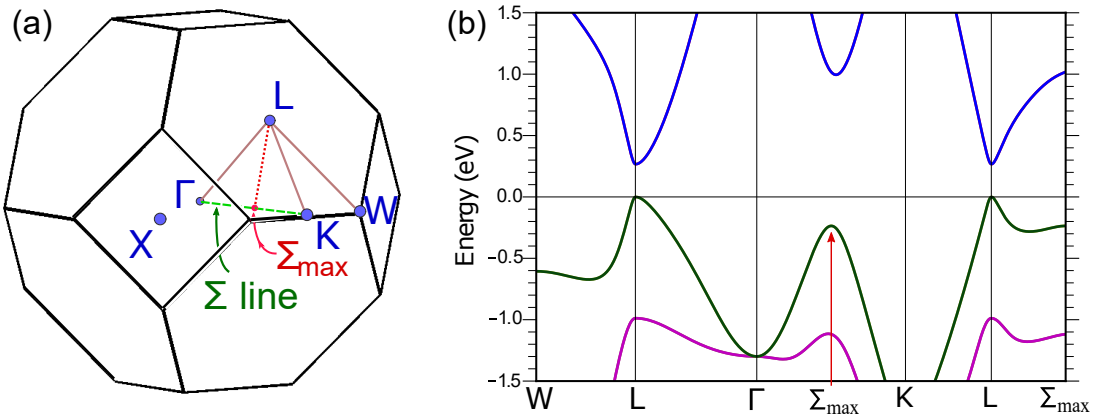

Figure 2.9 *(a) Brillouin Zone of PbTe. (b) Bandstructure of PbTe. Σ_{max} is the position of the maximum along the L–K line, and is the location of a local maximum of the valence band. The L–Σ_{max} line is a straight line through the Brillouin zone between the L-point and Σ_{max}.*

Around the conduction band minimum (CBM) and valence band maximum (VBM) at the L-point, the band edges are strongly non-parabolic. On the scale of tens of meV from the extrema, the bands have a Dirac-like dispersion with the curvature reducing as one moves further into the band[27,28]. A dispersion resembling a first order *Kane model* is often used to describe the the band edges[27–33]. The Kane model was originally derived to explain the bandstructure of indium antimonide, and is a successful model for describing the bandstructures and band gaps of many narrow-gap semiconductors[34]. This model is given by an equation of the form,

$$E\left(\Delta\boldsymbol{k}\right) = E_0 \pm \left(E_\alpha - \sqrt{E_\alpha^2 + \sum_i \left(\boldsymbol{P}_i \cdot \Delta\boldsymbol{k}\right)^2} \right), \tag{2.66}$$

where $\Delta\boldsymbol{k}$ is the distance in k-space from the band extremum, E_0 is the energy of

the band edge, E_α is a parameter which defines the energy scale over which the Kane-model appears parabolic, and $\boldsymbol{P}_1$–$\boldsymbol{P}_3$ are three orthogonal vectors, oriented along the major axes i of the carrier pocket, which describe the orientation of the band and its gradient at large $\Delta\boldsymbol{k}$. Technically, the Kane-model relates E_α and $\boldsymbol{P}_i$ to the band gap and effective mass at $\boldsymbol{k} = 0$ (Appendix A.5), however, for the purpose of fitting the bandstructure they can be treated like free parameters. More detail about the Kane model is given in Appendix A.5, the key point is that the effective mass is not the same for all states in the band: it increases as one moves away from the band edge.

The valence band has a more complex shape than the conduction band. There is a local maximum along the Σ line between Γ and K, often referred to as the Σ maximum (Fig. 2.9). The local maximum at Σ_{max} and the valence band maximum at L are all part of the same band, and are connected by a saddle point in the electronic bandstructure[27,28,33,35–38]. Figure 2.10 shows how energy isosurfaces of the valence band merge together, as the isoenergy moves deeper into the band. Energy isosurfaces below the saddle point reveal a tube-like structure, connecting the L-points via Σ_{max}[35,38]. At energies comparable to the maximum at Σ_{max} the bandstructure near the L-point deviates from the Kane-model[33].

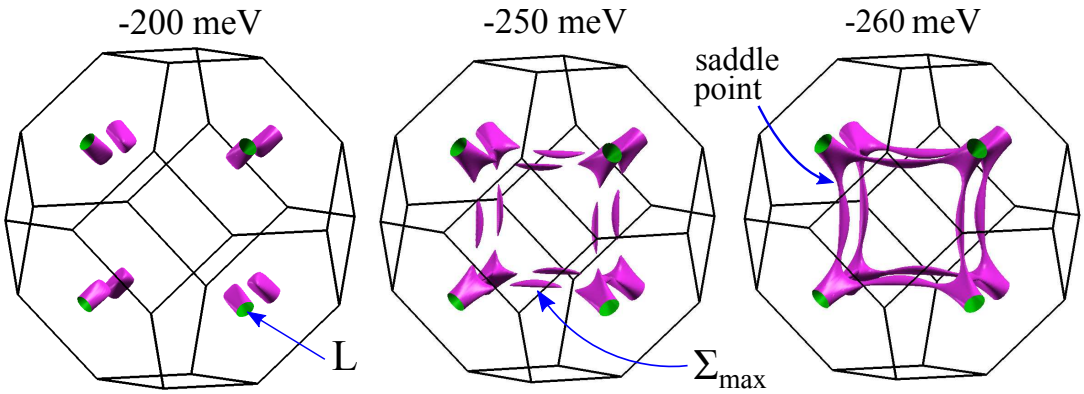

Figure 2.10 *Left to right: Energy isosurfaces 200, 250, and 260 meV below the valence band maximum.*

Experimental estimates of the energy difference between the maxima at Σ_{max} and L_{max}, $\Delta\epsilon_{L\Sigma}$, vary. At low temperatures, less than 70 K, $\Delta\epsilon_{L\Sigma}$ is estimated to be at least 140, or over 190 meV[27,33,39]. However, actual measurements of this are tricky[27] due to the difficulties of estimating carrier concentration, and the need to model the unknown bandstructure in some way.

2.3.3 Measuring the carrier concentration

Trends in transport properties with carrier concentration are often used to infer information about the bandstructure of semiconductors. The thermoelectric performance of a material is sensitive to carrier concentration. However, measuring the carrier concentration of a doped semiconductor to more than ∼1 significant figure is difficult. One approach is to carefully control the number of moles of dopant atoms before growing the crystal — however, this is not necessarily the number of electrons/holes which will carry charge. The crystal growing process does not guarantee that all the dopant atoms will be homogeneously distributed throughout the crystal; some may migrate to the surface, or form defect-like clusters within the sample. Furthermore, at very cold temperatures most semiconductors enter a "freeze-out" or "ionization" regime, where only a portion of the dopant atoms are ionized to contribute towards electronic transport. Crystal defects other than chemical impurities may act as donors or acceptors, meaning even an undoped semiconductor often has some effective doping concentration. Finally, typical thermoelectric doping concentrations are between 10^{17} and $10^{21}\mathrm{cm}^{-3}$, 6–2 orders of magnitude smaller than typical atom densities of the host crystal. Maintaining a high relative level of accuracy can be impractical.

A more common approach is to estimate the carrier concentration by measuring the Hall coefficient at a low temperature. The weak-field Hall coefficient R_0 of a semiconductor is related to the carrier concentrations of holes n_h and electrons n_e:

$$R_0 = \frac{\mu_h^2 n_h - \mu_e^2 n_e}{e\left(\mu_h n_h + \mu_e n_e\right)^2} r_H, \tag{2.67}$$

where μ_h and μ_e are the carrier mobilities of holes and electrons respectively. Sometimes called the *"Hall anisotropy factor"* or — I believe more helpfully — the *Hall mixing factor*[40], r_H is a factor which depends on the shape of the bandstructure and on electron scattering times[†]. At low temperatures, when

[†] *"The variation in the response of different carriers to the same force determines r_H in any particular case. This is one kind of anisotropy. A second kind is the anisotropic response of a given carrier to forces in different directions. For materials which do not have cubic symmetry, this may lead to a value of r_H which depends on the direction of applied force.*

The factor r_H is sometimes called an anisotropy factor in cases of metallic models. This can be confusing, because of the two distinct types of anisotropy just mentioned. It can also be misleading, since mixing can occur without anisotropy (e.g., $r_H \neq 1$ for a simple metallic model with two spherical, parabolic bands) while an anisotropic Fermi surface does not always produce mixing ($r_H = 1$ for a single, ellipsoidal energy surface). For these reasons it seems preferable to treat r_H as a mixing factor" — Allgaier (1968)[40]

only holes or electrons contribute to the Hall effect, measurements of the Hall coefficient can be used to derive a *Hall carrier concentration* n_H, which can be used to approximate the true carrier concentration n if r_H is of order unity:

$$n_H = \frac{1}{|R_0 e|} \sim n. \tag{2.68}$$

However, using the Hall coefficient to estimate the true carrier concentration has its dangers. The shape of the bands (manifested in the effective mass m^*) and the scattering time τ both affect the Hall coefficient. Mixing carriers with different effective masses and/or scattering times leads to a mixing factor r_H which differs from 1[40]. Materials with strongly non-parabolic bandstructures, such as PbTe, can have Hall carrier concentrations which significantly differ from the true carrier concentration.

Crocker & Rogers[41] measured the Hall carrier concentration n_H for a variety of sodium doping concentrations [Na]. If the sodium concentration is equal to the true doping concentration (not necessarily true), then the ratio $[\mathrm{Na}]/n_H$ gives an estimate of the Hall mixing factor: $[\mathrm{Na}]/n_H \approx 1/r_H$.

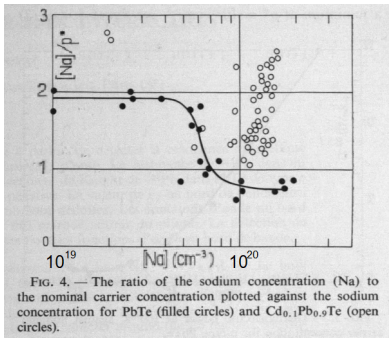

FIG. 4. — The ratio of the sodium concentration (Na) to the nominal carrier concentration plotted against the sodium concentration for PbTe (filled circles) and $Cd_{0.1}Pb_{0.9}Te$ (open circles).

Ratio of the sodium concentration [Na] to the Hall carrier concentration labelled here as p^*. Taken from Crocker & Rogers (1968)[41]. The axes labels have been enlarged.

Their results are shown in Fig. 2.11, which indicates that the true carrier concentration is significantly higher than n_H for sodium carrier concentrations below $\sim 5 \times 10^{19}\,\mathrm{cm}^{-3}$. For higher carrier concentrations $[\mathrm{Na}]/n_H$ is $\sim$1 or less, indicating a significant change in the overall shape of the bandstructure at these high doping concentrations.

Experimental measurements to estimate the effective mass of a band[42], or the energy difference between one band maximum and another[27], often rely on knowing the carrier concentration. For accurate results, it is vital to consider how the different bandstructures and scattering times can affect the Hall mixing factor.

2.3.4 Temperature and pressure dependence of the band gap

The band gap of PbTe increases with increasing temperature. This trend was first measured by Gibson (1952)[43] using optical absorption spectra to measure the band gap. Later optical absorption measurements, resistivity, and Hall coefficient vs temperature measurements by Tauber, MacHonis, and Cadoff[39] corroborated this trend[‡]. These early studies suggested that the band gap plateaus with temperature at approximately 450 K, but a 2013 re-examination of the data by Gibbs *et al.*[45] suggested that the band gap continues to increase with increasing temperature up to at least 670 K. Figure 2.12 shows a compilation of experimental and calculated results for the band gap as a function of temperature. From 0 to 400 K the band gap increases by over 50%. As the size of the band gap can greatly affect thermoelectric properties, it was important to include the temperature dependence of the band gap in my calculations. I will discuss this again later in the methodolgy section.

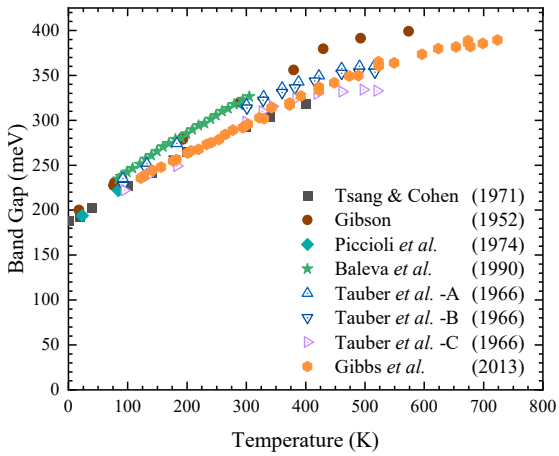

Figure 2.12 *Literature values of the PbTe band gap as a function of temperature[39,43,45–48]. All values shown are experimental, except for the Tsang and Cohen results. The Tauber et al. -A,-B, and -C are three different samples Tauber et al. measured.*

Prakash (1966)[49] investigated how the band gap of PbTe changes under pressure. They measured the optical absorption edge at different pressures, and determined the pressure coefficient of the band gap as −74 meV/ GPa. Averkin and

[‡]When Tauber, MacHonis, and Cadoff analysed the absorption spectrum in order to estimate the band gap, they assumed an indirect transition — which is not the case for PbTe. In 1966 it was still somewhat unclear whether or not PbTe had a direct band gap, so the assumption is understandable. A previous paper by Scanlon[44] had shown that the values of the optical band gap for PbTe were similar regardless of whether a direct or indirect transition was assumed. Thus the results from Tauber, MacHonis, and Cadoff are still in close agreement with other studies.

Dermenzhi[50] reported a similar coefficient of −82 meV/ GPa derived from Hall-coefficient measurements. The rate of change of the band gap with temperature, $\partial E_g/\partial T$, can be expanded into two contributions: expansion of the lattice with temperature; and another factor which accounts for how the band gap would change with temperature at fixed volume[46,49].

$$\frac{\partial E_g}{\partial T} = \left(\frac{\partial E_g}{\partial T}\right)_{\text{lattice}} + \left(\frac{\partial E_g}{\partial T}\right)_V. \tag{2.69}$$

The lattice expansion term is related to the pressure coefficient of the band gap $\partial E_g/\partial P$:

$$\left(\frac{\partial E_g}{\partial T}\right)_{\text{lattice}} = -\left(\frac{\partial E_g}{\partial P}\right)_T B_0 \frac{\partial \ln V}{\partial T}, \tag{2.70}$$

where V is the volume, B_0 is the bulk modulus, and $\partial \ln V/\partial T$ is the rate of thermal expansion. The constant-volume term accounts for all other effects, such as the thermal motion of the atoms. Prakash's measurements of the pressure coefficient show that lattice expansion can only partially account for the rate of change of the band gap with temperature. They calculated the lattice term to be 0.17 meV/ K at room temperature, compared to a total $\partial E_g/\partial T$ of 0.45 meV/ K. This shows that the constant-volume term is at least as significant as the lattice expansion term.

In 1971, Tsang and Cohen[48] published the first calculations of the band gap temperature dependence[48]. They used the framework of density functional theory to calculate the band gap, using pseudopotentials to describe the effective potential of the lead and tellurium ion cores. Finite temperature effects were modelled by (i) expanding the lattice according to empirical data on thermal expansion, and (ii) perturbing the pseudopotentials by a factor relating to the thermal average of the squared ion displacement — also experimentally measured. The empirical pseudopotential method they used had excellent agreement with the measurements by Gibson[43], and Tauber *et al*[39]., but more importantly they confirmed that the thermal motion of the atoms at constant volume is a significant term.

More recently, Querales-Flores *et al.*[51] reported *ab initio* calculations of the temperature dependent band structure of PbTe. They used methods in density function perturbation theory to calculate how electron-phonon coupling renormalizes the band structure — both at finite temperatures, and due to zero point motion. Their results reproduce the band gap increase with temperature

from a combination of thermal expansion, and electron-phonon coupling.

2.3.5 Band Convergence

The valence band of PbTe has a complex shape, with a local valence band maximum at Σ_{max} and the global L-point valence band maximum L_{max}. Estimates for the low-temperature energy difference between the two maxima, $\Delta\epsilon_{L\Sigma}$, vary between 140 and over 190 meV, however several studies have indicated that the two maxima converge in energy with increasing temperature [27,45,51–53].

Jaworski *et al.*[27] published a detailed discussion of the pre-2013 experimental evidence for $\Delta\epsilon_{L\Sigma}$ reducing with increasing temperature, alongside their own experimental data. They concluded that previous estimates of band convergence from experimental data should be reinterpreted, incorporating the existence of a region of positive curvature in the valence bandstructure — specifically the saddle point between the L-point and Σ_{max}. They indicate that a rate of change of $\Delta\epsilon_{L\Sigma}$ with temperature $\text{d}\Delta\epsilon_{L\Sigma}/\text{d}T \approx -0.2\,\text{meV/K}$ is plausible.

Walmsley *et al.*[33] conducted Hall effect and quantum-oscillation measurements at liquid-Helium temperatures and below. They concluded it was unlikely that $\Delta\epsilon_{L\Sigma}$ was less than 180 meV, and found no evidence that states near Σ_{max} were populated for any Hall carrier concentrations n_H measured (up to $2.5 \times 10^{20}\,\text{cm}^{-3}$). They also concluded that, at energies more than 160 meV below the valence band maximum, the valence bandstructure near the L-point deviates significantly from the Kane model, which further complicates attempts to estimate $\Delta\epsilon_{L\Sigma}$.

First-principles calculations by Querales-Flores *et al.*[51] also suggest a band convergence with increasing temperature. Electron-phonon coupling and thermal expansion both contributed to the converging energy difference; however, thermal expansion only contributed around 15–20% to the temperature coefficient of $\text{d}\Delta\epsilon_{L\Sigma}/\text{d}T$ to be either -0.217 or $-0.280\,\text{meV/K}$, depending on if the spin-orbit interaction was included in their calculations[§]. They estimated L_{max} and Σ_{max} would align at temperatures between 600–700 K, based on a low-temperature difference of 150–180 meV (likely an underestimate based on experimental data).

[§]It may seem surprising not to include the spin-orbit-interaction (SOI) as lead is a fairly heavy atom, and there have been several papers suggesting the importance of spin-orbit coupling in lead telluride[36,54–56]. Querales-Flores *et al.*[51] excluded SOI because, when using the local density approximation, it leads to the correct band-ordering at the L-point and good deformation potentials.

Converging multiple bands is generally thought to be beneficial to thermoelectric performance. The convergence of $\Sigma_{\max}$ and L-point maxima would likely improve the thermoelectric properties of *p*-type PbTe at higher temperatures. However, it presents a significant challenge to those who wish to model the valence bandstructure of PbTe. Much of the precise information about lead telluride's bandstructure is derived from experiments at low temperatures. Estimating how band convergence relates to thermoelectric transport usually relies on simplified models of the bandstructure, such as the Kane-model or the two-band model[57,58].

2.3.6 The two-band model

Throughout the literature, the valence band of PbTe has often been described in terms of a two-band model, with an *'upper valence band'* corresponding to the states near the L-point, and a *'lower valence band'* corresponding to states near $\Sigma_{\max}$[27,52,59]. Mention of a 'second valence band' appears to have originated with several papers all published simultaneously in the same 1961 issue of Journal of Applied Physics[60–63].

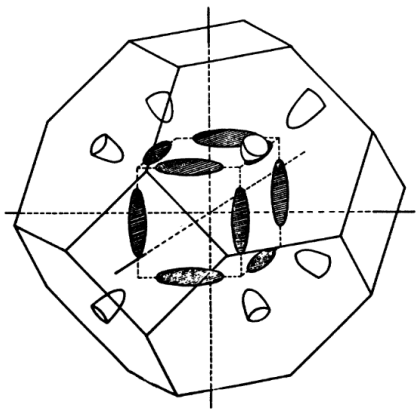

Figure taken from Sitter, Lischka, and Heinrich[52]. Illustration of a constant energy surface for the PbTe valence band. Ellipsoids of revolution at the L-points(Σ_{max}) are unfilled(shaded), respectively.

A paper by Stiles, Burnstein, and Langenberg[60] and another by Cuff, Ellet, and Kuglin[61], highlighted inadequacies in a model of the valence band consisting of carrier pockets, centered at the L-point, with constant energy surfaces like ellipsoids of revolution oriented along [111]. Both papers attempt to explain their data (de Haas-van Alphen measurements and oscillatory magnetoresistance data respectively) by positing a second valence band, with approximately spherical constant energy surfaces, centered at Γ.

In the same issue, Allgaier[62] and Rediker & Calawa[63] dispute this model. They instead suggested a form of the valence-band-model which persists today: an upper valence band, centred at the L-point, with constant energy surfaces like prolate ellipsoids oriented along the [111]; and a second — low mobility — lower valence band. The shape of the two-band model evolved over time, and has been used to explain, for example, anomalous transport behaviour with increasing *p*-

doping concentration[52,64,65], and the high Seebeck coefficient of heavily p-doped PbTe[66,67]. In particular it became apparent that the upper valence band is strongly nonparabolic[64].

When using a two-band model for the valence band of PbTe, the upper valence band is usually approximated using a Kane-model dispersion, while the lower valence band is approximated using a parabolic band. However, the two-band model fails to describe the positive curvature along the L–Σ_{max} line seen both in experiment and calculations[27,28,33,36–38].

To illustrate the difference between the true valence bandstructure and the two-band model, Fig. 2.14 shows my calculated bandstructure along a straight line through the Brillouin zone between L and Σ_{max}. The minimum of my calculated bandstructure has positive curvature, and lies ∼280 meV below the valence band maximum — only ∼20 meV below the Σ_{max} local maximum. When compared to a two-band model, the difference is stark. Instead of a region with positive curvature, the two-band model has a band crossing a much lower energy; which has a very different density of states and carrier velocities.

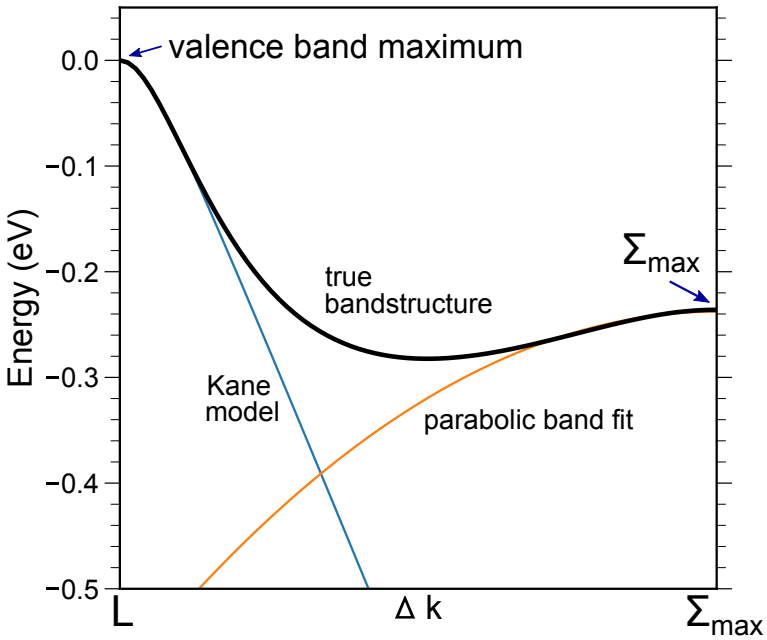

Figure 2.14 *Calculated bandstructure of the valence band along a straight line through the Brillouin zone between the L and Σ_{max} points, taken from my calculations. Kane model and parabolic fits, modelling 'upper' and 'lower valence bands', respectively, are also shown.*

Jaworski *et al.* examined the magnetic field dependence of the Hall resistivity in heavily p-doped PbTe. They concluded that there is a region of the bandstructure

between the L- and Σ-maxima which has positive curvature. As temperature increases, some holes will be scattered into this region and contribute electron-like behaviour to measurements of the Hall-resistivity. This affects models attempting to estimate the relative energies of the 'upper' and 'lower' valence bands using transport data, and/or using Hall-coefficient measurements to estimate carrier concentrations. In reality, there is only one valence band; using a two-band model fails to account for this region of positive curvature.

Hall effect and quantum oscillation measurements by Walmsley *et al.*[33] show a sharp increase in the valence band density-of-states, associated with the saddle point between L and Σ_{max}. They also indicate that the valence-band shape deviates from that of the single band Kane model at energies about 160 meV below the L-point maximum. ARPES measurements on thin films of PbTe[28] have experimentally shown that the valence bandstructure of PbTe is connected — rather than two separate bands which cross. Finally, numerous density functional theory calculations — including those described in the results section — have shown that the 'upper' and 'lower' valence bands are connected via a saddle point[36–38].

The calculations shown here indicate that the energy difference between Σ_{max} and the saddle point is on the order of 20 meV (Fig. 2.14). If the doping concentration or temperature is high enough that a significant concentration of holes are in states near Σ_{max}, there could also be a significant number in states near the L–Σ_{max} saddle points. Shubnikov-de Haas measurements by Giraldo-Gallo *et al.*[35] show deviations from the Kane-model dispersion for states near the L-pockets at p-doping concentrations exceeding $\sim 6 \times 10^{19}\,\text{cm}^{-3}$. It should be noted that while Giraldo-Galo *et al.* found that the Kane-model was a good description for low and intermediate p-doping concentrations, their measurements were all taken at temperatures below 60 K; at room temperature and above, a significant number of holes will be in states which the Kane-model does not describe properly.

In conclusion, the two-band model does not represent the shape of the valence band. Fitting transport data using the two-band-model may incorrectly estimate effective masses, and/or energy differences between the Σ_{max} and L-point maxima. The effects of strain or alloying on p-type PbTe are often framed in terms of the two-band model[31,57,66–70]; but, any change to the energy of Σ_{max} will likely accompany changes to the band curvature in the region of the L–Σ_{max} saddle point[33], and thus change the velocity of all holes occupying those states. This thesis will show that picturing the valence band as a single connected band is

key to understanding the results in this thesis for how stress along [001] affects p-doped thermoelectric properties.

2.3.7 Piezoresistance and the intervalley-electron-transfer effect

In 1967 Burke reported piezoresistance measurements for p-type PbTe[71]. Burke grew single crystals of p-type PbTe, then measured the electrical resistivity of the sample under hydrostatic pressure and uniaxial stress along the [001], [110], and [111] crystallographic directions. The change in electrical resistivity along one crystal direction is related to applied stress along another by the piezoresistance coefficients, much in the same way that stress and strain are related by the elastic constants. The piezoresistance tensor maps a 3×3 tensor of the applied stress to a 3x3 tensor of the change in resistivity. This would require a rank 4 tensor, but due to the cubic symmetry of PbTe it can be reduced to three coefficients π_{11}, π_{12}, and π_{44}; which are analogous to the three elastic constants C_{11}, C_{12}, and C_{44}.

Burke found that the temperature and carrier concentration dependence of the π_{44} coefficient aligned with a picture involving multiple carrier pockets centred at the L-points. Stress that removes the degeneracy of the [111] hole-pockets leads to a *intervalley-electron-transfer effect*[72]. The intervalley-transfer effect is explained in detail by Herring[72], but I will give a brief summary here.

Recalling the equations for the L-matrices, one can write the total electrical conductivity as the sum of conductivities from different regions p of the Brillouin Zone:

$$\sigma_{ij} = \sum_{p} \sigma_{ij}^{p} \tag{2.71}$$

$$= \sum_{p} e^2 \sum_{b} \int_{\boldsymbol{k}\in p} \frac{\mathrm{d}^3\boldsymbol{k}}{4\pi^3} \phi_{ij}\left(b, \boldsymbol{k}, \boldsymbol{r}\right), \tag{2.72}$$

where ϕ_{ij} is the energy-dependent-conductivity tensor, which quantifies how much each state contributes to the electrical conductivity (Eq. 2.39). For a multi-valley semiconductor like PbTe, each carrier pocket p contributes differently to the total conductivity. The relative contribution of each carrier pocket depends on (i) how many electrons/holes are populating states in the pocket, (ii) the group velocity of the carriers, and (iii) their scattering time. Each carrier pocket has anisotropic transport properties — with the lowest mobility along the L→ Γ direction. When

PbTe is unstrained, all the valence band carrier pockets are equally populated, and so the symmetry results in an isotropic total conductivity.

Applying stress which removes the degeneracy of the [111] pockets will redistribute carriers from the higher-energy pockets to the lower energy pockets (Fig. 2.15). If the mobility of carriers at each individual carrier pocket is anisotropic, then changing the relative population of the carrier pockets will result in the overall conductivity also becoming anisotropic[72]. As charges are redistributed, the total conductivity will gain an anisotropy like that of the most populous pockets — increasing the conductivity along some directions, and reducing it along others. The intervalley-transfer effect will be re-examined later, as it is responsible for why there is such a large improvement in the thermoelectric power factor of PbTe under uniaxial [111] stress.

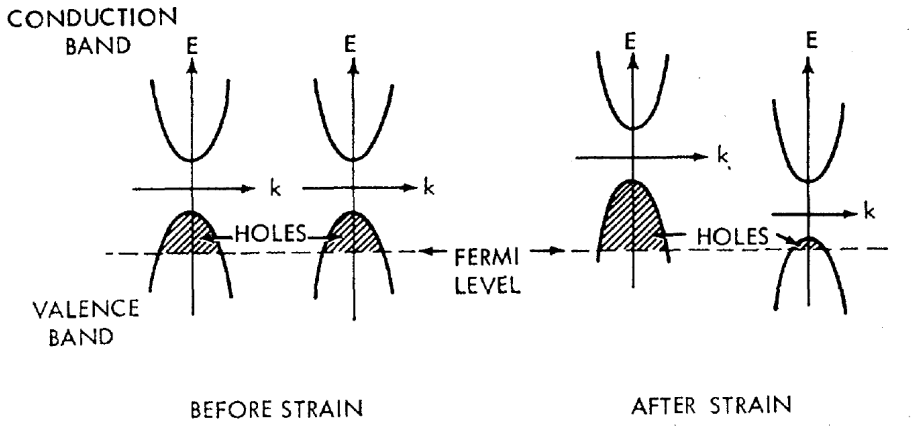

FIG. 2. Effect of a particular shear strain on two of the ⟨111⟩ valleys of the valence and conduction bands of PbTe.

Figure 2.15 *Figure from Burke (1967)[71], illustrating the redistribution of holes after strain is applied.*

Burke[71] also commented that π_{44} was unusually large compared to what would be expected from a parabolic valence carrier pocket, and tried to use a simple non-parabolic model similar to the Kane-model. However, they were unable to account for the temperature and carrier concentration dependence of π_{44}. Using a two-band model was also unable to explain their results. In their words: *"Evidence for the population of a second valence band is presented in a later section of this paper. However, even at room temperatures for [a p-doping concentration of] $4.09 \times 10^{17}\,cm^{-3}$, only about 20% of the carriers are in this band, and this percentage decreases as the temperature decreases".*

The coefficient $\pi_{11} - \pi_{12}$ was also examined by Burke[71], and found to be

surprisingly large. The size of this coefficient could not be explained by the charge-redistribution effect articulated before, as it is associated with a strain which preserves the degeneracy of the L-point carrier pockets. They speculated that the large value of $\pi_{11} - \pi_{12}$ could be due to a charge-redistribution effect in the "lower-valence band extrema centred along [110] between Γ and K" ($\Sigma_{\max}$). However, $\pi_{11} - \pi_{12}$ remained large even at temperatures and carrier concentrations low enough that the "second valence band" would be depopulated. This again points to the inadequacy for the two-valence-band picture of PbTe. Burke concluded that the inadequacy of the model *"strongly suggests the need for radical changes in the band parameters used in the calculation"*.

2.3.8 Mechanical Properties

When used in a device, any thermoelectric material will be subjected to a variety of stresses and strains — both from external forces, and from thermal expansion of the thermoelectric and the materials surrounding it. Understanding the mechanical properties of a thermoelectric is important for incorporating it into a real device. Mechanical properties can be affected by doping concentration, type of dopant, alloying, and methods of sample preparation[73]. Although this topic is outside the scope of this thesis, I will briefly summarise the results of Schmitz *et al.*[73] and Gelbstein *et al.*[74].

Schmitz *et al.* measured stress as a function of uniaxial strain for undoped polycrystalline PbTe prepared by a variety of methods (Fig. 2.17a). The stress-strain curves have three regions: an elastic deformation region, followed by a plastic deformation region, then an *ultimate compression strength point* is reached, above which the stress decreases. The elastic region is where the solid is responding elastically, with uniaxial strain being a linear function of the applied stress. If elastic stress is applied, the sample will return to its original dimensions when the stress is released. The maximum elastic stress is called the "yield strength", and it is the stress above which fractures first initiate. Schmitz *et al.* measured yield strengths of PbTe ranging from ∼90 to 135 MPa, depending on sample preparation method (Fig. 2.17). The yield points all occurred at ∼0.7%

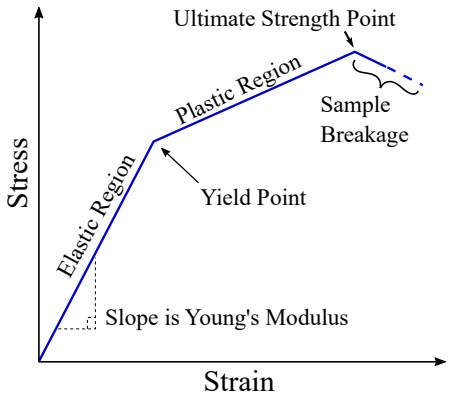

Illustration of a typical compressive stress-strain relationship.

strain.

Following the yield point is a large region of plastic deformation. During plastic deformation the material is reshaping under the applied stress, and will not return to its original shape upon decompression. The more ductile a material, the larger the region of plastic deformation. Schmitz *et al.*[73] found higher sintering temperatures produced lower yield strengths, but were also more ductile. The point at which the stress strain curve reaches a maximum after the plastic deformation is known as the ultimate strength point. Attempts to strain beyond this point — or to apply greater uniaxial stress — will break the sample. This can be seen clearly in Schmitz curves, where the stress-strain curves above the ultimate strength point become jagged, and the stress drops. The results of Schmitz *et al.* show that stresses of ∼140 MPa are realistic without damaging the sample, and stresses up to as high as ∼240 MPa can be achieved if plastic deformation is allowed. Elastic strains on the scale of 0.7% are achievable for polycrystalline PbTe.

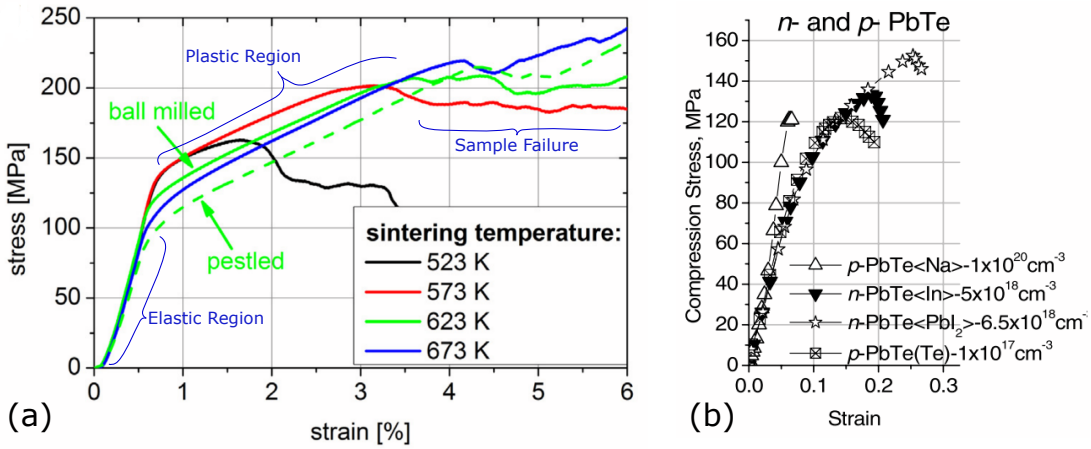

Figure 2.17 *Uniaxial stress as a function of strain for (a) undoped PbTe with different preparation methods, reported by Schmitz et al.*[73]*; and (b) doped PbTe, reported by Gelbstein et al.*[74]*. It should be noted that the scale on the right is not in percent.*

Gelbstein *et al.*[74] also measured stress-strain curves of doped PbTe, shown in Fig. 2.17b. Their results differ significantly from the results of Schmitz *et al.*. The *n*-type samples and the low-concentration *p*-type sample all exhibited an elastic and plastic deformation region. The ultimate compression strength they measured was between 120 and 150 MPa, much lower than what Schmitz *et al.* measured. Furthermore, the ultimate compression point occurred at strains between ∼6 and 25%, much greater than the 0.7% yield point strains measured by Schmitz *et al.*. The graphs indicate that Gelbstein *et al.* had samples with Young's moduli of

about 1.5 GPa, but the samples of Schmitz *et al.* had Young's moduli of around 18 GPa — greater by an order of magnitude.

There are several factors which may be responsible for the contrasting results of Gelbstein *et al.*[74] and Schmitz *et al.*[73]. One possibility is the different rates of compression used during the measurements. When measuring the stress-strain curves, Gelbstein *et al.* compressed the sample at a rate of 3 mm/ min on a 5 mm thick sample, whereas Schmitz *et al.* used a rate of 0.5 mm/ min on a $4 \times 4 \times 4$ mm cube — a strain rate almost five times slower. It is unclear to what extent compression speed could play a role in this material's response.

A second distinguishing factor is that Schmitz *et al.* studied undoped PbTe, whereas Gelbstein *et al.* were studying doped samples. Doping concentration can be important, as shown by the results of Gelbstein *et al.* for heavily *p*-doped PbTe. For high sodium *p*-doping concentrations PbTe becomes brittle and has little to no plastic deformation (Fig. 2.17b). Doping concentration and/or choice of dopant is a factor effecting the mechanical properties of PbTe. However, one sample of Gelbstein *et al.* is only slightly doped with excess tellurium ($1 \times 10^{17}\,\mathrm{cm}^{-3}$), yet the stress-strain curves more closely resemble the $-6.5 \times 10^{18}\,\mathrm{cm}^{-3}$ *n*-doped sample than the undoped PbTe samples by Schmitz *et al.*.

A third distinguishing factor is the method of sample preparation. Schmitz *et al.* show that ball milling the sample — rather than using a pestle — can increase the yield strength by over 25%. However, the paper by Schmitz *et al.* specifically examines how sample preparation can change mechanical properties, and yet all of their samples had roughly the same Young's moduli.

The results of Gelbstein *et al.*[74] and Schmitz *et al.*[73] both contrast with results from Ni *et al.*[75] and Ren *et al.*[76] who, using resonant ultrasound spectroscopy, measured room temperature Young's moduli of 53.1 and ∼58 GPa respectively: much greater than the values of ∼1.5 and 18 GPa from Gelbstein *et al.* and Schmitz *et al.*. However, it should not be a surprise that the Young's modulus measured by Resonant Ultrasound Spectroscopy differs from the values obtained by physical compression of a macroscopic sample. After all, μm scale structure like grain size and defects usually have a much larger effect on the yield strength than they do on the speed of sound.

In summary, two very similar experiments, both conducted on polycrystalline samples of PbTe, appear to measure Young's moduli which differ by almost an order of magnitude. Clearly, strain rates and/or preparation techniques can dramatically alter the mechanical properties of PbTe.

2.3.9 Electron scattering time

Within the relaxation time approximation, relationships for the L-matrices all involve the electron scattering time τ. If τ is assumed to be constant for all states within several k_BT of the chemical potential, then it can be factorized out of the L-matrix integrals. In this way, quantities like, for example, the reduced electrical conductivity σ/τ can be calculated. However, in order to present the electrical conductivity in units useful to experimentalists, an estimate of τ is needed.

One way to estimate the electron scattering time τ is to compare experimental values of the electrical conductivity σ_{exp} with calculated values of σ/τ. Katsura *et al.*[77] reviewed the transport properties from over 200 experimental measurements of n-type PbTe, and compared them with calculated σ/τ values in order to estimate τ. Their estimates ranged between 10^{-14} and 10^{-13} s at 300 K. I use a similar method to estimate my value for τ.

In light- to medium-doped semiconductors, τ is often determined by electron-phonon scattering. Several publications have reported *ab-initio* calculations of the electron-phonon interaction in PbTe[32,57,58,78]. They find electron-phonon scattering times on the order of 10^{-14}–10^{-13} s[¶], in line with the values estimated by Katsura *et al.*. However, it is worth noting that the publication in question only calculated the electron-phonon scattering time[‖]. In a typical sample of PbTe used for thermoelectric applications, defects and impurities will also affect how quickly electrons are scattered.

2.3.10 High Pressure and Strain

Experimental studies have suggested that pressure on the scale of a GPa can improve the power factor of doped PbTe anywhere between a factor of 2 and over 100[7–9]. If the power factor can be increased without a similar rise in thermal conductivity (κ), then high pressure could vastly improve the figure of merit ZT.

[¶] There is a small subtlety in how the scattering time $\tau\,(b, \boldsymbol{k})$ for the state $(b, \boldsymbol{k})$ is calculated. One version, referred to by Cao *et al.* as the Self-Energy-Relaxation-Time is simply how long it is, on average, for an electron in state $(b, \boldsymbol{k})$ to be scattered to any other state. However, scattering events which only slightly deflect the velocity of an electron will not have as big an impact on, for example, the electrical conductivity as a scattering event which completely changes the direction of the electron's motion. For this reason, the transport scattering time needs to be weighted by an angle of deflection. See Cao *et al.*[32] and Gunst *et al.*[79] for more details.

[‖] with the exception of Cao *et al.*[58], who also included a term to estimate scattering from ionized impurities.

However, the mechanism through which pressure increases the power factor in PbTe has remained unknown.

Ovsyannikov & Shchennikov[7] measured the Seebeck coefficient and electrical conductivity of various p- and n-doped samples of PbTe under high pressure. They observed a large increase of the power factor α with increasing pressure. Figure 2.18 shows how the Seebeck coefficient and electrical resistance changed with pressure for the variety of samples investigated.

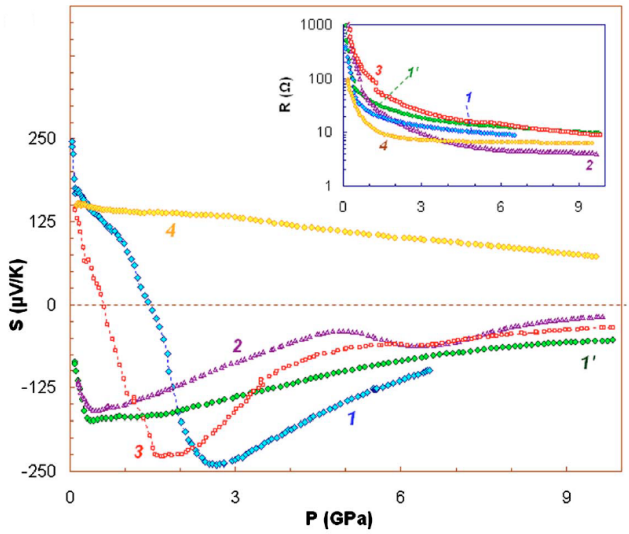

Figure 2.18 *Figure from Ovsyannikov & Shchennikov (2007)[7]. Pressure P dependencies of the Seebeck coefficient S (left scale) and electrical resistance R (inset), at $T = 293$ K. "1 and 1': p-PbTe for the first and second run, respectively (after the first run it has n-type behaviour because of 'doping' with defects); 2, n-PbTe; 3, p-$Pb_{0.55}Te_{0.45}$; 4, p-$Pb_{0.393}Sn_{0.157}Te_{0.45}$."[7]. Samples 1 and 2 had a carrier concentration of $n = 1.5 \times 10^{18} cm^{-3}$.*

Increasing pressure from 0 to ∼2 GPa decreased the electrical resistance of all their samples by almost two orders of magnitude. Above ∼2 GPa the resistance still decreased with increasing pressure, but much more gradually.

The trend in the Seebeck coefficients is more varied between samples, so I will first summarise the n-type samples data. The carrier concentration of sample 2 was given as $1.5 \times 10^{18}\,\mathrm{cm}^{-3}$, although this doping concentration likely changed as the quasihydrostatic pressure was applied[7]. Both n-doped samples had a Seebeck coefficient of about $-100\,\mu\mathrm{V/\,K}$ at the lowest pressures: ∼0.16 GPa. At ∼0.25 GPa of pressure the Seebeck coefficient had increased in magnitude to between about -150 and $-175\,\mu\mathrm{V/\,K}$. As the pressure was increased beyond ∼0.5 GPa, the Seebeck coefficient of both n-type samples gradually reduced

towards zero, dropping below $-100\,\mu V/\,K$ at pressures above 2.5 GPa. Although they differ quantitatively, the trends for both these samples are qualitatively similar. However, they differ significantly with data on another sample, also $1.5 \times 10^{18}\,cm^{-3}$ n-doped, published four years earlier by the same authors[80].

In their 2003 paper, Ovsyannikov & Shchennikov also estimated their n-doped sample to have a carrier concentration of $1.5 \times 10^{18}\,cm^{-3}$. The ambient pressure Seebeck coefficient of that sample was over $300\,\mu VK^{-1}$, and it decreases rapidly with increasing pressure — halving by 2.5 GPa. This differs greatly with the results in their 2007 paper, for which the Seebeck coefficient increased initially, peaked at approximately $-150\,\mu V/K$, then gradually decreased with pressure.

Other work in the literature has also measured the Seebeck coefficient of n-type PbTe under pressure. Baker *et al.*[8] observed a decrease in the magnitude of the Seebeck coefficient between ∼2 and 6 GPa. Jacobsen *et al.* also observed the Seebeck coefficient initially increase in magnitude from around −200 at ∼0 to $-240\,\mu VK^{-1}$ at ∼2 GPa, after which it decreased until a phase transition to the B16 phase at ∼6 GPa. This qualitatively agrees with the n-type data from Ovsyannikov & Shchennikov[7], who also observed the Seebeck coefficient increase initially, then tend towards zero with increasing pressure above ∼2 GPa. However, the actual magnitudes of the Seebeck coefficients are quite different, as is the pressure at which the Seebeck coefficient reaches a maximum.

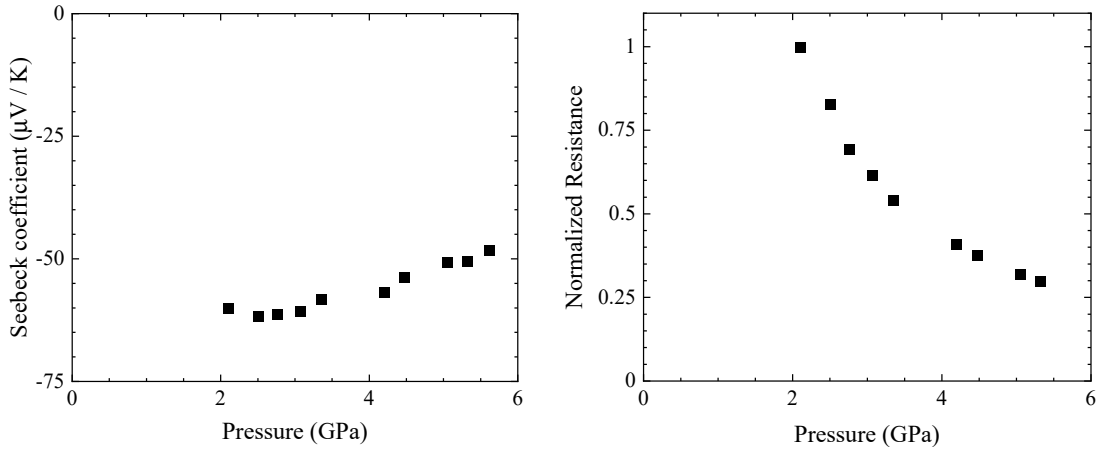

Figure 2.19 *Seebeck coefficient (left) and Noramlized resisistance (right) of n-type PbTe at 325 K, measured by Baker et al.[8]. Figure replotted by myself.*

Baker *et al.*[8] and Jacobsen *et al.*[9] both suggest the reason their results differ with those of Ovsyannikov & Shchennikov[7] is that they used polycrystalline samples, whereas Ovsyannikov & Shchennikov used single crystals. However, an equally important difference is the doping concentration. Ovsyannikov &

Shchennikov always reported on doped and/or alloyed samples; with ambient-pressure carrier concentrations on the order of $10^{18}\,\mathrm{cm}^{-3}$ and above. Baker *et al.* used an undoped sample, and Jacobsen *et al.* used a sample with an estimated n-type doping concentration of $\sim 5 \times 10^{17}\,\mathrm{cm}^{-3}$**. Furthermore, although Ovsyannikov & Shchennikov's samples were initially single crystals, after being compressed in a high-pressure cell — surrounded by a solid pressure-transmitting medium of lithographic stone — they likely did not remain single crystals.

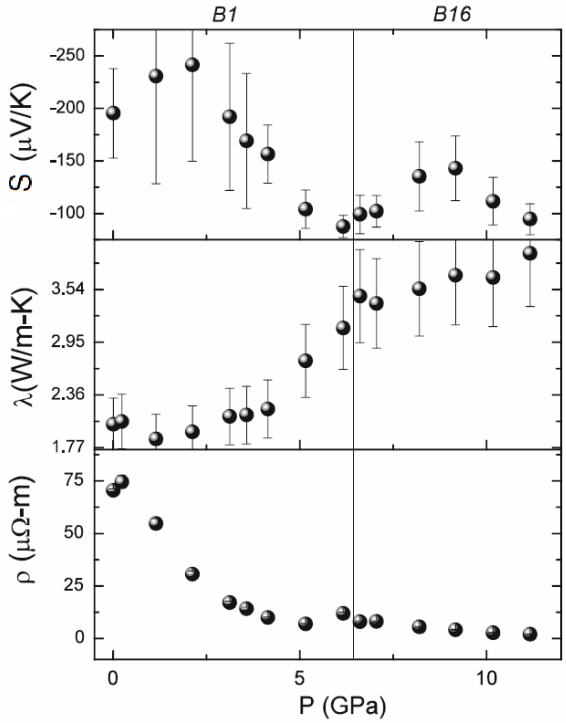

Figure 2.20 *Figure from Jacobsen et al.[9]: Seebeck coefficient S, thermal conductivity λ, and electrical resistivity ρ of PbTe with pressure. The vertical line represents the approximate structural transition from B1 to B16 phase.*

Indeed, Ovsyannikov & Shchennikov[7] suggest the introduction of defects could explain their results for p-type PbTe (Fig. 2.18). The Seebeck coefficient of their p-doped PbTe sample inverts from around +250 at $\sim$0 GPa, to $-250\,\mu\mathrm{VK}^{-1}$ at $\sim$2.5 GPa. This change was not reversed upon decompression, suggesting — as the authors mention — that introduction of defects is important. Indeed,

**Jacobsen *et al.* estimate their ambient-pressure carrier concentration by comparing their measured conductivity to data published by Allgaeir & Scanlon[81]. They quote an n-doping concentration of "$0.579\,\mathrm{cm}^{-3}$", however, by reading Allgaeir & Scanlon's paper I surmised they intended to write $0.579 \times 10^{18}\,\mathrm{cm}^{-3}$. It is also worth noting that if one instead uses the Seebeck coefficient measured by Jacobsen *et al.* to estimate the carrier concentration it yeilds a value of of approximately $5 \times 10^{18}\,\mathrm{cm}^{-3}$: an order of magnitude higher.

polycrystalline n-type PbTe with small grain sizes has a more negative Seebeck coefficient than PbTe with larger grains[82], and other experiments have indicated that the type of defects created in PbTe under high pressure preferably act as donors[73,83]. If the application of pressure initially creates n-type carriers within the first 1-2 GPa, that may explain why the Seebeck coefficient changes from positive to negative in the p-type PbTe samples, and also why the conductivity rose by an order of magnitude over the same pressure range.

In further contrast, a 1966 paper by Averkin & Dermenzhi[50] reports that the Seebeck coefficient of n-type PbTe decreases with pressure by around 10% per GPa, rather than initially increasing as observed by Jacobsen *et al.* and Ovsyannikov & Shchennikov. Averkin & Dermenzhi used a significantly different experimental setup, including a fluid pressure transmitting medium. This may have helped minimize the formation of defects.

Understanding to what extent the observations by Ovsyannikov & Shchennikov are due to the creation of defects, versus changes to the bandstructure, is one of the aims of this thesis. The results reported by Ovsyannikov & Shchennikov suggest a path towards vast improvement in the thermoelectric power factor of PbTe based devices. Thus, it is important to understand the origin of the effects they reported.

In electrical-transport experiments it is difficult to apply truly hydrostatic pressure, so it is unclear to which extent the effects observed by Baker *et al.*[8], Ovsyannikov & Shchennikov[7], and Jacobsen *et al.*[9], are due to changes in carrier concentration, hydrostatic pressure, or non-hydrostatic stress. I report *ab intio* calculations which examine both pressure and stress in isolation, and trace how stress alters the bandstructure — which in turn changes the transport properties. Understanding the connection between stress and transport properties in PbTe may also suggest methods to improve other thermoelectrics. Other means, such as chemical substitution and thin films, can also strain materials. Examining stress in isolation can guide the use of such techniques.

Finally, theoretical work by Murphy *et al.*[84] has shown uniaxial strain can reduce the thermal conductivity of PbTe. The thermal conductivity κ appears on the denominator of the thermoelectric figure of merit ZT; thus, if strain can reduce κ and also improve the thermoelectric power factor σS^2, then the figure of merit should increase significantly. I conducted *ab initio* calculations, within the framework of density functional theory and Boltzmann transport theory, to model how uniaxial and biaxial stress can improve the power factor of PbTe.

Chapter 3

Methodology

3.1 Foundations of Density Functional Theory

Density functional theory (DFT) is a popular method for calculating the properties of condensed matter from first-principles. It is valued across disciplines for its ability to generate reliable results with reasonable computation time. A brief introduction to the theory behind the method is given here.

Ordinarily, quantum mechanics deals with the wavefunction Ψ. In principle, the ground-state wavefunction contains all the information about a system[85]. Properties such as the expected positions of particles, the total energy of the system, and the spectra of excitations, can all be deduced from the ground-state wavefunction. This is a manifestation of the first theorem of Hohenberg & Kohn. The ground-state wavefunction determines the ground-state density; which in turn determines the external-potential and the Hamiltonian of the system; and thus all that can be deduced from the Hamiltonian.

The Schrödinger equation describes how Ψ evolves over time in response to a potential: for example, the Coulomb potential from a set of nuclei. Furthermore, for a given system and choice of coordinates, the lowest-energy solution to the Schrödinger equation is unique*. So, if the Schrödinger equation for the electrons in a solid is solved to yield the wavefunction, everything there is to know about that material could — in principle — be deduced.

For simple cases, like a single electron in the Coulomb potential of hydrogen,

*Excepting some nuances due to symmetry; for example, up/down spin degeneracy of a one-electron system

Ψ can be solved for analytically. However, when multiple electrons are involved (for example, in a helium atom, or a hydrogen molecule) numerical methods are needed. As the number of electrons increases, the computational cost grows exponentially. For typical crystal structures or molecules, with dozens of electrons in each unit cell, computing the many-body wavefunction is unattainably complicated.

Finding practical ways to perform quantum-mechanical calculations for systems with many electrons has been the subject of nearly a century of research[86]. *Density functional theory* is one such way.

There are five main pillars of practical implementations of density functional theory:

1. Treating the electrons and nuclei separately.
2. Focus on the ground state electron density.
3. The Kohn-Sham formalism.
4. Exchange-and-Correlation potentials.
5. The Self-Consistent Cycle.

I shall briefly summarize each of these.

3.1.1 The Born-Oppenheimer Approximation

The first pillar is known by various names: the clamped-nuclei approximation, the frozen-nuclei approximation, the adiabatic method; but it shall be referred to here as *the Born-Oppenheimer approximation*[87].

The Born-Oppenheimer approximation is hard to justify with mathematical rigour[88–90]. Here I will briefly summarize how the Born-Oppenheimer approximation is justified, and I refer those desiring a detailed derivation to a 2014 paper by Jecko[89].

Within the Born-Oppenheimer approximation, the many-body wavefunction of nuclei and electrons is factorized into one many-body wavefunction for the nuclei, Ξ_n, which depends on the nuclear positions $\boldsymbol{R}_l$; and a second many-body wavefunction for the electrons, Ψ_e, which depends on the electron positions $\{\boldsymbol{r}_i\}$ and the nuclear positions $\{R_n\}$[16,89]:

$$\Psi_{e,n} \rightarrow \Psi_e(\{\boldsymbol{r}_i\}, \{\boldsymbol{R}_l\})\ \Xi_n(\{\boldsymbol{R}_l\}). \tag{3.1}$$

The next step is to look at eigenvalues of the full many-body Hamiltonian for both electrons and nuclei[89]. The Hamiltonian can be broken down into three terms: a kinetic energy operator which acts on the coordinates of the electrons $\hat{K}_e$; a kinetic energy which acts on the coordinates of the nuclei, $\hat{K}_n$; separate Coulomb terms for the electrons and nuclei, $\hat{V}$:

$$\hat{H}_{\text{tot}} = \hat{K}_e + \hat{K}_n + \hat{V}, \tag{3.2}$$

$$\hat{K}_e = -\sum_i \frac{1}{2m_e} \nabla^2_{r_i}, \tag{3.3}$$

$$\hat{K}_n = -\sum_l \frac{\hbar^2}{2M_l} \nabla^2_{R_l}, \tag{3.4}$$

where m_e is the electron mass, M_l is the mass of nucleus l, and $\nabla^2_{r_i}$ and $\nabla^2_{R_l}$ are Laplacian operators acting on the coordinates of electron i and nucleus l, respectively.

When the Hamiltonian $\hat{H}$ acts on the factorized wavefunction (Eq. 3.7), multiple terms are produced. The key part of the Born-Oppenheimer approximation is noticing that terms which depend on the nuclei Laplacian Δ_{R_l}, are multiplied by $1/M_l$, whereas terms which depend on the momentum operator for the electrons, $\hat{p}_i$, are only multiplied by $1/m_e$.

When the term $\hat{K}_n$ acts on the Born-Oppenheimer wavefunction $\Psi_e \Xi_n$, it produces several terms:

$$\hat{K}_n \left[\Psi_e \Xi_n\right] = -\sum_l \frac{\hbar^2}{2M_l} \nabla^2_{R_l} \left[\Psi_e\big(\{\boldsymbol{r}_i\}, \{\boldsymbol{R}_l\}\big)\ \Xi_n\big(\{\boldsymbol{R}_n\}\big)\right], \tag{3.5}$$

$$= -\sum_l \frac{\hbar^2}{2M_l} \left[\left(\nabla^2_{R_l} \Psi_e\right)\ \Xi_n + \left(\nabla_{R_l} \Psi_e\right) \cdot \left(\nabla_{R_l} \Xi_n\right) + \Psi_e\ \left(\nabla^2_{R_l} \Xi_n\right)\right]. \tag{3.6}$$

The third term in equation 3.6 is simply the kinetic energy of the nuclei. The first and second terms capture coupling between the movement of the nuclei and the electronic wavefunction. Justified by the fact that these terms are suppressed by $1/M_l$, rather than $1/m_e$ in the kinetic energy of the electrons, the Born-Oppenheimer approximation neglects these first two terms [16,88,89].

This approximation is often called the *"clamped-"* or *"frozen-nuclei"* approximation, because the neglected terms correspond to the quantum-entanglement of the electron and nuclear wavefunctions. By ignoring these terms, the Born-Oppenheimer wavefunction becomes a product of a nuclear part $\Xi_n(\boldsymbol{R}_l)$ and an electronic part which only depends on the nuclear positions *parametrically*:

$$\Psi_{e,n} \approx \Psi_e(\{\boldsymbol{r}_i\}|\{R_l\})\ \Xi_n(\{\boldsymbol{R}_l\}). \tag{3.7}$$

Within this approximation, the electronic-wavefunction Ψ_e can be calculated for a set of nuclear positions R_l, and the nuclear part of the wavefunction Ξ_n is treated separately. Although the Born-Oppenheimer approximation does not strictly require it, the nuclei are usually treated as classical particles.

In an ordinary calculation of the total energy for a particular atomic structure, the electron-wavefunction Ψ_e is solved[†] with the nuclear positions R_l fixed on the atomic positions. Or, in a typical molecular-dynamics simulation, forces are calculated at one time-step as if the nuclei are stationary, then the nuclei move like classical particles to the next time step.

Obviously, these approximations have limits. If the nuclei are moving very fast — for example, if a material is exposed to α-radiation — then approximating the nuclei as *frozen* is not useful. The field of time-dependent density functional theory has methods to address this; however, for the calculations in this thesis, we treat the nuclei as stationary. Furthermore, for very light atoms (e.g. hydrogen),

[†]excepting the various approximations we will summarize shortly

it is not always appropriate to treat the nuclei classically. Although these approximations will not be a problem for the materials investigated in this thesis, they are worth bearing in mind.

3.1.2 The Role of Density

The second technique shared by all DFT methods is to ignore the many-body electron wavefunction Ψ_e, and instead focus on the electron *density* ρ. For a given set of nuclear positions $\{R_n\}$, the wavefunction Ψ_e for N electrons is a function that takes the positions of each individual electron, and returns a complex number. In other words, it is a function from a domain made up of $3 \times N$ real numbers (x, y, and z coordinates for each electron) to a single complex number:

$$\Psi_e : \mathbb{R}^{3N} \longrightarrow \mathbb{C}. \tag{3.8}$$

Thus, the domain of Ψ_e grows with the number of electrons. For the number of electrons found in a typical material, the wavefunction becomes too complex to compute.

Aside: An easy way to see why solving for the many-body wavefunction Ψ_e of a real material becomes unattainably complicated, is to imagine trying to compute the wavefunction for the electrons of a single carbon atom.
Carbon has six electrons, so the many-body wavefunction has 6×3 dimensions:

$$\Psi(r_1, r_2, ..., r_6)\,,$$

where r_i is the 3D position of the ith electron. For now, let's not worry about spin. To fully desribe Ψ_e, we need to compute a complex number for every possible position of every electron.
In order to compute the wavefunction, let us imagine that we partition space into a rather coarse $10 \times 10 \times 10$ grid. That means there are 1000 positions r_i for each electron i. Since carbon has 6 electrons, the number of configurations is $1000^6 = 10^{18}$, and we need a complex number for every configuration in order to write down Ψ_e.

If each complex number is saved on the computer as a pair of 8-bit numbers, therefore the memory required to save one instance of Ψ_e will be 10^{18} bytes,

or a million Terabytes. A supercomputer might be able to deal with this, and perhaps Ψ_e can be simplified with a clever choice of basis set, but the point has been made: the difficulties with computing the many-body wavefunction increase exponentially with the number of electrons.
Obviously, this is a crude example used to illustrate a point. There are many techniques out there designed to deal with this problem while keeping accuracy (quantum monte-carlo to name just one). However, if we struggle this much for a single carbon atom, consider computing Ψ_e for the unit-cell of elemental lead, or a molecular-dynamics simulation of a dozen nitrogen molecules.

In contrast, the domain of the electron *density* ρ has only three dimensions: x, y, and z:

$$\rho(\text{position}) = (\text{number of electrons}) \times |\Psi_e|^2 \tag{3.9}$$

$$\rho : \mathbb{R}^3 \longrightarrow \mathbb{R}. \tag{3.10}$$

Instead of solving the Schrödinger equation for the many-body wavefunction, a functional of the electron density ρ can be solved instead.

Intuitively, this may not appear to be equivalent to solving for the full Ψ_e. The density ρ seems much simpler than Ψ_e, so one may expect it carries less information. However, in 1964 Hohenberg & Kohn showed that the *ground-state* electron density and the ground-state wavefunction are infrangibly linked.

The first theorem of Hohenberg & Kohn states that the Hamiltonian is a unique function of the electron-density ρ, to within an additive constant. Because the ground-state wavefunction and the energy-spectrum can — in principle if not always in practice — be calculated from the Hamiltonian, the first theorem of Hohenberg & Kohn proves that the ground-state wavefunction is uniquely determined by the ground-state electron density (up to a phase factor $e^{i\theta}$):

$$\rho_{A,0} = \rho_{B,0} \Longleftrightarrow \Psi_{A,0} = \Psi_{B,0} \times e^{i\theta}, \tag{3.11}$$

$$\Rightarrow \qquad E[\rho_0] = E_0 = \hat{H}\Psi_0, \tag{3.12}$$

where $E[\rho]$ is some unknown energy-functional of the electron density ρ.

For nearly forty years physicists had been trying to numerically solve the

Schödinger equation for Ψ. In what some consider the founding paper of DFT, Hohenberg and Kohn showed that there was a much simpler function containing all the same information[91].

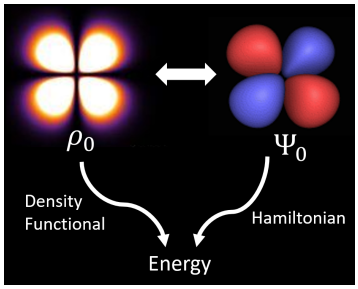

The key component of the Schrödinger equation is the Hamiltonian, which, for a time-independent potential, maps the wavefunction Ψ_e to an energy. The first theorem of Hohenberg and Kohn implies that there exists an *energy-density functional* $E[\rho_0]$, that maps the ground-state electron density ρ_0 to that same energy. The energy-density functional depends on factors like electric fields and the nuclear positions; much like the Hamiltonian. The second theorem of Hohenberg & Kohn proves that the electron density which minimizes this functional is indeed the ground-state density ρ_0. Thus, finding the electron density that minimizes $E[\rho]$ is equivalent to finding the many-body wavefunction that minimizes the Hamiltonian.

The first Hohenberg-Kohn theorem proves there exists an energy-functional which does the job of the Hamiltonian. The second Hohenberg-Kohn theorem shows that the ground-state density can be found by variationally minimizing this functional. However, neither theorem derives this functional. Indeed, the *exact* density functional remains unknown to this day. In order to conduct calculations, $E[\rho]$ must be approximated, and developing better approximations an active area of research. The method by Kohn & Sham provides a convenient way to form that approximation.

Aside: For me, this is the first surprise of density functional theory. The ground-state many-body wavefunction has such high-dimensionality, yet all the information it contains (energy-spectra, expected positions, etc) can be reduced down to a 3-parameter function: the density.

In information theory there is a concept called *"redundancy"*: it quantifies the amount of wasted memory used to store certain data. A highly redundant method of storing data uses lots of memory to store very little information. Shannon — the founder of classical information theory — famously estimated the redundancy of written English as 50% [92,93].

The complexity of the many-body electron wavefunction grows exponentially with the number of electrons, yet the amount of information is fully captured by the 3-parameter electron density. Considering the number of electrons in a teaspoon of salt well exceeds 10^{23}, the many-body wavefunction is probably the most redundant thing in the universe.

3.1.3 The Kohn-Sham equations

The energy-density functional $E[\rho]$ includes several complex interactions *between* individual electrons. There are three interactions that are useful to mention:

1. Due to the Pauli exclusion principle, the many-body wavefunction must be antisymmetric under exchange of two electrons with the same spin. This increases the total energy, and is often called the *exchange interaction*.

2. There is a pairwise classical electrostatic repulsion between electrons. This is known as the *Hartree* term:

$$E_H[\rho] = C \iint \mathrm{d}^3\boldsymbol{r}\ \mathrm{d}^3\boldsymbol{r'}\ \frac{\rho(\boldsymbol{r})\rho(\boldsymbol{r'})}{|\boldsymbol{r}-\boldsymbol{r'}|},$$

   where C is the constant needed to correct dimensions. Importantly, this is a *classical* term. The true Coulomb interaction between electrons is a quantum-mechanical operator, for which the Hartree term is only an approximation. The missing piece that the Hartree term leaves out are the quantum correlations.

3. *Correlations* arise between the motion of the electrons[‡]. This lowers the total energy, as it screens some of the Coulomb repulsion between electrons.

The interactions between electrons are complex, but in models like the Drude model, where electrons do not interact except by Pauli exclusion, calculations are relatively simple. Kohn & Sham exploit this; rephrasing the problem using a much simpler system of non-interacting electrons[94,95].

The Kohn-Sham approach is to imagine a set of fictional non-interacting electrons $\{\psi_1, \psi_2, ..., \psi_m, ..., \psi_N\}$, known as *Kohn-Sham electrons*, which have the same density ρ as the real system:

$$\rho(\boldsymbol{r}) = \sum_{m}^{N} |\psi_m(\boldsymbol{r})\,|^2, \tag{3.13}$$

where N is the number of electrons in the real system. The non-interacting Kohn-Sham orbitals are solutions to a set of time-independent Schrödinger equations:

[‡]Electron correlations are related to the concept of screening, where the electron distribution rearranges itself — reducing the range of the Coulomb force. The Kohn-Sham formalism defines correlation slightly differently (shown later), which guarantees the correlation energy to be negative.

$$\left[-\frac{\hbar^2}{2m_e}\nabla^2 + \nu_{\mathrm{KS}}(\boldsymbol{r})\right]\psi_i = \epsilon_i\psi_i, \tag{3.14}$$

where ϵ_i is the eigenenergy of the i^{th} orbital, and ν_{KS} is a yet-unknown potential. This *Kohn-Sham potential* ν_{KS} is essentially defined by the requirement that the solutions to Eq. 3.14 have the same density as ρ, and the sum of their eigenvalues ϵ_i equals the total energy E[§]:

$$\sum_{i \text{ occupied}}^{N} \epsilon_i = E[\rho]\,. \tag{3.15}$$

For this to be satisfied, ν_{KS} must be the sum of the external potential between the electrons and nuclei $\nu_{\text{e-n}}$, the Hartree term ν_H, and a third catch-all term called the *exchange-and-correlation potential* ν_{XC}:

$$\nu_{\mathrm{KS}}(\boldsymbol{r}) = \nu_{\text{e-n}}(\boldsymbol{r}) + \nu_{\mathrm{H}}(\boldsymbol{r}) + \nu_{\mathrm{xc}}(\boldsymbol{r})\,. \tag{3.16}$$

Some of these terms are easy to compute. The electron–nuclei potential $\nu_{\text{e-n}}$ has a simple form:

$$\nu_{\text{e-n}}(\boldsymbol{r}) = \frac{e^2}{4\pi\epsilon_0}\sum_n \frac{Z_n}{|\boldsymbol{r} - \boldsymbol{R}_n|}, \tag{3.17}$$

where Z_n is the atomic charge of nuclei n, $\boldsymbol{R}_n$ it's position, and D is just a constant.

The Hartree term ν_H is just a classical approximation to the coulomb interaction between electrons:

$$\nu_{\mathrm{H}}(\boldsymbol{r}) = \frac{e^2}{4\pi\epsilon_0}\iiint \mathrm{d}^3\boldsymbol{r'}\ \frac{\rho(\boldsymbol{r'})}{|\boldsymbol{r} - \boldsymbol{r'}|}, \tag{3.18}$$

where C is just a constant that gives ν_{H} the right units, and $\boldsymbol{r'}$ is a position vector to integrate over.

All the quantum exchange and correlation effects are pushed into the third term, known as the *exchange-and-correlation potential*: ν_{XC}. If this term were known exactly, then the Kohn-Sham approach would be exact. But, unfortunately, it needs to be approximated.

[§] To be precise, the Kohn-Sham potential ν_{KS} is given by the difference between the functional derivative of the energy-functional $\delta E[\rho]/\delta\rho$, and the functional derivative of the kinetic energy of a non-interacting electron gas which shares the same density $\delta K_{\mathrm{KS}}/\delta\rho$: $\nu_{\mathrm{KS}} = \delta E[\rho]/\delta\rho - \delta K_{\mathrm{KS}}/\delta\rho$

Aside: This is the second thing I found surprising about DFT. Up to this point, the Kohn-Sham formalism is exact. No approximation has taken place yet.

All of the difficult parts of the problem, the exchange and correlation effects, are combined into the catch-all term ν_{XC}. It may appear as if Kohn & Sham are simply kicking the can down the road.

However, for typical atomic systems, the Kohn-Sham kinetic-energy K_{KS}, the energy associated with the Hartree term E_{H}, and the electron-nuclei energy $V_{\text{e-n}}$, are generally much larger than the exchange-and-correlation energy E_{xc}. For example, for a single Neon atom the energies can be broken down as follows[96]:

K_{KS} (eV)	E_{H}	$V_{\text{e-n}}$	E_{XC}
3500	1800	-8470	350

By rewriting the energy-functional in this way, only a small portion of the total energy needs to be approximated. Kohn & Sham may have kicked the can down the road, but it is now a much smaller can.

3.1.4 Exchange-and-Correlation Potentials

Kohn & Sham arranged the energy-density functional so that the easy to calculate portions of the total energy could be computed. In doing so, they rolled up the unknown parts of the energy-density functional into a relatively small contribution to the total-energy: the exchange-and-correlation potential ν_{xc}. However, when calculating many chemical properties of interest — such as bulk moduli or band gaps — the exchange and correlation energies are crucial. Although an exact form for the exchange–correlation term is unknown, it cannot be neglected. Thus, when conducting a density functional theory calculation, an approximation to this term must be selected.

When selecting the exchange–correlation potential (ν_{XC}), a trade-off is made between accuracy, and efficiency. More complex potentials often, but not always, calculate results which have closer agreement to experiment. However, more complex potentials have a much higher computational cost. This is often

described as a *"Jacob's ladder"* of exchange-correlation functionals, with less accurate but computationally cheaper functionals at the bottom, and more accurate but more computationally expensive functionals higher up.

This thesis will use two exchange-and-correlation potentials: the generalized gradient approximation for solids (PBEsol)[97], and the modified Becke-Johnson potential by Tran and Blaha (TB-mBJ)[98]. The simplest class of exchange-and-correlation potentials is given by the local density approximation.

The Local Density Approximation (LDA)

LDA is the simplest, and computationally cheapest, class of exchange-correlation potentials. The exchange and correlation energies for an electron gas of uniform density have many constraints on the functional form they can take. This allows them to be calculated with extremely high accuracy. The local-density approximation uses these accurately known energies as the basis for approximating the exchange and correlation energies in a real solid, where the density of electrons is not uniform.

The LDA method approximates the exchange-correlation potential at a point $\boldsymbol{r}$ in a solid to be equal to the exchange-correlation potential for a uniform-density electron gas $\nu_{\mathrm{XC}}^{\mathrm{unif.}}$ with a density equal to the *local* density at that point $\rho(\boldsymbol{r})$. Thus, the total exchange-correlation energy E_{XC} is given by:

$$E_{\mathrm{XC}} = \iiint \mathrm{d}^3\boldsymbol{r} \;\; \nu_{\mathrm{XC}}^{\mathrm{unif.}}\big[\rho(\boldsymbol{r})\big]\,\rho(\boldsymbol{r}). \tag{3.19}$$

The exchange-correlation potential for the uniform gas $\nu_{\mathrm{XC}}^{\mathrm{unif.}}$ has been calculated to extremely high accuracy using quantum monte carlo, a method much more accurate than density functional theory but far more computationally expensive. Thus, LDA can be said to be exact for any material which has a uniform electron density. Of course, no real material has this. However, the approximation is generally accurate as long as the electron density varies slowly with space, i.e. that the density divided by the gradient of the density, $\rho/|\nabla\rho|$, is a very large length compared to other relevant lengths — such as the inverse of the Fermi wave-vector or the electron screening length. The key point is that the local density approximation tends to work well with simple metals, where the electron density varies slowly. However, in many other materials the local density approximation is not sufficiently good because the electron density does not very slowly. For these materials, more accurate — but more computationally expensive

— approximations to the exchange-and-correlation potential are needed.

The Generalized Gradient Approximation (GGA)

In LDA the exchange-correlation potential was approximated to be that of an electron gas of uniform density. Thus, the exchange-correlation potential $\nu_{\mathrm{LDA}}(\boldsymbol{r})$ was a function of only one argument: the local density $\rho(\boldsymbol{r})$. More computationally expensive, but perhaps more accurate, approximations to $\nu_{\mathrm{XC}}(\boldsymbol{r})$ generally include additional ingredients. In the class of GGA functionals, the added ingredient is the local-gradient of the electron density.

The generalized gradient approximation (GGA) describes a class of exchange-and-correlation potentials which are functions of both the electron density $\rho(\boldsymbol{r})$, and the gradient of the density, $\nabla\rho(\boldsymbol{r})$. Within this approximation, the exchange-correlation energy is written as:

$$E_{\mathrm{xc}} = \iiint \mathrm{d}^3\boldsymbol{r} \;\; \rho(\boldsymbol{r}) \; \nu_{\mathrm{GGA}}\big[\rho(\boldsymbol{r}), |\boldsymbol{\nabla}\rho(\boldsymbol{r})|\big] \,, \tag{3.20}$$

where the function ν_{GGA} depends on which version of GGA is being used. Probably the most popular versions are by Perdew, Burke, and Ernzerhof[99] (*PBE*), and the later revision by Perdew *et al.*[97] known as *PBEsol*.

For PBE and PBEsol, the exchange-and-correlation potential ν_{GGA} is calculated as the exact-exchange potential for a uniform electron gas $\nu_{\mathrm{X}}^{\mathrm{unif}}(\rho)$, multiplied by a factor F_{XC} which ranges between around 1 and 1.7, and depends on both the density ρ and its' gradient $\nabla\rho$:

$$E_{\mathrm{xc}}^{\mathrm{GGA}} = \iiint \mathrm{d}^3\boldsymbol{r} \;\; \nu_{\mathrm{X}}^{\mathrm{unif.}}\big[\rho(\boldsymbol{r})\big] \;\; \rho(\boldsymbol{r}) \; F_{\mathrm{XC}}\big[\rho(\boldsymbol{r}), |\boldsymbol{\nabla}\rho|\big] \,, \tag{3.21}$$

where $\nu_{\mathrm{X}}^{\mathrm{unif.}}$ is the exact exchange potential for a uniform-density electron gas[¶].

The key factor which differs GGA from LDA is the term F_{XC}. In the high density limit, for a non-spin-polarized electron gas with uniform density, F_{XC} tends to 1 — giving exact exchange for the uniform electron gas. For lower uniform-densities, F_{XC} is greater than 1 — indicating that the exchange-correlation energy has increased due to correlations. The functional form of F_{XC} was designed to be

[¶]For clarity, this F_{XC} is as defined in Equation (15) of Perdew *et al.*[99]. In practice, the PBE and PBEsol exchange-and-correlation functionals are usually calculated in two seperate parts: local exchange ν_{X} times an enhancement over local exchange F_{X}, plus local correlation ν_{C}, plus an enhancement over local correlation H_{C}. One can combine all three terms into a total effective enhancement over LDA, F_{XC}. See Eq. (15) and Fig. 1. from Perdew *et al.*.

exact in cases where exact solutions are known (e.g. high-electron density & low gradient, or uniform gradient & low density).

The PBEsol potential is generally good at calculating the total-energy of solids, and consequently their elastic properties — such as the bulk modulus and lattice constants. However, it is not known to calculate accurate bandstructures of materials.

The modified Becke-Johnson potential (mBJ)

Exchange-correlation potentials within the local-density approximation or the generalized gradient approximation tend to yield results which are accurate enough to help interpret many experimental results, or hold predictive power. They also have the advantage of being relatively computationally cheap. However, in some cases they have generally bad agreement with experiment. In particular, the band gaps calculated for semiconductors or insulators tend to be significantly off. Given that the band gap — and the change in the band gap under strain — will be important for this thesis, it is important to use an exchange-correlation potential which better estimates the band gap.

The next run on Jacob's ladder of exchange-and-correlation potentials are the *"meta-GGAs"*. These potentials add an additional argument on top of the local density ρ and the gradient of the local density $|\nabla\rho|$. This additional ingredient is usually the second derivative of the density $\nabla^2\rho$ or the kinetic energy density. As such, meta-GGAs are generally more computationally expensive than GGAs or LDAs, but they have the potential to be more accurate.

The modified Becke-Johnson potential by Tran & Blaha[98] was designed specifically to improve band gap calculations for semiconductors and insulators. It is optimized for this method: i.e. there are actually free parameters in the potential which were chosen by the creators of the functional to fit a large number of band gaps of solids. Figure 3.1 shows how this functional compares with other functionals at calculating the band gaps for a variety of materials. The key point is that the mBJ potential produces more accurate calculations of semiconductor band gaps than potentials like LDA, for relatively little additional computational cost[98,100,101]. Other methods which perform well in Fig. 3.1, such as GW and G_0W_0, are both much more computationally epensive than the modified Becke-Johnson potential[98,100,101].

The exact expression for the modified Becke-Johnson potential (mBJ) is rather

complex[98] and will not be detailed here. The design goal of Tran and Blaha was to create a functional which accurately calculates the band gap of solids, while also being relatively computationally cheap compared to other methods designed to achieve good band gaps, such as the *GW* method. It has been demonstrated to work well for many semiconductors and insulators, but it may not be a wise choice for metals — in particular ferromagnetic metals — or for antiferromagnetic insulators[101]. As the potential was never really designed for metals, this should not be a surprise.

One additional note is that optimizing the mBJ functional for band gaps came at the expense of accurately calculating the total-energy. The potential is designed for accurate band gaps, not for accurate total energies. Indeed, the modified Becke-Johnson potential is not actually the functional derivative of an energy functional (akin to how a force potential could be written which is not the analytical derivative of an energy potential). Thus, the mBJ functional should not be used for total-energy calculations[102].

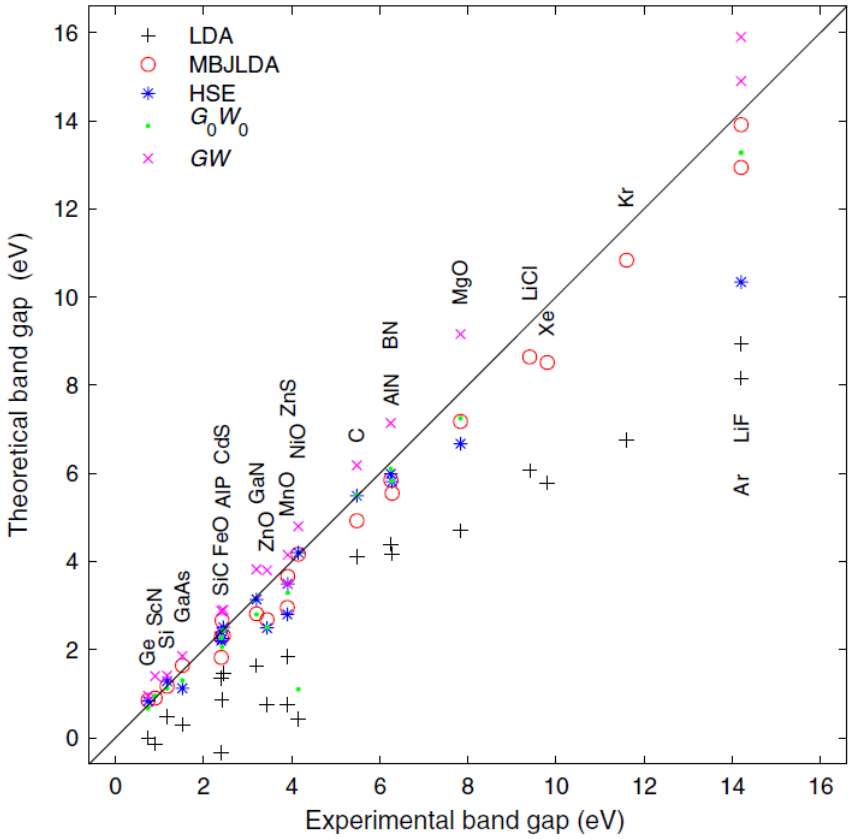

Figure 3.1 *Figure taken from Tran & Blaha[98]. Calculated band gaps vs experimental band gaps for a variety of materials. The results for a variety of different exchange-correlation functionals are shown. The modified Becke-Johnson functional is here labelled MBJLDA.*

3.1.5 The Self-Consistent Cycle

The last pillar of DFT is the *self-consistent cycle*.

DFT calculations, within the Kohn-Sham formalism, aim to find the set of Kohn-Sham orbitals $\{\psi_i\}$ that minimize the total energy. The Kohn-Sham potential ν_{KS} is a functional of the density ρ. So, in practice, the density and ν_{KS} have to be found together, iteratively.

Each iteration involves several steps:

1. For a given density ρ_k for iteration k, the Kohn-Sham orbitals will be found (Eq. 3.14) using the Kohn-Sham potential $\nu_{\mathrm{KS}}(\rho_k)$.
2. Generate a new density ρ_{k+1}, based on the lowest N Kohn-Sham orbitals: $\{\psi_i\}$. This is usually done by mixing the old and new densities: e.g. $\rho_{k+1} = (1-\alpha)\,\rho_k + \alpha \sum_{i=1}^{N} |\psi_i|^2$ for some parameter α between 0 and 1.
3. Repeat using ρ_{i+1}.

As long as the mixing parameter α is not too large, each step in this cycle will reduce the total-energy[103]. The energy of the ground-state is a lower bound, so the cycle should converge to this energy. Cycles are repeated until some convergence criterion has been reached; for example, the total energy no longer changes by more than 1 meV. At that point the density is called *self-consistent*.

3.1.6 Conclusion

Density functional theory is a method to efficiently perform meaningful first-principles calculations. The choice of exchange-and-correlation potential is important, and can greatly affect the outcome of the calculation and the computation time. Some aspects have not been discussed — such as the basis choice used to expand the Kohn-Sham orbitals, and Bloch's theorem. Some further background pertinent to the implementation of DFT used in this work, Wien2k, can be found in appendix A.2. I have also catalogued some useful references in appendix A.1. Details specific to my density functional theory calculations on the properties of lead telluride are in the following sections.

3.2 Methodology for PbTe

3.2.1 Convergence Tests

When conducting a calculation using Wien2k, several parameters must be chosen. Increasing these parameters generally improves the accuracy of the calculation, but at the expense of computing time. It is important to *converge* these parameters, to ensure they are sufficiently high to achieve results which are sufficiently accurate, within the approximations of the chosen exchange-correlation potential, while keeping computational cost at a minimum. This section briefly illustrates two convergence tests that were performed; full details are in the next section.

One parameter is the number of k-points used to sample the Brillouin zone. A regular grid of points within the Brillouin-zone is generated on which to calculate the Kohn-Sham orbitals. The denser the k-point grid — the better the Brillouin-zone will be sampled, at the expense of computation time. Figure 3.2(a) shows how the total-energy per atom converges as the Brillouin-zone is more densely sampled. For k-grids denser than $\sim 20 \times 20 \times 20$, there is negligible change in the total energy. An appropriate tolerance should be chosen, e.g. ± 1 meV/atom, and the k-point number needs to be sufficient to satisfy that.

When the goal is to calculate stresses, it is useful to check that the curve of total-energy, under some deformation, is converged. Figure 3.2(b) shows energy against a uniaxial [111] deformation for different k-point grids. There is negligible change upon increasing the k-point density. Indeed, the second derivatives are within 1 % of each other. This shows that a $20 \times 20 \times 20$ k-point grid is converged.

Another important parameter which needs to be converged is the largest reciprocal lattice vector used in for the Kohn-Sham orbital basis vectors[‖]. Wien2k parametrizes this using a dimensionless number known as $RKmax$. The number of basis vectors, and thus the computation time, grows approximately with the cube of RKmax. Thus, it is important to keep RKmax low. Unfortunately, the band gap of PbTe converges slowly with RKmax. Figure 3.2(c) shows how the calculated band gap continues to increase significantly with RKmax, even for RKmax $\sim$9, which is generally considered a high value.

However, the goal was not to calculate the band gap — but to calculate the thermoelectric properties, and how they change when the crystal is strained. For

[‖] Further details in appendix A.2

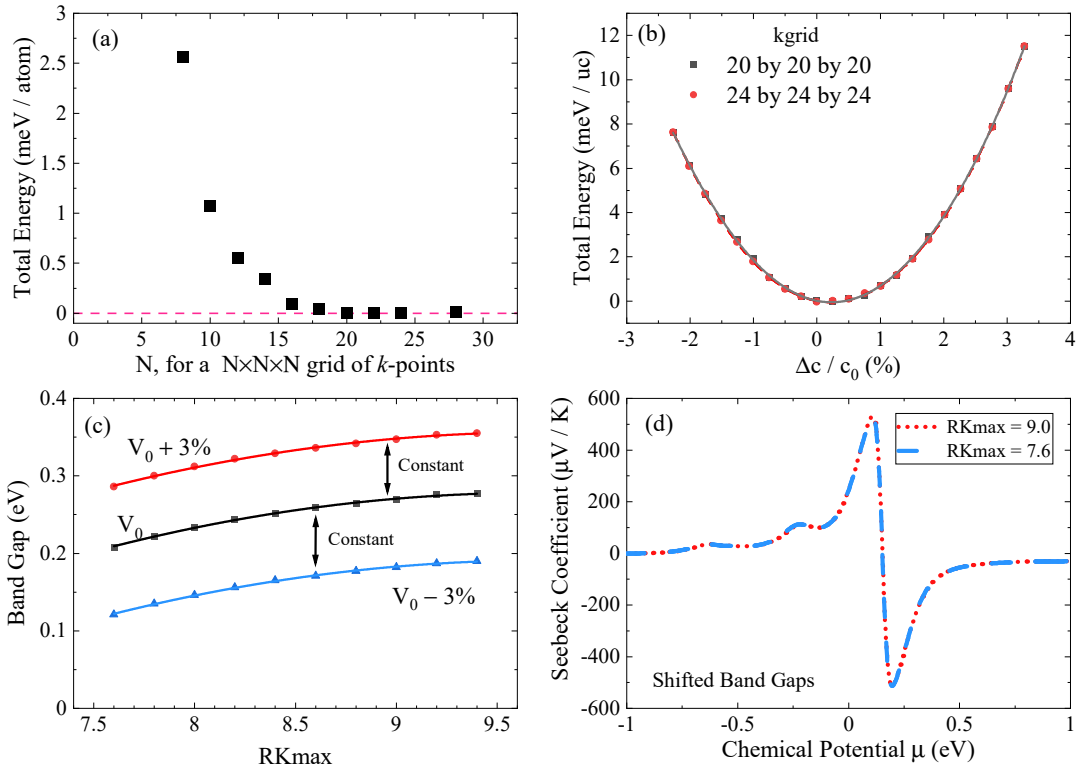

Figure 3.2 *Selected convergence tests for PbTe. (a) total-energy vs number of k-points for the PBEsol exchange-correlation potential. (b) comparison of the total-energy against a uniaxial deformation along the [111] axis for two different k-point numbers. Lines are guides to the eye. The PBEsol functional was used. (c) Band gap vs RKmax for the mBJ potential at three different volumes. (d) Seebeck coefficient vs chemical potential, at 300 K, for two different RKmax settings. The band gap was shifted to be equal.*

reasons explained in the next section, the absolute band gap was going to be shifted in any case. What mattered was the shape of the bandstructure, and how much the band gap changed when PbTe was strained. Figure 3.2(c) shows how, although the calculated band gap increases with increasing RKmax, the relative band gap at different volumes is constant (within ±1 meV).

I checked that increasing RKmax does not change the thermoelectric properties beyond the shift in band gap. The electron-transport properties of PbTe were calculated using two different RKmax values, but with the band gap shifted to be the same for both cases. Figure 3.2(d) shows that the Seebeck coefficient of PbTe at 300 K is negligibly different if RKmax is increased, as long as the band gap is shifted.

Similar convergence calculations were undertaken for the parameters mentioned in the next section.

3.2.2 Overview

At ambient conditions, lead telluride adopts the sodium chloride crystal structure. There are three main axes along which uniaxial stress can be applied: the [111], [001], and [110] crystal directions.

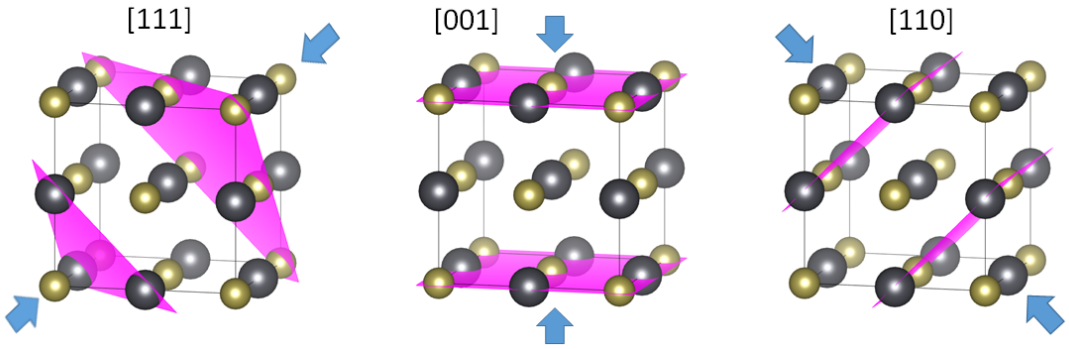

For each direction, the crystal was strained both along the axis, and perpendicularly, to make a wide range of strain combinations. Figure 3.3 illustrates how this was done for investigating stress combinations in the [001] direction. Stress along [001] changes the symmetry of the unit cell from face-centered cubic to a body-centered tetragonal symmetry. Many combinations of strains along c, parallel to [001], and along the new a axis, perpendicular to [001], were calculated.

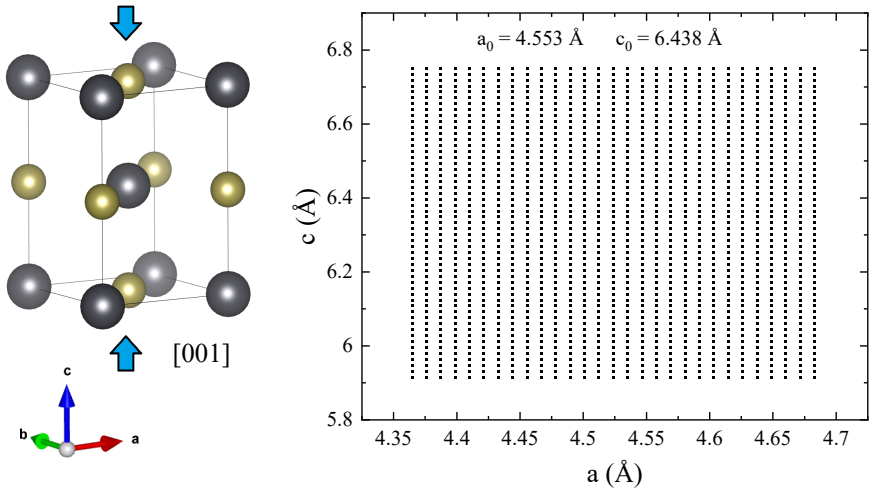

Figure 3.3 *Left: Body-centered tetragonal unit cell used for the stress combinations along [001] calculations, space group 139, I4/mmm. Right: Lattice parameter combinations chosen for investigating stress along [001]. Each point indicates a combination of lattice parameters used in the investigation.*

For each strain combination, two types of calculations were performed. The first type calculated the total-energy of the strained unit cell. The second type

calculated the electron transport properties. The former was used to determine the stress for each strain combination. Combining both types of calculations yields the stress dependence of electrical transport properties.

All calculations were performed in the framework of density functional theory (DFT) and the full-potential augmented-plane-wave + local orbital [(L)APW+lo] approach as implemented in the Wien2k code[104]. Further details about this approach can be found in appendix A.2. The $5d$, $6s$, and $6p$ orbitals of Pb, and the $4d$, $5s$, and $5p$ orbitals of Te were treated as valence states. Spin-orbit coupling was included in all calculations. Tests indicated that it was important to include an extra local orbital, shaped similar to the relativistic $6p_{1/2}$ semi-core state, in the basis set of orbitals on the lead atoms[105]. A DFT study of Bi_2Te_3 showed that it is important to include relativistic local orbitals for the thermoelectric properties of atoms with $6p$ valence states[106].

3.2.3 Stress as a function of strain

In Wien2k, stress cannot be calculated for a single unit cell. Instead, multiple calculations were conducted to compute total-energy as a function of strain, the derivative of which yields the stress. For example, straight horizontal or vertical lines of points in Fig. 3.3 correspond to uniaxial or biaxial strains of the body-centered tetragonal unit cell. For each combination of strain, the total energy was computed. Total energy as a function of strain was then fitted using a 4th order polynomial (Fig. 3.4). The derivative of this polynomial with respect to strain yeilded the stress.

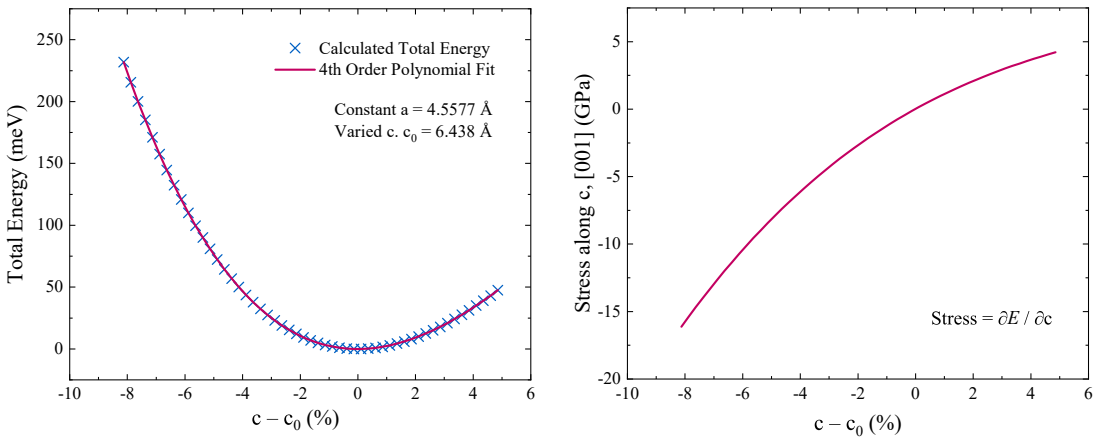

Figure 3.4 *Left: Total energy vs uniaxial strain along c, parallel to [001]. Right: Stress along [001] as a function of strain, given by the partial derivative of the total energy.*

For this set of calculations, Exchange and correlation effects were treated with the revised generalized gradient approximation for solids (PBEsol-GGA [97]). This functional is known to produce good calculations of elastic properties. However, it does not accurately calculate the bandstructure of PbTe. Indeed, calculations using PBEsol predict that the band gap increases with increasing pressure — contrary to experimental results. Thus, although the PBEsol exchange-and-correlation potential is good for predicting stress as a function of strain, it could not be used to calculate the electron-transport properties of PbTe. Further details are given in appendix A.6.

Regular Monkhorst-Pack $20 \times 20 \times 20$ grids of k-points (equivalent to a k-point spacing of $2\pi \times 0.0078\,\text{Å}^{-1}$) were used for Brillouin zone sampling. An atomic sphere muffin tin radius (R_{MT}) of 2.5 bohr was chosen for both the Pb and Te atoms. The largest Kohn-Sham plane-wave vector $K_{\max}$ was given by $R_{MT} \times K_{\max} = 9.0$. The magnitude of the largest vector used in the charge density Fourier expansion (GMAX) was 12 bohr^{-1}.

To compute the lattice parameters corresponding to uniaxial stress, I computed the lattice parameters corresponding to zero stress perpendicular to the direction of applied stress. Figure 3.5 shows how the lattice parameters corresponding to uniaxial stress along a specific direction, in this case [001], can be computed.

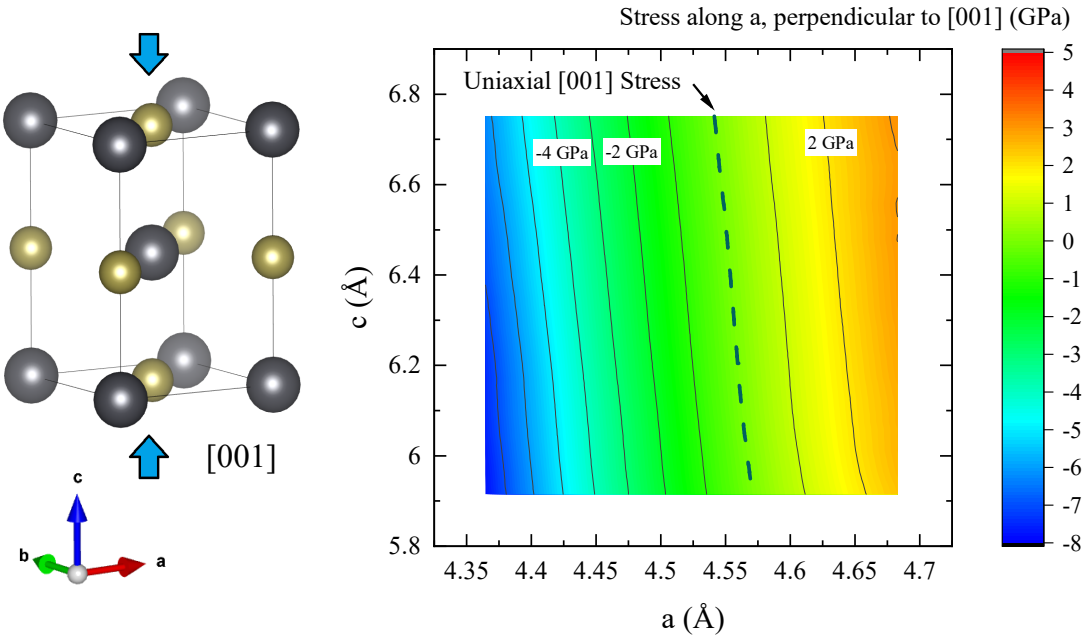

Figure 3.5 *Stress perpendicular to [001] as a function of the lattice parameters a and c. The line of zero stress shows the lattice parameters corresponding to uniaxial stress along [001]. The scale of this plot is the same as that of Fig. 3.3.*

3.2.4 Electron transport properties

The second set of calculations determined the electronic transport properties for each strain. Exchange and correlation effects were treated with the modified Becke Johnson potential by Tran and Blaha (TB-mBJ)[98], with the parameters optimized for narrow-gap semiconductors[100]. This exchange-correlation potential is optimized to calculate the relative energies of states near the band gap, at the expense of accurately calculating the total energy. Thus, although the mBJ potential could calculate the electron-transport properties of PbTe, it could not be used for calculating the stresses.

Regular Monkhorst-Pack $28 \times 28 \times 28$ grids of k-points (equivalent to a k-point spacing $\approx 2\pi \times 0.0056\,\text{Å}^{-1}$) were used for Brillouin zone sampling. An atomic sphere muffin tin radius, R_{MT}, of 2.5 bohr was chosen for both the Pb and Te atoms. The largest Kohn-Sham plane-wave basis vector, $K_{\max}$, was given by $R_{MT} \times K_{\max} = 7.5$ (RKmax). The magnitude of the largest vector used in the charge density Fourier expansion, GMAX, was set to 12 bohr^{-1}. A table of all these parameters can be found in appendix A.3.

In Wien2k, additional local orbitals (LOs) are added to the basis set used to calculate the Kohn-Sham orbitals. The energy of these local orbitals need to be chosen carefully to prevent errors (so-called *"ghost bands"*[107]). Full details of the local orbital settings can be found in appendix A.3.

After self-consistency had been reached, the Kohn-Sham orbital eigenvalues were computed on a dense $56 \times 56 \times 56$ k-point grid in a single, non-self-consistent, calculation. From these eigenvalues, electrical transport properties were calculated using the framework of Boltzmann transport theory as implemented in the BoltzTraP code[108].

BoltzTraP

BoltzTraP[108] and its successor BoltzTraP2[109] are computer programs designed to calculate the transport coefficients of a material, using the electronic band-structure as input.

BoltzTraP takes as input a set of k-points and electron eigenenergies, corresponding to the bandstructure of the material in question. It then interpolates the bandstructure, in order to (i) increase the density of the Brillouin-zone sampling, and (ii) obtain the velocity and curvature of the bands at each k-point. Then the

electron-transport integrals (the L-matrix integrals) can be evaluated within the constant-scattering-time approximation.

As is standard practice, doping was treated using the *rigid band approximation*, which assumes the band structure is independent of doping concentration. Doping is thus treated by adjusting the chemical potential μ to give a set doping concentration. The rigid band approximation breaks down in the limit of a mixed crystal, when the high concentration of dopant atoms can distort the electronic structure. Our calculated results compare excellently to experimental data for doping concentrations up to at least $10^{19}\,\mathrm{cm}^{-3}$, as demonstrated in the *experimental comparison* section.

Calculation of the Charge-Carrier Concentration

The exact concentration of conduction-band electrons n_e and valence-band holes n_h was be computed by integrating the product of the electron density of states $g(\varepsilon)$ and the Fermi-Dirac distribution $f_{\mathrm{FD}}(\varepsilon)$ over states in the conduction or valence-band, respectively:

$$n_e = \int_{\varepsilon_{\mathrm{CBM}}}^{\infty} \mathrm{d}\varepsilon f_{\mathrm{FD}}(\varepsilon) \times g(\varepsilon), \tag{3.22}$$

$$n_h = \int_{-\infty}^{\varepsilon_{\mathrm{VBM}}} \mathrm{d}\varepsilon \left[1 - f_{\mathrm{FD}}(\varepsilon) \times g(\varepsilon)\right], \tag{3.23}$$

where $\varepsilon_{\mathrm{CBM}}$ and $\varepsilon_{\mathrm{VBM}}$ are the energies of the conduction-band minimum and valence-band maximum, respectively.

From n_e and n_h, the total concentration of charges which will contribute to electrical transport, the doping-concentration of the semiconductor, and the concentration of charge-carriers caused by temperature exciting electrons across the band-gap, can be computed:

$$n_{\mathrm{total}} = n_e + n_h = n_{\mathrm{doping}} + n_{\mathrm{intrinsic}}, \tag{3.24}$$

$$n_{\mathrm{doping}} = |n_e - n_h|, \tag{3.25}$$

$$n_{\mathrm{intrinsic}} = 2 \times \min\left[n_e, n_h\right] = n_{\mathrm{total}} - n_{\mathrm{doping}}. \tag{3.26}$$

It is worth noting that the intrinsic-carrier concentration $n_{\mathrm{intrinsic}}$ depends not just on the temperature and band gap, but also on the chemical potential. Indeed, if two samples with different doping concentrations are held at the same temperature, it is unlikely that the intrinsic carrier concentration will be equal.

It will be shown that the trends in electron-transport properties under stress are qualitatively different in the *saturated regime*, where $n_{\text{intrinsic}} \ll n_{\text{doping}}$, compared to the *intrinsic regime*, where $n_{\text{intrinsic}}$ is similar to or greater than n_{doping}. I classify combinations of doping concentration and temperature as being in the intrinsic regime if the intrinsic carrier concentration is greater than $\sim$10 % of the doping concentration. Although this condition is arbitrary, it is useful for discussing the different behaviours seen in each regime. By computing these charge-carrier concentrations directly, the effects in each regime could be distinguished.

3.2.5 Electron scattering time

The BoltzTraP code assumes the constant-scattering-time approximation which states that the electron scattering time τ is independent of the electron energy [108]; at least within the energy range of importance for transport properties. Detailed studies have shown that an isotropic τ is often a good approximation [108,110]. Modest anisotropies in τ can sometimes affect quantities like the Hall coefficient, depending on the material [110], but, as will be shown, the change in bandstructure under stress are so large that they are likely the dominant effect.

It is however possible that there is a different scattering regime, such as a constant mean-free-path. In a regime like this, the scattering time of electrons would be strongly dependent on their velocity. However, in most thermoelectric materials, electron–phonon scattering is the dominant form of scattering. Calculations of electrical transport properties in PbTe, where the electron–phonon scattering time was calculated directly, have shown good agreement with experimental measurements [32]. These calculations indicate an electron-scattering time which is approximately constant with energy.

The constant-scattering-time approximation does not require the scattering time to be constant with respect to temperature, and indeed the scattering time should be lower at higher temperatures. To enable easy comparison with experiment, the electron scattering time τ was estimated. Good experimental agreement was found using a scattering time of 5×10^{-14} s at 300 K. This value is similar to the electron–phonon scattering times derived by directly calculating the electron–phonon scattering terms [32,78], and to times obtained by comparing experimental electrical conductivities with calculations [77].

Figure 3.6 shows the results calculated here for the electrical conductivity at 300 K

alongside experimental literature values. Our calculated conductivities assume a scattering time $\tau = 5 \times 10^{-14}$ s, and are plotted as a function of Hall carrier concentration ($n_H = 1/|eR_H|$, where R_H is the Hall coefficient).

For very heavily doped cases above $n_H \approx 3 \times 10^{19}\,\mathrm{cm}^{-3}$ the scattering time appears to change from 5×10^{-14}s. Above a carrier concentration of $\sim 3 \times 10^{19}\,\mathrm{cm}^{-3}$, experimental values for the conductivity slightly flatten off as the carrier concentration increases, whereas our calculated values do not. If the dopant concentration is high, the scattering time due to impurities, and electron-electron scattering, will become similar to the electron-phonon scattering time. It should be expected that, at very high doping concentrations, the scattering time τ will become a function of dopant concentration. Overall, there is excellent agreement with the experimental data, using a scattering time of 5×10^{-14} s at 300 K.

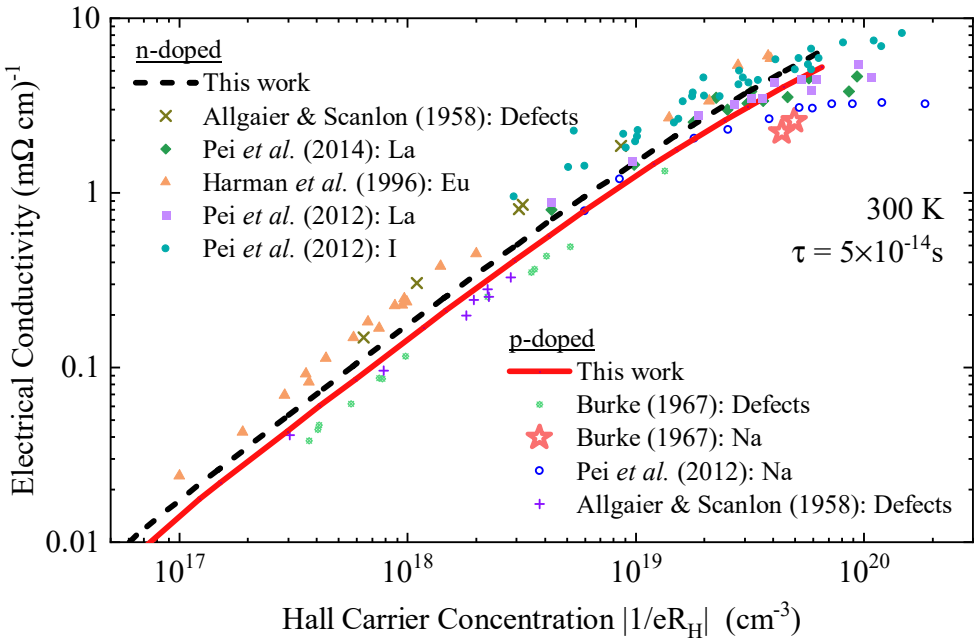

Figure 3.6 *Electrical conductivity vs Hall carrier concentration (n_H) for p- and n-doped PbTe. Lines show our calculated results, with the electron scattering time set to be 5×10^{-14}s. Symbols show experimental results from the literature for a variety of p- and n-doped cases*[29,29,71,81,111–113].

To account for increased scattering at higher temperatures, the scattering time τ should be rescaled with temperature T. Estimating how τ changes with temperature from first-principles would require calculation of the electron–phonon scattering times, which in turn would require the phonon-spectrum to be accurately calculated. Experimental measurements of how mobility scales with temperature vary considerably, depending on temperature and doping

concentration[59]. The scattering time was scaled inversely with temperature:

$$\tau = 5 \times 10^{-14}\,\mathrm{s} \times \left(\frac{300\,\mathrm{K}}{T}\right). \tag{3.27}$$

This scaling is based on the assumption that electron–phonon scattering is the dominant mechanism for scattering electrons, with $\tau \propto T^{-1}$ originating from the phonon population increasing linearly with temperature, as it does in the classical case. Experimental measurements indicate that PbTe has a Debye temperature between 115 and 180 K[114,115], significantly less than room temperature. Although the electron scattering time τ is scaled as a function of temperature, it is kept constant for all stresses. The value of τ is only important for ease of comparison with experimental data, and does not affect the trends observed with stress.

The electron scattering time τ is not expected to change significantly with stress. Stresses of order 1 GPa will have a relatively small impact on the phonon spectrum, and thus the phonon scattering time, whereas the change in electronic structure will be shown to be substantial. As a result, the changes in transport properties under stress should be dominated by the changing bandstructure, rather than the electron scattering time.

3.2.6 The Band Gap

The size of the band gap influences the position of the chemical potential and the number of intrinsic charge carriers. This is crucial for calculating thermoelectric properties. However, density functional theory, in combination with standard LDA or GGA exchange-correlation functional, is known to underestimate band gaps[116]. Moreover, the experimental band gap of PbTe has a significant temperature dependence[39,43,45–48] (Fig. 2.12), increasing by roughly 50% from 0 to 300 K. This is not captured by standard, ground state density functional theory calculations — even if thermal expansion is included[59].

To account for the temperature dependence of the band gap, the conduction bands are rigidly shifted to adjust the gap, as is standard practice[117]. The gap was shifted for each strain by the same amount, chosen so the gap would agree with experimental values for a single fixed point at zero stress[45].

The band gap G for each stress σ and temperature T was set to be the experimental value at zero stress $G_{\mathrm{exp.}}$[45] modified by the calculated difference

between the stressed band gap $G_{\text{calc.}}(\sigma)$, and the calculated zero stress band gap $G_{\text{calc.}}(\sigma = 0)$:

$$G(\sigma, T) = \underbrace{G_{\text{calc.}}(\sigma) - G_{\text{calc.}}(\sigma = 0)}_{\text{calculated}} + G_{\text{exp.}}(T)\,. \tag{3.28}$$

In summary, there are two types of calculations: the stress as a function of strain, and electron-transport properties as a function of strain. Combined, this allows electron transport properties to be presented as a function of stress. The key approximations are:

1. the constant-scattering-time approximation, i.e. the scattering time is the same for all electrons contributing to electrical transport.
2. the rigid-band approximation.
3. the band gap is adjusted to account for the change in band gap with temperature. It is adjusted by the same amount for every stress.
4. the electron-scattering-time τ is approximately constant under stress.
5. aside from the band gap, the shape of the bands remains similar as a function of temperature.

Within these assumptions, our calculations give excellent agreement with available experimental results in the literature, as will be shown in the following chapter.

Chapter 4

Thermoelectric Properties of PbTe under Stress

4.1 Experimental Comparison

4.1.1 Bandstructure

Our calculated zero stress bandstructure (Fig. 4.1) has good agreement with previous experimental and theoretical work[27,28,36,60,62,118]. As discussed in the background section on the bandstructure of PbTe, there are many distinctive features of the bandstructure. The band edges indeed appear like anisotropic Kane-model dispersions, with much lower mobility along the L–Γ direction, and the valence band has a local maximum along the Γ–K line.

The anisotropic transport properties of each carrier pocket is sometimes quantified by the ratio between an effective mass parallel to the [111] direction $m^*_{[111]}$, and an effective mass perpendicular to it $m^*_\perp$. Experimental measurements of this "effective mass anisotropy" ($A = m^*_{[111]}/m^*_\perp$) vary, depending on how the effective masses are estimated. Measurements of A for PbTe vary between 6.4 and 14 for the valence band, and 5.5–10 for the conduction band, depending on the method used[35,59–61,119,120]. This variation may be due to the non-parabolic bandstructure of PbTe, making estimations of the effective mass highly dependent on doping concentration. Fitting our calculated bandstructure gives an effective mass anisotropy $A \approx 12$ for the valence band, and $A \approx 9$ for the conduction band; both in good agreement with experiment[35,59,119,120].

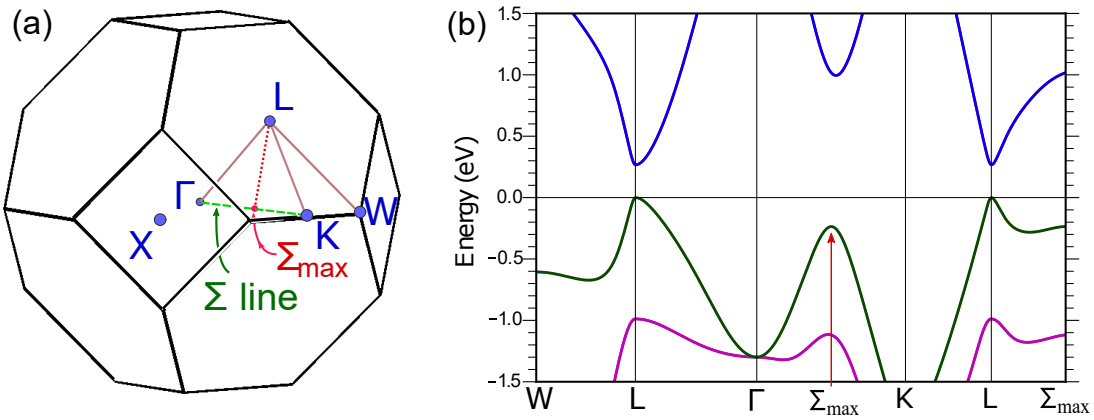

Figure 4.1 *(a) Brillouin Zone of PbTe. (b) Bandstructure of PbTe. Σ_{max} is the position of the maximum along the L–K line, and is the location of a local maximum of the valence band. The L–Σ_{max} line is a straight line through the Brillouin zone between the L-point and Σ_{max}. This figure was shown in the background chapter; it is repeated here for convenience.*

We calculate the energy of $\Sigma_{\max}$ to be ∼0.24 eV below the maximum at the L-point, in good agreement with ARPES measurements[28] and Hall coefficient data[27,41] in the literature, and we capture the region of positive curvature of the valence band between L and $\Sigma_{\max}$ (Fig. 4.1).

4.1.2 Electron Transport Properties

To gauge the accuracy of our calculations, we compared our transport calculations with some experimental data at zero stress. In experiment, the doping concentration n is often estimated by measuring the Hall carrier concentration: $n_H = 1/|eR_H|$, where R_H is the Hall coefficient and e is the electron charge. As discussed in the background section, for semiconductors with only one kind of carrier n_H generally differs from the true doping concentration by a factor of order unity[16,27,40,41,59,121].

Figure 4.2(a) shows both the true carrier concentration n, and the calculated Hall carrier concentration n_H, as a function of chemical potential. The true carrier concentration is consistently larger than n_H, apart from when the chemical potential is near the middle of the band gap. At very low doping concentrations the Hall carrier concentration diverges. The validity of using the Hall coefficient to estimate carrier concentration depends on there only being one type of carrier (electrons or holes). As the chemical potential increases from a p-type sample to an n-type sample, the Hall coefficient must change from positive to negative. Thus

there is a region where the Hall coefficient approaches zero, and the Hall carrier concentration diverges. This divergence usually occurs when the intrinsic carrier concentration is significant compared to the dopant concentration. Figure 4.2(a) also indicates the energy scales of importance. For typical doping concentrations, on the order of $10^{19}\,\mathrm{cm}^{-3}$, the chemical potential can be several tens of meV into the valence or conduction band. For cases with dopant concentrations above $10^{20}\,\mathrm{cm}^{-3}$, the chemical potential can be over 100 meV into the relevant band.

The ratio n/n_H is shown in Fig. 4.2(b). Figure 4.2(b) can be used to translate between experimentally measured Hall carrier concentration n_H, and the real carrier concentration n of the crystal. The true doping concentration exceeds the Hall carrier concentration by $\sim 70\%$, for n between 10^{17} and $10^{19}\,\mathrm{cm}^{-3}$, in good agreement with experiment[41]. At doping concentrations above $\sim 10^{19}\,\mathrm{cm}^{-3}$, n/n_H, deviates. As the chemical potential moves further into the band, energy isosurfaces no longer appear as prolate ellipsiods. This occurs at energies several k_BT above the local maximum at Σ_{max} [see the -200 meV isosurface in Fig. 2.10(a)]. The deviation of n/n_H from 1.7 should not be attributed to holes being redistributed into the lower valence band maximum at Σ_{max}. Figure 2.10(b) shows that the true bandstructure is deviating from a modified Kane model at energies $\sim$100 meV above the local maximum at Σ_{max}. If the p-doping concentration and/or temperature are high enough such that states near Σ_{max} are important, then the bandstructure near the L-point has already deviated from the Kane-model.

Both Fig. 4.2(a) and b were calculated at 300 K. Hall coefficient data is often measured at low temperatures (77 K). The lowest temperature we calculated was 100 K, for which n/n_H remained $\sim$1.7. Calculations at lower temperatures are difficult, as the narrow energy range of importance means a very dense sampling of the Brillouin zone is required.

Figure 4.3(a) compares our calculated Seebeck coefficient (solid lines) with experimental values from the literature (symbols) for room temperature PbTe with a range of carrier concentrations. There is excellent agreement for n-doped PbTe up to $\sim 10^{19}\,\mathrm{cm}^{-3}$, with more pronounced deviations at the highest doping levels.

For p-doped PbTe there is significant variation across experiments, even at low doping levels. Choice of dopant has a large effect on the Seebeck coefficient, especially if multiple different dopants are introduced (e.g. Mn co-doped with Na). Overall we have very good agreement.

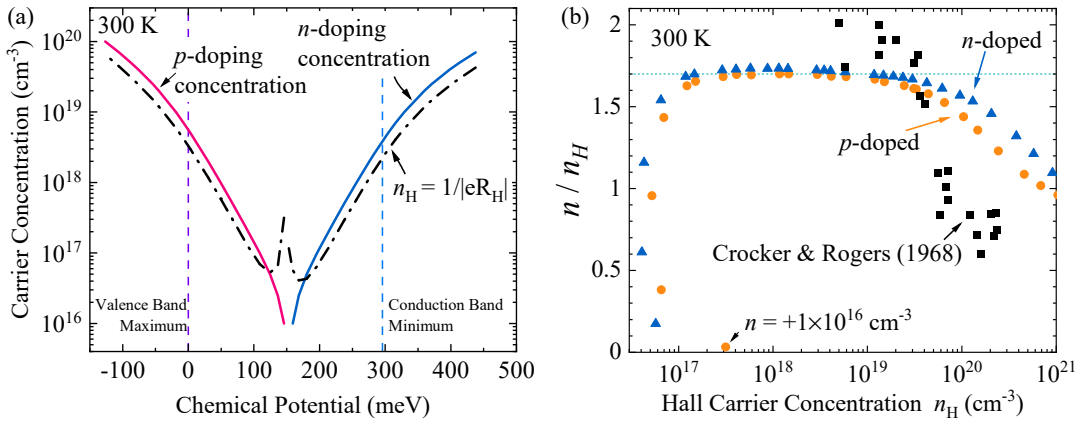

Figure 4.2 *(a) Carrier concentration versus chemical potential μ at 300 K, where $\mu = 0$ is at the valence band maximum. (b) Ratio between the true dopant concentration, and the calculated Hall carrier concentration for p-doped (orange circles) and n-doped (blue triangles) at 300 K. Also shown is experimental data of the ration between the sodium concentration and the Hall carrier concentration (measured at 77 K) for heavily Na-doped PbTe[41].*

Figure 4.3(b) shows our calculations, alongside experimental results from literature, for the Seebeck coefficient of several different n-doped PbTe samples as a function of temperature. The solid lines are our calculated values, while the symbols are taken from experiments in the literature. Overall there is excellent agreement between the two, but there is a deviation for the sample with the highest dopant concentration ($n_H = 1.8 \times 10^{19}\,\mathrm{cm}^{-3}$). When a sample of PbTe is more and more heavily doped, the bandstructure will begin to change as the material tends toward a mixed crystal. This means the rigid band approximation will break down, and the choice of dopant atom becomes important[126]. As we expect, if the carrier concentration exceeds $\sim 10^{19}\,\mathrm{cm}^{-3}$ there will be a more pronounced difference between individual experiments, and between our calculations and experiment. We also see this difference when PbTe is heavily p-doped [Fig. 4.3(c)].

Overall, we calculate a bandstructure in excellent agreement with existing literature. We also have good agreement with experimental results for the electron transport properties.

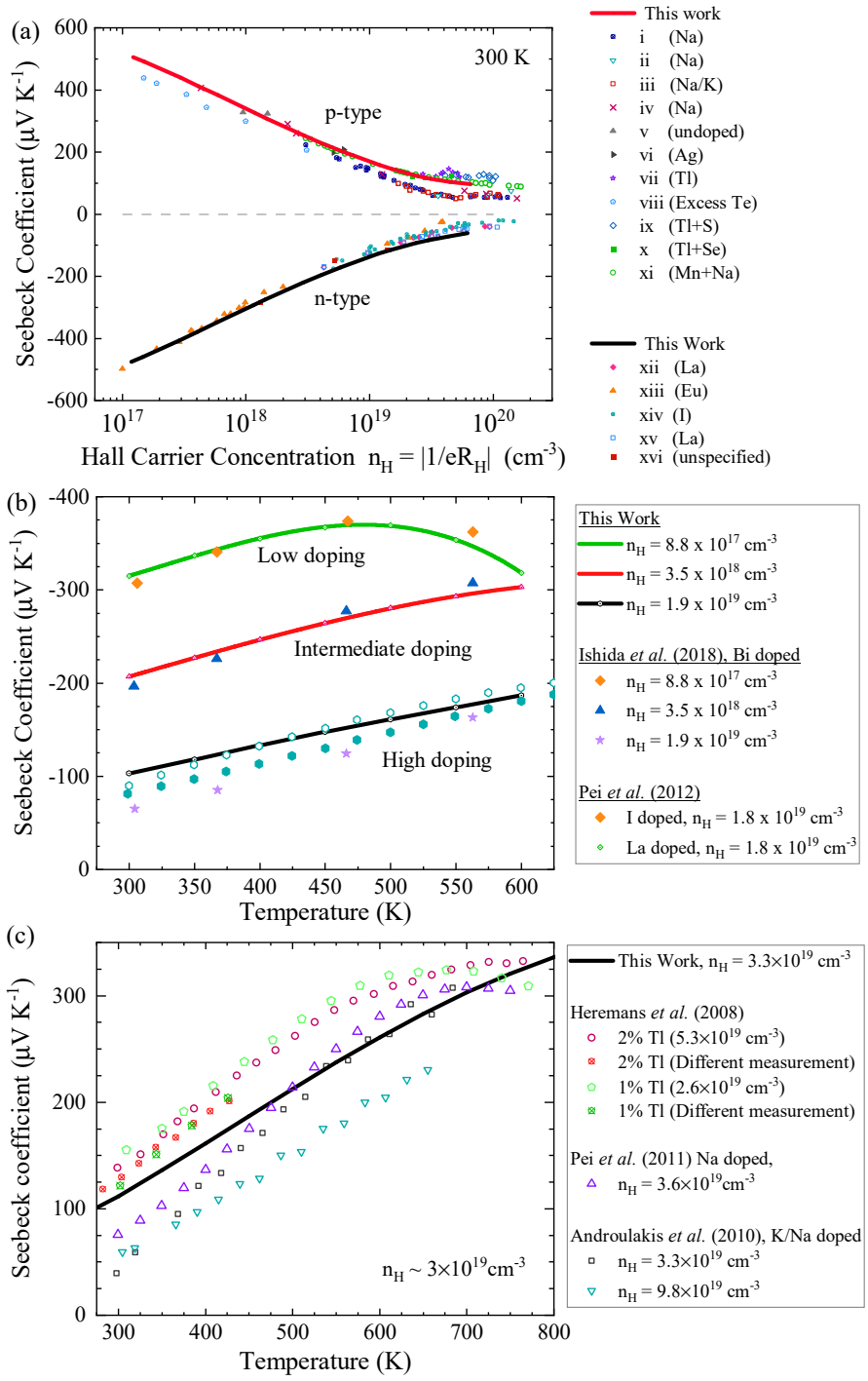

Figure 4.3 *(a) Seebeck coefficient vs Hall Carrier Concentration (n_H) for p- and n-doped PbTe at room temperature. Key is as follows: (i) Pei et al. (2012)[113] (ii) Pei et al. (2011)[67], (iii) Androulakis et al. (2010)[66], (iv) Crocker & Rogers (1967)[65], (v) Martin et al. (2009)[122], (vi) Martin et al. (2009)[122], (vii) Heremans et al. (2008)[123], (viii) Scanlon (1962)[124], (ix) Jaworski et al. (2011)[125], (x) Jaworski et al. (2011)[125], (xi) Pei et al. (2012)[113], (xii) Pei et al. (2014)[29], (xiii) Harman et al. (1996)[111], (xiv) Pei et al. (2012)[112], (xv) Pei et al. (2012)[112], (xvi) Averkin & Dermenzhi (1966)[50]; (b) Seebeck coefficient vs Temperature for n-doped PbTe.[70,112]; (c) Seebeck coefficient vs Temperature for p-doped PbTe[66,67,123].*

4.1.3 Elastic properties

Calculated elastic properties (Tab. 4.1) show good agreement with experimental values. The largest disagreement is for the elastic constant C_{44}, which is about half the experimental value. However, this discrepancy does not indicate a problem, as will be explained below. For clarity, the elastic constants were not used to determine the stress of PbTe as a function of strain. They are simply included here for comparison with experiment.

Table 4.1 *Calculated elastic properties of PbTe, compared to experimental results from the literature.*

Property	This work	Experimental comparison
$(C_{11} - C_{12})/2$ (GPa)	56	61.85 / 50.15 (0/303 K) [114]
B_0 (GPa)	43.53	45.63 / 41.13 (0/303 K) [114]
C_{44} (GPa)	7.73	15.14 / 13.43 (0/303 K) [114]
a_0 (Å)	6.44	6.4611 [127], 6.4541/6.4384 (298/120 K) [128]

Houston *et al.* [114] estimated the elastic-constants of PbTe based on measurements of the speed of ultrasound. They measured shear and longitudinal sound-velocities along different crystal directions. The elastic-constants were then related to the sound-velocity, using theory based on the assumption that inter-atom potential is parabolic (a Hookean solid). However, in some cases this assumption may not be appropriate. If, on the length scale of the sound-wave amplitude, the interatomic potential is not parabolic, then the simple equations relating sound-velocity to elastic-constants may not be valid.

In this work, the calculated total-energy of PbTe vs uniaxial [111] strain was fitted using a fourth order polynomial. The elastic-constant C_{44} was then computed from the second derivative of the polynomial at zero strain.

However, the total-energy vs strain was strongly non-parabolic. A lattice strain of only 2.3% was enough to make the quartic contribution to the polynomial larger than the parabolic. For comparison, room temperature thermal fluctuations have a length scale on the order of 2% of a_0 [55]. This shows that the potential for deformations along [111] is non-parabolic on the length scale of thermal fluctuations: approximately the same length-scale as experimental sound-waves. PbTe is known to have highly anharmonic phonons, and so it was not a surprise that assumptions of parabolicity behind elastic constant measurements would break down for this material.

4.2 Hydrostatic Pressure

The band gap of PbTe closes almost linearly with increasing hydrostatic pressure, tending towards a Dirac-semimetal at 5.5 GPa and 300 K. This is in proximity to a first-order structural transition to a phase with *Pnma* symmetry, which was reported to occur between 6 and 7 GPa[129]. Figure 4.4 shows the valence and conduction band extrema at the L point along two directions: Γ–L–Γ and K–L–K, which are parallel and perpendicular to the [111] direction, respectively [Fig. 4.1]. The difference in band curvature along the two directions indicates anisotropic transport properties for both hole and electron states near the L point. These band curvatures all increase with increasing pressure. Qualitatively, this increases the carrier mobility and decreases the Seebeck coefficient with increasing pressure.

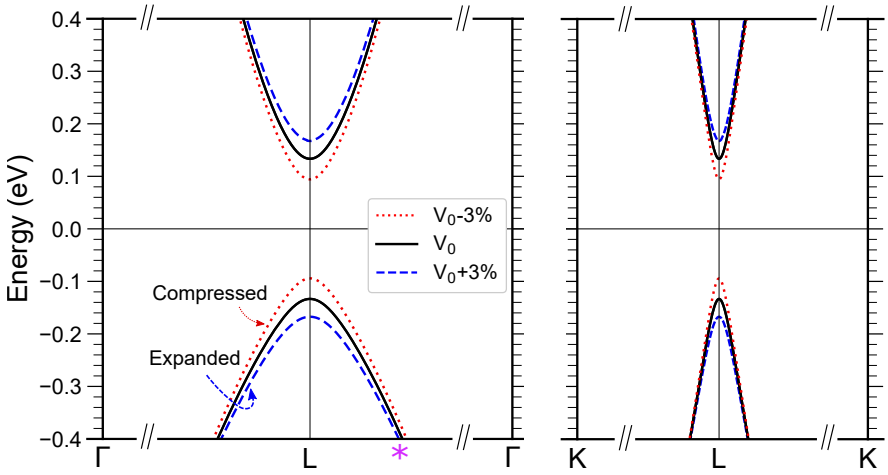

Figure 4.4 *Valence and conduction band extrema at the L point of PbTe under hydrostatic pressure. Electronic bands are shown for the calculated zero-pressure unit-cell volume, $V_0 = (6.44\,\text{Å})^3 = 267\,\text{Å}^3$, and volumes changed by ±3%, which correspond to pressures of −1.2 and 1.4 GPa. For comparison, the thermal expansion of PbTe between 0 and 300 K amounts to 1.5% at ambient pressure. The magnitudes of the wave vectors in the two directions are drawn to scale. The asterisk ∗ is ∼25% of the way from the L-point to Γ.*

This notion is quantified in Fig. 4.5(a) for *p*-type PbTe with an extrinsic (doping) carrier concentration of $n_d = 1.0 \times 10^{19}\,\text{cm}^{-3}$ at ambient conditions. The doping level per unit cell is held constant under pressure, so that the reduction in volume results in a nearly linear increase of the total charge carrier concentration, n_{tot}, with increasing pressure. The volume changes by approximately 2.4% per GPa of pressure. Therefore, the change in carrier concentration has little effect on the electrical conductivity relative to the change in bandstructure. Closing the band gap under pressure causes the intrinsic contribution to the carrier concentration

to increase exponentially, but at 300 K the intrinsic carrier concentration remains negligible compared to the doping concentration of $n_d = 1.0 \times 10^{19}\,\mathrm{cm}^{-3}$ considered here. At this doping level and temperature, PbTe is in the saturated regime.

Simple models, such as the degenerate parabolic band, suggest that increasing band curvature — or lowering the effective mass at the extrema — will decrease the Seebeck coefficient. As expected from the change in band curvature, the Seebeck coefficient S of PbTe reduces with increasing pressure, for all p- or n-doping concentrations considered.

The electrical conductivity σ increases with increasing pressure, predominantly due to the increase in hole mobility. The overall result is that the power factor, $\alpha = \sigma S^2$, decreases monotonically with increasing pressure.

The total carrier concentration and its change under pressure depend crucially on the combination of doping level and temperature. Whereas the total carrier concentration in the saturated regime increases nearly linearly, the reduction of the band gap causes an exponentially increasing carrier concentration if the intrinsic contribution is similar to or larger than the extrinsic. The pressure dependence of the power factor is determined by the relative changes in the Seebeck coefficient and electrical conductivity, with the former decreasing and the latter increasing with increasing pressure. For almost all relevant combinations of p- or n-doping level and temperature, I found the reduction in the Seebeck coefficient to dominate and the power factor to decrease with increasing pressure.

A more complicated behaviour can be observed for low doping doping concentrations, below $\sim 10^{18}\,\mathrm{cm}^{-3}$, and temperatures below $\sim 325\,\mathrm{K}$. Here, I found the power factor initially increases with increasing pressure, before reaching a maximum and decreasing again at higher pressures. Figure 4.5(b) illustrates this behaviour for n-type PbTe with a doping concentration of $5 \times 10^{17}\,\mathrm{cm}^{-3}$ at 300 K, where a maximum of the power factor is observed near 1 GPa. The turnaround coincides with the concentration of intrinsic carriers becoming significant compared to the extrinsic concentration, as can be seen by the transition from the linear increase of the carrier concentration under pressure to an exponential increase. In other words, the maximum in the power factor coincides with a transition from a low-doped saturated regime to the intrinsic regime.

In a low-doped saturated regime, almost all free-charge-carrier states are near a single band edge, where the curvature — and thus the average mobility

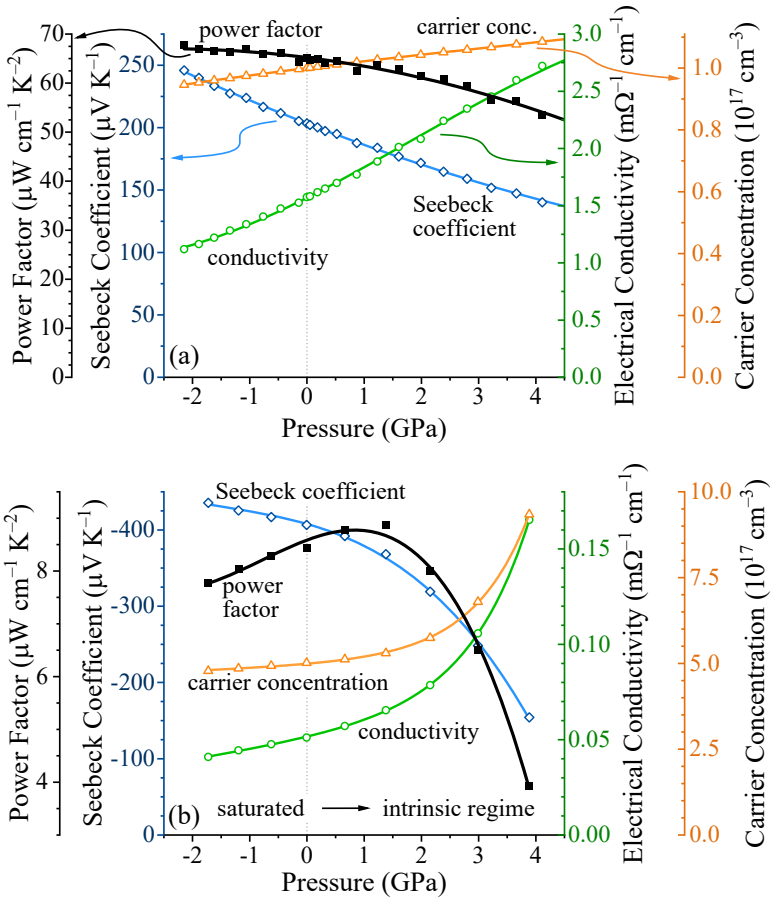

Figure 4.5 *Calculated electronic transport properties of PbTe under hydrostatic pressure at 300 K. (a) p-type PbTe with a doping concentration of $1.0 \times 10^{19}\,cm^{-3}$ at normal pressure. (b) n-type PbTe with a low doping concentration of $5 \times 10^{17}\,cm^{-3}$. The transition from the saturated (extrinsic) to the intrinsic regime is indicated by the total carrier concentration (orange) changing from a linear increase with increasing pressure to an exponential increase. Symbols show the calculated results, and solid lines are guides to the eye.*

— increases significantly with increasing pressure (Fig. 4.4). In such a case, the application of hydrostatic pressure can initially improve the thermoelectric power factor. However, for the majority of experimentally relevant doping levels and temperatures, our calculations predict the power factor the decrease with increasing hydrostatic pressure. Under the assumptions of (i) hydrostatic pressure and (ii) a constant doping level, I can therefore not reproduce nor explain the large increases in thermoelectric power factors observed by Ovsyannikov & Shchennikov[7], and Jacobsen *et al.*[9].

There is limited qualitative agreement between the results of this work and those from Baker *et al.*[8]. They observed the Seebeck coefficient reduce with increasing pressure, and the conductivity concomitantly increase, which agrees

with the results of this work. However, the increase in the conductivity was large enough that the thermoelectric power factor increased with increasing pressure — which differs from our findings. The Seebeck coefficient of their sample was between −50 and −60 µV/K, indicating that — although the sample was not intentionally doped — it had an effective n-doping concentration of $\sim 5 \times 10^{19}\,\mathrm{cm}^{-3}$ [Fig. 4.3(a)]. For this doping concentration, our calculations indicate that the conductivity of PbTe increases with increasing pressure by approximately 10 %/GPa. The results by Baker *et al.* imply their sample's conductivity increased by ∼60 % GPa — significantly larger. This discrepency may be due to increasing the carrier concentration under pressure by forming defects.

Calculations for the pressure dependence of the Seebeck coefficient were compared against existing experimental data. Figure 4.6 shows a comparison between data from two $-1.5 \times 10^{18}\,\mathrm{cm}^{-3}$ n-doped samples reported in papers by Ovsyannikov & Shchennikov[7,80], and calculated results from this work that used a carrier concentration of $n = -2.5 \times 10^{18}\,\mathrm{cm}^{-3}$, equivalent to a Hall coefficient $\sim 1.5 \times 10^{18}\,\mathrm{cm}^{-3}$ [Fig. 4.2(b)]. Also shown is an extrapolated trend based on the pressure gradient of the Seebeck coefficient ($\partial S/\partial P$) for a sample with a reported carrier concentration of $-1.3 \times 10^{18}\,\mathrm{cm}^{-3}$, measured by Averkin & Dermenzhi[50].

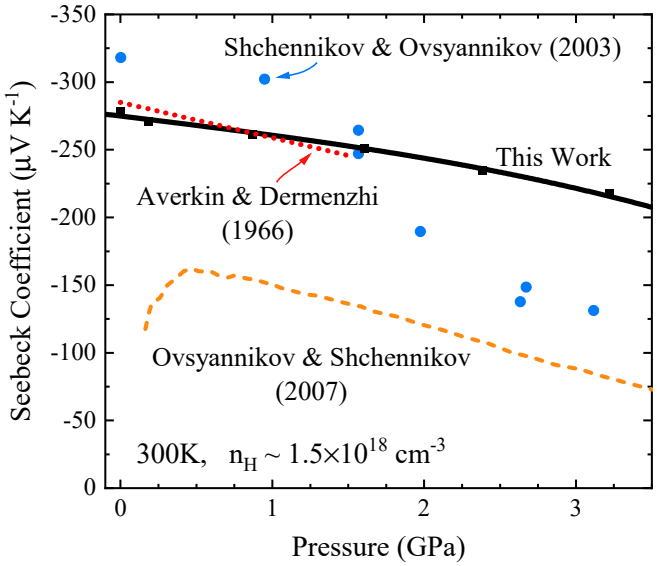

Figure 4.6 *Seebeck coefficient as a function of pressure for n-type PbTe, comparison between our calculated results (black line), and experimental values[7,50,80]. All samples have $n_H \approx 1.5 \times 10^{18}\,\mathrm{cm}^{-3}$, except the sample of Averkin & Dermenzhi who reported a Hall carrier concentration of $1.3 \times 10^{18}\,\mathrm{cm}^{-3}$.*

There is excellent agreement with the data from Averkin & Dermenzhi. The

disparity between the calculated results from this work and the data from either experiment by Ovsyannikov & Shchennikov is substantially less than their disparity with each other, suggesting that small details in experimental setup — such as the gasket material — may have altered the integrity of the (initially) single-crystal sample. However, it should be noted that our calculations, Averkin & Dermenzhi, Shchennikov & Ovsyannikov's 2003 paper, and Baker *et al.* all reported data with the same trend: the n-type Seebeck coefficient decreases with increasing pressure, and the conductivity increases[8,50,80].

The observations by Ovsyannikov & Shchennikov are most likely explained by a dramatic change in the carrier concentration — likely due to defect doping. Ovsyannikov & Shchennikov mention in their paper that the change of Seebeck coefficient from positive to negative seen in one of their samples is due to *"doping with defects"*. Increasing the dopant concentration may also explain why they observed the electrical resistance drop by an order of mangitude when increasing the pressure from 0 to $\sim$1 GPa. Perhaps the same effect is responsible for improvements under pressure seen by Baker *et al.* and Jacobsen *et al.*. Repeat measurements upon decreasing pressure would help indicate if the trends reported are caused by irreversibly forming crystal defects with increasing pressure, or reversibly changing the bandstructure due to strain.

4.3 Stress along the [111] direction

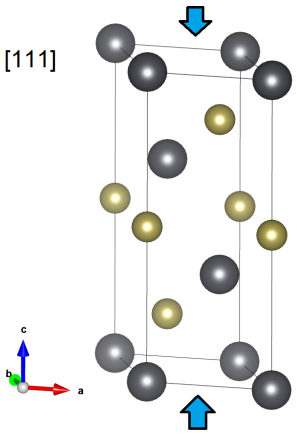

Stress along [111] transforms the symmetry of PbTe into a rhombohedral lattice, with spacegroup *R-3m*.

Non-hydrostatic stress breaks the cubic symmetry of PbTe. Figure 4.7(a) shows an energy isosurface of the PbTe conduction band. Stress along, and perpendicular to, [111] splits the originally degenerate carrier-pockets into a single T-point carrier-pocket, and three L-point carrier-pockets[130]. Figure 4.7(b) shows a bandstructure calculation of states near the T- and L-points under uniaxial tensile stress along [111]. Applying tensile [111] stress raises the energy of states near the T-point relative to the L-points, which would transfer conduction-band electrons from the T-point valley to the L-point valleys, and valence-band holes from the L- to the T-point. Compressive uniaxial stress does the opposite: redistributing conduction-band electrons to the T-point valley, and valence-band holes to the L-points. This *intervalley-transfer effect* leads to anisotropic transport properties[16,71,72].

As discussed above, the T- and L-point carrier-pockets have anisotropic transport properties. This anisotropy is quantified in Fig. 4.7(c), which shows the magnitude of the carrier velocity, parallel to [111], of states near the T- and L-point carrier-pockets. The velocity $v_{||}$ is calculated from the gradient of the bandstructure along a straight line shown by the $k_{||}$ arrows in Fig. 4.7(a). As each electron state along the $k_{||}$ lines corresponds to a unique energy, we can plot the band velocities as a function of energy instead of a function of k. Fig. 4.7(c) shows that states near the L-points have [111] velocities which are, on average, 2–3 times greater than for states near the T-point.

The intervalley-transfer effect, illustrated by Fig. 4.7(b), leads to transport properties gaining an anisotropy like that of the most populous carrier-pockets. Qualitatively, compressive uniaxial stress increases p-type conductivity along [111], and tensile stress increases n-type conductivity.

The effect of non-hydrostatic stress on the electrical conductivity is quantified in Fig. 4.8(a). The doping level per unit cell was held constant with stress, so the reduction in volume under pressure ($\sim$7% at 3 GPa) results in a similar increase in dopant carrier concentration. At the doping level and temperature considered

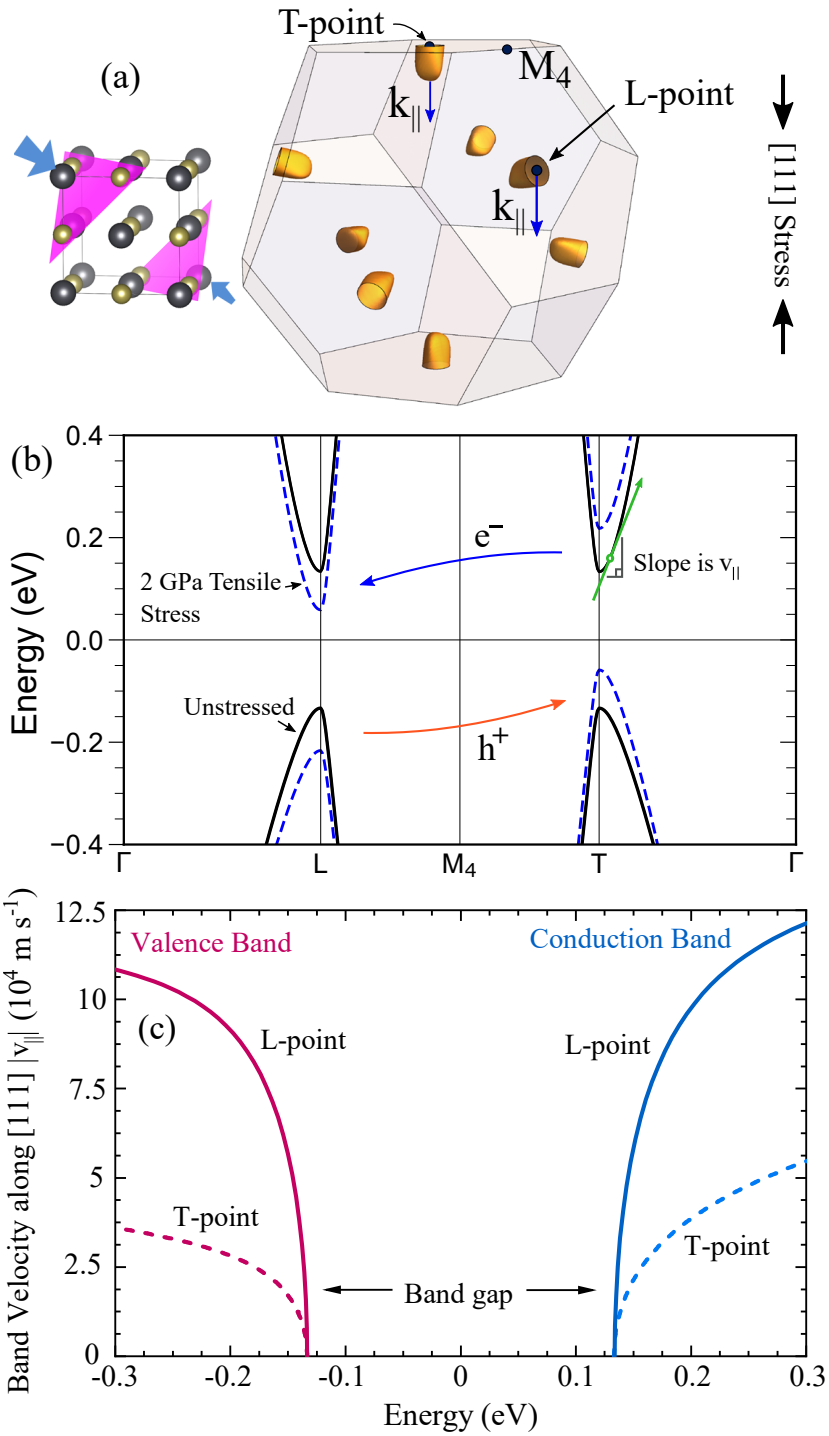

Figure 4.7 *(a) Energy isosurface 150 meV above the conduction band minimum for unstrained PbTe. (b) Change in the bandstructure under large tensile uniaxial [111] stress. Electrons in the conduction band are redistributed from the single T-point, to three L-points. Valence band holes move from L to T. (c) Magnitude of the band velocities along [111], $v_{||} = \hbar^{-1}|dE/dk_{||}|$, for the T and L-points. The velocity $v_{||}$ is along [111], parallel to the direction of stress. It is illustrated by the blue $k_{||}$ arrows in (a) and the green arrow in (b). The band gap has not been adjusted in this figure, although it was for all transport calculations.*

here, PbTe is in the saturated regime. As detailed in the last section, increasing hydrostatic pressure (vertically along $x = 0$) increases the electrical conductivity. In the saturated regime this is primarily due to increased electron mobility. Figure 4.8(a) shows tensile uniaxial stress also increases the conductivity. Increasing tensile stress transfers electrons from the low-[111]-mobility T-point to the high-mobility L-points [Fig. 4.7(b)] increasing the average electron mobility; 0.5 GPa of tensile stress will increase the conductivity along [111] by ∼25%. For all relevant combinations of n-doping level and temperature, we found the conductivity along [111] increased with increasing tensile uniaxial stress.

Figure 4.8(b) shows how the Seebeck coefficient along [111] changes under anisotropic stress. Tensile uniaxial stress transfers electrons from the single T-point carrier-pocket to the three L-point pockets. Reducing the number of carrier-pockets generally reduces the Seebeck coefficient, as fewer carrier-pockets implies a lower rate of change of the density of states[31,131,132]. Indeed, increasing the tensile stress reduces the Seebeck coefficient, but only slightly; 0.5 GPa of tensile uniaxial stress reduces the Seebeck coefficient by ∼3%, compared to a ∼25% increase of the electrical conductivity. Crucially, the contours of Fig. 4.8(a) and 4.8(b) point in different directions — meaning stress can be applied which increases the electrical conductivity and holds the Seebeck coefficient constant. Figure 4.8(c) shows that tensile uniaxial stress can increase the n-doped power factor. Across all doping concentrations and temperatures, we consistently found that uniaxial stress had a much larger effect on the power factor than hydrostatic stress.

Figure 4.9 quantifies the effect of uniaxial stress on the transport properties of $1.0 \times 10^{19}\,\mathrm{cm}^{-3}$ p-type PbTe at a range of temperatures. In Fig. 4.9(d), at 300 and 600 K, the total carrier concentration remains approximately constant under stress, because the intrinsic carrier concentration is negligible compared to the doping concentration. Compressive stress transfers holes to the high-mobility L-points, increasing the conductivity and reducing the Seebeck coefficient. At 300 K these changes balance to leave the Power Factor α along [111] approximately constant [Fig. 4.9(c)], but above room temperature there is a significant improvement in $\alpha_{[111]}$ with increasing compressive stress.

Tensile uniaxial stress transfers holes to the single low-mobility T-point, reducing the conductivity along [111] [Fig. 4.9(b)]. Conventional wisdom suggests that transferring charges to a single carrier-pocket will also reduce the Seebeck coefficient[31,131,132], however, Fig. 4.9(a) shows that, at 300 and 600 K, applying

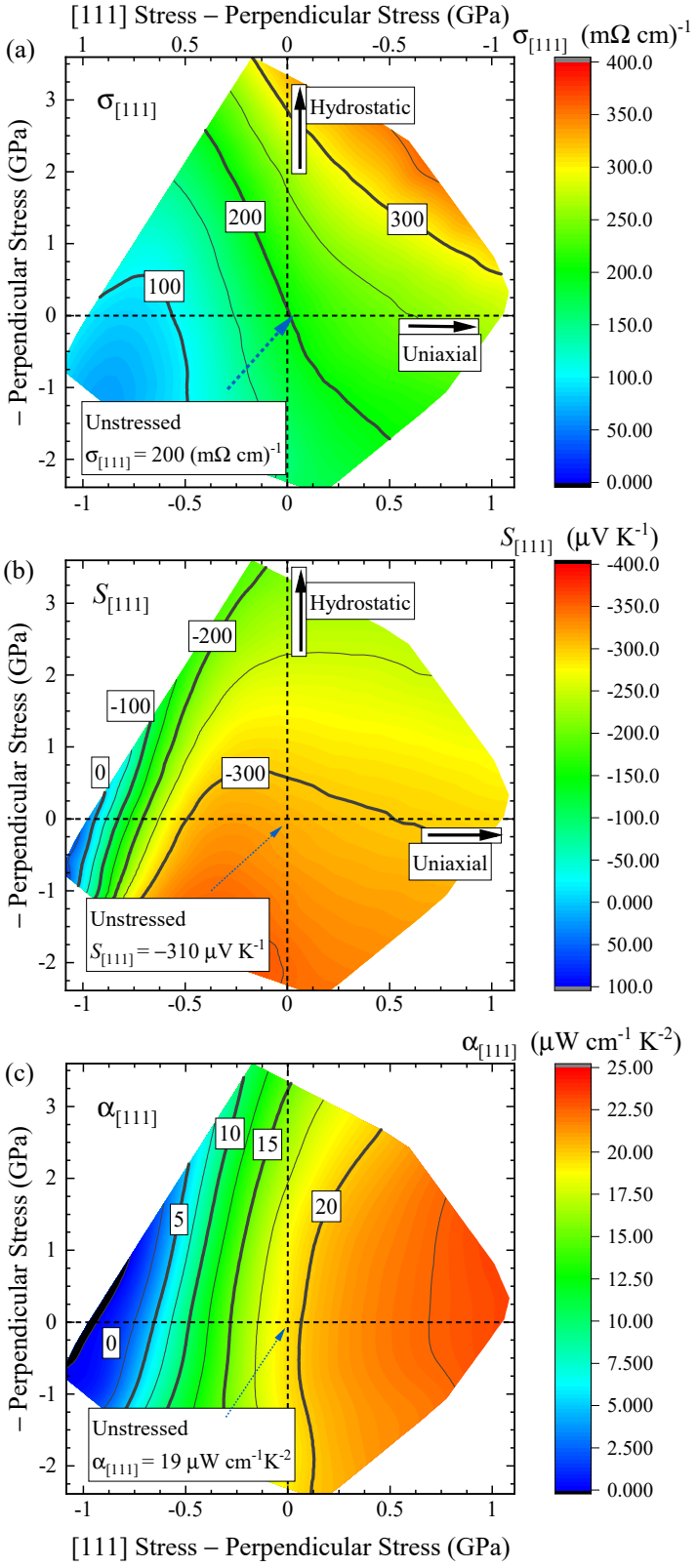

Figure 4.8 *(a) Electrical conductivity, (b) Seebeck coefficient, and (c) Power Factor* $\alpha_{[111]} = \sigma_{[111]} S^2_{[111]}$ *for* $-5.0 \times 10^{18}\,\mathrm{cm}^{-3}$ *n-doped PbTe at 600 K. The y-axis is stress applied perpendicular to the [111] direction; and the x-axis is the difference between stress applied along [111], and stress perpendicular to the [111] direction.*

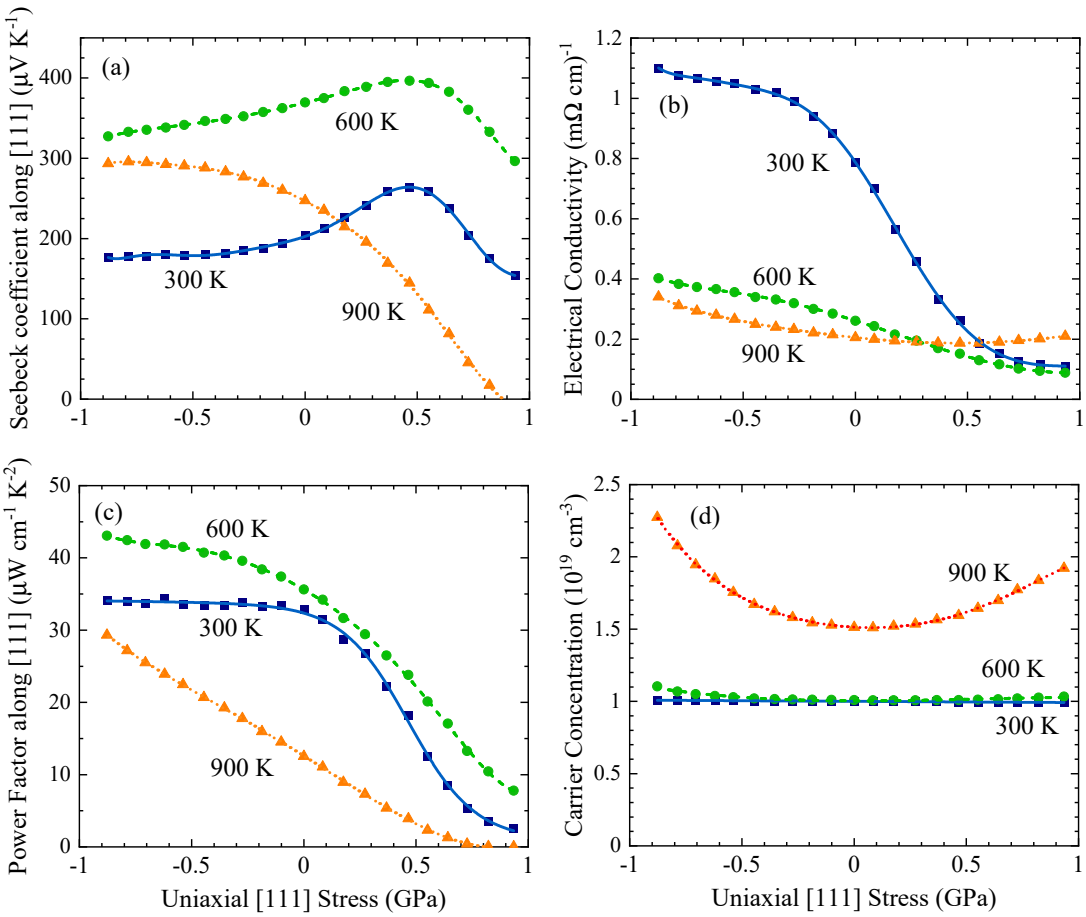

Figure 4.9 *Calculated (a) Seebeck coefficient along [111], (b) Electrical conductivity along [111], (c) Power Factor along [111], and (d) total carrier concentration of* $1 \times 10^{19}\,\mathrm{cm}^{-3}$ *p-doped PbTe as a function of uniaxial stress along [111].*

tensile stress of up to 0.5 GPa actually increases the Seebeck coefficient. This unusual trend was also observed for n-type PbTe, in the saturated regime, under compressive stress.

This unexpected trend in the Seebeck coefficient is due to the interplay between the $L^{(12)}$ matrix and the electrical conductivity, the ratio of which gives the Seebeck coefficient (Eq. 2.44). Figure 4.10 shows the how the Seebeck coefficient of $-1 \times 10^{19}\,\mathrm{cm}^{-3}$ n-doped PbTe at 300 K initially increases under increasing compressive stress, reaches a maximum around −0.5 GPa, then decreases. This case is firmly in the saturated regime.

The contribution of any particular state in the electron bandstructure is weighted differently in the integrand of the electrical conductivity, than it is for the $L^{(12)}$-matrix (Fig. 2.6). Increasing compressive stress transfers conduction-band electrons from the L-point carrier pockets to the T-point pocket [Fig. 4.7(b)]. This intervalley-transfer reduces both σ and L^{12} along [111] — but at different rates because of their different energy ranges of importance (Fig. 4.10). Compressive [111] stress initially increases the Seebeck coefficient because of the interplay between these two properties.

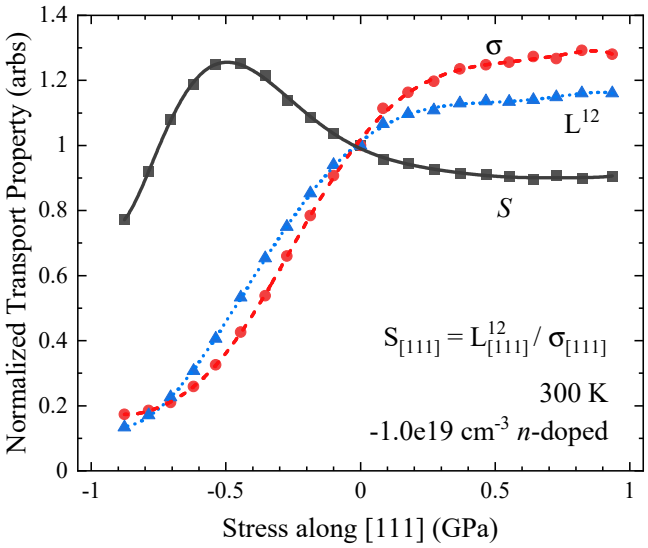

Figure 4.10 *Normalized Seebeck coefficient, L^{12}, and electrical conductivity along [111], against uniaxial [111] stress, for $-1 \times 10^{19}\,cm^{-3}$ n-doped PbTe at 300 K. Symbols are calculated values, lines are a guide to the eye.*

Overall, the power factor α along [111] increases with increasing compressive uniaxial stress [Fig. 4.8(c)]; 0.5 GPa of tensile stress increases $\alpha_{[111]}$ by ∼16%. Across all relevant p-doping concentrations and temperatures we consistently

found that compressive uniaxial stress increased the power factor, or kept it constant. Conversely, the power factor of n-doped PbTe was consistently increased with increasing tensile stress.

The Intrinsic Regime

Regardless of doping concentration, there will always be some charge-carriers excited across the band gap. If the temperature is sufficiently high, this *"intrinsic carrier concentration"* will be significant compared to the doping concentration. The *"intrinsic carrier concentration"* is the concentration of electrons and holes which can be attributed to charges being excited over the band gap, rather than the doping concentration (sec. 3.2.4). The intrinsic carrier concentration depends not just on the temperature, but also the doping concentration. Figure 4.11 shows how the intrinsic carrier concentration changes with temperature for two different doping concentrations. As the temperature is increased, the concentration of intrinsic carriers increases. At the low doping concentration of $1 \times 10^{18}\,\mathrm{cm}^{-3}$ [Fig. 4.11(a)], unstressed PbTe is in the intrinsic regime at temperatures of $\sim$500 K and above. At higher doping concentrations, e.g. $1 \times 10^{19}\,\mathrm{cm}^{-3}$ [Fig. 4.11(b)], the intrinsic regime begins at a higher temperature of $\sim$750 K; not just because of the greater doping concentration, but also because the intrinsic carrier concentration is lower when compared to $1 \times 10^{18}\,\mathrm{cm}^{-3}$ p-doped PbTe at the same temperature.

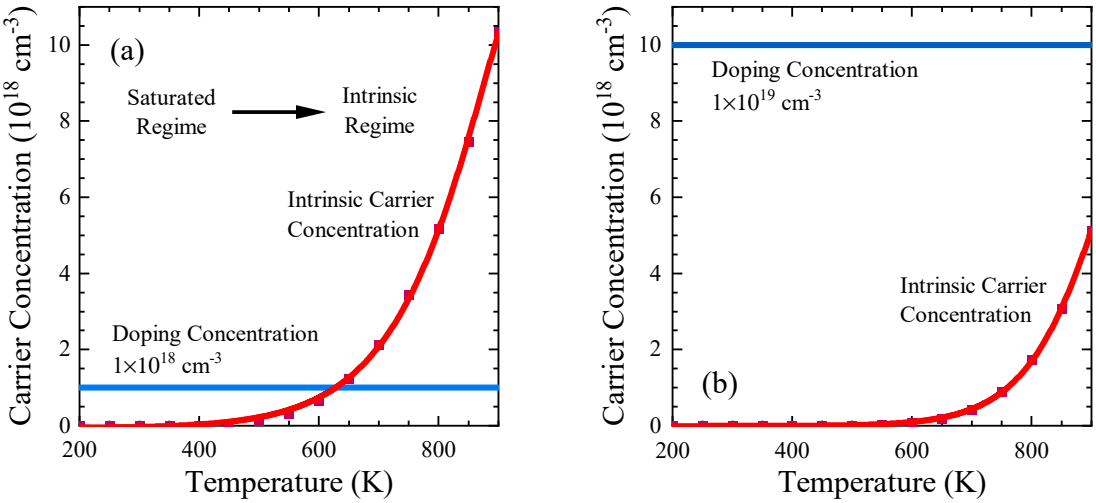

Figure 4.11 *p-doping concentration and intrinsic carrier concentration of unstressed PbTe against temperature. (a) p-doping concentration of $1 \times 10^{18}\,cm^{-3}$, (b) p-doping concentration of $1 \times 10^{19}\,cm^{-3}$. Symbols are calculated values, lines are guides to the eye. Details of how the intrinsic carrier concentration is computed are given in section 3.2.4.*

At 900 K, the concentration of intrinsic carriers is significant compared to $1 \times 10^{19}\,\mathrm{cm}^{-3}$. Both compressive and tensile stress close the band gap, increasing the total carrier concentration [Fig. 4.9(d)]. In this intrinsic regime, the contribution of conduction-band electrons to the Seebeck coefficient cannot be neglected. By examining a range of doping concentrations and temperatures, and by artificially increasing the band gap to suppress intrinsic carriers, we could disentangle the effects of stress on each band at high temperatures. Figure 4.9(c) shows that, in the intrinsic regime, the Seebeck coefficient along [111] increases with increasing compressive [111] stress.

Uniaxial stress redistributes electrons and holes between the T- and L-point carrier-pockets of the Brillouin zone. Increasing compressive [111] stress transfers electrons to the single, low-mobility, T-point pocket, and holes to the three, high-mobility, L-point pockets. This *simultaneous-intervalley-transfer* increases the relative mobility of holes to electrons.

A simple explanation for why changing the relative mobilities of electrons and holes can increase the Seebeck coefficient is to break down the total Seebeck coefficient S_{tot} into a separate contribution from the valence and conduction bands. Partial electrical conductivities associated with the valence and conduction bands can be calculated by only computing a partial integral of the $\mathrm{L}^{(11)}$ matrix (Eq. 2.40) over valence or conduction-states, respectively. These two conductivities, σ_V & σ_C, combine to give the total conductivity:

$$\sigma_{\mathrm{tot}} = \sigma_V + \sigma_C. \tag{4.1}$$

In a similar way, a Seebeck coefficient for the valence and conduction bands, S_V & S_C, can be computed from a partial integral of the $\mathrm{L}^{(12)}$ matrix (Eq. 2.41), divided by the electrical conductivity for that band:

$$S_V = \mathrm{L}_V^{(12)}/\sigma_V \quad ; \quad S_C = \mathrm{L}_C^{(12)}/\sigma_C. \tag{4.2}$$

It is worth noting that S_V will be positive, and S_C will be negative.

These Seebeck coefficient for each band can be combined to give the total Seebeck coefficient S_{tot} via a weighted sum:

$$S_{\mathrm{tot}} = \frac{\sigma_V S_V + \sigma_C S_C}{\sigma_V + \sigma_C}. \tag{4.3}$$

If some deformation increases the conductivity of the valence-band σ_V relative

to the conductivity of the conduction-band σ_C, but keeps the total conductivity $\sigma_V + \sigma_C$ and the Seebeck coefficients of each band, S_V & S_C, constant, then the total conductivity S_{tot} will become more positive. This improvement will only be significant if the relative contributions to the Seebeck coefficient from each band — $\sigma_V S_V$ & $\sigma_C S_C$ — are both significant, as is the case in the intrinsic regime. Thus, in the intrinsic regime, *simultaneous-intervalley-transfer* can improve the Seebeck coefficient, via changing the relative mobilities of the valence and conduction bands.

To further illustrate how changing the relative mobilities of electrons and holes can increase the Seebeck coefficient, we considered a toy-system. This toy-system has a bandstructure with one valence-band carrier-pocket and one conduction-band carrier-pocket, both located at Γ. Both carrier-pockets are ellipsoidal in shape, with low carrier mobility along the axis of rotation. Both the valence and conduction bands have the same magnitude effective masses, so the density of states above and below the band gap is symmetric. When undoped, the symmetry of this toy system pins the chemical potential halfway between the band edges. There will be the same number of holes as electrons. Each elliptical carrier-pocket has low mobility along its' axis of rotation. Thus, on average, valence-band holes will move much faster along $\hat{y}$ than conduction-band electrons. Conversely, electrons have greater mobility along $\hat{x}$ than do holes.

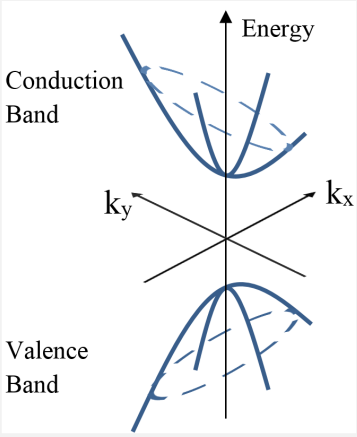

Band structure of toy system. The valence and conduction band have ellipsoidal shapes, but with orthogonal axes of rotation.

Similar to the forms in section 2.2.3, the electrical transport properties of

this toy-system can be computed according to the following equations:

$$\tilde{\sigma}_{ij}(\varepsilon) = q^2 \oint_{BZ} \frac{\mathrm{d}^3k}{(2\pi)^3} \sum_b \tau \; v_{b,i} v_{b,j} \; \delta(\epsilon(k,b) - \varepsilon), \tag{4.4}$$

$$\sigma_{ij} = -\int \mathrm{d}\varepsilon \; \tilde{\sigma}_{ij}(\varepsilon) \; \times \frac{\mathrm{d}f_{FD}}{\mathrm{d}\varepsilon}, \tag{4.5}$$

$$L^{12}_{\beta j} = -\frac{1}{q} \int \mathrm{d}\varepsilon \; \tilde{\sigma}_{\beta j}(\varepsilon) \; \times \; \frac{\varepsilon - \mu}{T} \quad \frac{\mathrm{d}f_{FD}}{\mathrm{d}\varepsilon}, \tag{4.6}$$

$$S_{ij} = \sum_\beta \sigma^{-1}_{i\beta} \times L^{12}_{\beta j}, \tag{4.7}$$

where q is the elementary charge, σ_{ij} the electrical conductivity, τ the electron scattering time (set to be constant), S_{ij} the Seebeck coefficient, f_{FD} the Fermi-Dirac distribution, $v_{b,i}$ the band velocity for band 'b' in the $\hat{i}$ direction ($v_{b,i} = \partial\epsilon(k,b)/\partial k_i$), $\oint_{BZ} \mathrm{d}^3k$ is an integral over the Brillouin Zone, and μ is the chemical potential.

The functional $\tilde{\sigma}_{ij}(\varepsilon)$ can be seen like a conductivity for electrons with a specific energy ε[20]. It is an integral and sum over all states at energy ε weighted by their velocity ($v_{bi}v_{bj}$), and it has the same dimensions as the conductivity. The electrical conductivity σ and the L^{12}_{ij} coefficient are both integrals of $\tilde{\sigma}(\varepsilon)$ over energy, weighted by $\mathrm{d}f_{FD}/\mathrm{d}\varepsilon$ and $\mathrm{d}f_{FD}/\mathrm{d}\varepsilon \times (\varepsilon - \mu)$, respectively.

If the valence and conduction bands of our toy-system were perfect mirror images of each other, then the integrand of L^{12}_{ij} (eq. 4.6) would be an odd function in energy and thus S_{ij} would be zero. However, because — on average — holes move much faster along $\hat{y}$ than electrons (Fig. 4.12) the energy-dependent conductivity along y is $\tilde{\sigma}_{yy}(\varepsilon)$ is greater for energies within the valence band than it is for energies within the conduction band. Thus, $\tilde{\sigma}_{yy}(\varepsilon)$ will be larger for energies below μ than for energies above μ. For this toy-system the integrand of L^{12}_{yy}, $\tilde{\sigma}_{yy}(\varepsilon)$, is not an odd function of ε, so if the Seebeck coefficient S_{yy} is measured, a positive result should be expected. Similarly, because electrons moving along $\hat{x}$ have greater velocities than holes do, S_{xx} should be negative. In this toy-system the density of states remains mirrored in energy; and yet a difference in mobility leads to a non-zero S_{ij}.

The key point to gain from examining this toy-system is that changing the relative mobilities of electrons and holes in a specific direction can increase or decrease the Seebeck coefficient along that direction. When

PbTe is in the intrinsic regime, the effect of anisotropic stress on the Seebeck coefficient cannot be understood by examining the rate-of-change of the density-of-states — which fundamentally has no directional information. One has to consider how anisotropic stress is changing the relative mobility of conduction-band electrons and valence-band holes.

Compressive stress redistributes holes to three pockets at the high-mobility L-point, and simultaneously transfers conduction band electrons to the low-mobility T-point pocket [Fig. 4.7(b)]. This *simultaneous-intervalley-transfer* means valence-band holes will have, on average, higher velocities than the intrinsic conduction-band electrons. As a result, the energy-dependent conductivity $\tilde{\sigma}(\varepsilon)$ (Eq. 4.4) will be greater at the energies of the valence-band than at the energies of the conduction-band.

Increasing $\tilde{\sigma}(\varepsilon)$ at low ε relative to high ε results in L^{12} increasing with increasing compressive stress. Thus, in the intrinsic regime, compressive stress makes the Seebeck coefficient PbTe more positive [Fig. 4.9(a)–(b)]. Conversely, tensile uniaxial stress makes the Seebeck coefficient more negative.

The effect of simultaneous-intervalley-transfer on the Seebeck coefficient can most clearly be seen for the pure intrinsic regime: undoped PbTe. Figure 4.13(a) quantifies how, for undoped PbTe at 400 K, uniaxial stress changes the Seebeck coefficient both along and perpendicular to [111]. When unstressed, undoped PbTe has a Seebeck coefficient S of $\sim\!-50\,\mu\mathrm{VK}^{-1}$. If tensile stress is applied, electrons and holes are simultaneously transferred [Fig. 4.7(b)] increasing the mobility of electrons relative to holes. This makes the Seebeck coefficient S along [111] more negative than it is at ambient stress.

Conversely, under compressive stress the mobility of holes is increased relative to electrons, the Seebeck coefficient S along [111] becomes positive [Fig. 4.13(a)]. At large enough stress all the charges have been redistributed, and S reaches a maximum. Increasing stress further increases the carrier concentration [Fig. 4.13(b)], but does not change the relative mobility of electrons compared to holes.

Increasing compressive stress initially makes the Seebeck coefficient perpendicular to [111], $S_\perp$, more negative. The T-point has a high mobility perpendicular to [111]. Compressive stress transfers electrons into the T-point pocket which has high mobility perpendicular to [111], increasing the relative mobility of electrons to holes and thus increasing $S_\perp$. Simultaneous intervalley transfer changes the relative mobility of the conduction and valence bands, and the relative number

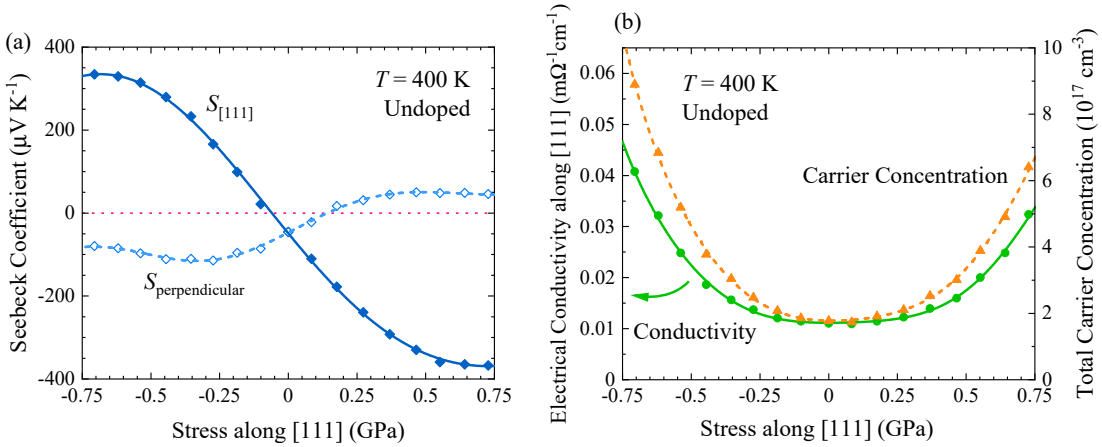

Figure 4.13 *Calculated (a) Seebeck coefficient parallel and perpendicular to the [111] direction, as a function of stress applied parallel to [111]. (b) electrical conductivity along [111] (green circles) and total carrier concentration (orange triangles), against uniaxial [111] stress for undoped PbTe at 400 K.*

of carrierpockets. Compressive stress reduces the number of conduction-band carrier pockets from 4 to 1, which counteracts increasing the relative mobility of electrons vs holes. The differing behaviour of $S_{[111]}$ and $S_{\perp}$ under [111] stress shows that the relative change in carrier mobility is as important as the change in the density of states, or the number of carrier pockets.

Figure 4.13(b) shows that the conductivity of stressed PbTe, both tensile and compressed, is larger than the conductivity of unstressed PbTe. The band gap of PbTe closes with both increasing compressive stress, and increasing tensile stress — which in turn increases the intrinsic carrier concentration.

In summary, in the intrinsic regime compressive (tensile) uniaxial [111] stress increases both the Seebeck coefficient along [111] and the conductivity of p-type (n-type) PbTe.

Generalizing to other materials I

A common attribute of high-performance thermoelectrics is a large number of carrier pockets, each of which has anisotropic transport properties[31]. Non-hydrostatic stress can break the degeneracy of the carrier pockets, redistributing charge to pockets with high mobility in a specific direction. If the number of carrier pockets remains high, the Seebeck coefficient may remain high — especially at larger temperatures. Materials which could benefit by strain-induced intervalley transfer should have the characteristics of (i) multiple charge-carrier-

pockets, and (ii) each individual carrier-pocket has strongly anisotropic transport properties. These characteristics may help identify materials which could have improved power factors under stress.

Furthermore, in the intrinsic regime, stress which causes a simultaneous-intervalley-transfer effect [Fig. 4.7(b)] can simultaneously improve the conductivity and the Seebeck coefficient. There may be materials which have previously been discounted for thermoelectric applications due to a low Seebeck coefficient. If the Seebeck coefficient is low because the material has a narrow band gap and a large concentration of intrinsic carriers, anisotropic stress may improve it significantly.

4.4 Stress along the [001] direction

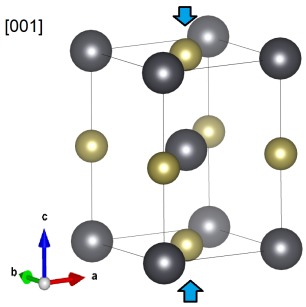

Stress along [001] transforms the symmetry of PbTe into a body-centered tetragonal symmetry, with space-group *I4/mmm*. Because stress along [001] changes the symmetry of the unit cell the L-point is technically now renamed the N-point [Fig. 4.14(a)], but for convenience I will continue to refer to it as the L-point.

Stress along [001] preserves the degeneracy of the L-point carrier-pockets, so there is not an intervalley-transfer effect as was seen under [111] stress. Instead, [001] stress changes the shape of the bandstructure near the L-points, and thus the carrier mobilities. Figure 4.14(b) shows the valence and conduction bands along two directions: [100] and [001], which are perpendicular and parallel to the applied [001] stress, respectively. Unstressed PbTe has the same bandstructure along both [100] and [001], but uniaxial [001] stress breaks the symmetry and changes the shape of the bandstructure.

Qualitatively, Fig. 4.14(b) shows little change in the shape of the conduction band. Aside from an increase in the curvature of states within ∼20 meV of the conduction band edge, the gradient of the conduction bands is constant with stress. This is expected, as the conduction band consists of carrier-pockets centered at the L-points, and has no significant features near the band edge in parts of the Brillouin zone which have their symmetry split by [001] stress. For most relevant n-doping concentrations and temperatures, the majority of conduction band electrons will be at energies greater than 20 meV above the conduction band minimum [Fig. 4.14(c) and 4.2(a)]. The average electron mobility is approximately constant with [001] stress. For this reason, in the saturated regime, the transport properties of n-doped PbTe remain similar under [001] stress.

In contrast, the valence bandstructure along [001] changes greatly with uniaxial [001] stress [Fig. 4.14(b)]. Figure 4.15 shows how [001] stress splits the degeneracy of the Σ local maxima into two sets: labelled Σ^1_{max} and Σ^2_{max}. Compressive uniaxial stress reduces the energy of Σ^2_{max} relative to the L-point maximum and, because the valence-band is one connected band, the gradient of states near the L-point also changes [Fig. 4.14(b)]. Increasing compressive [001] stress increases the gradient of the valence-band along [001], but leaves the gradient along [100]

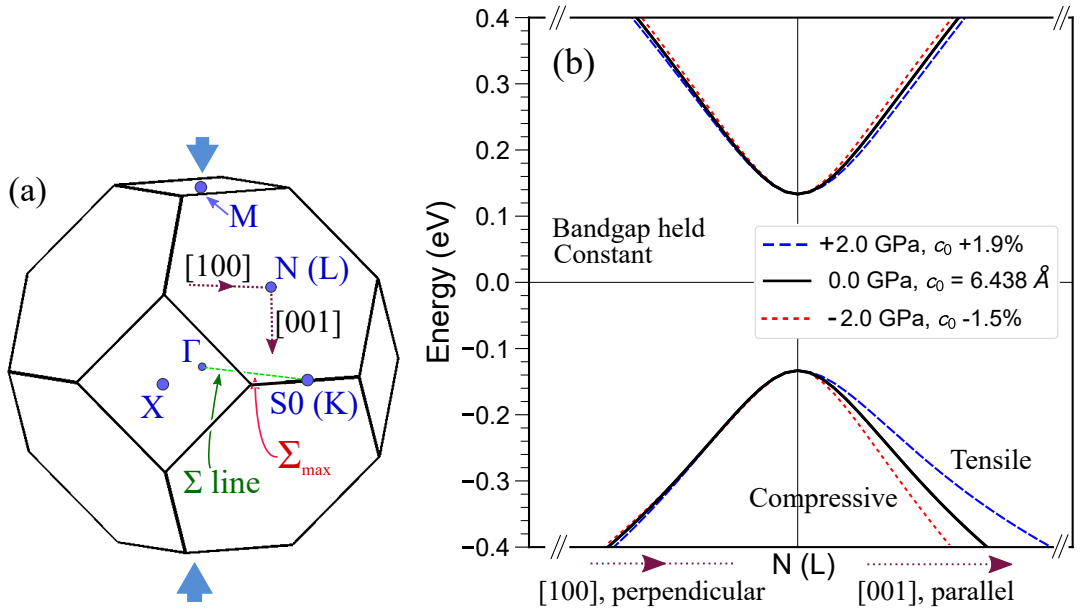

Figure 4.14 *(a) Diagram of the Brillouin Zone for [001] strained PbTe, with labels taken from the Bilbao Crystallographic Server[130]. When the crystal is unstressed, the N point is equivalent to the L-point. The dotted red lines show the path through the Brillouin zone plotted in 4.14(b). (b) Bandstructure for PbTe under compressive, unstressed, and tensile [001] stress (red-dotted / black-solid / blue-dashed lines, respectively). To emphasize the change in the gradient of the bands, the band gap is held constant.*

constant. As a result, the hole-mobility along [001] increases with increasing stress, but the hole-mobility perpendicular to [001] remains unchanged.

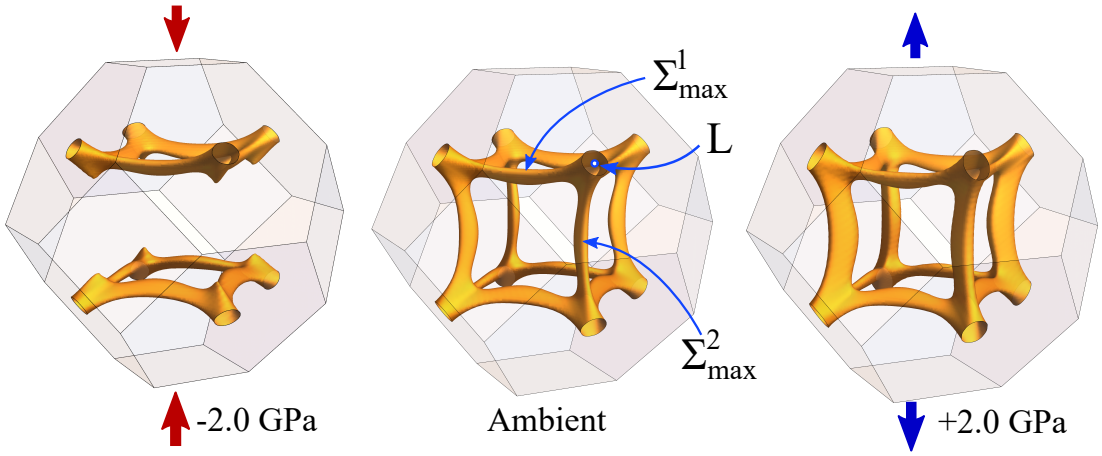

Figure 4.15 *Energy isosurface set 300 meV below the valence band maximum of PbTe under uniaxial stress along [001].*

Figure 4.16(a) quantifies this notion for p-type PbTe with a doping concentration of $1 \times 10^{19}\,\mathrm{cm}^{-3}$ at 300 K. As expected from Fig. 4.14(b), the electrical

conductivity along [001] increases linearly with increasing [001] stress. At this p-doping concentration and temperature, PbTe is in the saturated regime; thus the increasing conductivity is due primarily to increasing hole mobility.

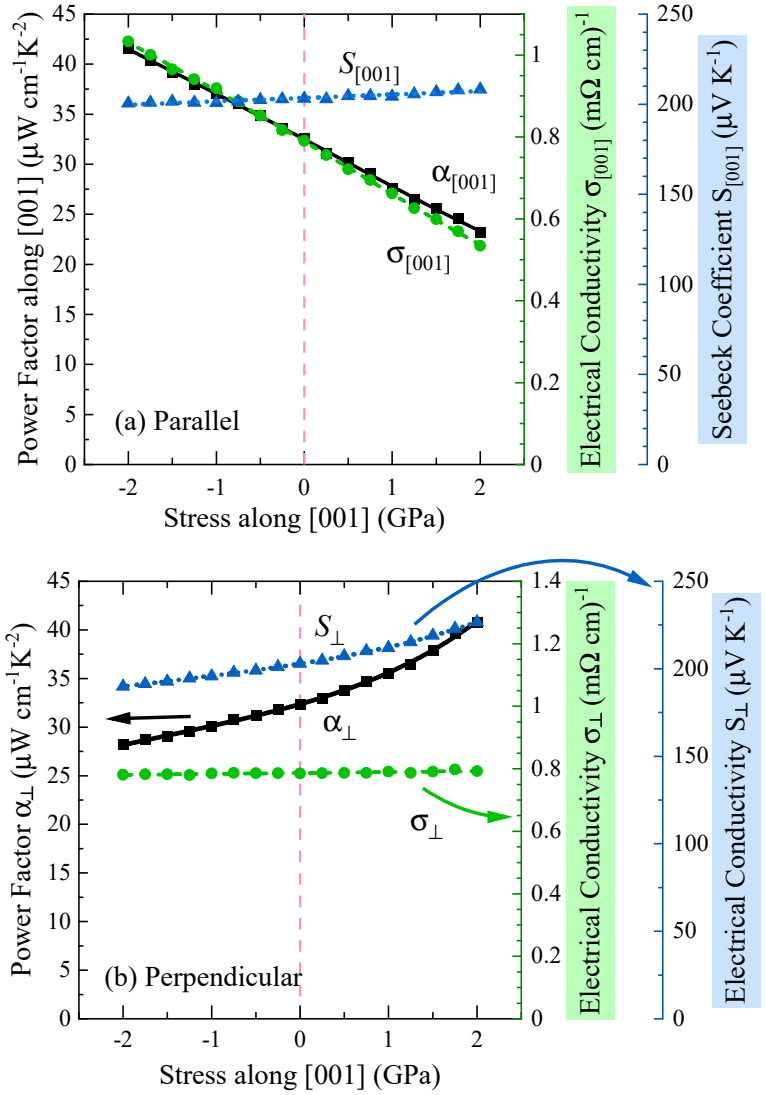

Figure 4.16 *Calculated transport properties for* $1 \times 10^{19}\,\mathrm{cm}^{-3}$ *p-doped PbTe at 300 K both parallel (**a**) and perpendicular (**b**) to the applied uniaxial* [001] *stress. This case is firmly in the saturated regime, so the carrier concentration remains approximately constant. For a sense of scale,* 0.5 GPa *corresponds to a strain of* ∼0.4 %

The Seebeck coefficient along [001] [Fig. 4.16(a)] is approximately constant with [001] stress. This is not a surprise given the electron transport integrals (Eq. 2.43–2.44). The square of the carrier-velocity v appears in the integrand of both the electrical conductivity σ and the L^{12} coefficient, the ratio of which gives the Seebeck coefficient S. Thus, strain which increases the carrier velocity along [001] can keep $S_{[001]}$ approximately constant, and concomitantly increase $\sigma_{[001]}$.

At higher temperatures, the transport properties of p-type PbTe have a greater response to [001] stress, even while still in the saturated regime. Figure 4.17 shows the calculated transport properties for p-type PbTe with the same doping concentration as in Fig. 4.16(a), but at the higher temperature of 600 K. As the temperature is increased, a larger proportion of holes are in states further away from the degenerate L-points, and instead in states between L and Σ_{max}. Thus, the response in the conductivity to uniaxial [001] stress increases: for $1 \times 10^{19}\,\mathrm{cm}^{-3}$ p-doped PbTe at 300 K the power factor changed by ∼14 %/GPa [Fig. 4.16(a)] but at 600 K it changes by ∼22 %/GPa (Fig. 4.17).

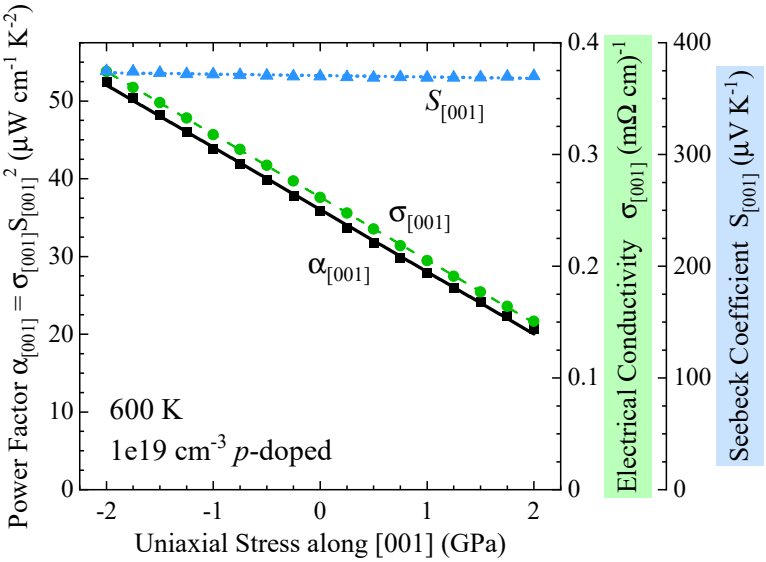

Figure 4.17 *Calculated transport properties parallel to the applied uniaxial* [001] *stress, for* $1.019\,\mathrm{cm}^{-3}$ *p-doped PbTe at 600 K. This case is firmly in the saturated regime, so the carrier concentration remains approximately constant.*

Intuition based on the parabolic band model would suggest that increasing carrier velocities along [001], $v_{[001]}$, should reduce the Seebeck coefficient $S_{[001]}$. In the parabolic band model, reducing the effective mass — and thus increasing v — will inevitably reduce S. However, the effect of [001] stress on the valence band of PbTe differs in two significant ways: (i) the valence band is strongly non-parabolic, with a dispersion that is mostly linear and remains linear when stressed [Fig. 4.14(b)]; and (ii) the gradient perpendicular to [001] remains constant with [001] stress. The fact $S_{[001]}$ remains constant under [001] stress demonstrates how intuition based on the parabolic band model can be misleading for p-type PbTe.

Figure 4.16(b) quantifies how the transport properties perpendicular to [001] change under uniaxial [001] stress. As expected from the invariance of the

valence band gradient along [100] [Fig. 4.14(b)] Fig. 4.16(b) shows the electrical conductivity $\sigma_\perp$ for saturated p-type PbTe remains approximately constant. However, increasing [001] stress reduces the rate of change of the density of states for the valence band. This leads to a decrease in the Seebeck coefficient perpendicular to [001] with increasing [001] stress. In this case, applying 0.5 GPa of tensile [001] stress increases the power factor perpendicular to [001] $\alpha_\perp$ by $\sim$5 %.

It is tempting to describe this effect in terms of intervalley-transfer between the Σ local maxima. As shown in Fig. 4.14(d), uniaxial [001] stress breaks the symmetry of the Σ local maxima into two sets: Σ^1_{max}, and Σ^2_{max}. States near Σ^2_{max} have low mobility along [001], so compressive [001] stress which transfers holes from Σ^2_{max} to Σ^1_{max} would increase the conductivity along [001]. However, even for cases where the p-doping concentration and temperature were chosen to be low enough that states near Σ_{max} were unpopulated, I still observed trends similar to those shown in Fig. 4.16. The response of p-type PbTe transport properties to [001] stress should not be interpreted in terms of the two-band model.

Supporting our observations, experimental measurements reported by Burke[71] show that the piezoresistance coefficient associated with uniaxial [001] stress remains high, even for low ($< 1 \times 10^{18}\,\text{cm}^{-3}$) p-doping concentrations, at low temperatures. They found the response of the electrical resistivity to [001] stress was still high, even when states near Σ_{max} were depopulated. Burke comments on the [001] piezoresistive response: *"the temperature and concentration dependence show, however, that this is not due to the multivalley nature of the second valence band"*[71]. To understand the effect of [001] stress, it is important to think of the valence band as one connected band, and that energy changes of the Σ maxima are commensurate with changes in the bandstructure near the L-point maximum.

A more complicated behaviour can be observed in the intrinsic regime. Figure 4.18(a) shows how, in the intrinsic regime, the Seebeck coefficient along [001] of p-type PbTe increases with increasing compressive [001] stress. This effect does not occur if the band gap is artificially increased to suppress intrinsic carriers, which shows the presence of conduction band electrons — rather than simply a high temperature — is key.

In the intrinsic regime, the relative mobilities of holes and electrons is important. Increasing compressive [001] stress increases the hole-mobility along [001], and keeps the electron-mobility similar. For p-type PbTe in the saturated regime this increases the conductivity along [001], and, in the intrinsic regime, the Seebeck

coefficient along [001] also increases [Fig. 4.18(a)].

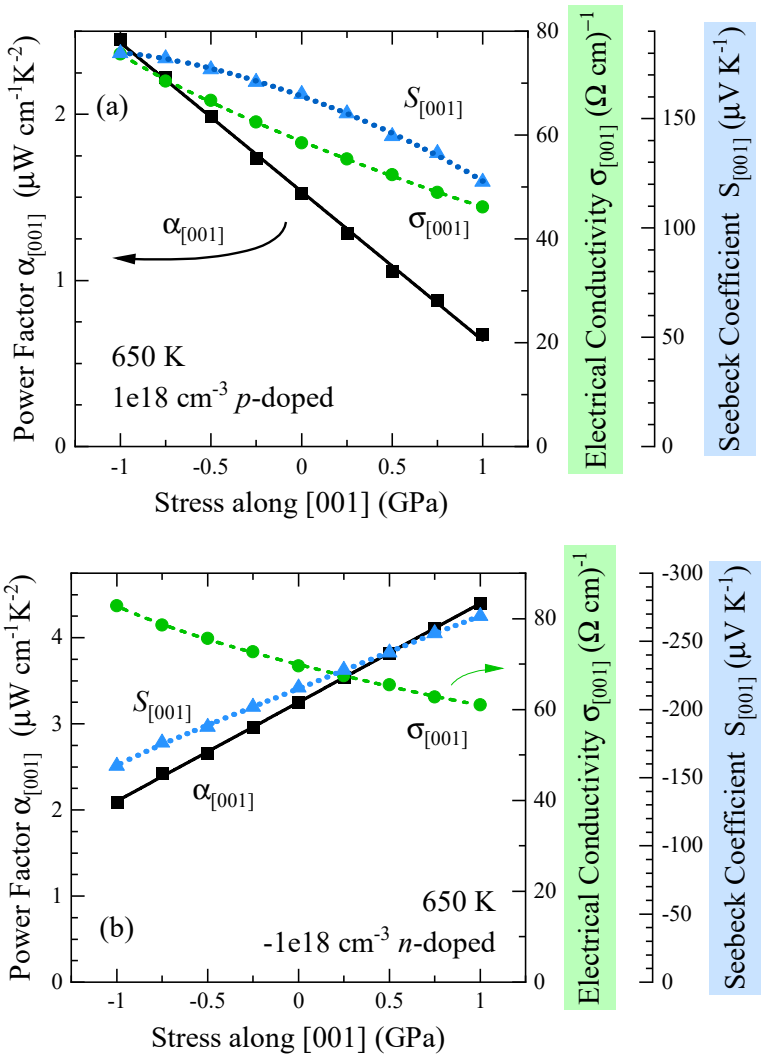

Figure 4.18 *Transport properties along [001] against uniaxial [001] stress for (a)* $1 \times 10^{18}\,\mathrm{cm}^{-3}$ *p-doped and (b)* $-1 \times 10^{18}\,cm^{-3}$ *n-doped PbTe at 650 K. In both cases the intrinsic carrier concentration is above* $1 \times 10^{18}\,cm^{-3}$*, so PbTe is in the intrisic regime. For scale, 0.5 GPa of stress corresponds to* ∼0.4 % *strain.*

Furthermore, for n-type PbTe in the intrinsic regime, the Seebeck coefficient along [001] decreases with increasing compressive [001] stress [Fig. 4.18(b)] and the conductivity increases concomitantly. This occurs because (i) the hole-mobility increases significantly and (ii) the band gap closes, so the concentration of intrinsic carriers increases. Unlike in the saturated regime, where [001] stress had little effect on the transport properties of n-type PbTe, in the intrinsic regime increasing [001] stress reduces the power factor along [001] significantly.

In summary, I found [001] stress had little effect on the transport properties of n-type PbTe in the saturated regime. However, in the intrinsic regime,

increasing tensile [001] stress would increase the power factor along [001] of n-type PbTe, primarily by increasing the Seebeck coefficient. Furthermore, in the intrinsic regime, increasing compressive [001] stress would increase the power factor perpendicular to [001] by both increasing $S_{\perp}$ and $\sigma_{\perp}$.

For p-type PbTe, across all p-doping concentrations and temperatures examined, increasing compressive uniaxial [001] consistently increases the power factor along [001] by raising the electrical conductivity along [001] while (i) the Seebeck coefficient $S_{[001]}$ remained constant if in the saturated regime, or (ii) also increasing $S_{[001]}$ if in the intrinsic regime. Tensile [001] stress increases the power factor perpendicular to [001], primarily by increasing the Seebeck coefficient $S_{\perp}$.

Generalizing to other materials

The valence band of PbTe has large cylindrical features on the order of 200 meV below the valence band maximum [Fig. 4.18(d)]. Applying [001] stress, which breaks the symmetry of these features, changes the shape of the valence band. Correctly applied, stress can (i) improve carrier-mobility along one direction, (ii) increase Seebeck coefficient in another, or (iii) changing the relative mobilities between the conduction and valence bands.

Many high-performance thermoelectrics have bandstructures which are highly non-parabolic[22]. Other candidate materials may have anisotropic features similar to the PbTe valence band. Anisotropic stress which breaks the symmetry of these features should alter the shape of the valleys: improving transport-properties by manipulating the shape of the bands.

4.5 Stress along the [110] direction

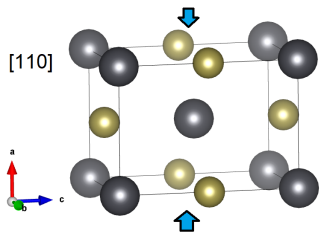

Stress along [110] transforms the symmetry of PbTe into a body-centered orthorhombic lattice, with spacegroup *Immm*.

As discussed previously, the transport properties of each individual carrier pocket are highly anisotropic, with the lowest average mobility along the L–Γ line (Figs. 4.1 & 4.4). Uniaxial stress along [110] splits the L-points into two sets, S and R, each of which are oriented differently. The S-point carrier pockets of PbTe have their lowest group velocities along the S–Γ line, which is oriented perpendicular to [110] (Fig. 4.19 inset). Thus, both holes and electrons in the S-point pockets have, on average, greater mobility along [110] than they do in-plane. In contrast, the R–Γ line points at an angle to [110]. Because of their different orientations, the S-point carrier pockets have greater mobility along [110] than the R-point pockets.

Figure 4.19 shows increasing compressive stress raises the energy of both conduction and valence-band states near the S-point relative to the R-point. Much like under [111] stress, this causes charges to be redistributed: with valence-band holes transferred from R to S, and conduction-band electrons from S to R. Because the S- and R-pockets have different [110] mobilities, intervalley-transfer causes the transport properties to become anisotropic. For example, increasing compressive [110] stress transfers valence-band holes of *p*-type PbTe from the R-point pockets to the S-point pockets. This increases the conductivity along [110]; however, because the number of carrier pockets is reduced, the Seebeck coefficient is also reduced.

Figure 4.20(b) quantifies this notion for *p*-doped PbTe, with a carrier concentration of $1 \times 10^{19}\,\mathrm{cm}^{-3}$, at 600 K. At this doping concentration and temperature the intrinsic carrier concentration is negligible compared to the extrinsic dopant concentration: this case is in the saturated regime. The conductivity along [110], $\sigma_{[110]}$, increases with increasing [110] stress, as holes are transferred to the high-mobility S-point pockets. The Seebeck coefficient increases slightly under tensile [110] stress, reaches a maximum at a stress of approximately 0.1 GPa, then decreases again. The shape of this curve is due to the interplay between the L^{12} matrix and the conductivity, which both contribute to the Seebeck coefficient (Eq. 2.44). It is similar to what was observed under uniaxial stress along [111]

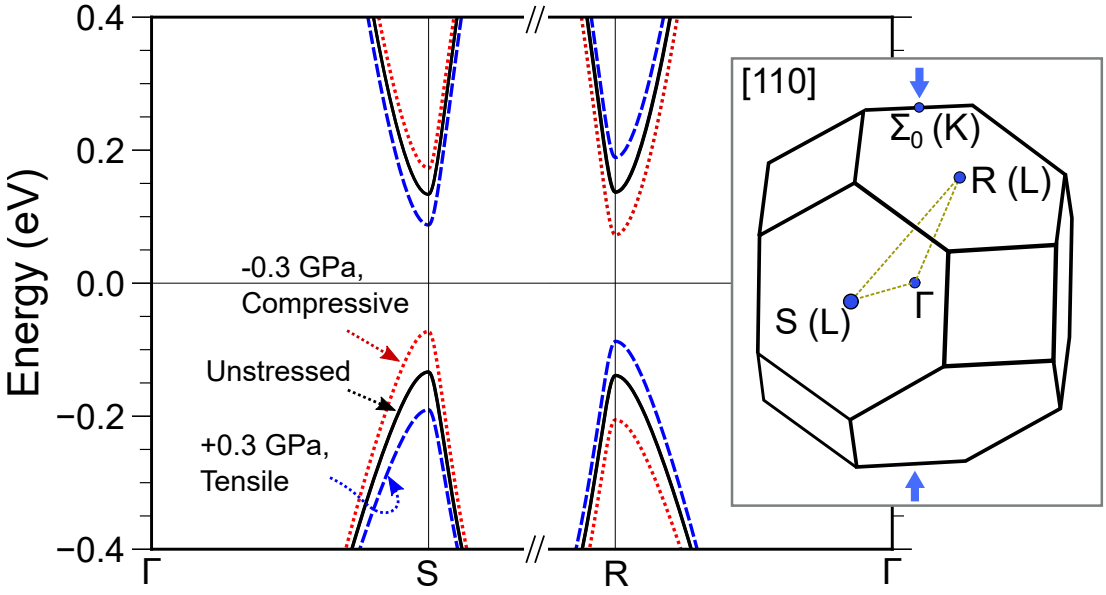

Figure 4.19 *Calculated bandstructure of PbTe under uniaxial [110] stress. Inset: diagram of the Brillouin zone[130]; when unstressed, the R- and S-points are equivalent to the L-point, and the Σ_0 point is equivalent to the K-point.*

(Fig. 4.13). This similarity is expected because, in both cases, an intervalley-transfer effect occurs.

The stress dependence of the power factor is determined by the relative changes to the Seebeck coefficient $S_{[110]}$ and conductivity $\sigma_{[110]}$ along [110]. At this p-doping concentration and temperature [Fig. 4.20(b)] the power factor along [110] increases with increasing compressive [110] stress. For p-type PbTe at lower temperatures, such as $T = 300\,\mathrm{K}$, the reduction in $S_{[110]}$ dominates, and the power factor is largest for unstressed PbTe [Fig. 4.20(a)].

The trends of conductivity and Seebeck coefficient along [110] for n-type PbTe match expectations based on the intervalley-transfer-effect. Increasing compressive stress transfers conduction-band electrons from the high-[110]-mobility S-point to the low-mobility R-point (Fig. 4.19), thus reducing the conductivity. Figure 4.20(c) quantifies this notion for $-1 \times 10^{19}\,\mathrm{cm}^{-3}$ n-doped PbTe. At this doping concentration, as was the case shown in Fig. 4.20(b), PbTe is in the saturated regime. Unlike for p-doped PbTe with an equal carrier concentration and temperature [Fig. 4.20(b)], uniaxial [110] stress does not increase the power factor of n-doped PbTe significantly above the value at zero stress. This was a general trend across all n-doping concentrations examined: in the saturated regime, the power factor for unstressed PbTe was close to the

maximum value.

Near the L-point maximum, the conduction-band is more isotropic than the valence-band. This can be shown both by comparing the bandstructure along L–Γ and L–K (Fig. 4.4); and by experimental estimates for the ratio between the effective mass along L–Γ and the perpendicular effective masses: the effective mass anisotropy[35,59,119,120]. Because the individual carrier pockets for the conduction-band are more isotropic than the valence-band carrier pockets, intervalley-transfer changes the conductivity of n-type PbTe proportionally less than for p-type PbTe.

Quantifying this notion, in Fig. 4.20(b) at 0 stress the gradient of the conductivity is $\sim$−160 %/GPa, whereas the gradient for n-type PbTe [Fig. 4.20(c)] is 90 %/GPa. I made a similar observation comparing p- and n-doped PbTe stressed along [111]. Overall, the power factor along [110] of n-type PbTe in the saturated regime is not improved significantly by applying uniaxial [110] stress.

However, as was the case for [001] and [111] stress, in the intrinsic regime a more complex behaviour is observed. Uniaxial [110] stress will simultaneously transfer both holes and electrons between the R and S carrier pockets. Simultaneous intervalley-transfer means increasing compressive (tensile) uniaxial [110] stress will concomitantly increase both the Seebeck coefficient and conductivity along [110], for p-type (n-type) PbTe. Figure 4.21 quantifies this for $-1 \times 10^{19}\,\mathrm{cm}^{-3}$ n-doped PbTe at 900 K. Near zero stress, both the conductivity and Seebeck coefficient increase under increasing tensile [110] stress which, in turn, increases the thermoelectric power factor.

Thus far I have discussed thermoelectric properties parallel to the applied [110] stress, but the transport properties perpendicular to [110] also change. Compressive uniaxial stress along [110] induces PbTe to expand along two directions: $[1\bar{1}0]$ and [001]. Associated with each direction is a distinct Poisson's ratio: $\nu_{[110],[1\bar{1}0]}$ and $\nu_{[110],[001]}$, which I calculated to be 0.64 and 0.07, respectively. A Poisson's ratio greater than 0.5 is allowed, as only the directionally-averaged Poisson's ratio $[(\nu_{[110],[1\bar{1}0]} + \nu_{[110],[001]})/2]$ must be below 0.5 in order to reduce the volume with increasing stress.

As $\nu_{[110],[1\bar{1}0]}$ is large, strain along [110] induces a similar magnitude strain along $[1\bar{1}0]$. Because of this similarity, it is not surprising that trends of the transport properties along $[1\bar{1}0]$, under [110] stress, appear like trends of transport properties along [110] that have been mirrored around zero stress. Figure 4.22 demonstrates this notion for the electrical conductivity of p-doped PbTe. At both

$T = 300$ and 600 K, the trend of $\sigma_{[1\bar{1}0]}$ against [110] stress mirrors the trend of $\sigma_{[110]}$. Thus, observations about how uniaxial [110] stress affects transport along [110] can be extended to transport along $[1\bar{1}0]$, simply by reversing the direction of stress.

In summary, uniaxial [110] stress causes an intervalley-transfer-effect, much like that caused by stress along [111]. In the saturated regime, increasing compressive [110] stress causes holes to be transferred to the high-[110]-mobility S-point carrier pockets, and electrons to be transferred to the R-point pockets.

For p-type PbTe in the saturated regime, this increases the conductivity and reduces the Seebeck coefficient. Whether or not the thermoelectric power factor increases or decreases depends on the temperature and doping concentration. At higher temperatures the power factor increases with increases stress, at low temperatures the power factor had a maximum at, or close to, zero stress.

For saturated n-type PbTe, [110] stress did not improve the power factor significantly above the value at zero stress. However, in the intrinsic regime, uniaxial [110] stress induces simultaneous-intervalley-transfer for holes and electrons. This allows the conductivity and Seebeck coefficient along [110] to be concomitantly increased with increasing compressive (tensile) [110] stress for p-type (n-type) PbTe; greatly improving the power factor.

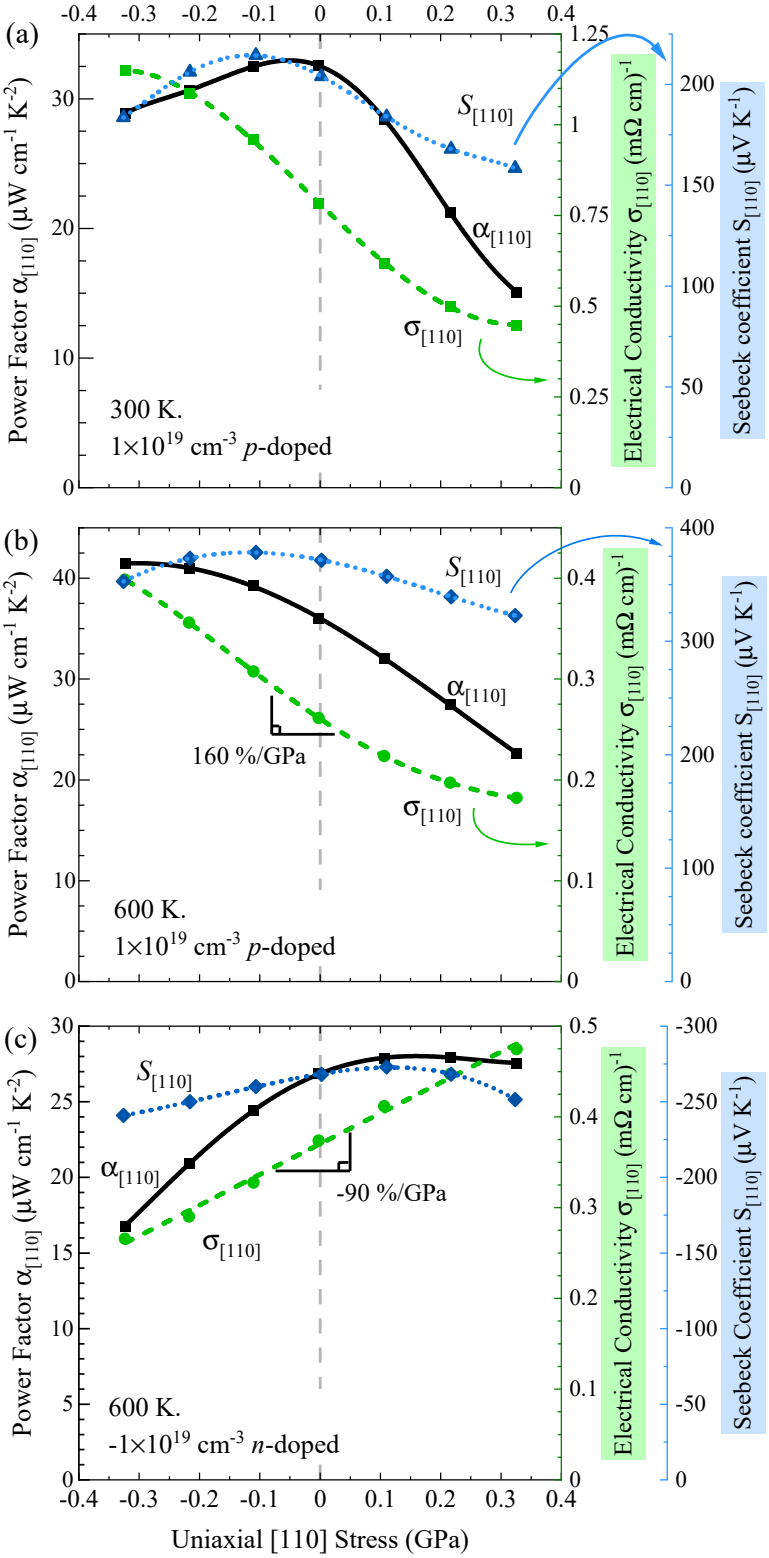

Figure 4.20 *Calculated transport properties along [110], against uniaxial [110] stress, for PbTe with a doping concentration n and temperature T of: (a) $n = 1 \times 10^{19}\,\mathrm{cm}^{-3}$ and $T = 300\,\mathrm{K}$; (b) $n = 1 \times 10^{19}\,\mathrm{cm}^{-3}$ and $T = 600\,\mathrm{K}$; (c) $n = -1 \times 10^{19}\,\mathrm{cm}^{-3}$ and $T = 600\,\mathrm{K}$. All three of these cases are in the saturated regime. For a sense of scale, 0.1 GPa corresponds to a strain of ∼0.5 %.*

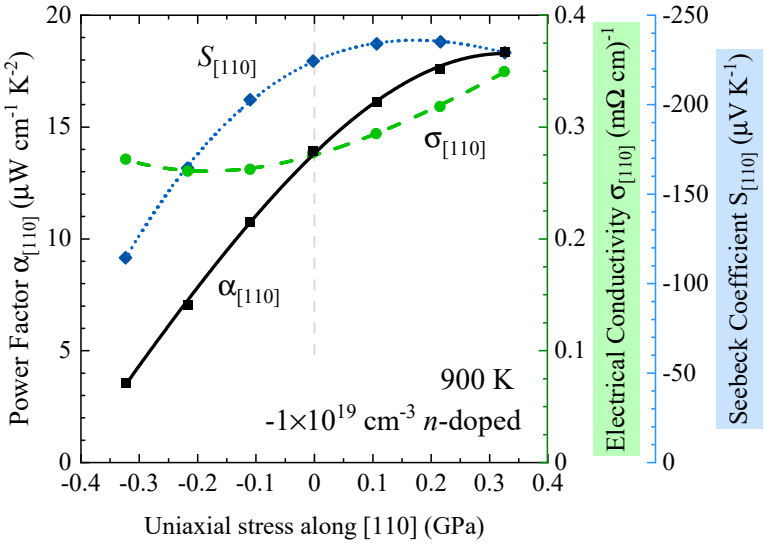

Figure 4.21 *Calculated transport properties along [110] as a function of uniaxial [110] stress for n-doped PbTe at* $T = 900\,\mathrm{K}$ *with an extrinsic n-doping concentration of* $-1 \times 10^{19}\,cm^{-3}$*, and an intrinsic carrier concentration ranging between* 0.5 *and* $0.7 \times 10^{19}\,cm^{-3}$*. This case is in the intrinsic regime. For a sense of scale,* 0.1 GPa *corresponds to a strain of* ∼0.5 %*.*

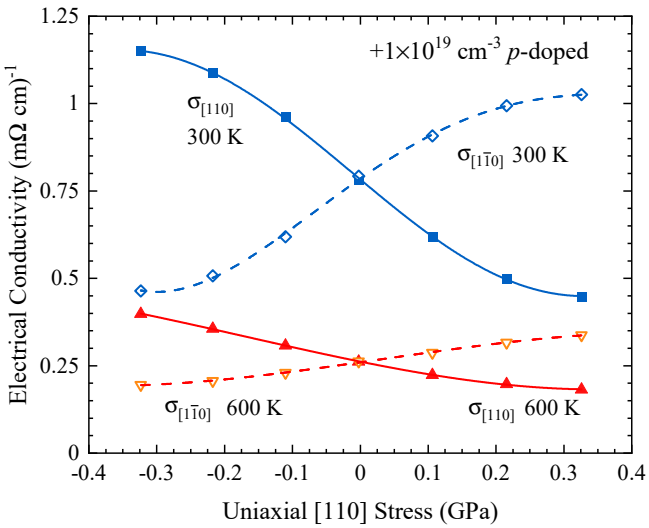

Figure 4.22 *Calculated electrical conductivity along [110] (solid lines) and* $[1\bar{1}0]$ *(dashed lines) against uniaxial [110] stress. Calculations are for* $1 \times 10^{19}\,\mathrm{cm}^{-3}$ *p-doped PbTe at two different temperatures: 300 K and 600 K.*

4.6 Summary

I investigated the application of stress along the three principle directions of PbTe. Under the assumption of a constant doping concentration, increasing hydrostatic pressure did not increase the thermoelectric power factor. However, stress which breaks the cubic symmetry of PbTe can greatly increase the power factor. In general, increasing compressive (tensile) stress increased the power factor, parallel to the applied stress, of p-type (n-type) PbTe.

I identified two different mechanisms through which anisotropic stress affects the transport properties of PbTe: (i) intervalley-transfer and (ii) valley-reshaping.

(i) *Intervalley-transfer* occurs for stress along [111], and [110]. Stress along these directions breaks the symmetry of the four L-point carrier-pockets, redistributing electrons between them. Because each individual carrier-pocket has highly anisotropic transport properties, intervalley-transfer can improve the conductivity along certain directions.

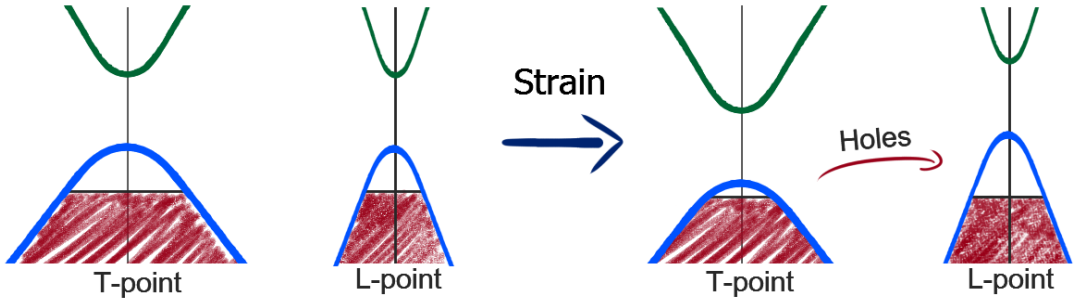

When the intrinsic carrier concentration is significant, the redistribution of both conduction-band electrons and valence-band holes becomes important. *Simultaneous intervalley-transfer* can increase both the Seebeck coefficient and electrical conductivity concomitantly. Correctly applied anisotropic stress along [111] or [110] can greatly improve the power factor for PbTe in the intrinsic regime.

The key characteristic enabling this effect is that PbTe has multiple carrier-pockets, each of which has highly anisotropic transport properties [Fig. 4.7(a)]. Applying stress which breaks the degeneracy of these pockets leads to intervalley-transfer.

(ii) *Valley-reshaping* was the dominant effect for stress along [001]. In this case, the L-point carrier-pockets remained degenerate. However, because the valence-band of PbTe has large anisotropic features, compressive stress along [001] could significantly reshape the valence-band; either increasing the p-type conductivity along [001]. Alternatively, increasing tensile [001] stress could increase the Seebeck coefficient perpendicular to [001].

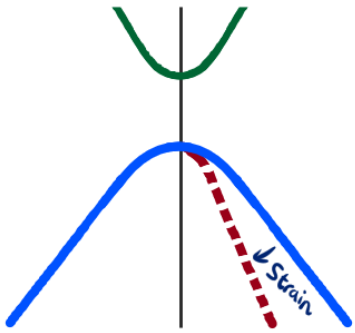

The key characteristic of this effect is the large anisotropic features in the valence-bandstructure, close to the valence-band maximum [Fig. 4.14(d)].

By looking for other thermoelectrics which share these key characteristics, new materials which can have their power factors improved under anisotropic strain can be identified. There are perhaps many materials, previously disregarded due to a low power factor, which could achieve a high figure of merit under anistropic strain. This work also suggests that the power factor of samples may be improved by using techniques which lock-in stresses and strains — such as high-pressure pressing, thin-films, etc.

Chapter 5

Background and Methodology for the Investigations of Mg_2Si and Mg_2Sn

5.1 Motivation

In my work on lead telluride, I identified several guiding principles to help identify thermoelectrics which can have their power factor improved by straining them. After completing the work on lead telluride, I searched for thermoelectric materials with several key characteristics:

1. a bandstructure with multiple carrier pockets, each of which has anisotropic transport properties, and/or a bandstructure with large anisotropic features near the band-edge — akin to the Σ_{max} local maxima in PbTe,

2. a bulk material, not layered. Layered materials can usually only be strained within the plane — as a thin film grown on a substrate — or compressed perpendicular to the plane. I ideally would have a material which could be strained along multiple crystal directions.

In order to allow easily interpreted bandstructures to be plotted, I also decided to focus on materials which had a relatively small unit cell. After looking through many known thermoelectrics, I decided Mg_2Si and Mg_2Sn fulfilled these criteria, and warranted further investigation. I will briefly summarize the key parts of the bandstructure of Mg_2Si, and how they motivated this investigation.

5.1.1 Mg_2Si Bandstructure

Mg_2Si and Mg_2Sn both have indirect band gaps. The valence band maximum is located at the Γ point, and the conduction band minimum is located at the X-point (Fig. 5.1)[133]. Experimental measurements of the band gap vary from 0.6–0.78 eV (See table A.6 in Appendix A.8.1) in contrast to the narrower band gap range of 0.18–0.23 eV for Mg_2Sn.

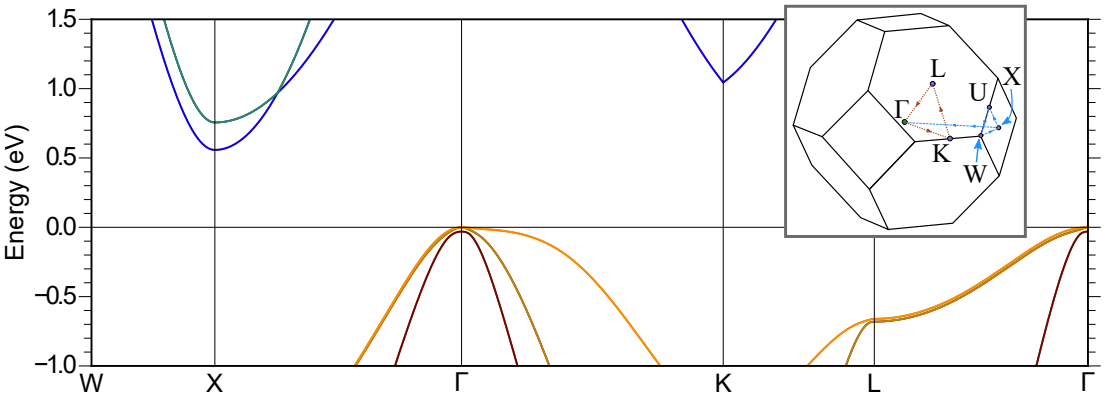

Figure 5.1 *Main: Calculated bandstructure of Mg_2Si. The band gap has not been altered. Inset: diagram of the Brillouin zone, showing special points. Details of this calculation are given in section 5.3.*

At the X-point of the Brillouin zone, Mg_2Si has two conduction band minima. Figure 5.2(a) shows one minimum is ∼0.20 eV lower in energy than the other. For simplicity I will call these the *'lower'* and *'upper'* conduction bands. Both the lower and upper conduction bands have very different curvatures along X–U, X–W, and X–Γ: thus, each of the conduction band carrier pockets will have anisotropic transport properties. Applying strain along [001] breaks the symmetry of the X-points, and should cause an intervalley-transfer-effect for *n*-type Mg_2Si.

Figure 5.2(c) shows an energy isosurface 250 meV above the Mg_2Si conduction band minimum. At each X-point is a pair of carrier pockets: the larger lower-conduction-band pocket shaped like a four-pointed star; and the smaller upper-conduction-band pocket shaped like a spheroid. The highly anisotropic features of the lower-conduction-band suggests that strain which breaks the symmetry of those features — such as strain along [111] Γ–L — will cause the lower-conduction-band pockets to reshape significantly.

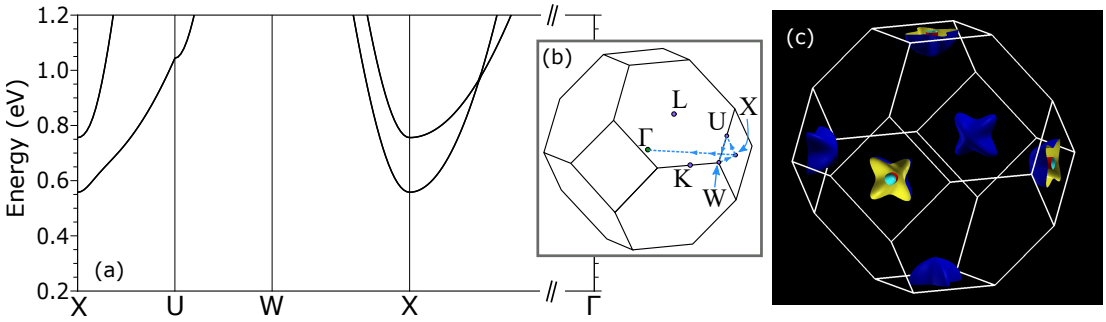

Figure 5.2 *(a) Calculated bandstructure for the conduction bands of Mg_2Si. Zero eV is set to be the valence band maximum. (b) Diagram of the Brillouin zone (c) Energy isosurface 0.25 eV above the conduction band minimum of Mg_2Si.*

Mg_2Si has three important valence bands, all with maxima at the Γ point. Figure 5.3(a) shows all three bands, termed vb1, vb2, and vb3, all of which will contribute to *p*-type thermoelectric properties. Each band has a distinct shape: vb1 has a relatively steep gradient along the Γ – X line ([001]) and a very shallow gradient along Γ – K ([110]) and Γ–L ([111]). This implies that holes in vb1 will have much greater velocities along the [001] direction than along [110] or [111]. Energy isosurfaces of vb1 (Fig. 5.3(b)) appear like a raspberry, with 'drupelets' that point out along [110]. Strain along [110] will break the degeneracy of each lobe, causing valley-reshaping.

The second valence band vb2 (Fig. 5.3(a)) has a much steeper gradient along the Γ–X ([001]) or Γ–K ([110]) directions than along Γ–L ([111]). Energy isosurfaces of this band appear like a stellated octahedron, with the points oriented along $\Gamma \rightarrow$ L. Strain along [111] should cause the largest change in mobility for states in vb2. vb1 also has a relatively low gradient along [111] (Fig. 5.3(a)).

The third valence band, vb3, sits lower in energy than vb1 & vb2, and is a much lighter band. This is reflected by the small volume enclosed by the energy isosurface of vb3 (Fig. 5.3(b)). vb3 is relatively isotropic, so I do not expect any significant change in shape for this band under anisotropic strain. However, the vb3 maximum may still shift in energy relative to vb1 and vb2.

The electronic bandstructure of Mg_2Si indicates that strain along [001] & [111] should have a significant effect on the *n*-type transport properties of Mg_2Si, and strain along [110] and [111] should have a large effect on *p*-type transport. By generalizing the findings of our study on PbTe, I have identified another material which could be improved by anisotropic strain.

Mg_2Sn has a broadly similar bandstructure to Mg_2Si. I will discuss the key

differences when discussing the results for Mg_2Sn, however, the bandstructures are similar enough to suggest strain could improve it in a similar way.

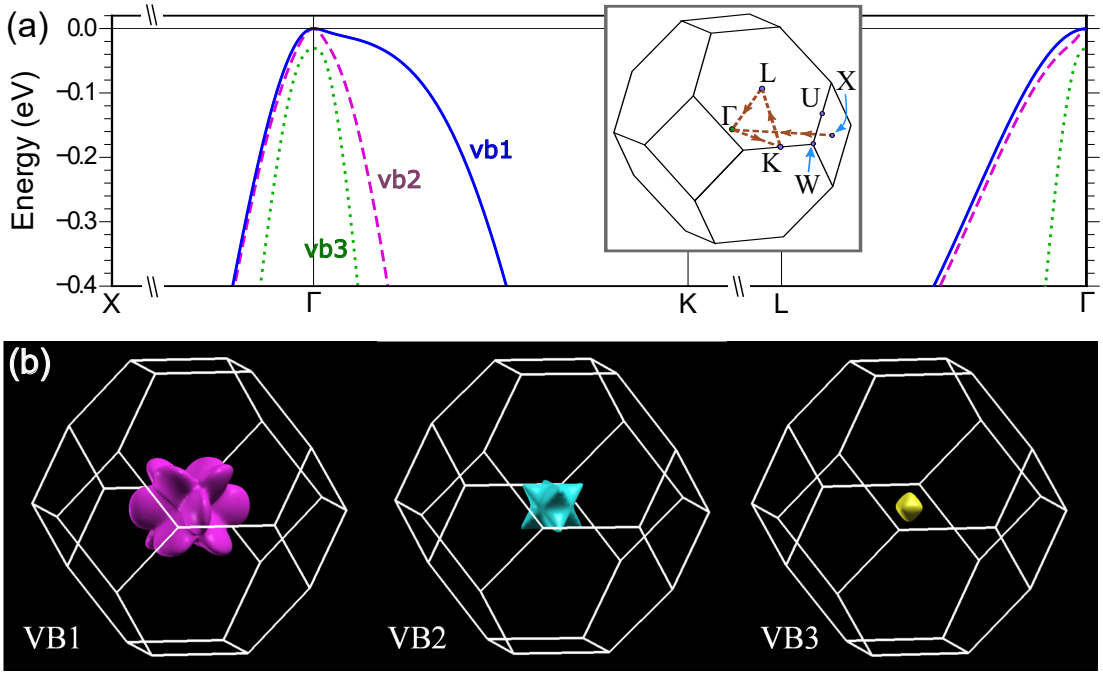

Figure 5.3 *(a) Calculated bandstructure of Mg_2Si around the valence band maximum. There are three important bands. The highest energy band (vb1) plotted using a solid blue line, the second highest energy band (vb2) using a magenta dashed line, and the third highest energy band (vb3) plotted using a green dotted line. (b) Energy isosurfaces of the three valence bands, 0.2 eV below the global valence band maximum.*

5.2 Background

This section briefly summarizes some previously existing literature on Mg_2Si and Mg_2Sn.

The family of materials Mg_2Si, Mg_2Ge, and Mg_2Sn are well known in the field of thermoelectric research. Indeed, the oldest citation in this thesis — other than Thomas Johann Seebeck's original book — is a 1941 publication on this family of compounds[134]. Recently, there has been renewed interest in the Mg_2X family as candidate thermoelectric materials[132,135–138] for three main reasons:

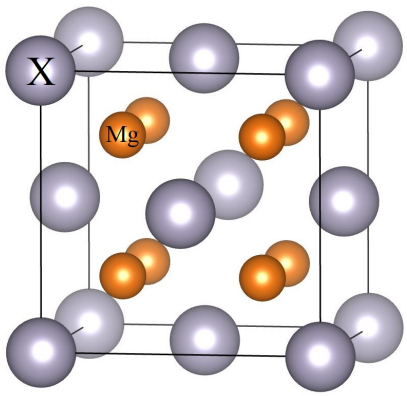

Crystal structure of Mg_2X for X = Si, Ge, or Sn.

(i) A low thermal conductivity can be achieved by alloying different members of the Mg_2X family together[132]. All three Mg_2X compounds — Mg_2Si, Mg_2Ge, and Mg_2Sn — share the same basic crystal structure, where the X ions form a face-centered-cubic lattice, and the magnesium ions form a simple-cubic sublattice. If the X positions have mixed occupancy, caused by alloying different members of the family together, the thermal conductivity can be reduced.

(ii) Mg_2Si, Mg_2Ge, and Mg_2Sn can all operate at high temperatures, with thermoelectric measurements being reported up to at least 850 K[132]. Experimental melting points for the pure crystals range from ∼1050 K for Mg_2Sn, to over 1380 K for Mg_2Ge*. Having a large temperature difference across a thermoelectric material increases the efficiency of thermoelectric power generation, so it is desirable for thermoelectrics to be mechanically stable over a large temperature range.

(iii) Compared to other thermoelectrics, e.g. lead telluride, the component elements of Mg_2X compounds are comparatively cheap and environmentally friendly[137,141,142].

The Mg_2X compounds are already promising thermoelectrics, so it is definitely worth exploring if they can be further improved through strain.

5.2.1 Mg_2X Alloys

Alloying different members of the Mg_2X family together is a common method to create a thermoelectric material with a low thermal conductivity. Not only does alloying reduce the thermal conductivity, but it can also improve the thermoelectric power factor. Experimental results reported by Liu *et al.*[143] show that the power factor of n-type $Mg_2Si_{1-x}Sn_x$ alloys can be greater than those of Mg_2Si or Mg_2Sn alone. They attributed this to the convergence, in energy, of the upper and lower conduction bands as x is changed. Liu *et al.* conducted first-principles calculations on $Mg_2Si_{1-x}Sn_x$ for a range of x values, to examine how changing x affected the bandstructure. They found that there was a band-crossing at approximately $x = 0.65$–0.7, which corresponded to the largest power factor they measured.

Vegard's law states that the unit-cell volume of a solid solution of two materials

*A quick summary with citations: Mg_2Si, 1070–1105 °C[134,139]; Mg_2Ge, 1115 °C[134]; Mg_2Sn, 778 °C[134,140].

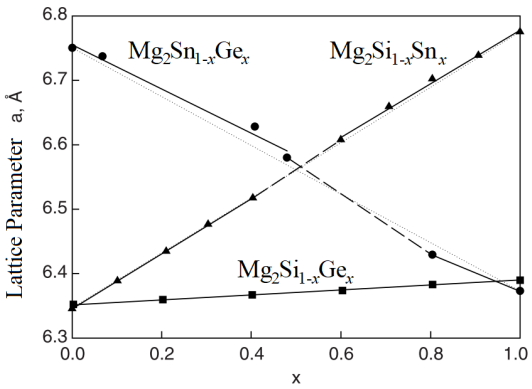

Figure 5.5 *Experimentally measured lattice parameter against composition for solid solutions Mg_2X compounds. Figure illustrates Vegard's law. Figure taken from Rowe et al.[136]; it has been slightly simplified for this thesis.*

is a weighted mean of the volumes of the constituent materials. Mg_2Sn has a larger lattice parameter than Mg_2Si, ~6.8 Å vs ~6.4 Å[136,144], and solid solutions of the two closely follow Vegard's law[136].

First-principles calculations by Balout, Boulet, and Record[145] indicate that the two conduction bands of Mg_2Si converge as the volume of the unit-cell is increased. Seperate calculations by Guo & Wang[146] have shown that, for Mg_2Sn, the two conduction bands converge as the unit-cell volume is decreased. Thus, it is likely that the band convergence shown by Liu *et al.* is an effect predominatly caused by hydrostatic strain of the crystal structure. This shows that strains of a magnitude which can be achieved by chemical alloying, can also lead to significant improvement in the thermoelectric power factor[143,146].

5.2.2 Effect of Strain: Mg_2Si

Balout, Boulet, and Record published first-principles calculations of the thermoelectric properties of Mg_2Si under hydrostatic strain, and strain along various axes[145,147–149]. They found some strains did increase the power factor, but, there are two main issues with their calculations.

Firstly, it is unclear whether they presented direction-dependent values for the Seebeck coefficient and conductivity tensors (e.g. one of $\sigma_{xx}, \sigma_{yy}, \sigma_{zz}$), or if they present results for the trace of the tensors ($\sigma_{AVG} = \frac{1}{3}\left(\sigma_{xx} + \sigma_{yy} + \sigma_{zz}\right)$). Anisotropic strain will make the electrical properties anisotropic — thus it is important to examine each direction individually.

Secondly, Balout *et al.*[145,147–149] calculated a bandgap of only 0.256 eV, far lower than experimental estimates which vary from 0.6 to 0.78 eV (Appendix A.8.1). It is common for density-functional-theory calculations to underestimate the band gap, but, Balout *et al.* do not shift the conduction bands to correct for this. The concentration of intrinsic carriers n_i scales, roughly, with the exponential of the band gap E_g:

$$n_i \propto \exp\left\{-\frac{E_g}{2k_BT}\right\}, \tag{5.1}$$

where k_B is the Boltzmann constant and T is the temperature[150]. By underestimating the band gap, their calculations will overestimate the concentration of intrinsic charge carriers. To give an example, their band gap overestimates the intrinsic carrier concentration of undoped Mg_2Si at 300 K by a factor of 5000 — equivalent to introducing $2 \times 10^{18}\,cm^{-3}$ more carriers — which would completely change all their results for low doping concentrations of $\sim 1 \times 10^{18}\,cm^{-3}$ and below.

5.2.3 Effect of Pressure: Mg_2Si

At ambient conditions, Mg_2Si crystallizes in the cubic anti-flourite structure shared with the other members of the Mg_2X family. Under increasing pressure, Mg_2Si undergoes two structural phase transitions[151]: first, a transition to a orthorhombic phase occurring at 7.5 GPa, followed by a second transition to a hexagonal phase at 21.3 GPa.

Morozova *et al.*[152] studied how the electrical properties of Mg_2Si doped with aluminium change under high pressure. Aluminium is a donor to Mg_2Si, and the Seebeck coefficient and Hall coefficient measurements they reported were both negative — showing n-type conduction. The samples they measured were all heavily doped, with 1% aluminium. Hall coefficient measurements on ambient-pressure samples indicated a carrier concentration of approximately $6 \times 10^{19}\,cm^{-3}$, although difficulties associated with estimating carrier concentration using Hall coefficient should be taken into account.

Figure 5.6 shows some of the electronic transport properties measured by Morozova *et al.*. They found increasing pressure reduces the electrical resistivity significantly, then at ~2 GPa the slope became more shallow and the rate of increase of the conductivity with pressure became lower. Increasing stress reduced the Seebeck coefficient, although, again, the rate of change with pressure was lower above 2 GPa. They were able to reproduce these trends over a second

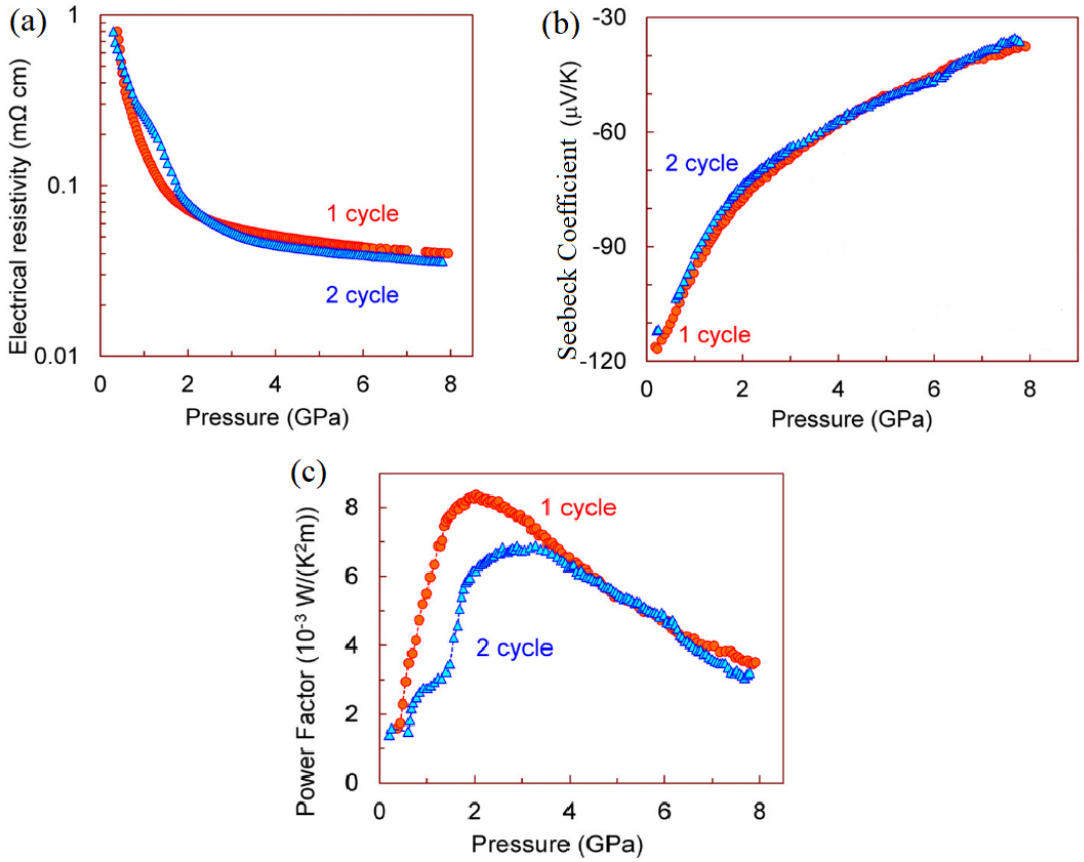

Figure 5.6 *Experimentally measured pressure dependencies of the room-temperature (a) electrical resistivity, (b) Seebeck coefficient, and (c) Thermoelectric power factor of Mg_2Si. Figure taken from Morozova et al. (2014)[152]. They measured two pressure cycles. For clarity, some minor presentation details have been changed from the original paper, but nothing quantitative has been altered.*

pressure cycle, indicating that increasing the number of defects in their samples was not responsible for the decrease in resistivity.

Morozova *et al.*[152] suggested that a change in the band gap may be responsible. If increasing pressure decreased the band gap, that could increase the intrinsic carrier concentration, and perhaps metallize Mg_2Si at sufficiently high pressure. However, infrared absorption measurements on Mg_2Si under pressure indicate the pressure coefficient of the band gap is very small, $0 \pm 5\,\mathrm{meV/GPa}$[153].

Morozova *et al.* mention two theoretical works[154,155] which *"predicted a gradual band gap closure and metallization [at] 6–8 GPa"*. Both of these studies conducted *ab-initio* calculations on Mg_2Si under pressure, and presented data which could be — in this author's opinion — misinterpreted to show that the band gap of Mg_2Si closes at 6–8 GPa. However, these studies should not be considered positive support for metallization of Mg_2Si under pressure for the

following reasons: One study, by Yu *et al.*[155], uses the Perdew-Burke-Ernzerhof (PBE) generalized gradient approximation (GGA) to take into account exchange-correlation effects of the electrons. This is the same functional used by Balout *et al.*[145,147–149] and which, for Balout *et al.*, drastically underestimated the band gap. It is unclear what band gap they calculated for Mg_2Si at 0 GPa, as they do not report it. Indeed, the plots of their calculated Mg_2Si density-of-states (Fig. 5.7) suggest the band gap was closed or nearly closed at zero pressure.

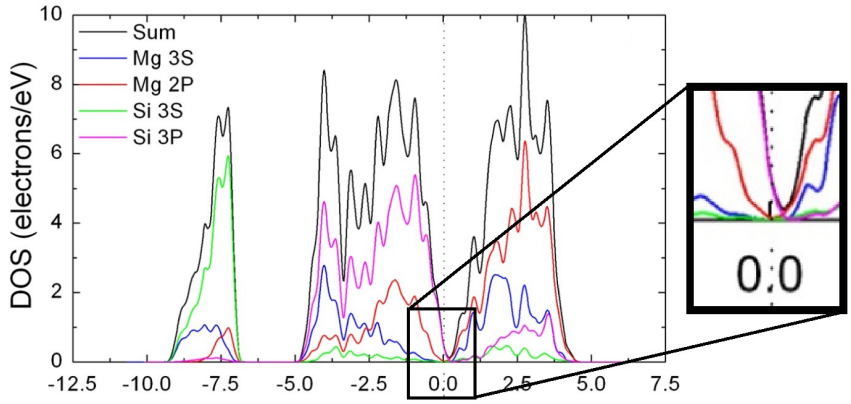

Figure 5.7 *Figure taken from Yuet al. (2010)[155], with the window on the right added. Left: Calculated electron density-of-states (DOS) vs energy for Mg_2Si. Zero eV is set as the Fermi energy. Right: portion of the DOS near the Fermi-energy, zoomed in to emphasize that the DOS appears non-zero.*

The other paper that Morozova *et al.*[152] cite is by Kalarasse & Bennecer[154]. They use the local-density-approximation (LDA) for the exchange-correlation potential. Although they present calculations of the band gap as a function of pressure, they explicitly say *"The LDA underestimates the bandgap"*, and *"the pressure coefficients of bandgaps within LDA, even underestimated, are more reliable than the absolute gaps"*. The zero pressure band gap they calculate is only ∼0.12 eV. They calculate the rate of change of the band gap with pressure to be −0.021 eV/ GPa, which has good agreement with infrared absorption measurements[153]. Considering experimental values for the zero-pressure band gap are in the range 0.6–0.78 eV (Appendix A.8.1), it is clear that the results by Kalarasse & Bennecer do not show that Mg_2Si metallizes at approximately 6 GPa. Indeed, their results indicate that metallization would only occur after several 10s of GPa, unless a structural transition occurs first. The large reduction in resistivity observed by Morozova *et al.* cannot be explained by band gap closure.

In summary, it remains unclear what is the cause of the trends in transport properties with pressure observed by Morozova *et al.*[152]. There is significant

evidence against the idea that rapid pressure-induced narrowing of the band gap is responsible. In order to exploit the effects of pressure to improve thermoelectric performance, it is crucial to understand whether the improvements seen are caused by changes in the bandstructure — or if some other effect is at play.

5.2.4 Effect of Pressure: Mg_2Sn

Previous investigations into the effect of pressure on magnesium stannide have been reported in the literature. Mg_2Sn transitions to a high-pressure phase somewhere in the range 2.5–3 GPa[156–160].

Guo & Wang[146] performed first-principles calculations on Mg_2Sn under hydrostatic pressure well beyond this, going up to 17.2 GPa. It is unclear how they calculated the pressure, and Guo & Wang do not report a bulk modulus or other elastic constants to enable easy comparison with experiment, but for our purposes it is the qualitative trends which are important.

Guo & Wang's main result is that, for n-doped Mg_2Sn, increasing pressure initially increased both the electrical conductivity[†] and Seebeck coefficient, then reached a maximum above which both σ and S decreased with increasing pressure. This trend was associated with convergence of the upper and lower conduction bands under pressure, with the crossing point around 5–6 GPa. This indicates that the power factor improvement seen upon alloying Mg_2Si and Mg_2Sn together is likely a volume effect. Guo reported the same trend in an earlier paper[161].

It is clear that further investigation is needed into the effects of hydrostatic and non-hydrostatic strain on the thermoelectric properties of Mg_2Si and Mg_2Sn. My calculations will show that large improvements in the thermoelectric power factor can be achieved through strain.

[†]Specifically, they calculated the reduced-electrical-conductivity σ/τ.

5.3 Methodology

5.3.1 Choice of Strain Combinations

At ambient conditions, Mg_2X adopts the cubic anti-fluorite crystal structure. Four types of strain were considered: strain along [001], [111], and [110]; and hydrostatic strain. In experiments that measure electronic properties of a strained crystal, it is common to apply pure uniaxial stress. In these experiments, stress is applied along one axis, and the crystal can relax according to Poisson's ratio. Transport properties are then measured along, or perpendicular to, the direction of stress. To enable easy comparison with future experiments, strains commensurate with uniaxial stress along [001], [111], and [110] were applied.

Stress as a function of strain and Poisson's ratio along each direction were computed using the elastic constants reported in the literature[162,163]. Using standard equations[164–167], the elastic constants for a cubic material were used to derive the elastic compliance, and the Poisson's ratios in each direction. The specific equations used to relate the elastic constants to elastic compliance, Young's moduli, and the Poisson's ratios can be found in appendix A.4. Table A.1 lists the elastic constants C_{ij} measured in experiment, for Mg_2Si and Mg_2Sn, respectively. The elastic compliance values S_{ij} and relevant Poisson's ratios ν_i^j I derived from the elastic constants are also included. For the Poisson's ratios, I use the notation:

$$\nu_{[hkl]}^{[\alpha\beta\gamma]} = -\frac{\Delta\epsilon_{[\alpha\beta\gamma]}}{\Delta\epsilon_{[hkl]}}, \tag{5.2}$$

where $\Delta\epsilon_{[hkl]}$ and $\Delta\epsilon_{[\alpha\beta\gamma]}$ is the strain perpendicular to the plane given by the Miller indices $[hkl]$ and $[\alpha\beta\gamma]$, respectively. Electron-transport-properties were computed under strains principally along [001], [110], and [111], with the relative strain perpendicular to the principle direction given by the Poisson's ratios in table A.1.

5.3.2 Electron Transport Properties

The method for the electronic transport calculations of Mg_2X was similar to the calculations for PbTe. Exchange and correlation effects were treated with the modified Becke-Johnson potential by Trans and Blaha (TB-mBJ)[98]. Regular Monkhorst-Pack $14 \times 14 \times 14$ grids of k-points (equivalent to a k-point spacing of $\sim 2\pi \times 0.01\ \text{Å}^{-1}$) were used for Brillouin zone sampling. Atomic sphere muffin tin

radii, R_{MT}, of 2.39, 2.5, and 2.5 bohr were chosen for the Si, Sn, and Mg atoms, respectively. The magnitude of the largest vector used in the charge density Fourier expansion, GMAX, was set to 12 bohr^{-1}.

The largest Kohn-Sham plane-wave basis vector, K_{max}, was given by $R_{MT} \times K_{\mathrm{max}} = 7.0$ for the Mg_2Si calculations, and 8.0 for the Mg_2Sn calculations. Spin-orbit coupling was included in all calculations. Including spin-orbit coupling was particularly important for *p*-type Mg_2Sn[170], as without it there is no splitting at Γ of the three highest-energy valence-bands. A table of parameters used is in appendix A.3.

After self-consistency had been reached, the Kohn-Sham orbital eigenvalues were computed on a dense $50 \times 50 \times 50$ k-point grid in a single non-self-consistent calculation. From these eigenvalues, electrical transport properties were calculated using the framework of Boltzmann transport theory as implemented in the BoltzTraP2 code[109].

BoltzTraP2 is a computer program designed to calculate electron-transport-properties within the framework of Boltzmann transport theory, and the relaxation time approximation. It works in a similar way to BoltzTraP1, used for the calculations on PbTe in this work, but was rewritten in the Python and C++ computer languages, to make it more flexible for people to change and improve.

Again, as is standard practice, doping was treated using the *rigid band approximation*, which simulates crystal doping by changing the chemical potential μ, and keeps the bandstructure fixed, or *rigid*, across all doping concentrations.

5.3.3 The Band Gap

In order to calculate the transport properties accurately, it is important to have a good estimate of the band gap at each temperature and strain. The temperature dependence of the band gap is not captured by standard, ground state density functional theory calculations. To account for the temperature dependence of the band gap, the conduction bands are rigidly shifted to adjust the gap, as is standard practice[117]. The gap was shifted for each strain by the same amount, chosen so the gap would agree with experimental values for a single fixed point at zero stress[45].

The band gap of Mg_2Si as a function of temperature T was measured by Udono

et al.[171]. I fitted their data using the function:

$$\mathrm{Gap}(T) = G_0 + G' T_\lambda \ln\left(\cosh\left(\frac{T}{T_\lambda}\right)\right), \tag{5.3}$$

where T is the temperature; G_0 is the zero-temperature band gap; T_λ determines the temperature scale over which the band gap begins to decrease; and, at high temperatures $T \gg T_\lambda$, the band gap decreases linearly with increasing T:

$$\mathrm{Gap} \to \left(G_0 - G' T_\lambda \ln(2)\right) + G' \times T, \qquad \text{as } \frac{T}{T_\lambda} \to \infty, \tag{5.4}$$

where the gradient of the band gap with temperature parametrized by G'. Figure 5.8 shows the fit to the data reported by Udono *et al.*. The band gap as a function of temperature was then extrapolated above 300 K using the fitted function, which is approximately linear above 300 K.

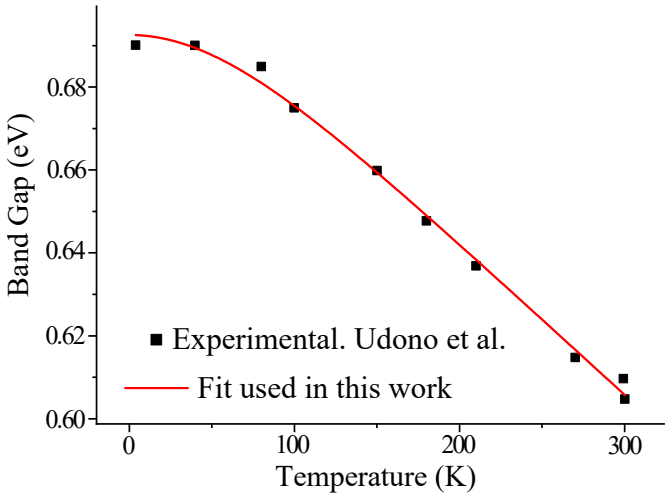

Figure 5.8 *Fit of the band gap of Mg_2Si to experimental data from Udono et al.*[171]*. Final fit parameters in table 5.2. $\chi^2 = 0.002\,eV$.*

Band Gap of Mg_2Sn

The band gap of Mg_2Sn as a function of temperature was reported by Lipson & Kahan[172] (Fig. 5.9). They measured the band gap using infrared absorption at temperatures between 15 and 296 K. They reported a linear decrease of the band gap with increasing temperature, with a gradient of -3.13×10^{-4} eV/K and a band gap of 0.185 eV at 0 K. Although one expects the band gap as a function of temperature to level off as the temperature approaches 0 K, a linear decrease at high temperatures is commensurate with the trend observed for the Mg_2Si

band gap. Because the thermeoelectric properties of Mg_2Sn were only going to be calculated at temperatures above 200 K, a linear trend was sufficient.

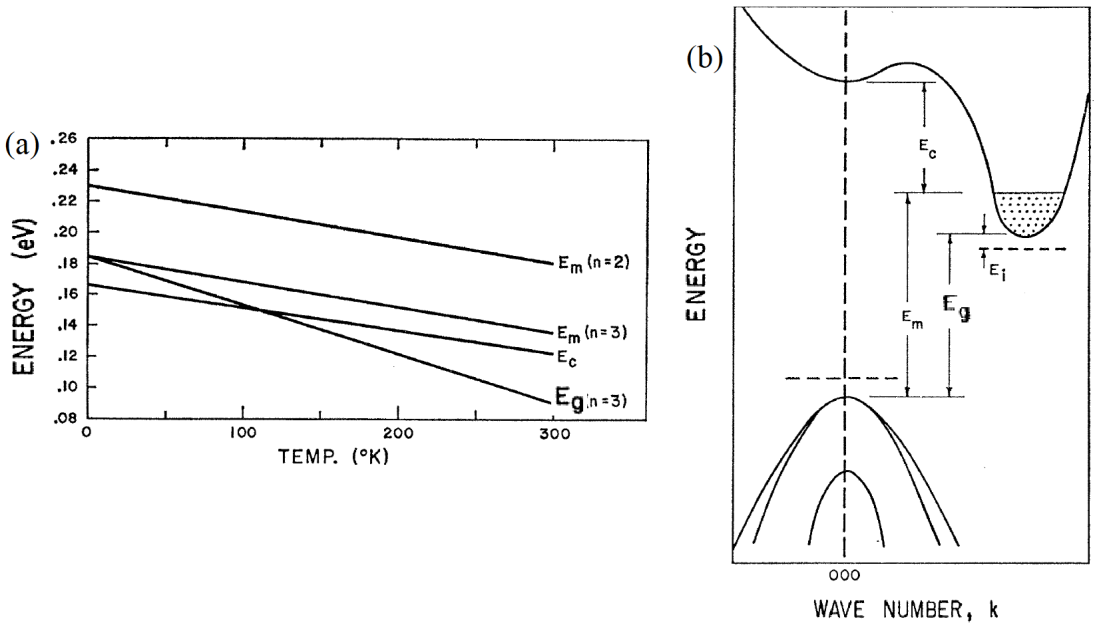

Figure 5.9 *(a) The band gap of Mg_2Sn as a function of temperature, as measured by Lipson & Kahan. (b) Diagram of the bandstructure of Mg_2Sn. Both figures taken from Lipson & Kahan (1964)[172]. E_g is the band gap in question. E_i, E_m, and E_c are a variety of other energy differences relevant to the optical absorption experiments conducted by Lipson & Kahan.*

In this work, for both Mg_2Si and Mg_2Sn, the band gap was adjusted to match the estimated zero-pressure band gap based on data from experiments reported in the literature[171,172]. The estimated band gap G for each strain ε and temperature T was set to be the experimental value at zero strain $G_{\text{exp.}}$[171,172] modified by the calculated difference between the stressed band gap $G_{\text{calc.}}(\varepsilon)$, and the calculated zero stress band gap $G_{\text{calc.}}(\varepsilon = 0)$:

$$G(\varepsilon, T) = \underbrace{G_{\text{calc.}}(\varepsilon) - G_{\text{calc.}}(\varepsilon = 0)}_{\text{calculated}} \; + \; G_{\text{exp.}}(T)\,. \tag{5.5}$$

Using this method, the electron-transport properties for Mg_2Si and Mg_2Sn were calculated under strains which mimic uniaxial stress along [100], [110], and [001]. The calculated transport properties have excellent agreement with data from experiment, as will be shown in the following chapter.

Table 5.1 *Lattice constants and elastic constants from literature, followed by elastic compliances, Poisson's ratios, and direction-dependent Young's Moduli I derived. The lattice constants used have close agreement with the values measured by Kasai et al.[144]*

Property	Mg_2Si	Mg_2Sn
a_0(Å)	6.521[168]	6.765[169]
C_{11} (GPa)	121[162]	82.4[163]
C_{12} (GPa)	22[162]	20.8[163]
C_{44} (GPa)	46.4[162]	36.6[163]
B_0 (GPa)	55	41
S_{11} (GPa^{-1})	0.00875	0.0135
S_{12} (GPa^{-1})	-0.0013468	-0.00272
S_{44} (GPa^{-1})	0.02155	0.0273
$\nu^{[100]}_{[001]} = \nu^{[010]}_{[001]}$	0.154	0.202
$\nu^{[1\bar{1}0]}_{[111]} = \nu^{[11\bar{2}]}_{[111]}$	0.171	0.158
$\nu^{[1\bar{1}0]}_{[110]}$	0.185	0.118
$\nu^{[001]}_{[110]}$	0.148	0.223
$Y_{[001]}$ (GPa)	114	74.0
$Y_{[111]}$ (GPa)	109	84.8
$Y_{[110]}$ (GPa)	110	81.8

Table 5.2 *Fitting parameters for the Mg_2Si band gap as a function of temperature. Equation 5.3 details the function. A plot of the fit is shown in Fig. 5.8. $\chi^2 = 0.002\,eV$.*

Parameter	Value	Uncertainty
G_0	0.692 56 eV	±0.002 eV
G_{grad}	$-0.365\,019 \times 10^{-3}$ eV/K	$\pm 0.02 \times 10^{-3}$ eV/K
λ	89.9 K	±20.8 K

Chapter 6

Thermoelectric Properties of Mg_2Si and Mg_2Sn under Anisotropic Stress

6.1 Mg_2Si

6.1.1 Comparison with Experimental Data

To gauge the accuracy of this work, results for the electron-transport properties for unstrained Mg_2Si were compared with experimental data for Mg_2Si at zero pressure.

Within the constant-scattering-time approximation, the Seebeck coefficient is independent of the electron-scattering-time τ. Figures 6.1(a) and 6.1(b) show that the Seebeck coefficient for n-type Mg_2Si again has excellent agreement with experimental data; both as a function of temperature, and Hall carrier concentration.

To compare calculated results for the electrical conductivity of Mg_2Si with experimental data, the electron-scattering time must be estimated. Figure 6.1(c) shows that a scattering time $\tau = 2.5 \times 10^{-14}\,\mathrm{s}$ at $300\,\mathrm{K}$ gives excellent agreement with experiment for n-type Mg_2Si. The scattering time is held constant for all strains, so it is only important for numerical comparison to experiment.

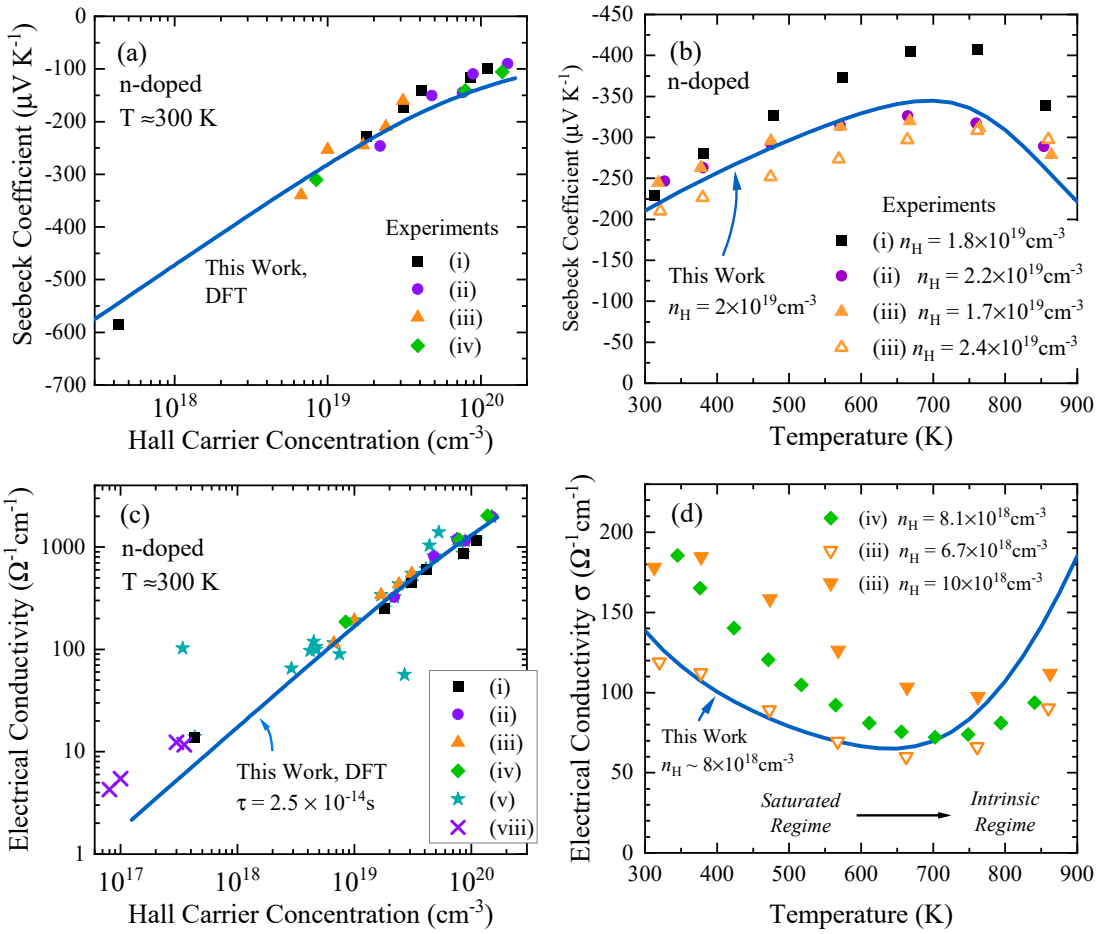

Figure 6.1 *Electron-transport properties for n-doped Mg_2Si. Calculated results from this work are shown using solid lines, symbols are experimental results from Tani & Kido [(i)[173], (ii)[174], (iii)[175], and (v)[176]], Akasaka et al.[(iv)[177]], and Morris et al.[(viii)[178]]. (a) Seebeck coefficient vs Hall carrier concentration at temperatures near 300 K; (b) Seebeck coefficient vs temperature; (c) Electrical conductivity vs Hall carrier concentration; (d) Electrical conductivity vs temperature. In (c) and (d) the scattering time τ was set as $2.5 \times 10^{-14}\,\mathrm{s} \times (300\,\mathrm{K}/T)$.*

Comparing the calculated electrical conductivity against experiment across a range of temperatures is difficult, as the electron-scattering time τ should reduce as the temperature increases. Higher temperature means higher phonon population, and thus greater electron-phonon scattering. To account for this, I set the scattering time τ to be inversely related to the temperature T:

$$\tau = 2.5 \times 10^{-14}\,\mathrm{s} \times \left(\frac{300\,\mathrm{K}}{T}\right). \tag{6.1}$$

Figure 6.1(d) shows that, by scaling τ inversely with temperature T, the electrical conductivity of $8 \times 10^{18}\,\mathrm{cm}^{-3}$ n-doped Mg_2Si first reduces with increasing temperature, reaches a minimum at $\sim$700 K, then increases rapidly, in good agreement with experimental data. A key feature of Fig. 6.1(d) is the temperature at which the saturated regime transitions to the intrinsic regime. At temperatures below $\sim$700 K the electrical conductivity reduces with increasing temperature due to the reduction of the electron-scattering time. Above $\sim$700 K, Mg_2Si is in the intrinsic regime, where the electrical conductivity increases exponentially due to increasing intrinsic carrier concentration. The calculated results shown in Fig. 6.1(d) capture this transition, indicating that the set band gap, and the calculated density-of-states near the band edges, are accurate.

Figure 6.2(a) shows a comparison between the calculated Seebeck coefficient for p-type Mg_2Si at 300 K and experimental data. As the p-doping concentration increases, the Seebeck coefficient decreases. There is excellent agreement between my calculated values and the data from Akasaka *et al.*[177] and Ihou-Mouko *et al.*[179]((iv) and (vi), respectively).

There is less favourable agreement with the results from Kolezynski *et al.*[180] (vii). However, the data from Kolezynski *et al.* is for mixed-crystal samples of $Mg_{2-x}Li_xSi$. The calculations in this work are valid within the boundaries of the rigid-band approximation, which treats doping by changing the chemical potential — and keeping the bandstructure constant. This approximation breaks down if the sample is a mixed crystal, as were the samples of Kolezynski *et al.*. In their samples the concentration of lithium is very high, ranging from 5–30 % by formula-unit. These concentrations are more similar to a mixed crystal than a doped semiconductor. Indeed, the authors mention that the trends they observed between the fraction of lithium in the alloy and the Hall carrier concentration were unusual, as is the trend between Hall carrier concentration and electrical conductivity. The results of Kolezynski *et al.* have been included in Fig. 6.2 for the sake of completeness; the unfavourable agreement with our calculated results

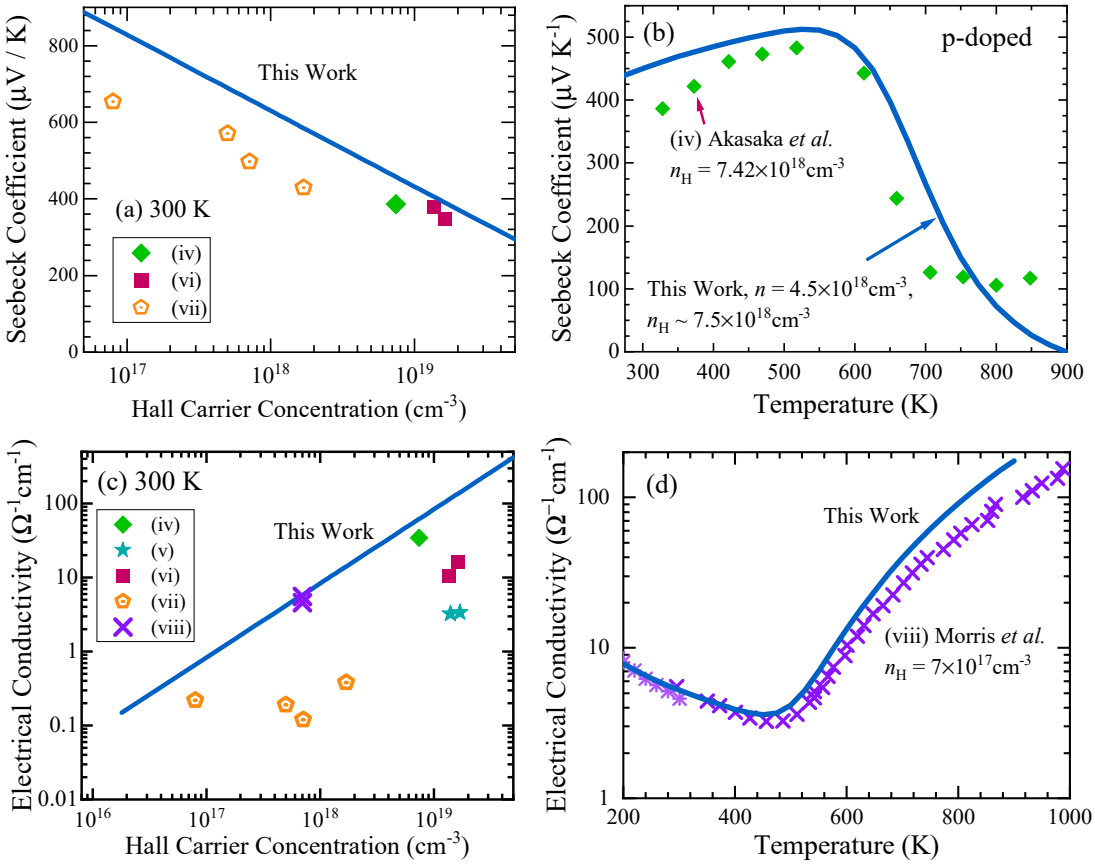

Figure 6.2 *Comparison of calculated electrical transport properties for p-doped Mg_2Si (solid lines) with experimental results (symbols) from (iv) Akasaka et al.*[177]*, (v) Tani & Kido*[176]*, (vi) Ihou-Mouko et al.*[179]*, (vii) Kolezynski et al.*[180]*, (viii) Morris et al.*[178]*. (a) Seebeck coefficient vs Hall carrier concentration at* ∼300 K*; (b) Seebeck coefficient vs temperature; (c) Electrical Conductivity vs Hall Carrier Concentration; (d) Electrical Conductivity vs temperature. In (c) and (d) the scattering time τ was set to* $2.5 \times 10^{-14}\,\mathrm{s} \times (300\,\mathrm{K}/T)$.

is expected. Taking this into account, Fig. 6.2(a) shows excellent agreement between my calculations and the remaining experimental results.

Figure 6.2(b) shows the Seebeck coefficient S as a function of temperature for p-doped Mg_2Si. There is excellent agreement with the experimental data. In particular, it should be noted that the temperature at which S reaches a maximum is 500–600 K for both this work and data from experiment. This indicates that the band gap, and the density of states near the band edges, must be approximately correct.

Finally, Figs. 6.2(c) and (d) show the electrical conductivity at different carrier concentrations and temperatures. The same electron-scattering time is used as for n-type Mg_2Si. The results of Kolezynzki *et al.*[180](vii) are included for

completeness. There is good agreement overall. Figure 6.2(d), in particular, shows that the calculated temperature at which $7 \times 10^{17}\,\mathrm{cm}^{-3}$ p-doped Mg_2Si transitions from a saturated to an intrinsic regime closely aligns with the experimental measurements by Morris *et al.*[178].

Overall, there is excellent agreement between the calculated transport properties of unstrained Mg_2Si and experimental data from the literature.

6.1.2 Chemical Potential and Hall Carrier Concentration

Within the rigid-band approximation, the doping concentration is controlled by chemical potential, with the bandstructure held fixed. Figure 6.3(b) shows the relationship between the chemical potential and the doping concentration for Mg_2Si at 300 K. The charge carriers that contribute significantly to electrical transport properties tend to be within several k_BT of the chemical potential. At 300 K, this amounts to approximately ± 0.1 eV.

Figure 6.3(a) shows the bandstructure of Mg_2Si near the conduction and valence band extrema. The bandstructure was discussed in detail in the Mg_2X background section. It is included here to enable comparison with Fig. 6.3(b).

For n-doping concentrations above $\sim 10^{19}\,\mathrm{cm}^{-3}$, the chemical potential is above the lower-conduction-band minimum. The electrons which contribute to electron-transport properties are in states with a range or energies above and below the chemical potential (Sec. 2.2.3). As the n-doping concentration increases, more and more electrons are thermally excited into the upper conduction band. Changing the proportion of electrons in the upper conduction band vs the lower conduction band changes the Hall mixing factor. This can be seen in the ratio between the true doping concentration n, and the Hall carrier concentration n_H [Fig. 6.3(c)]. For heavily n-doped Mg_2Si, the ratio n/n_H reduces as the doping concentration increases, showing a change in the Hall mixing factor as μ approaches the upper conduction band.

The results for n/n_H provide a link between the calculations in this work, which use the true doping concentration n, and experimental results based on n_H. Figure 6.3(c) can also be used to improve experimental estimates of the doping concentration.

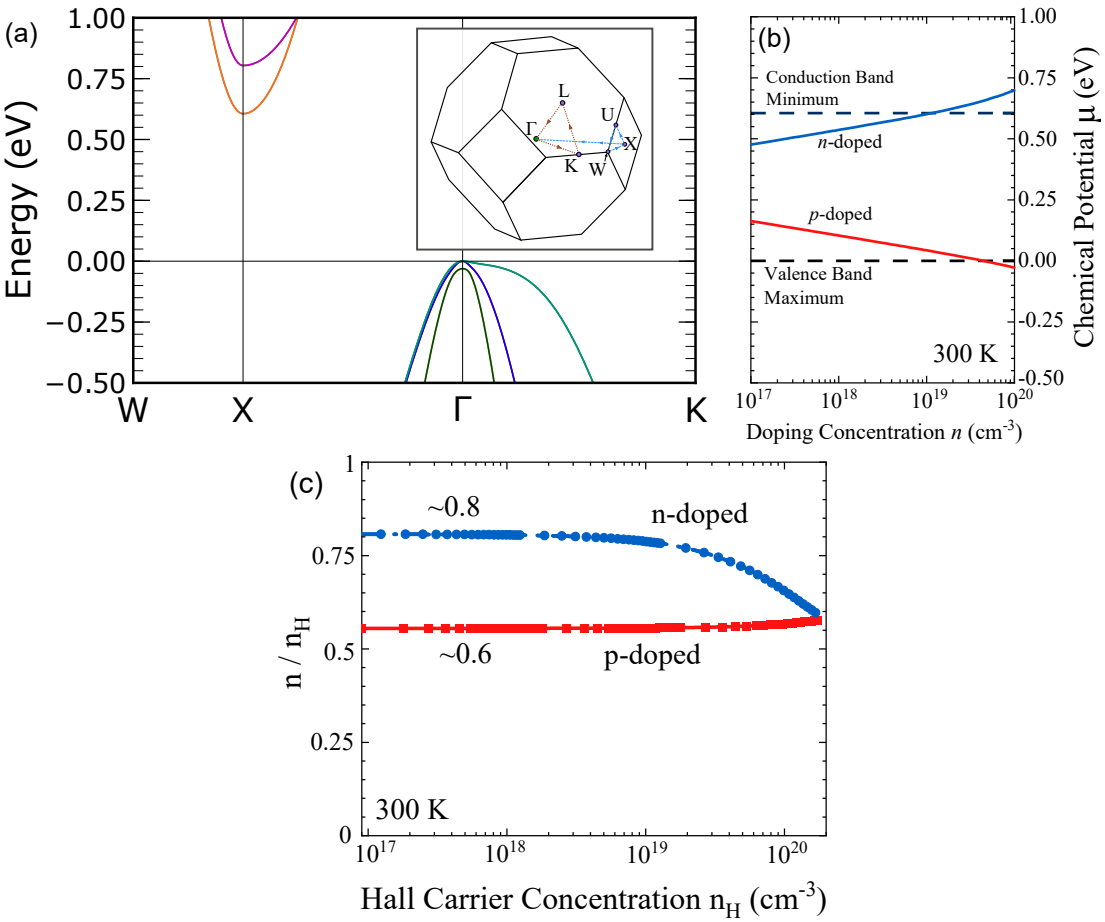

Figure 6.3 *(a) Calculated bandstructure of Mg_2Si. The band gap has been shifted to the value for 300 K. (b) Calculated chemical potential vs doping concentration for Mg_2Si at 300 K. (c) Ratio of the true carrier concentration n to the calculated Hall carrier concentration $n_H = 1/|eR_H|$ for n- and p-doped Mg_2Si at 300 K.*

6.1.3 Intrinsic Carrier Concentration

The relative magnitudes of the intrinsic carrier concentration and the doping concentration determines whether Mg_2Si is in the intrinsic or saturated regime. To give a sense of what tempertature deterimes the boundary between these two regimes, Fig. 6.4 shows the intrinsic carrier concentration as a function of temperature for unstressed Mg_2Si.

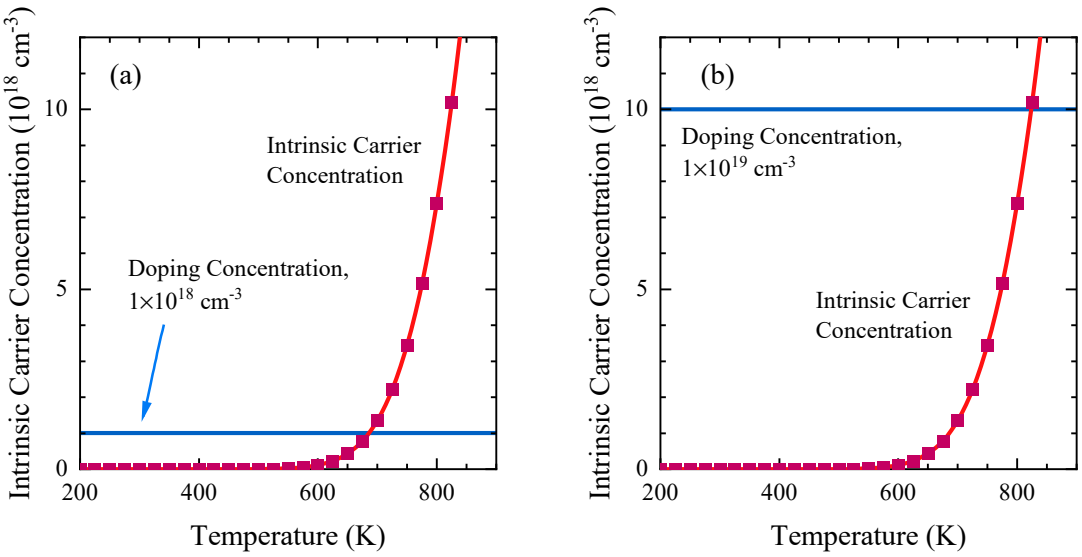

Figure 6.4 *Intrinsic and doping concentrations against temperature for unstressed Mg_2Si.*

6.1.4 Uniaxial Stress Along [001]

n-type Mg_2Si in the saturated regime

Uniaxial stress along [001] splits the degeneracy of the conduction-band carrier pockets into two sets: a pair of degenerate pockets at the X-points, and a single carrier pocket at the M-point. The electrical transport properties of Mg_2Si were computed for strains along [001], with perpendicular strains applied according to Poisson's ratio. This allowed the effect of uniaxial [001] stress to be calculated.

Figure 6.5 shows the conduction band structure of Mg_2Si under uniaxial stress along [001]. Increasing tensile stress raises the energy of the conduction-band carrier pockets at the M-point relative to those at the X-points. This causes an intervalley-transfer effect, redistributing electrons from the M-point carrier pocket to the two X-point pockets. The gradient of the conduction bands is steeper along X→P than M→Γ, showing that states near the X-point carrier pocket have higher average mobility along [001] than states near the M-point. Thus, redistribution of electrons will increase the conductivity along [001].

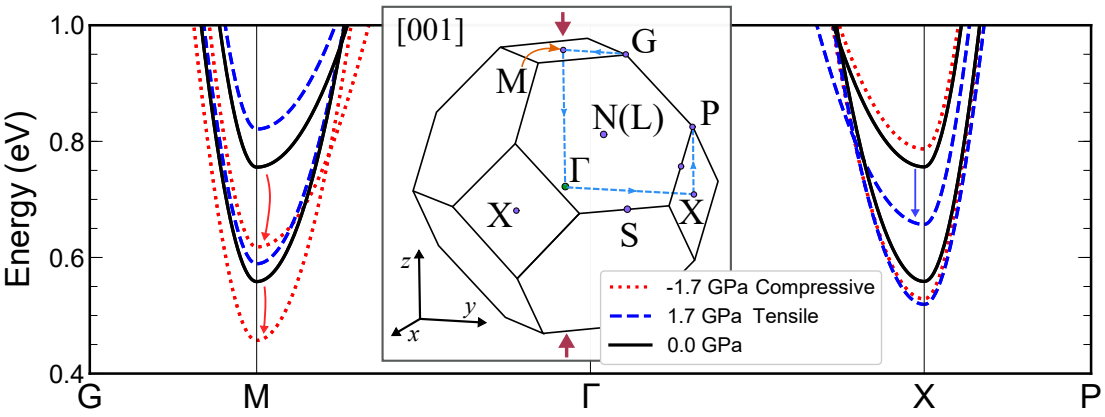

Figure 6.5 *Detail of the calculated conduction bandstructure of Mg_2Si under compressive (red dotted line) and tensile (blue dashed line) stress along [001]. These stresses correspond to -1.5% compressive and 1.5% tensile strain along [001], respectively. The black solid line shows the unstressed bandstructure. Arrows are guides to the eye. In each case, the zero point on the energy scale is the valence band maximum. Both compressive and tensile stress reduce the band gap. Inset: diagram of the Brillouin zone.*

Figure 6.6(a) shows this trend for $-1 \times 10^{19}\,\mathrm{cm}^{-3}$ n-doped Mg_2Si at 300 K. As tensile stress increases, the conductivity along [001] increases. Intervalley-transfer leads to an increase in the electron mobility along [001], which in turn increases the conductivity. Because the total number of carrier pockets is reducing, the

Seebeck coefficient decreases. Overall, there is a small increase in the power factor with increasing tensile stress.

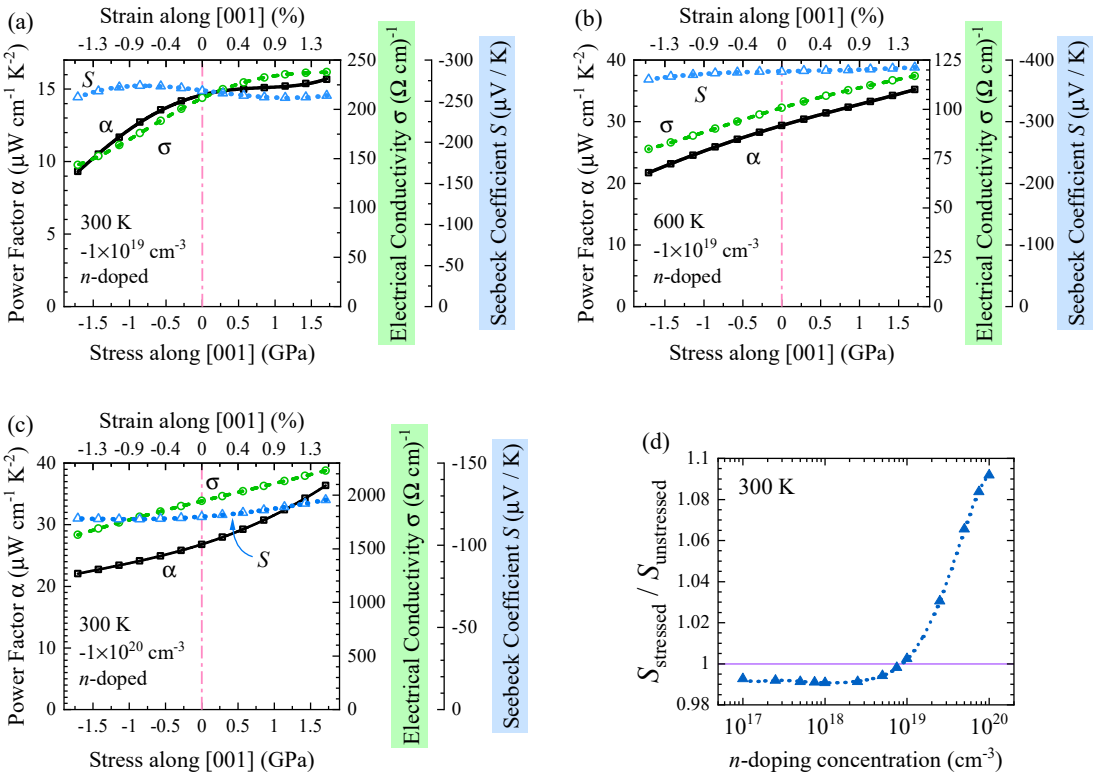

Figure 6.6 *Transport properties n-doped Mg_2Si, in the saturated regime, against uniaxial [001] stress according to Poisson's ratio for: (a) $-1 \times 10^{19}\,\mathrm{cm}^{-3}$ doping concentration at 300 K, (b) $-1 \times 10^{19}\,\mathrm{cm}^{-3}$ doping concentration at 600 K, and (c) $-1 \times 10^{20}\,\mathrm{cm}^{-3}$ doping concentration at 300 K. (d) Ratio between the Seebeck coefficient for 1.5% tensile-strained Mg_2Si and unstrained Mg_2Si at a variety of n-doping concentrations. All cases are in the saturated regime, with negligible intrinsic carrier concentrations. Symbols are calculated values, lines are guides to the eye.*

Figure 6.5 also shows that, at the X-point, increasing tensile [001] stress lowers the energy of the upper conduction band towards the lower conduction band. Converging multiple carrier pockets, such that the energy difference between their minima is only a few k_BT, generally improves the thermoelectric power factor [143]. At zero-strain, the energy difference between the lower and upper conduction bands of Mg_2Si is $\sim$0.2 eV [Fig. 6.3(a)]. The chemical potential for an n-doping concentration of $-1 \times 10^{19}\,\mathrm{cm}^{-3}$ at 300 K lies near the lower-conduction-band minimum [Fig. 6.3(b)]. Thus, at 300 K, the chemical potential is approximately $8k_BT$ below the upper conduction band — outside the energy range of importance for this temperature (Fig. 2.6). Because the upper conduction-band is many k_BT

away from the chemical potential, band convergence has little benefit for this doping-concentration and temperature.

In contrast, band convergence does have an effect at the higher temperature of 600 K. At this higher temperature, the chemical potential μ for unstressed $-1 \times 10^{19}\,\mathrm{cm}^{-3}$ n-doped Mg_2Si is $\sim$0.27 eV, $\sim 5.5 k_B T$, below the upper conduction band. Although the chemical potential is further below the upper conduction band at this temperature than at 300 K, it is fewer $k_B T$ below. The upper conduction band is now within the energy scale of importance for the Seebeck coefficient [Fig. 2.6(b)]. As a result, the Seebeck coefficient increases with increasing tensile stress.

Figure 6.6(b) shows that, for $-1 \times 10^{19}\,\mathrm{cm}^{-3}$ n-doped Mg_2Si at 600 K, the Seebeck coefficient along [001] remains almost constant with increasing tensile [001] stress. The convergence of the upper and lower conduction bands at the X-point is compensating for the loss of the carrier pocket at M. Concomitantly, intervalley-transfer of n-type electrons from the M-point carrier pocket to the X-point pockets increases the electrical conductivity along [001] [Fig. 6.6(b)]. As a result, 1% of tensile strain ($\sim$1.1 GPa) increases the power-factor along [001] by approximately 14 %. An overall trend was observed for every n-doping concentration: the higher the temperature, the greater the proportional increase in the power factor with tensile [001] stress.

At doping-concentrations of $\sim 10^{20}\,\mathrm{cm}^{-3}$, the chemical potential is much closer to the upper conduction band than it is at $\sim 10^{19}\,\mathrm{cm}^{-3}$ [Fig. 6.3(b)]. Because of this, in the saturated regime, there is greater proportional improvement in the power factor at high n-doping concentrations than at low doping-concentrations.

Figure 6.6(d) shows how the effect of band convergence becomes significant for high doping concentrations. For n-doping concentrations below approximately $-5 \times 10^{19}\,\mathrm{cm}^{-3}$, the Seebeck coefficient along [001] is always lower for stressed Mg_2Si than unstessed Mg_2Si. However, if the doping concentration is high enough that the chemical potential is within $\sim$0.15 eV, $6 k_B T_{300\,\mathrm{K}}$, of the upper conduction band [Fig. 6.3(b)] convergence of the two conduction bands under increasing tensile [001] stress improves the Seebeck coefficient.

The benefit of this can be seen for $-1 \times 10^{20}\,\mathrm{cm}^{-3}$ n-doped Mg_2Si at 300 K. 1 % of tensile strain ($\sim$1.1 GPa) increases the power factor along [001] by $\sim$20 % [Fig. 6.6(c)], whereas the increase for the lower doping concentration of $-1 \times 10^{19}\,\mathrm{cm}^{-3}$ was only 5 % [Fig. 6.6(a)].

In the saturated regime, the higher the temperature and the larger the n-doping

concentration, the greater the proportional increase of the power-factor along [001] with increasing tensile stress.

p-type Mg_2Si in the saturated regime

The valence band of Mg_2Si does not have strongly anisotropic features pointing in the [001] direction. As discussed in the Mg_2X background section, the low-curvature anisotropic shapes in the valence bandstructure of Mg_2Si point along Γ–L ([111]) and Γ–K ([110]), rather than along Γ–X ([001]). Thus, it was not expected that strain along [001] would improve the thermoelectric properties of Mg_2Si.

Indeed, bandstructure plots of Mg_2Si strained along [001] do not show deformations in the bandstructure that are likely to improve the thermoelectric properties. Figure 6.7(a) shows how the valence bandstructure of Mg_2Si changes under [001] strain. Both compressive and tensile strain lower the second and third valence-band maxima (vb2 and vb3) relative to the first valence band (vb1). Compressive strain increases the curvature of vb1 along [001] (Γ → M) but reduces the curvature of vb2 and vb3. In contrast to the effect [001] strain had on PbTe [Fig. 6.7(b)], the valley-reshaping of Mg_2Si under [001] strain is not clearly beneficial.

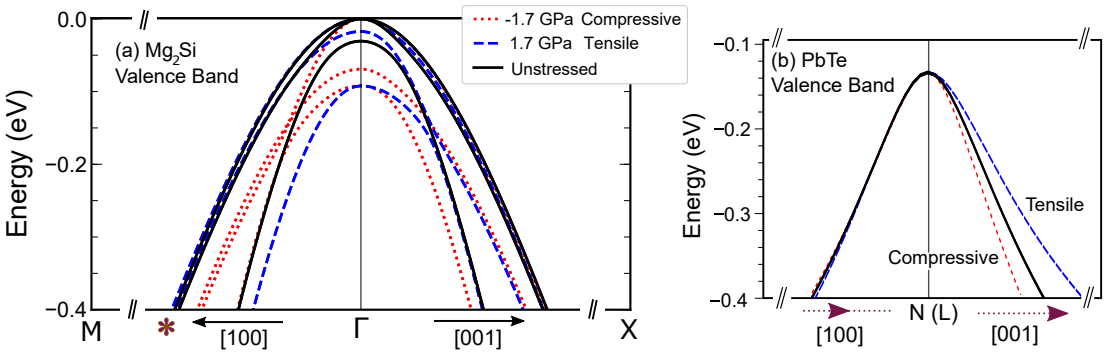

Figure 6.7 *(a) Detail of the valence bandstructure of Mg_2Si under uniaxial [001] stress. Compressive and tensile stress are plotted using red-dotted and blue-dashed lines, respectively. ±1.7 GPa compressive/tensile stress corresponds to a strain along [001] of ∓1.5 %. For a sense of scale, the asterisk ∗ is approximately 25% of the way between Γ and M. (b) Part of Fig. 4.14 shown for comparison, valence bandstructure of PbTe under compressive, unstressed, and tensile [001] stress (red-dotted / black-solid / blue-dashed lines, respectively)*

Figure 6.8 illustrates how the transport properties for *p*-type Mg_2Si in the saturated regime typically change under [001] strain. The electrical conductivity along [001] increases slightly with increasing compressive strain, but the Seebeck

coefficient decreases concomitantly. Overall, the power factor reduces both with increasing tensile and increasing compressive strain. Indeed, for all p-doping concentrations in the saturated regime, applying [001] strain did not improve the power factor parallel to, nor perpendicular to, [001]: the greatest power factor was for unstrained or near-unstrained p-type Mg_2Si.

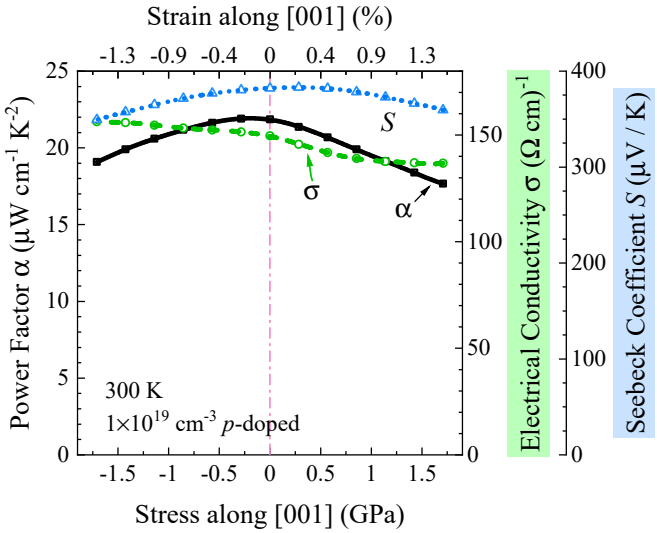

Figure 6.8 *Transport properties along [001] for $1 \times 10^{19}\,cm^{-3}$ p-doped Mg_2Si at 300 K under uniaxial [001] stress.*

Intrinsic Regime

In the intrinsic regime, the effect of strain on both conduction and valence bands is important. Strain along [001] simultaneously reshapes the valence band, and transfers conduction-band electrons between the M-point and X-point carrier pockets. This *simultaneous-valley-transfer-and-reshaping*, or *simultaneous-valley-transform* for short, can greatly improve the thermoelectric properties of Mg_2Si in the intrinsic regime.

Figure 6.9(a) shows how thermoelectric properties of $1 \times 10^{19}\,cm^{-3}$ p-doped Mg_2Si at 900 K changes under [001] strain. The electrical conductivity increases under both increasing compressive and increasing tensile strain. This is due to the increase in the intrinsic-carrier-concentration as the band gap closes (Fig. 6.5). Increasing compressive [001] strain increases the p-type Seebeck coefficient due to the reduction in the conduction-band conductivity, relative to that of the valence band (see the trends of σ shown in Fig. 6.6(a) & Fig. 6.8). As a result, a compressive [001] strain of 1 % increases the power-factor along [001] by ∼100 %.

Similarly, simultaneous-valley-transform can improve the power factor of n-type

Mg_2Si in the intrinsic regime. Figure 6.9(b) shows that, in this regime, increasing tensile strain can greatly increase both the Seebeck coefficient and the electrical conductivity of n-type Mg_2Si. In this case, 1 % of tensile strain increases the power-factor along [001] by ∼50 %.

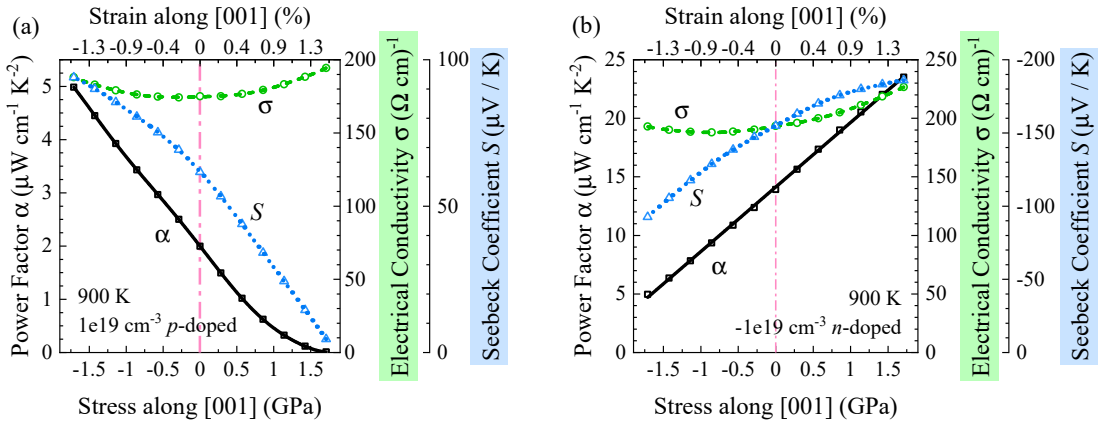

Figure 6.9 *Transport properties along [001] against strain along [001] for (a) $1 \times 10^{19}\,cm^{-3}$ p-doped, and (b) $-1 \times 10^{19}\,cm^{-3}$ n-doped Mg_2Si, respectively. The temperature is 900 K, and Mg_2Si is firmly in the intrinsic regime for both cases.*

Summary

For n-type Mg_2Si, increasing tensile [001] strain causes an *intervalley-transfer-effect*, transferring electrons into the high-[001]-mobility X-point carrier pockets. This consistently improves the thermoelectric power-factor along [001].

Increasing [001] strain also converges the upper and lower conduction bands at the X-point. The benefit of band convergence is more significant the higher the doping-concentration, and/or the higher the temperature.

Both compressive and tensile [001] strain reduce the power-factor along [001] of p-type Mg_2Si in the saturated regime.

Finally, when the concentration of intrinsic-charge-carriers is significant, strain along [001] leads to a *simultaneous-valley-transform* effect. Increasing compressive (tensile) strain greatly improves the power-factor along [001] of p-type (n-type) Mg_2Si.

6.1.5 Uniaxial Stress Along [111]

n-type Mg_2Si in the saturated regime

Strain was applied along and perpendicular to the body diagonal of Mg_2Si ([111]) according to Poisson's ratio, to mimic uniaxial [111] stress. This stress transforms the symmetry of Mg_2Si from face-centered cubic to *R-3m*. Stress along [111] preserves the degeneracy of the conduction-band carrier pockets. The X-point becomes renamed to the FB-point, but all three carrier-pockets remain degenerate by symmetry. However, stress along [111] can still warp the shapes of the carrier pockets.

The lower-conduction-band valleys of Mg_2Si have a cross shape, with flanges pointing along the FB→M_2 and FB→Q directions [Inset of Fig. 6.10(a)]. Uniaxial stress along [111] breaks the symmetry of these large anisotropic features, causing valley-reshaping.

Figure 6.10(a) shows how uniaxial stress along [111] alters the shape of the conduction-band edges. Tensile [111] stress increases the gradient of the lower conduction band along FB→M_2 and reduces the gradient along FB→Q. As FB→M_2 points approximately parallel to [111], this valley-reshaping increases electron mobility along [111]. Increasing tensile stress also reduces the gradient of the lower conduction band along FB→Q, which increases the rate of change of the density of states at the band edge. Increasing the rate of change of the density of states at the band edge generally increases the Seebeck coefficient [22,132]. Thus, tensile stress concomitantly increases the electrical conductivity and Seebeck coefficient along [111]. Figure 6.11(a) demonstrates this idea for $-1 \times 10^{19}\,\mathrm{cm}^{-3}$ n-doped Mg_2Si at room temperature. In this case, increasing tensile stress greatly increase the power-factor along [111]: with 1.1 GPa of tensile stress (1 % of strain) increasing the power factor by 60 %.

Compressive stress along [111] increases the gradient along FB→Q, leading to higher electron mobility perpendicular to [111] [Fig. 6.10(a)]. Figure 6.11(b) shows that increasing compressive stress improves the power factor perpendicular to [111] of n-type Mg_2Si, driven by an increase in the electrical conductivity.

Overall, stress along [111] causes valley-reshaping of the Mg_2Si conduction-band, which can increase the mobility of conduction-band electrons either parallel or perpendicular to the applied stress. For all combinations of n-doping concentration and temperature for which Mg_2Si is in the saturated regime,

increasing tensile (compressive) [111] stress improves the power factor parallel (perpendicular) to [111]. There is an incredibly strong relationship between the power factor and stress. This strongly indicates that the effect of the bandstructure on transport properties under stress will dominate over subtle changes in electron–phonon scattering times.

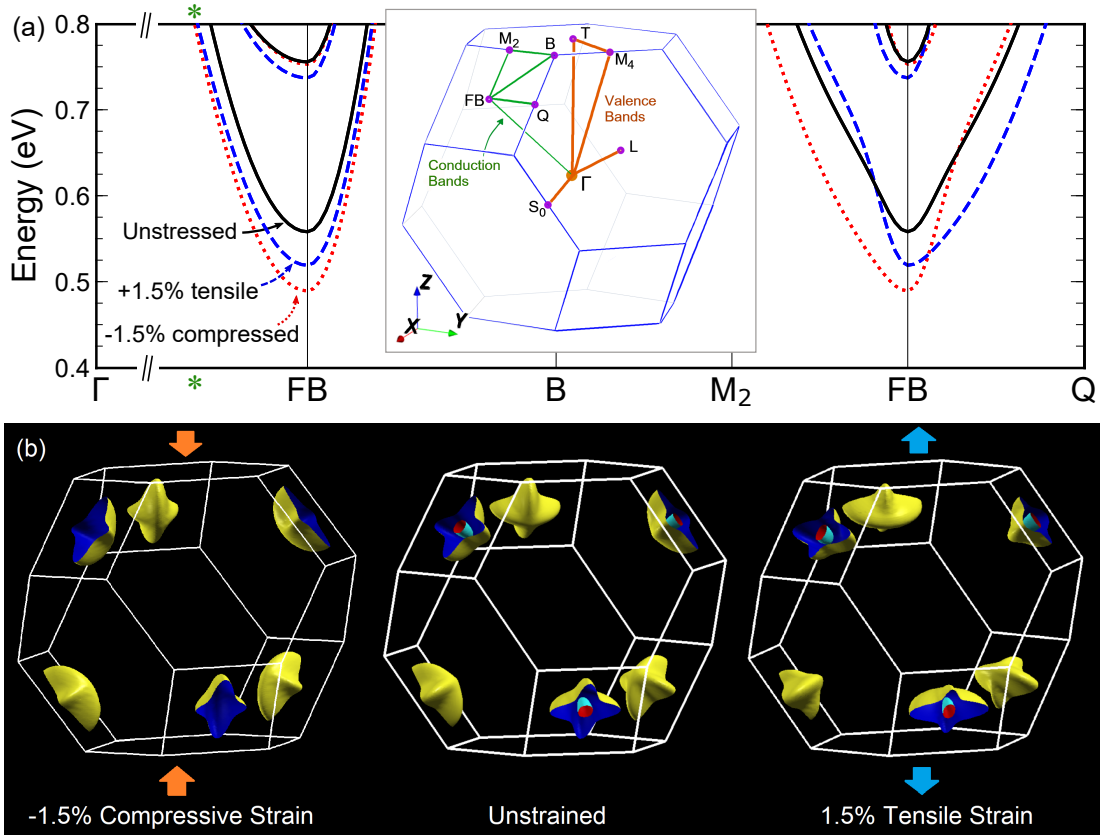

Figure 6.10 *(a) Conduction bandstructure of Mg_2Si under uniaxial [111] stress. Black is the unstrained bandstructure, blue dashed is for 1.5% tensile strain according to Poisson's ratio, equivalent to 1.6 GPa uniaxial [111] stress; the red dotted line is −1.5 % compressive strain, equivalent to −1.6 GPa stress along [111]. The asterisk ∗ is ∼20 % of the way between FB→Γ. Inset: a diagram of the Brillouin zone under this strain. (b) Energy isosurfaces for Mg_2Si strained along [111] according to Poisson's ratio. The isosurfaces are 250 meV above the conduction band minimum.*

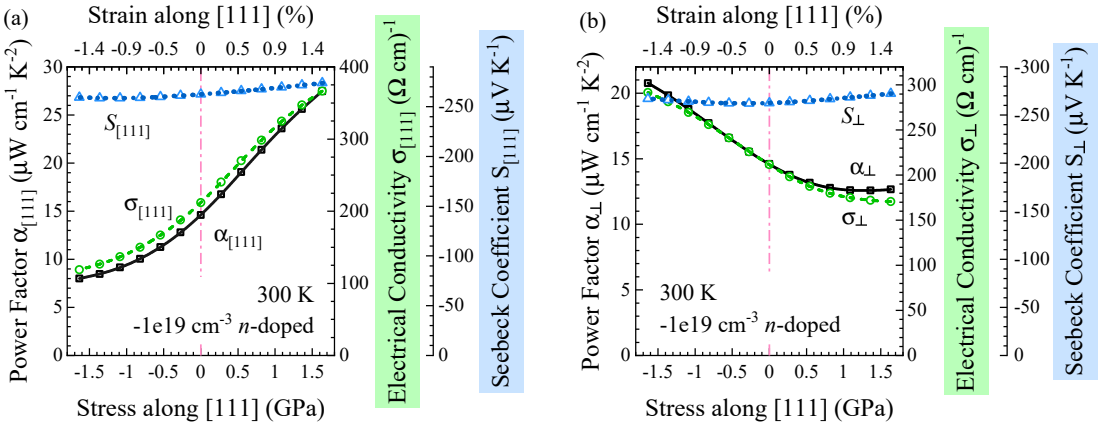

Figure 6.11 *Thermoelectric properties of -1×10^{19} cm^{-3} n-doped Mg_2Si at 300 K (a) parallel to and (b) perpendicular to [111], against uniaxial [111] stress. Symbols are calculated values, lines are guides to the eye.*

p-type Mg_2Si in the saturated regime

The Mg_2Si valence bands are highly anisotropic. As Fig. 6.12 shows, the Fermi-surfaces of the valence bands are not spherical. The first valence band (vb1) has much lower curvature along [110] than along [111] or [001]. The second valence-band (vb2) has much lower curvature along [111] than along [110] or [001]. Applying stress along [111] breaks the symmetry of these features of vb1 & vb2, which leads to a valley-reshaping-effect.

Figure 6.12(a) shows how the valence bands of Mg_2Si change under compressive [111] strain. Stress along [111] reshapes the valence bands, making the transport properties of *p*-type Mg_2Si anisotropic. The gradients of vb1 & vb2 along $\Gamma \rightarrow T$ and $\Gamma \rightarrow M_4$, which are related to the hole mobility along [111], are increased with increasing compressive [111] stress. Thus, the average mobility along [111] of valence-band holes is increased.

Figure 6.12(a) also shows that increasing compressive stress does not significantly change the gradient of the valence bands perpendicular to [111] ($\Gamma \rightarrow S_0$, and $\Gamma \rightarrow L$). As a result, the rate of change of the density of states decreases with increasing compressive stress, and thus reducing the Seebeck coefficient. Furthermore, increasing compressive stress lowers vb2 and vb3 relative to the upper valence band vb1, diverging the three valence-band maxima. This also causes the Seebeck coefficient to be reduced with increasing compressive stress.

Figure 6.13(a) quantifies this notion for *p*-doped Mg_2Si with an extrinsic concentration of $1 \times 10^{19}\,\mathrm{cm}^{-3}$ at $T = 300\,\mathrm{K}$. Increasing compressive stress along [111] increases the conductivity along [111] significantly, by reshaping the valence-band valleys [Fig. 6.12(a)]. The Seebeck coefficient along [111] decreases concomitantly. The change in the power factor is determined by the relative changes of the conductivity and Seebeck coefficient. For this combination of *p*-doping concentration and temperature, the power-factor along [111] increases with increasing compressive [111] stress. Applying $-1.1\,\mathrm{GPa}$ of compressive stress ($-1\,\%$ strain) leads to a $16\,\%$ increase in the power factor along [111].

Increasing tensile [111] stress reduces the gradients of vb2 and vb3 along $\Gamma \rightarrow L$ and $\Gamma \rightarrow S_0$, approximately perpendicular to [111]. Thus, tensile [111] stress increases the conductivity perpendicular to [111]. Figure 6.13(b) shows how uniaxial [111] stress affects the transport-properties perpendicular to [111] for $1 \times 10^{19}\,\mathrm{cm}^{-3}$ *p*-doped PbTe at 300 K. In this case, the electrical conductivity perpendicular to [111] increases with increasing tensile stress, and the Seebeck coefficient reduces:

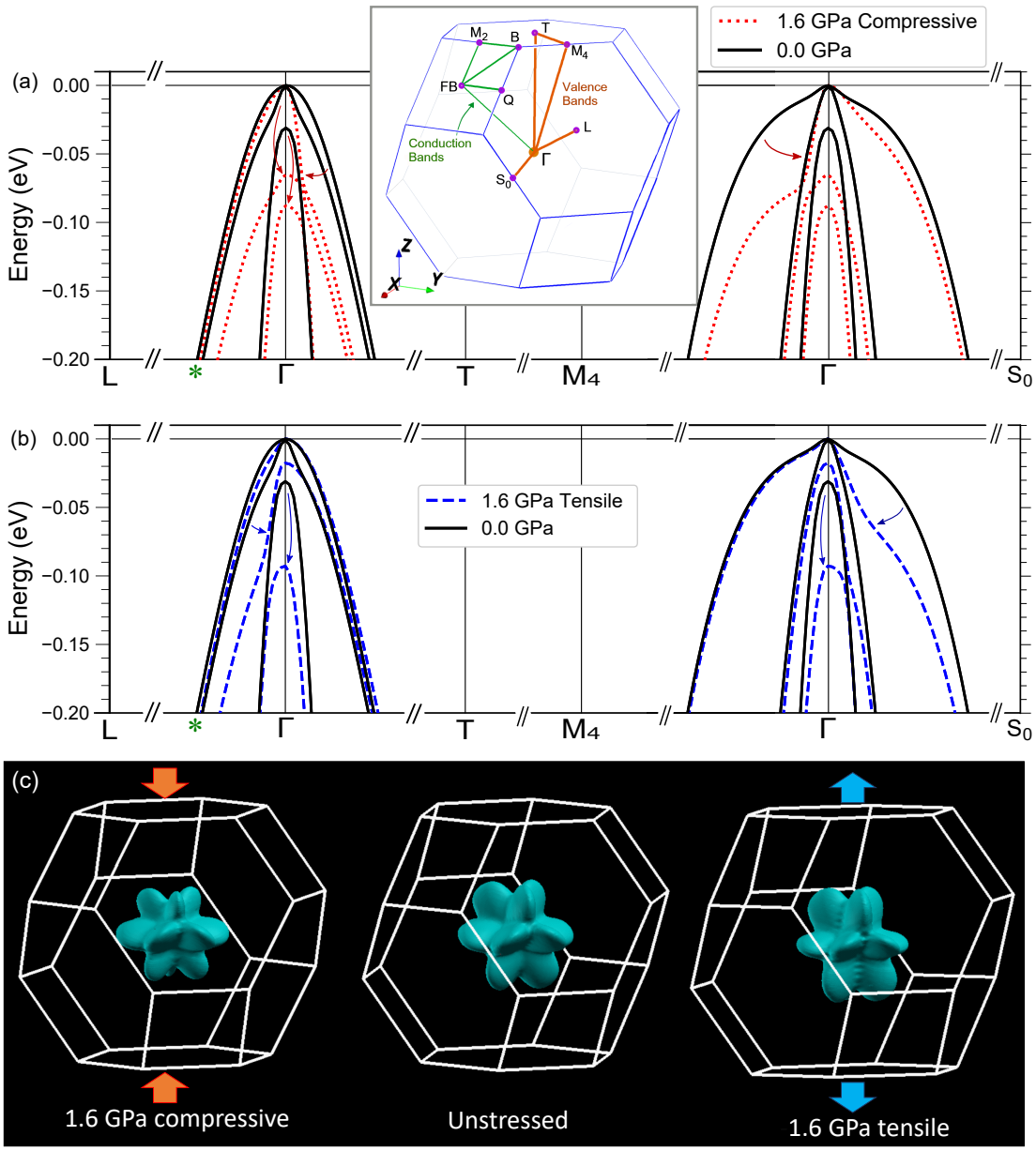

Figure 6.12 *Valence-band maxima for (a) unstressed (black) and uniaxially stressed [111] Mg_2Si (red-dotted), and (b) Mg_2Si under uniaxial [111] stress (blue-dashed). For a sense of scale: the asterisk $*$ is approximately 30% of the way from Γ to L. Arrows are a guide to the eye. (c) Energy isosurfaces for the first valence band (vb1) of Mg_2Si under uniaxial [111] stress. The isoenergy is set 0.2 eV below the valence-band maximum.*

mirroring the trends shown in Fig. 6.13(a). 1.1 GPa of tensile stress (1 % of tensile strain) increases the power factor by 6 %.

The qualitative trend in the power factor along [111] for *p*-doped Mg_2Si is dependent on the doping concentration. At relatively low doping concentrations [Fig. 6.13(c)] the improvement in the power factor is large: −1.1 GPa of

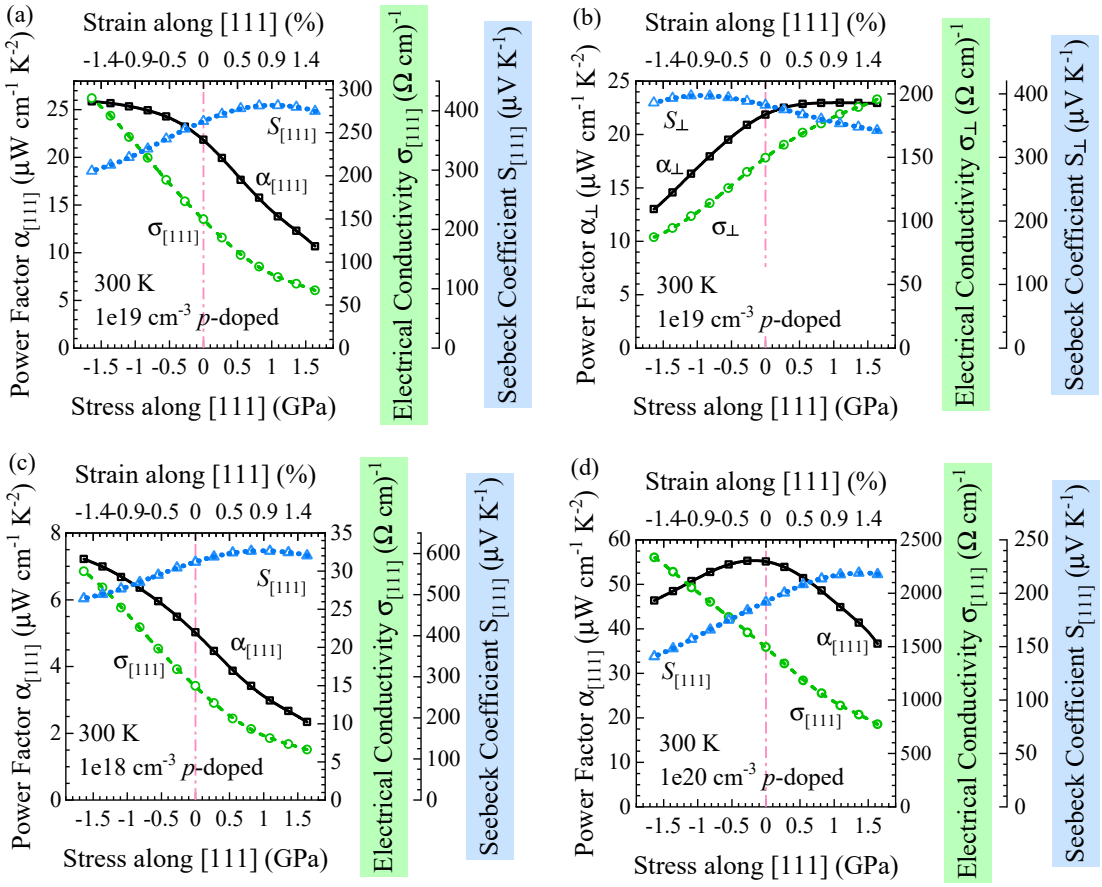

Figure 6.13 *Electrical-transport properties for p-doped Mg_2Si against uniaxial [111] stress. (a) Transport properties for a doping concentration of $1 \times 10^{19}\,cm^{-3}$ at 300 K along [111] and (b) perpendicular to [111]. Transport properties along [111] for (c) $1 \times 10^{18}\,cm^{-3}$ and (d) $1 \times 10^{20}\,cm^{-3}$ Mg_2Si at 300 K. Symbols show calculated values, solid lines are guides to the eye.*

compressive stress increases the power factor by ∼30 %. Indeed, for all doping concentrations below $\sim 5 \times 10^{19}\,\mathrm{cm}^{-3}$ the power factor along [111] increases with increasing compressive stress. However, if the *p*-doping concentration exceeds $\sim 5 \times 10^{19}\,\mathrm{cm}^{-3}$, then increasing compressive stress reduces the power factor.

vb3 is has a large curvature compared to vb1 and vb2, giving it high hole mobility on average. Increasing compressive [111] stress lowers vb3 relative to vb2 and vb1, redistributing holes from this high-mobility band to the lower-mobility vb1 and vb2. At low and intermediate *p*-doping concentrations, the chemical potential at 300 K lies above the valence-band maximum [Fig. 6.3(b)] and there are relatively few holes in vb3. As a result, the divergence of vb3 from vb2 and vb1 under [111] stress has relatively little effect. However, at *p*-doping concentrations, above $\sim 5 \times 10^{19}\,\mathrm{cm}^{-3}$, a significant proportion of holes are in the lowest valence band,

vb3. At these high doping concentrations, the divergence between vb3 and the other two valence bands under [111] stress reduces the Seebeck coefficient, and reduces the proportional increase of the conductivity. Overall, this results in a net decrease of the thermoelectric power factor with increasing compressive [111] stress.

Figure 6.13(d) shows the transport properties of $1 \times 10^{20}\,\mathrm{cm}^{-3}$ p-doped Mg_2Si at 300 K. As is the case at lower doping concentrations, increasing compressive stress increases the conductivity along [111] and concomitantly reduces the Seebeck coefficient. However, at this high p-doping concentration, the power factor reduces with increasing stress. This is likely because the relative importance of the lowest valence band, vb3, is different at high p-doping concentrations.

In summary, for Mg_2Si with low and intermediate p-doping concentrations, in the saturated regime, increasing compressive stress increases the power factor along [111]. At very high p-doping concentrations (exceeding $\sim 5 \times 10^{19}\,\mathrm{cm}^{-3}$) the largest power factor is for unstressed Mg_2Si.

Mg_2Si in the intrinsic regime

Whatever the doping concentration of Mg_2Si, the concentration of intrinsic carriers will be significant at sufficiently high temperatures. If the doping concentration is low ($\sim 1 \times 10^{17}\,\mathrm{cm}^{-3}$) then Mg_2Si will be in the intrinsic regime for temperatures at or exceeding $\sim$400 K; a higher doping concentration of $\sim 1 \times 10^{19}\,\mathrm{cm}^{-3}$ will only be in the intrinsic regime if the temperature is at or exceeds $\sim$700 K. However, in both cases the qualitative trends were the same. The key factor is that the concentration of intrinsic carriers is significant, and thus the changes of both the conduction and valence bands under stress must be considered.

In the intrinsic regime, *simultaneous-valley-transform* can increase both the Seebeck coefficient and the electrical conductivity. For example, increasing tensile stress increases the mobility along [111] of conduction-band electrons [Fig. 6.11(a)], and concomitantly decreases the mobility of valence-band holes [Fig. 6.13(a)]. As a result, in the intrinsic regime, this simultaneous transform of both conduction-band and valence-band valleys increases the Seebeck-coefficient along [111] for n-type Mg_2Si. Figure 6.14(a) quantifies this notion for $-1 \times 10^{19}\,\mathrm{cm}^{-3}$ n-doped Mg_2Si at 800 K. Increasing tensile stress along [111] increases both the conductivity and the Seebeck coefficient along [111], leading to a large increase in the power factor. Conversely, increasing compressive stress increases both the

Seebeck coefficient and conductivity along [111] of p-type Mg_2Si [Fig. 6.14(b)].

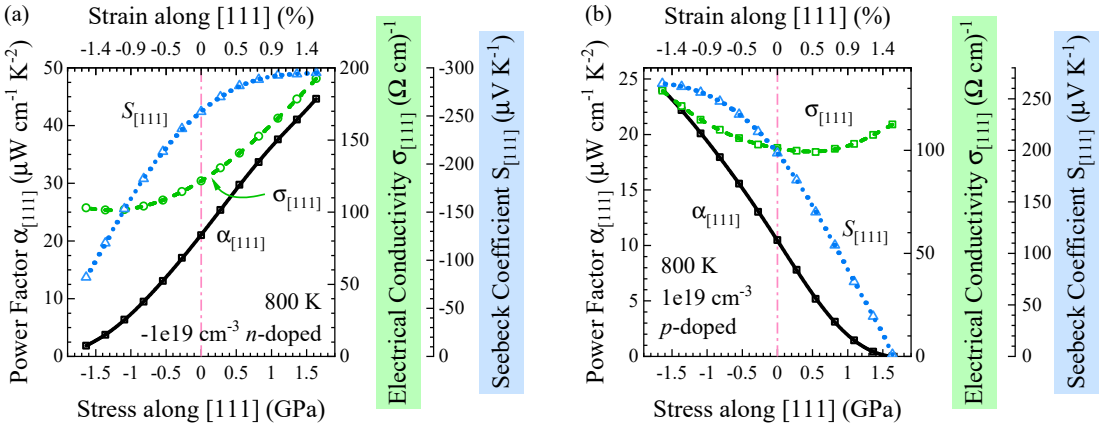

Figure 6.14 *Electrical-transport properties along [111] for Mg_2Si in the intrinsic regime under uniaxial [111] stress. The temperature is set to 800 K, and the doping concentration is (a) -1×10^{19} cm^{-3} n-doped, and (b) 1×10^{19} cm^{-3} p-doped.*

The improvement in the Seebeck coefficient seen at high temperatures is not because broadening of the Fermi-Dirac distribution is scattering electrons (holes) deeper into the conduction (valence) bands. Instead, it is specifically because the concentration of intrinsic carriers is significant at high temperatures. In the intrinsic regime, the *relative* mobility of conduction-band electrons and valence-band holes is important.

This can be demonstrated by artificially adjusting the band gap of Mg_2Si. The transport properties along [111] for stressed and unstressed n-Mg_2Si were calculated over a range of band gaps. The shapes of the conduction and valence bands were kept constant; only the band gap was adjusted. Figure 6.15(a) shows the Seebeck coefficient along [111] for stressed and unstressed -1.0×10^{19} cm^{-3} n-doped Mg_2Si as a function of band gap. When the band gap is set to be much larger than k_BT, the intrinsic carrier concentration is suppressed and the doping concentration dominates. In this saturated regime, the Seebeck coefficient of unstrained Mg_2Si is slightly greater than for strained Mg_2Si. Furthermore, in this regime the Seebeck coefficient is independent of the band gap.

As the band gap closes, the concentration of intrinsic carriers increases [Fig. 6.15(b)]. At the onset of the intrinsic regime, the Seebeck coefficient for both stressed and unstressed n-type Mg_2Si decreases with decreasing band gap. However, when the intrinsic carrier concentration is significant (when the band gap is less than 0.4 eV), the Seebeck coefficient for stressed Mg_2Si exceeds the Seebeck coefficient at zero stress. By adjusting the relative mobilities of the

conduction and valence bands, increasing tensile stress along [111] makes intrinsic electrons contribute more to the Seebeck coefficient than intrinsic holes. Thus, simultaneous-valley-transform can increase both the Seebeck coefficient and the conductivity along [111] of n-type Mg_2Si in the intrinsic regime.

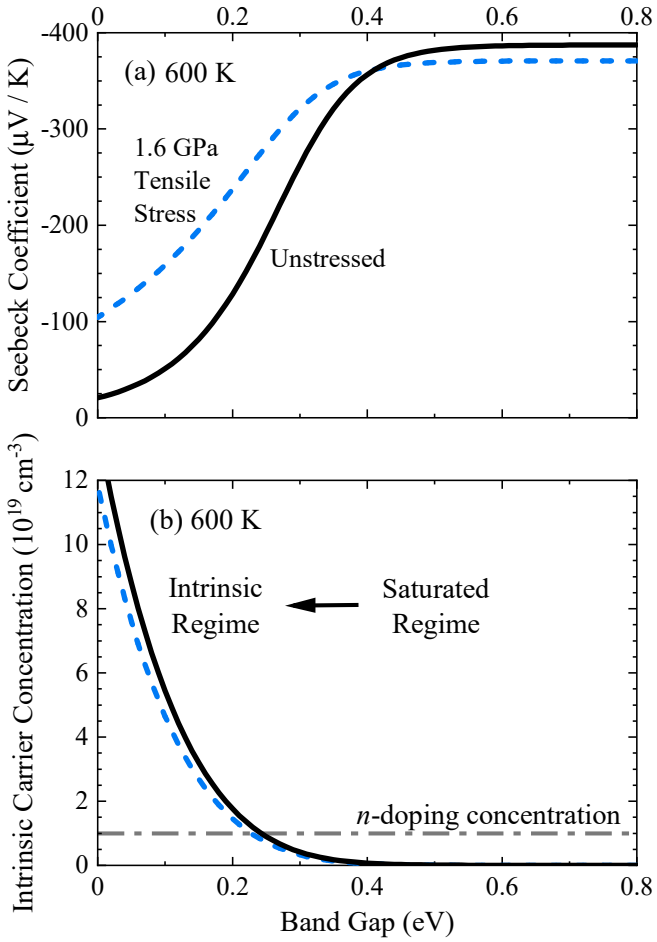

Figure 6.15 *(a) Seebeck coefficient along [111] and (b) intrinsic carrier concentration for stressed and unstressed $-1 \times 10^{19}\,cm^{-3}$ n-doped Mg_2Si at 600 K as a function of the set band gap. The true band gaps for stressed and unstressed Mg_2Si at 600 K are 0.46 and 0.50 eV, respectively. Ordinarily, for this combination of doping concentration and temperature, Mg_2Si is in the saturated regime.*

Summary

Uniaxial stress along [111] does not remove the degeneracy of the conduction-band carrier pockets at the X-points. Instead, because the lower-conduction-band valley has large anisotropic features that extend away from the X-point, stress along [111] induces a valley-reshaping effect. Increasing tensile (compressive) [111] stress thus increases the power factor along (perpendicular to) [111] for n-doped Mg_2Si.

Stress along [111] reshapes the valence bands of Mg_2Si. For p-type Mg_2Si in the saturated regime, increasing compressive (tensile) stress along [111] increases the conductivity along (perpendicular to) [111], and concomitantly reduces the Seebeck coefficient. This increases the power factor for low and intermediate p-doping concentrations. At very high p-doping concentrations, exceeding $5 \times 10^{19}\,\mathrm{cm}^{-3}$, the largest power factor is for unstressed Mg_2Si.

In the intrinsic regime, simultaneous-valley-transform under uniaxial [111] stress allows both the Seebeck coefficient and conductivity to be concomitantly improved. In this regime, increasing compressive (tensile) stress greatly improves the power factor along [111] of p-type (n-type) Mg_2Si.

6.1.6 Uniaxial Stress Along [110]

n-type Mg_2Si in the saturated regime

Uniaxial stress along [110] transforms the symmetry of Mg_2Si from face-centered cubic to *Immm*. This stress breaks the symmetry of the conduction-band carrier pockets into two sets: a pair of carrier pockets at the T-points, and a single carrier pocket at the X-point. Increasing tensile [110] stress lowers the energy of the X-point carrier pocket relative to the T-point pockets, and also reshapes the X-point valley. Figure 6.16 shows how, under tensile stress, the gradient of the lower conduction band along X→F_2 increases. Furthermore, the lower-conduction-band minimum at X is reduced relative to the minimum at T, which causes intervalley transfer. Thus, increasing tensile stress increases the conductivity along [110]. Notably, there is no significant reshaping of the T-point valley.

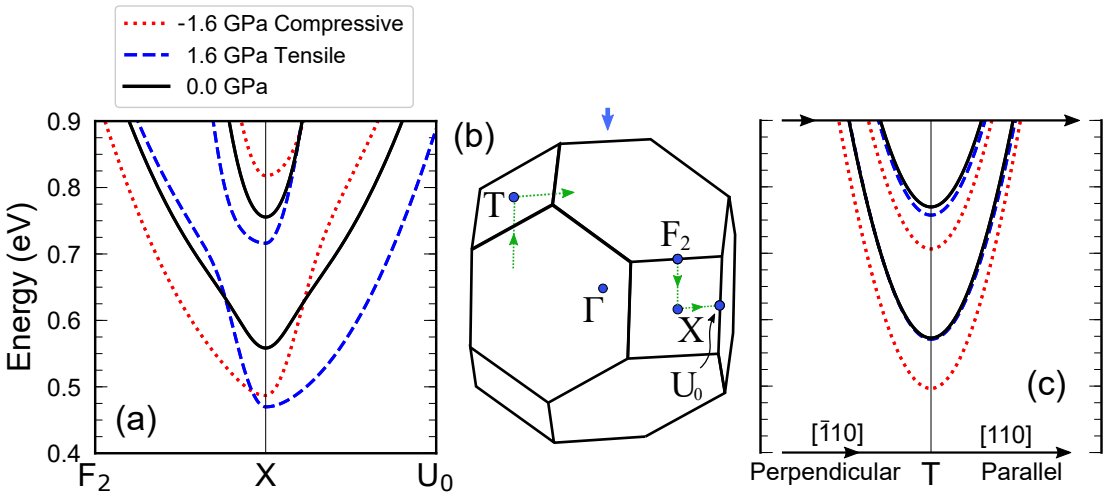

Figure 6.16 *Conduction-band valleys of Mg_2Si under −1.6 GPa compressive-uniaxial-stress along [110] (red-dotted line), −1.6 GPa tensile stress (blue-dashed line), and zero stress (black-solid line). 1.6 GPa is equivalent to a strain of ∼1.5 %. (a) Conduction-band valley at X; (b) diagram of selected special points in the Brillouin zone of [110] stressed Mg_2Si; (c) conduction-band valley at T perpendicular and parallel to [110]. Figures (a) and (c) are drawn to the same scale. The energy of the valence band maximum is set to 0 eV.*

Figure 6.17(a) shows how stress along [110] affects the transport properties parallel to [110] for $-1 \times 10^{19}\,\mathrm{cm}^{-3}$ n-doped Mg_2Si. Increasing tensile stress increases the conductivity along [110], due to reshaping of the X-point carrier pocket, and intervalley-transfer from T to X. The Seebeck coefficient is concomitantly reduced because the X-point and T-point valleys are diverging in energy. Despite this,

the power-factor along [110] increases with increasing tensile stress.

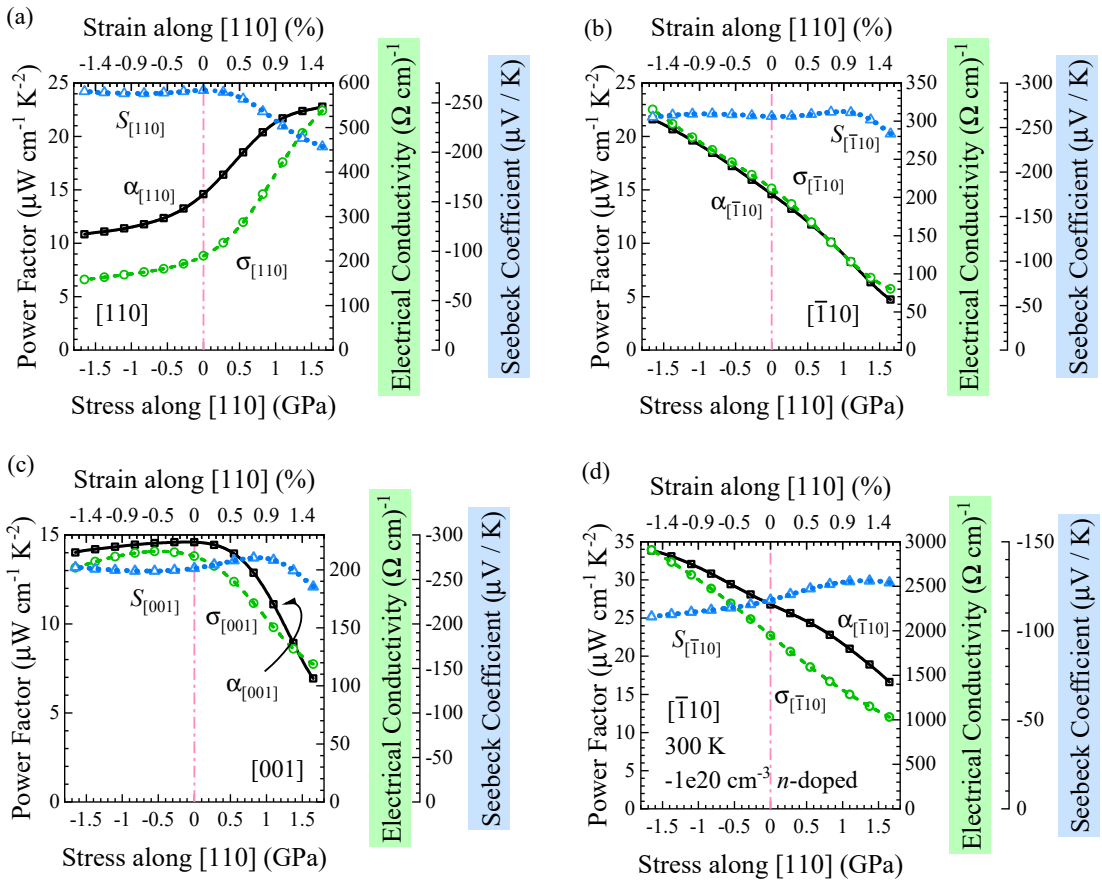

Figure 6.17 *Transport properties of n-type Mg_2Si at 300 K under stress along [110]. (a) Transport properties along [110] of -1×10^{19} cm^{-3} n-doped Mg_2Si; (b) Transport properties along [$\bar{1}$10] of -1×10^{19} cm^{-3} n-doped Mg_2Si; (c) Transport properties along [001] of -1×10^{19} cm^{-3} n-doped Mg_2Si; (d) Transport properties along [$\bar{1}$10] of -1×10^{20} cm^{-3} n-doped Mg_2Si. Symbols are calculated values, lines are guides to the eye.*

Increasing compressive stress along [110] reduces the gradient of the lower conduction band at X along [$\bar{1}$10], perpendicular to the applied stress [Fig. 6.16(a)]. The energy of the X- and T-point valleys are also reduced by the same amount, meaning there is no intervalley-transfer under compressive stress. Because there is little intervalley-transfer, the Seebeck coefficient remains similar under increasing compressive [110] stress. Concomitantly, reshaping of the X-point valley increases the conductivity along [$\bar{1}$10]. Figure 6.17(b) quantifies this notion for n-doped Mg_2Si at 300 K with a doping concentration of -1×10^{19} cm^{-3}. The power factor along [$\bar{1}$10] increases with increasing compressive [110] stress.

However, increasing compressive stress does diverge the lower and upper conduction-

bands at X [Fig. 6.16(a)]. At high doping concentrations ($\sim -1 \times 10^{20}\,\mathrm{cm}^{-3}$ and above), when the upper conduction-band is within a few k_BT of the chemical potential [sec. 2.2.3, Fig. 6.3(a)] this divergence causes the Seebeck coefficient to decrease with increasing compressive stress. Figure 6.17(d) demonstrates this effect for $-1 \times 10^{20}\,\mathrm{cm}^{-3}$ n-doped Mg_2Si at 300 K. At this high doping concentration, the Seebeck coefficient decreases under increasing compressive stress, but the power-factor still increases overall.

Electrical-transport properties along [001] exhibit different trends under [110] stress than do the transport properties along [110] or [$\bar{1}$10]. The reshaping of the carrier pockets does not significantly affect conduction-band electron transport along [001]. The dominant mechanism is intervalley transfer between the X and T-point carrier pockets. Figure 6.18 shows the conduction-band edge of Mg_2Si under [110] stress. There are two valleys at the T-point, and a single valley at X. For the lower conduction band, the mobility along [001] is much lower for the X-point valley than for the T-point valleys. This can be seen by comparing the gradient of the band along X–Γ to the gradient along T–W, both of which run parallel to [001].

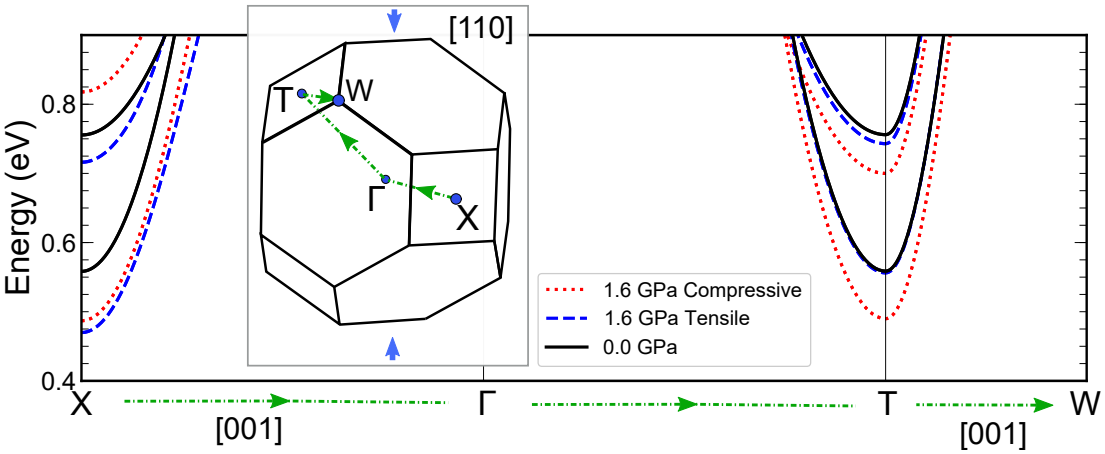

Figure 6.18 *Calculated conduction-band edges of Mg_2Si under uniaxial [110] stress. 0 eV on the energy scale is the valence band maximum. Insert: diagram of special points in the Brillouin-zone. The X–Γ and T–W lines are parallel to [001].*

Increasing tensile stress causes conduction-band electrons to be redistributed from the T-point valleys, to the single low-[001]-mobility X-point valley. As a result, the conductivity along [001] is significantly decreased. Conversely, increasing compressive stress keeps the relative energies of the conduction-band minima at X and T approximately equal. Thus, increasing compressive stress keeps the conductivity along [001] approximately constant. Figure 6.17(c) quantifies this

notion. Increasing compressive stress keeps the conductivity along [001] similar, but increasing tensile stress significantly reduces the conductivity along [001]: and thus reduces the power factor as well.

Across all combinations of doping concentration and temperatures examined for which Mg_2Si is in the saturated regime, increasing tensile stress consistently improved the power-factor along [110], and increasing compressive stress improved the power-factor along $[\bar{1}10]$. Conversely, the power-factor along [001] was consistently highest for unstressed Mg_2Si.

p-type Mg_2Si in the saturated regime

Uniaxial stress along [110] reshapes the valence band of Mg_2Si in a fashion similar to that seen under [111] stress. Increasing compressive stress reduces the gradient of the first valence band (vb1) along [110], and keeps the gradient along $[\bar{1}10]$ similar (Fig. 6.19). As a result, increasing compressive (tensile) stress increases the conductivity of *p*-type Mg_2Si along [110] ($[\bar{1}10]$).

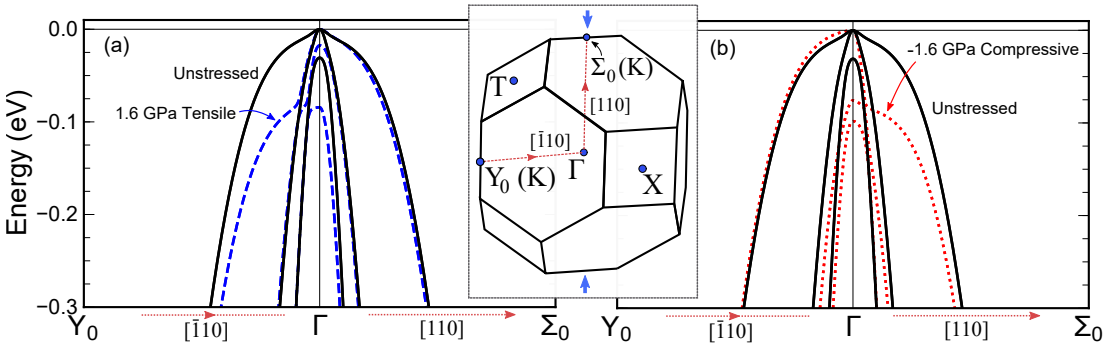

Figure 6.19 *Valence-band edge of Mg_2Si under (a) tensile and (b) compressive uniaxial stress along [110].*

However, both compressive and tensile stress lower the energy of vb2 and vb3 relative to the valence-band maximum. Such divergence of the bands under stress reduces the Seebeck coefficient, especially at high doping concentrations when there is a significant portion of the valence-band holes in these valence bands (Fig. 6.3).

Figure 6.20(a) quantifies this notion for $1 \times 10^{18}\,\mathrm{cm}^{-3}$ *p*-doped Mg_2Si at 300 K. Increasing compressive [110] stress improves the conductivity, but concomitantly reduces the Seebeck coefficient. At this low doping concentration, there is a net increase in the power factor along [110] with increasing compressive stress. However, at the high doping concentration of $1 \times 10^{20}\,\mathrm{cm}^{-3}$ [Fig. 6.20(c)] the power factor decreases with increasing stress.

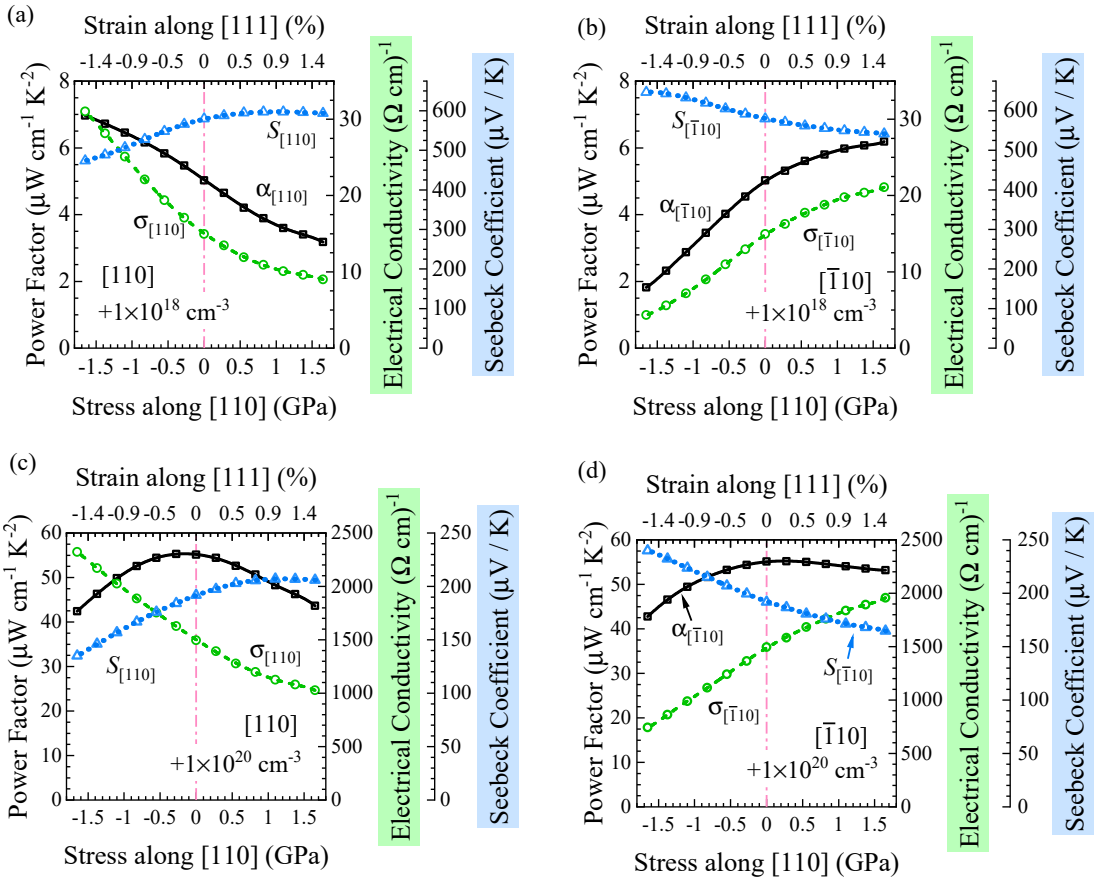

Figure 6.20 *Transport properties of p-type Mg_2Si at 300 K against uniaxial [110] stress. (a) transport properties along [110] of 1×10^{18} cm^{-3} p-doped Mg_2Si, (b) transport properties along [$\bar{1}$10] for a p-doping concentration of 1×10^{18} cm^{-3}, (c) transport along [110] for 1×10^{20} cm^{-3} p-doped Mg_2Si, (d) transport properties along [$\bar{1}$10] for a p-doping concentration of Mg_2Si. Symbols are calculated values, lines are guides to the eye.*

A similar trend is observed under increasing tensile stress. Tensile stress reduces the gradient along [$\bar{1}$10] of the first valence band (Fig. 6.19), and causes the lowest valence band (vb3) to lower in energy. As a result, the conductivity along [$\bar{1}$10] increases with increasing tensile stress, and the Seebeck coefficient is concomitantly reduced. At low and intermediate doping concentrations, this leads to an increase in the power factor along [$\bar{1}$10] [Fig. 6.20(b)]. Conversely, at doping concentrations of 5×10^{19} cm^{-3} and above, the power factor along [$\bar{1}$10] is greatest for unstressed Mg_2Si [Fig. 6.20(d)].

The transport properties along [001] must be examined separately. Figure 6.21 shows that, under uniaxial [110] stress, valence band edges of Mg_2Si are only marginally perturbed. Under compressive stress, there is a significant reduction in

the second-valence band maximum. This results in a larger proportion of valence-band holes being in the first valence band, rather than the lower two. Because the first valence band has a slightly lower curvature along [001] than the second or third valence bands, increasing compressive stress reduces the conductivity along [001] of p-doped Mg_2Si in the saturated regime.

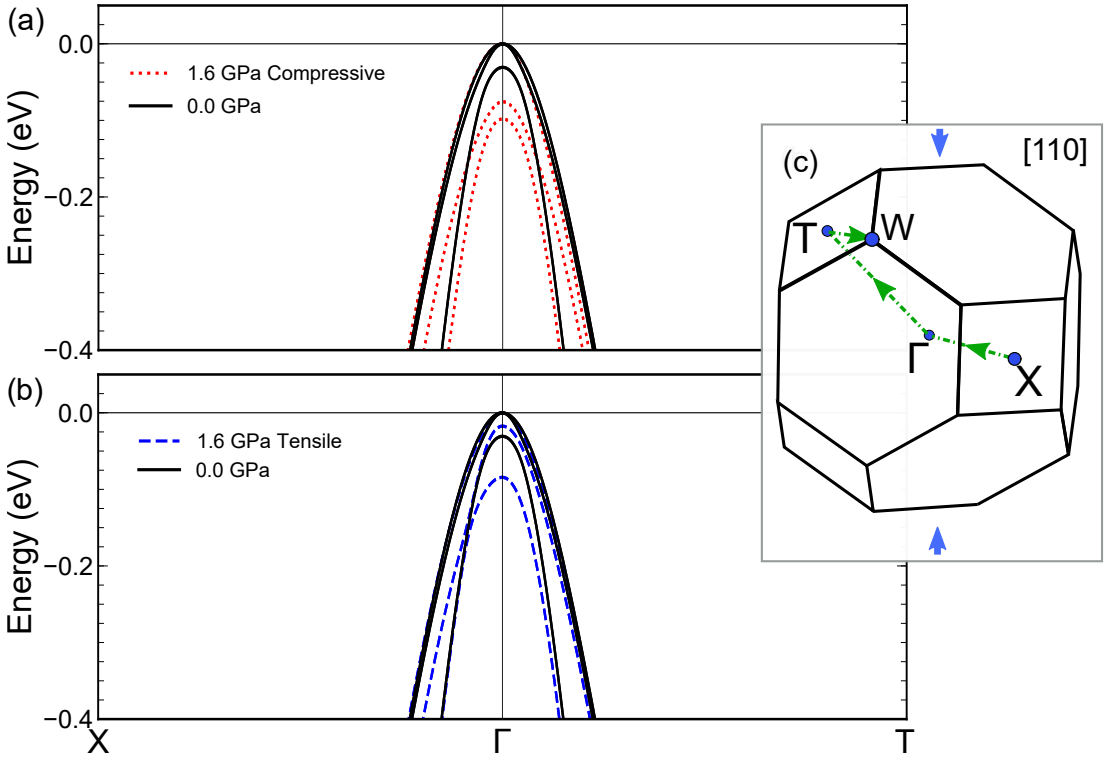

Figure 6.21 *Calculated valence-band edge of Mg_2Si under uniaxial [110] stress. Insert: diagram of special points in the Brillouin-zone. The Γ–X line is parallel to [001].*

Figure 6.22 quantifies this notion for $1 \times 10^{20}\,\mathrm{cm}^{-3}$ p-doped Mg_2Si. Increasing compressive stress reduces the conductivity along [001], and thus reduces the power factor. Increasing tensile stress also reduces the power factor, but this time because the Seebeck coefficient along [001] is suppressed. Tensile stress increases the curvature along [001] of the second valence band [see the Γ–X line in Fig. 6.21(b)], which slightly increases the conductivity along [001]. However, the third valence band is reduced in energy. This band divergence reduces the Seebeck coefficient, resulting in a reduction of the power factor.

Overall, for low and intermediate doping concentrations, at all temperatures for which Mg_2Si is in the saturated regime, the power factor along [110] ([$\bar{1}$10]) consistently increases with increasing compressive (tensile) uniaxial stress along [110]. The power factor along [001] was consistently greatest for unstressed Mg_2Si.

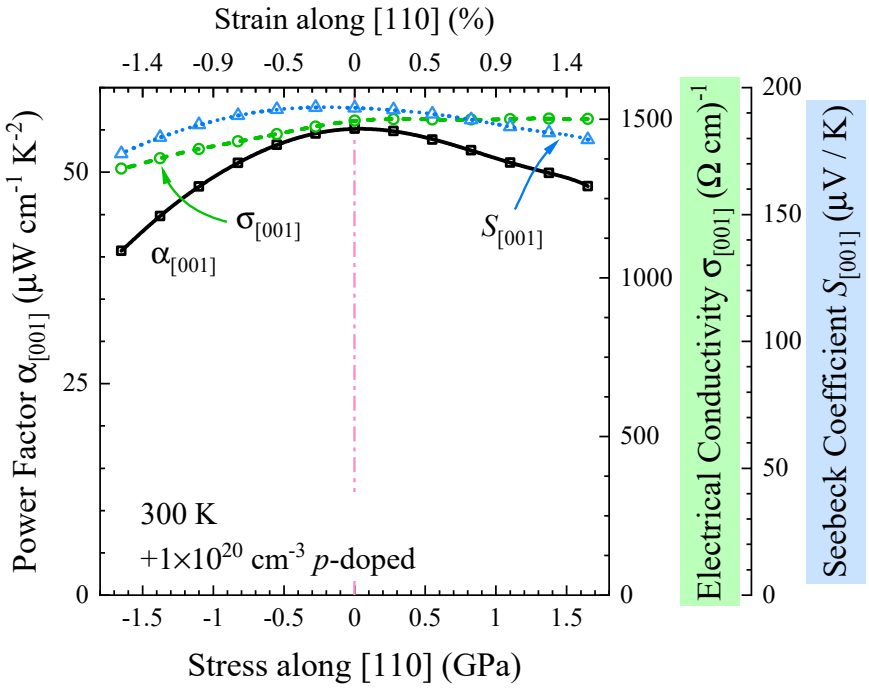

Figure 6.22 *Calculated electron-transport properties along [001] for* $1 \times 10^{20}\ cm^{-3}$ *p-doped* Mg_2Si *at 300 K.*

The Intrinsic Regime

As was the case with other directions of stress, in the intrinsic regime the Seebeck coefficient and electrical conductivity can be concomitantly increased. Figure 6.23(a) demonstrates this notion for $1 \times 10^{18}\,\mathrm{cm}^{-3}$ p-doped Mg_2Si at 800 K. For this combination of doping concentration and temperature, Mg_2Si is in the intrinsic regime. Increasing compressive [110] stress causes the simultaneous transform of the valence and conduction bands, increasing the mobility along [110] of valence-band holes relative to that of conduction-band electrons. Consequently, the Seebeck coefficient [110] is increased in addition to the conductivity: greatly increasing the power factor. Similarly, increasing tensile [110] stress greatly improves the power factor along [110] of n-type Mg_2Si [Fig. 6.23(b)].

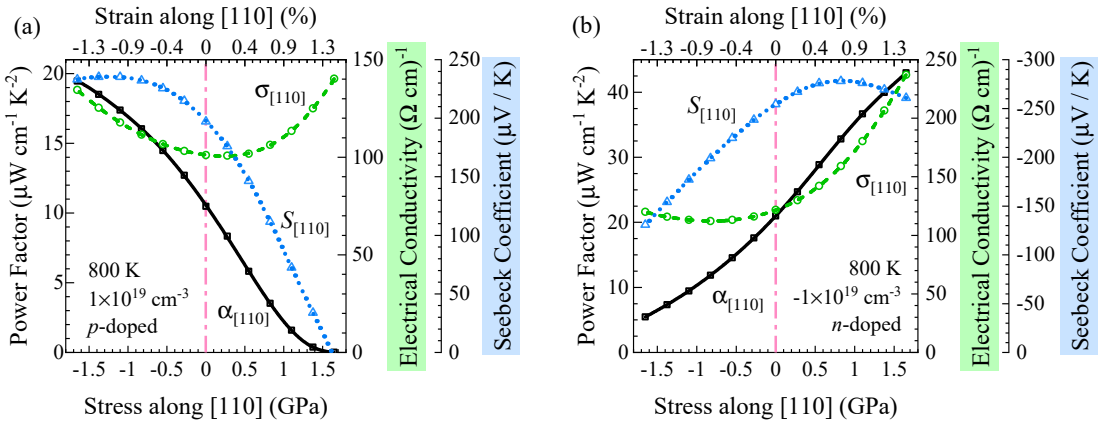

Figure 6.23 *Transport properties along [110] under uniaxial [110] stress for Mg_2Si at 800 K with doping concentrations of (a) $1 \times 10^{19}\,cm^{-3}$ and (b) $-1 \times 10^{19}\,cm^{-3}$, respectively. Symbols are calculated values, lines are guides to the eye.*

Summary

In summary, for the majority of combinations of doping concentration and temperature, increasing compressive (tensile) [110] stress improves the power factor along [110] of p-doped (n-doped) Mg_2Si. Furthermore, increasing tensile (compressive) stress also improves the power factor along $[\bar{1}10]$, perpendicular to [110], for p-doped (n-doped) Mg_2Si.

The key exception is p-type Mg_2Si in the saturated regime with intermediate or high doping concentrations ($10^{19}\,\mathrm{cm}^{-3}$ and above), for which the greatest power factor is for Mg_2Si with no stress along [110].

6.2 Mg_2Sn

6.2.1 Electronic Structure of Mg_2Sn

Figure 6.24 shows the calculated bandstructure of Mg_2Sn. Unsurprisingly, as Si and Sn are in the same group of the periodic table, there are many similarities between the bandstructures of Mg_2Sn and Mg_2Si:

- they both have two conduction bands that are relevant for electrical transport: one upper and one lower, with minima at the X-point;
- each individual the lower-conduction-band valley has lower average mobility along X–Γ than perpendicular to it. This can be seen from the bandstructure (Figs. 6.24 & 5.2), which has lower curvature at the minima along X–Γ than along X–W or X–U.
- there are three valence bands with maxima at Γ: VB1, VB2, and VB3. The first valence band, VB1, has a much lower gradient along Γ–K and Γ–L compared to that along Γ–X.

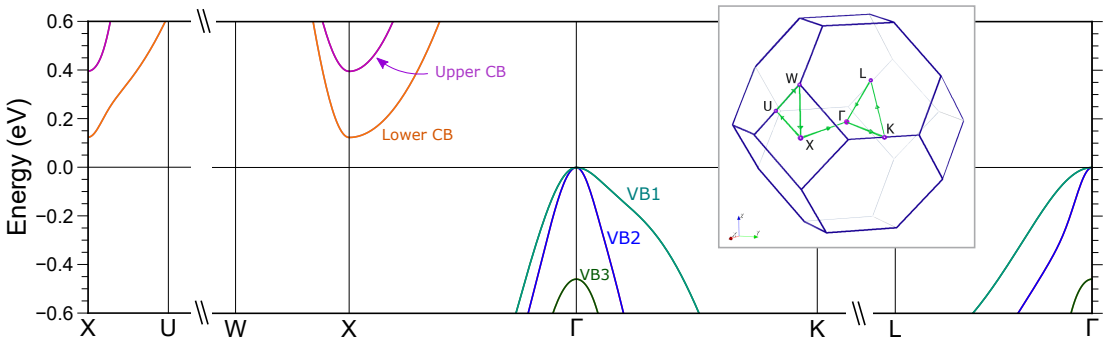

Figure 6.24 *The bandstructure of Mg_2Sn. The band gap has not been adjusted. Labelled are the upper and lower conduction bands, along with valence band 1, 2, and 3. Insert: a diagram of the FCC Brillouin zone with special points labelled*[130].

However, there are three notable differences between the electronic bandstructures of Mg_2Sn (Fig. 6.24) and Mg_2Si (Figs. 5.1 & 5.3)):

(i) The band gap of Mg_2Sn is much smaller than that of Mg_2Si. The band gap of Mg_2Si at 300 K is approximately 0.6 eV, whereas the band gap of Mg_2Sn is ∼0.1 eV. Furthermore, extrapolating the band gap vs temperature data from Lipson & Kahan[172] to temperatures above 300 K indicates that the band gap of Mg_2Sn closes at ∼600 K. The narrow band gap of Mg_2Sn means that, for a set

doping concentration, the intrinsic regime of Mg_2Sn will begin at a much lower temperature than it would for Mg_2Si.

(ii) For Mg_2Sn, the energy of the third-valence-band maximum, VB3, is over 0.4 eV below the maximum of VB1. The splitting between the third valence band and the upper two at Γ is caused by spin-orbit coupling. Because Si is a (relatively) light atom, the spin-orbit splitting is small: ∼0.04 eV. In Mg_2Sn, the heavier Sn atom causes a much larger spin-orbit splitting. Indeed, if the effect of spin-orbit coupling is not included in the calculations, the splitting between the three valence bands at Γ disappears. As a result, the transport properties of Mg_2Sn are dominated by holes in the first two valence bands, with the third only becoming important at very high *p*-doped concentrations and/or very high temperatures. In contrast, all three valence bands VB1–3 contributed to hole-transport for Mg_2Si.

(iii) The shape of the second valence band, VB2, is different for Mg_2Sn. In Mg_2Si, VB2 had a much lower gradient along Γ–L that it did along other directions, which made energy the isosurface of this band look like a stellated octahedron [Fig. 5.3(b)]. In Mg_2Sn, VB2 does not have this feature. Overall, VB2 in Mg_2Sn much more isotropic (Figs. 6.24 & 6.25). Thus, our *rules of thumb* suggest this band will be not be improved as much by any particular direction of stress. In particular, this suggests that stress along [111] will not affect *p*-type Mg_2Sn as much as *p*-type Mg_2Si.

Although the bandstructures of Mg_2Si and Mg_2Sn are similar in many ways, the differences outlined above will help explain some of the differences we see in how their transport properties respond to non-hydrostatic stress.

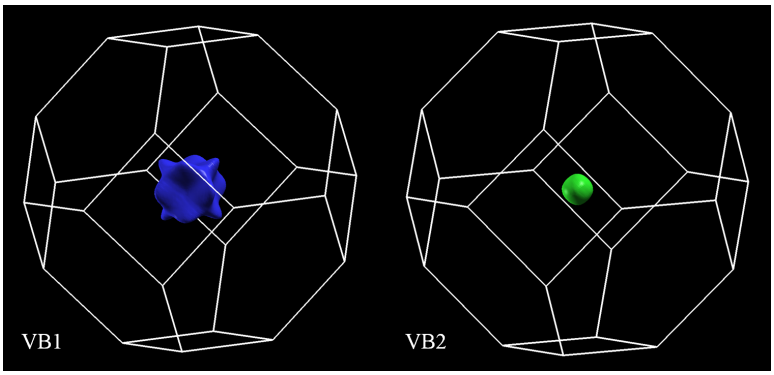

Figure 6.25 *Energy isosurfaces of the Mg_2Sn valence bands: VB1 (left); and VB2 (right). Both isosurfaces are 0.2 eV below the valence-band maximum of VB1. The third valence band (VB3) is not shown as its maximum is* ∼0.4 eV *below the global valence-band maximum.*

6.2.2 Experimental Comparison

To compare calculated results for the electrical conductivity of Mg_2Si with experimental data, the electron-scattering time must be estimated. Figure 6.26(a) shows that a scattering time $\tau = 0.75 \times 10^{-14}$ s at 300 K gives excellent agreement with experiment for n-type Mg_2Sn. The scattering time is held constant for all strains; it is only important for numerical comparison with experiment.

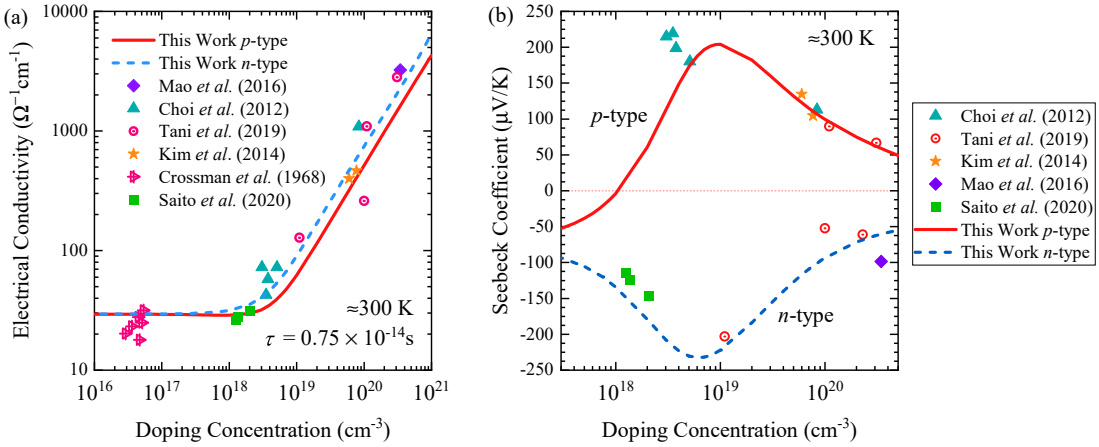

Figure 6.26 *Comparison between calculated values and experimental data[181–187] of the (a) electrical conductivity and (b) the Seebeck coefficient of unstressed Mg_2Sn at ∼300 K vs doping concentration. The doping concentration of the experimental data is generally estimated using the Hall carrier concentration, which was measured at different temperatures by the individual experiments. As such, the doping concentrations of the experimental data may have some variation. For my calculations, the band gap has been shifted according to the methodology.*

Within the constant-scattering-time approximation, the Seebeck coefficient is independent of the electron-scattering time τ. Figure 6.26(b) shows there is excellent agreement between the calculated Seebeck coefficient, and experimental data from the literature. Figs. 6.26(a) and 6.26(b) also show that, at 300 K, Mg_2Sn is in the intrinsic regime for doping concentrations below $\sim 10^{19}\,\mathrm{cm}^{-3}$, and in the saturated regime above that.

Crossman and Danielson[187] measured the piezoresistance coefficients of n-type Mg_2Sn with a very low Hall carrier concentration of $n_H \approx 6 \times 10^{16}\,\mathrm{cm}^{-3}$. They made the measurements at temperatures between 50 and 300 K. For comparison, I calculated piezoresistance coefficients at 300 K and 200 K for Mg_2Sn with a doping concentration of $5 \times 10^{16}\,\mathrm{cm}^{-3}$. The change of resistivity under uniaxial stress along different directions was calculated. The relative rate-of-change of

resistivity with respect to stress was then used to compute the piezoresistance coefficients:

$$\pi = \frac{1}{\rho}\frac{\partial \rho}{\partial \zeta}, \tag{6.2}$$

where ρ is the resistivity and ζ is the applied stress. The specific piezoresistance coefficient computed depends on the applied stress tensor and the direction in which the resitivity is measured. A useful diagram illustrating how the different deformations relate to piezoresistance coefficients can be found in Fig. 3, Burke (1967)[71]. Overall, there is excellent agreement between the calculated piezoresistance coefficients, and the experimental values from Crossman & Danielson.

Table 6.1 *Piezoresistance coefficients of lightly n-doped Mg_2Sn. Calculated values use an n-doping concentration of $5 \times 10^{16}\,cm^{-3}$. Experimental values had a low-temperature Hall carrier concentration of ∼5–$10 \times 10^{16}\,cm^{-3}$.*

Coefficient	Temperature (K)	Calculated Value (GPa^{-1})	Experimental Value (GPa^{-1})[187]
π_{11}	300	-0.89	-0.84
π_{12}	300	0.17	0.22
π_{44}	300	-0.30	-0.27
π_{11}	200	-1.64	-2.06
π_{12}	200	0.35	0.77
π_{44}	200	-0.20	-0.35

6.2.3 Concentration of Intrinsic Carriers

Mg_2Sn has a much smaller band gap than Mg_2Si: ∼0.1 eV[172] at room temperature, vs ∼0.6 eV[171]. As a result, the intrinsic regime onsets at a much lower temperature for Mg_2Sn than it does for Mg_2Si with a similar doping concentration. Figure 6.27 quantifies the intrinsic carrier concentration of doped Mg_2Sn as a function of temperature. For n-doping concentrations close to $-1 \times 10^{19}\,cm^{-3}$, the concentration of intrinsic carriers is significant for temperatures near or exceeding 300 K. I classify combinations of doping concentration and temperature as being in the intrinsic regime if the intrinsic carrier concentration is greater than ∼10 % of the doping concentration. Although this condition is arbitrary, it is useful for discussing the different behaviours seen in each regime. Even with the high doping concentration of $-1 \times 10^{20}\,cm^{-3}$, Mg_2Sn is in the intrinsic regime at temperatures above 600 K.

The trends shown in Fig. 6.27 are quantitatively very similar if Mg_2Sn is p-doped

with the same magnitude doping concentration. Indeed, figure 6.27(b) shows the intrinsic carrier concentration for $+1 \times 10^{20}\,\mathrm{cm}^{-3}$ p-doped Mg_2Sn and for the n-doped case on the same axis: they have near perfect quantitative agreement*.

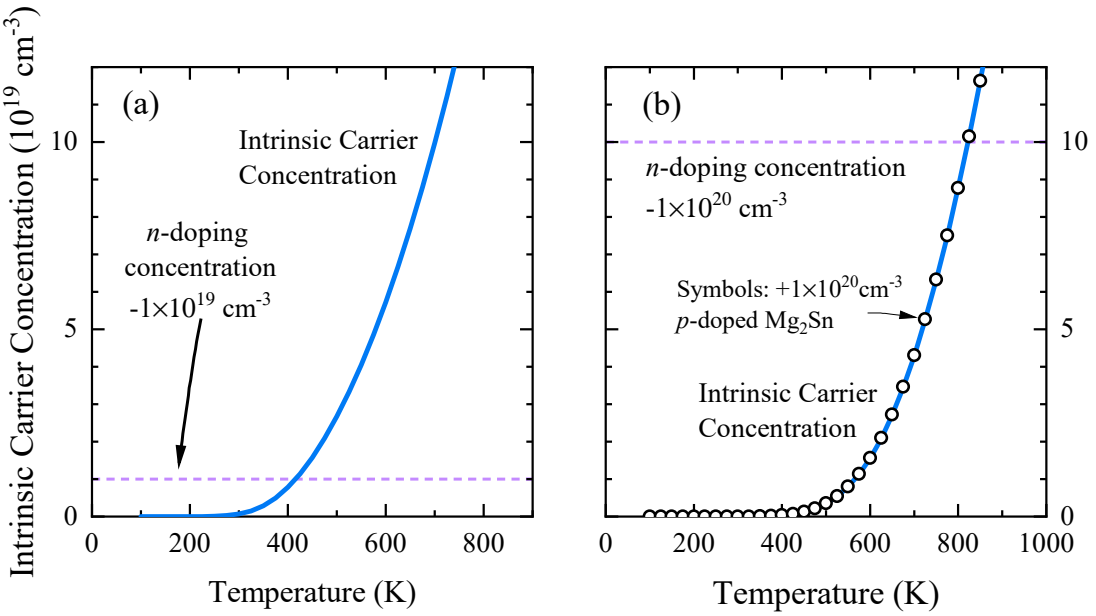

Figure 6.27 *The intrinsic carrier concentration, $n_{int} = 2 \times min\,[n_e, n_h] = n_{total} - n_{doping}$, as a function of temperature for Mg_2Sn with an n-doping concentration of (a) $1 \times 10^{19}\,cm^{-3}$. In (b), the solid line is the intrinsic carrier concentration for $-1 \times 10^{20}\,cm^{-3}$ n-doped Mg_2Sn, and the symbols are for $+1 \times 10^{20}\,cm^{-3}$ p-doped Mg_2Sn. The trends are quantitatively nearly identical for p-doped Mg_2Sn.*

6.2.4 Hall Coefficient

Measurements of the Hall coefficient R_H are often used to estimate the doping concentration n of a sample, using the approximation that $n \approx n_\mathrm{H} = 1/|eR_\mathrm{H}|$. For a narrow-gap semiconductor like Mg_2Sn, this approximation breaks down if the intrinsic carrier concentration is significant. Figure 6.28(c) shows how the Hall carrier concentration at 300 K changes with doping concentration. The peak in n_H for p-doping concentrations around $\sim 10^{18}\,\mathrm{cm}^{-3}$ is due to the Hall coefficient tending towards zero. Importantly, for all doping concentrations below $\sim 10^{19}\,\mathrm{cm}^{-3}$, the Hall carrier concentration is much larger than the true doping concentration. Thus, if the Hall carrier concentration is measured at temperatures

*I speculate that this is not coincidental. To me, it makes intuitive sense that the intrinsic carrier concentration, for a given material and temperature, should only depend on the magnitude of the doping concentration and not its' sign. However, I have not attempted to prove this.

near 300 K, then it cannot accurately estimate doping concentrations below $10^{19}\,\mathrm{cm}^{-3}$.

This can also be seen by examining the ratio between the true doping concentration and the Hall carrier concentration n/n_{H} at this temperature [Fig. 6.28(a)]. If the true doping concentration n is at or below $\sim 10^{19}\,\mathrm{cm}^{-3}$, the Hall carrier concentration far exceeds the true doping concentration, and n/n_H is close to zero.

Measuring the Hall carrier concentration at a lower temperature, e.g. 150 K, allows smaller doping concentrations to be estimated. To allow experimental measurements of n_{H} to more accurately estimate the doping concentration, Fig. 6.28(b) shows n/n_{H} as a function of doping concentration at 150 K.

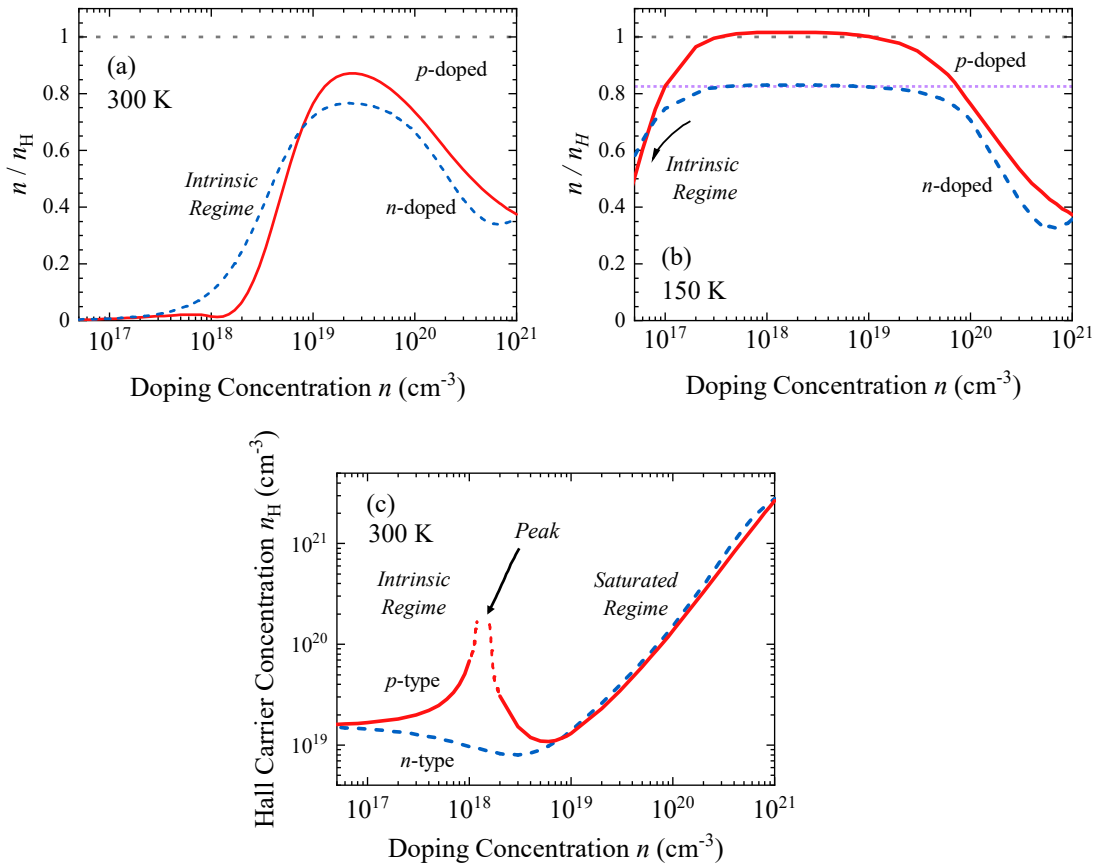

Figure 6.28 *Ratio between the true doping concentration n and the Hall carrier concentration $n_H = |eR_H|$ at (a) 300 K and (b) 150 K as a function of doping concentration. (c) Hall carrier concentration n_H at 300 K.*

6.2.5 Chemical Potential

Figure 6.29 shows how the chemical potential of Mg_2Sn relates to the doping concentration. This can be used to gauge which parts of the bandstructure are within the energy range of importance for different doping concentrations.

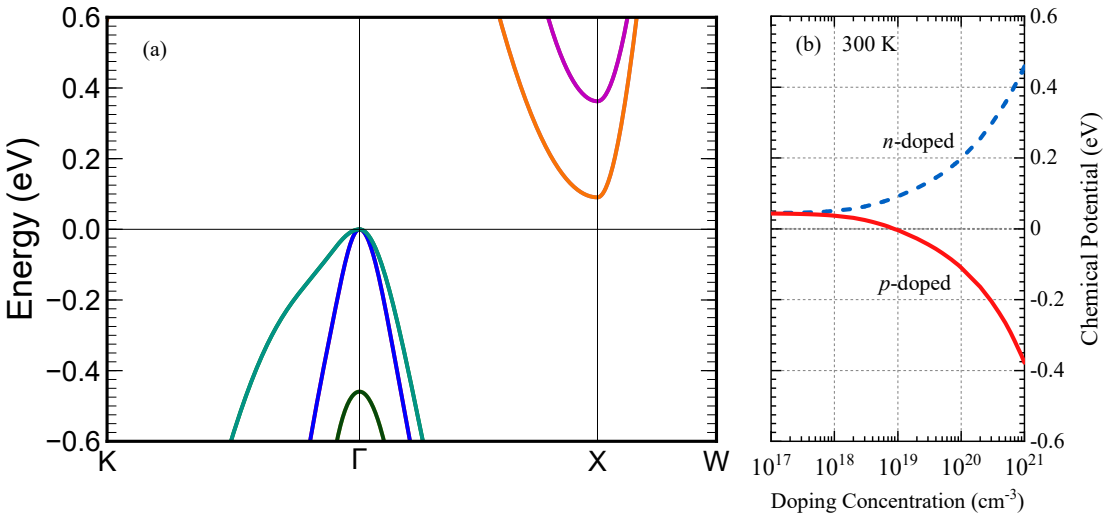

Figure 6.29 *(a) Calculated bandstructure of Mg_2Sn, with the band gap shifted to the experimental value at 300 K of 0.09 eV[172]. This is the same band gap used in the electron-transport calculations (sec. 5.3.3). (b) Calculated chemical potential for doped Mg_2Sn at 300 K as a function of doping concentration.*

6.2.6 Uniaxial Stress along [001]

n-type Mg_2Sn in the saturated regime

For n-type Mg_2Si, increasing tensile uniaxial stress along [001] induced an intervalley-transfer-effect, redistributing dopant electrons from the single M-point carrier pocket to the two X-point pockets. This caused the power factor along [001] of n-type Mg_2Si to increase with increasing tensile stress. If tensile stress induces the same effect for Mg_2Sn, then it is reasonable to assume that it will also apply for alloys of the type $Mg_2Sn_{1-x}Si_x$.

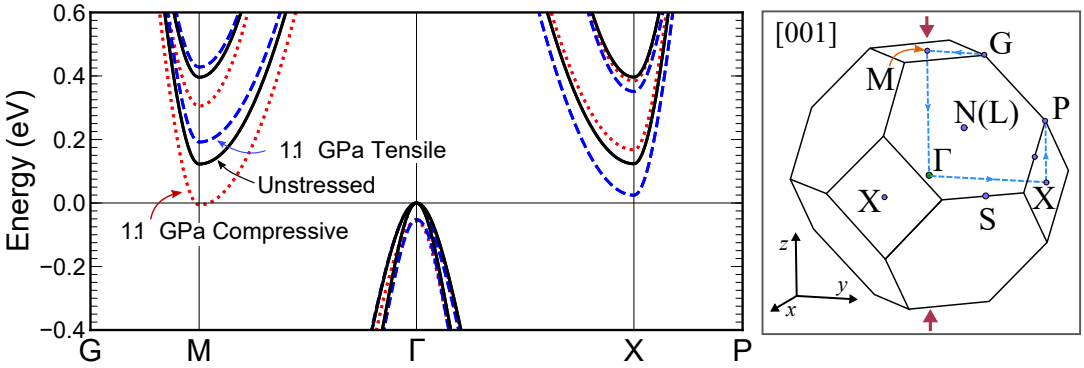

Figure 6.30 *Features of the Mg_2Sn bandstructure under uniaxial [001] stress. Left: calculated bandstructure. Right: Diagram of the Brillouin zone under [001] stress, with labels taken from the Bilbao Crystallographic Server[130].*

Figure 6.30 shows that, indeed, increasing tensile stress raises the energy of the single M-point conduction-band carrier pocket, relative to the two X-point pockets. This redistributes conduction-band electrons from the M-point to the X-point pockets, which have greater mobility along [001] relative to the M-point pocket. As a result, the conductivity along [001] of n-type Mg_2Si increases with increasing tensile [001] stress.

Furthermore, applying tensile stress reduces the band gap of Mg_2Sn. This increases the intrinsic carrier concentration: further increasing conductivity if the intrinsic carrier concentration is significant compared to the doping concentration. However, reducing the number of carrier pockets under tensile stress reduces the Seebeck coefficient.

Figure 6.31(b) quantifies this notion for $-1 \times 10^{20}\,\mathrm{cm}^{-3}$ n-doped Mg_2Sn at room temperature. Increasing tensile stress increases the conductivity along [001], and

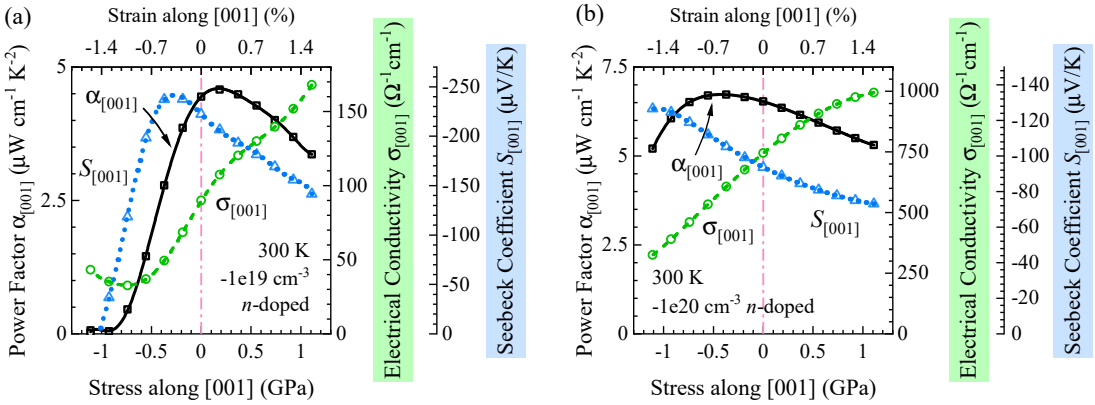

Figure 6.31 *Electronic transport properties along [001] of Mg_2Sn at 300 K with an n-doping concentration of (a) $-1 \times 10^{19}\,cm^{-3}$ and (b) $-1 \times 10^{20}\,cm^{-3}$, under uniaxial stress along [001]. Case (a) is on the border between the intrinsic and saturated regimes, whereas case (b) is firmly in the saturated regime.*

concomitantly reduces the Seebeck coefficient. Overall, this leads to a decrease in the power-factor along [001] with increasing tensile uniaxial [001] stress.

Increasing compressive stress increases the Seebeck coefficient along [001], partly due to the interplay between the conductivity and the L^{12} matrix, and partly because increasing compressive stress converges the upper and lower conduction-band carrier pockets at X (Fig. 6.30). At high doping concentrations, $10^{20}\,cm^{-3}$ and above, the upper conduction bands are within the energy range of importance (Fig. 6.29), and so convergence of the upper and lower conduction bands at X under compressive stress increases the Seebeck coefficient. As a result, for these high doping concentrations, the power factor along [001] initially increases with increasing compressive [001] stress, before reaching a maximum beyond which it decreases. At very high doping concentrations ($10^{21}\,cm^{-3}$) the power factor along [001] increases under increasing compressive [001] stress. Figure 6.32 quantifies this notion for $-1 \times 10^{21}\,cm^{-3}$ n-doped Mg_2Sn at 300 K. Just as for lower doping concentrations [e.g. Fig. 6.31(b)], the Seebeck coefficient increases with increasing compressive stress, and the conductivity concomitantly reduces. But at this very high doping concentration, the power factor overall improves with increasing compressive stress.

If the doping concentration and intrinsic carrier concentration are similar, then increasing the intrinsic carrier concentration reduces the Seebeck coefficient significantly. Figure 6.31(a) shows this effect for $-1 \times 10^{19}\,cm^{-3}$ n-doped Mg_2Sn at room temperature. In this case, Mg_2Sn is on the border between the intrinsic and saturated regimes [Fig. 6.27(a)].

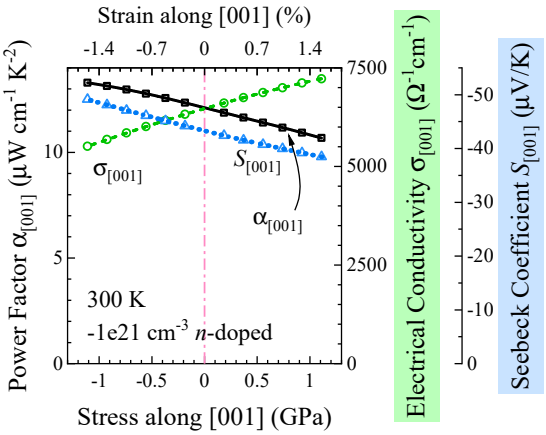

Figure 6.32 *Transport properties along [001] for -1×10^{21} cm^{-3} n-doped Mg_2Sn at 300 K under uniaxial [001] stress.*

Increasing compressive stress initially reduces the electrical conductivity along [001], reaches a minimum at ∼0.75 GPa, above which it increases. Turning points like this are characteristic of cases in or near the intrinsic regime (Figs. 6.14, 6.9, and 4.21). Conduction-band mobility along [001] reduces under increasing compressive stress, but concomitantly increases the total charge-carrier concentration due to the narrowing band gap (Fig. 6.30). A turning point in the conductivity–stress graph, such as that shown in Fig. 6.27(a), indicates that Mg_2Sn with this combination of doping concentration and temperature is in, or close to, the intrinsic regime.

Overall, if *n*-doped Mg_2Sn is in the saturated regime, increasing tensile stress reduces the overall power factor along [001]. This contrasts with Mg_2Si, which saw an increase in the power factor along [001] with increasing tensile stress. However, although the trend in the power factor under stress differs for Mg_2Sn and Mg_2Si, the change in shape of the conduction bands is qualitatively the same. Under increasing tensile [001] stress, both *n*-type Mg_2Si and *n*-type Mg_2Sn undergo an intervalley transfer effect, from the low-mobility M-point valley to the high-mobility X-point valleys. In both materials, the electrical conductivity along [001] increases with increasing tensile stress, and the Seebeck coefficient concomitantly decreases. As a result, it is reasonable to infer that $Mg_2Si_xSn_{1-x}$ alloys will exhibit the same qualitative trends under uniaxial [001] stress. To what extent this improves the power factor along [001] will depend on the specific alloy concentrations and doping concentration, and thus warrants further investigation.

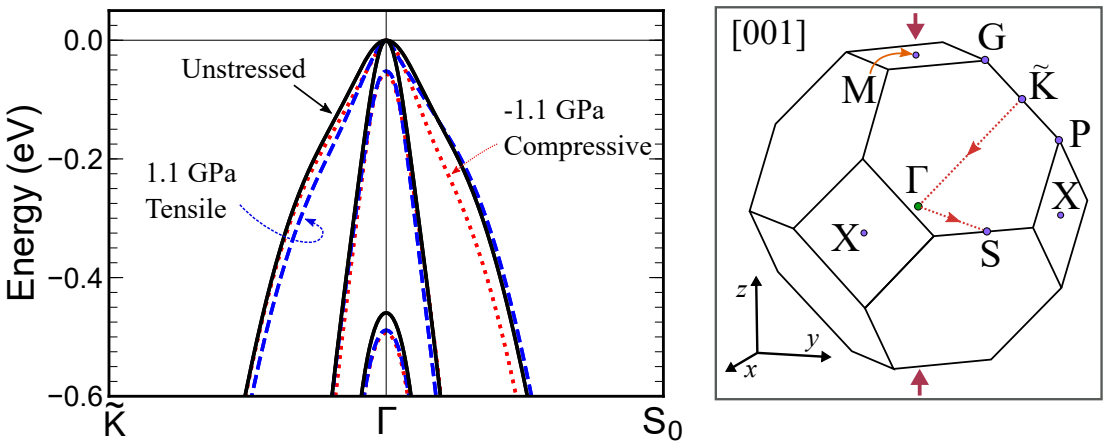

Figure 6.33 *Left: Calculated valence band edge of Mg_2Sn under uniaxial stress along [001]. Right: Diagram of the primitive Brillouin zone under [001] stress. The $\tilde{K}$-point is located halfway between the G and P points. Stress along [001] makes Mg_2Sn adopt a tetragonal symmetry, in which $\tilde{K}$ is not a high-symmetry point. However, when unstressed, the $\tilde{K}$-point is equivalent to the S-point, both of which are equivalent to the K-point in FCC symmetry (Fig. 6.24).*

p-type Mg_2Sn in the saturated regime

Figures 6.30 and 6.33 show how the valence band structure of Mg_2Sn changes under uniaxial stress along [001]. Both tensile and compressive stress diverge the first and second valence bands. The curvature of vb1 along Γ–S_0 also changes slightly under compressive stress, but the gradient along Γ–S_0 remains approximately constant. There is not a large increase in the gradient of the entire band, such as that for PbTe under [001] stress (Fig. 4.14).

The third valence band is approximately 0.4 eV lower in energy than vb1 and vb2, and so is outwith the energy range of importance for most combinations of *p*-doping concentration and temperature investigated (up to $10^{21}\,cm^{-3}$ and up to 900 K, respectively).

Overall, there is relatively little change to the valence bandstructure of Mg_2Sn under uniaxial stress along [001]. As a result, there is also little change to the electrical transport properties for *p*-doped Mg_2Sn in the saturated regime. Figure 6.34(a) quantifies this for $1 \times 10^{20}\,cm^{-3}$ *p*-doped Mg_2Sn at 300 K. There is a slight increase in the Seebeck coefficient along [001] with increasing compressive [001] stress, which leads to a slight increase in the power factor: approximately 6 %/ GPa. Overall, there is little change with [001] stress. However, in the intrinsic regime, the power factor of *p*-doped Mg_2Sn can be significantly improved.

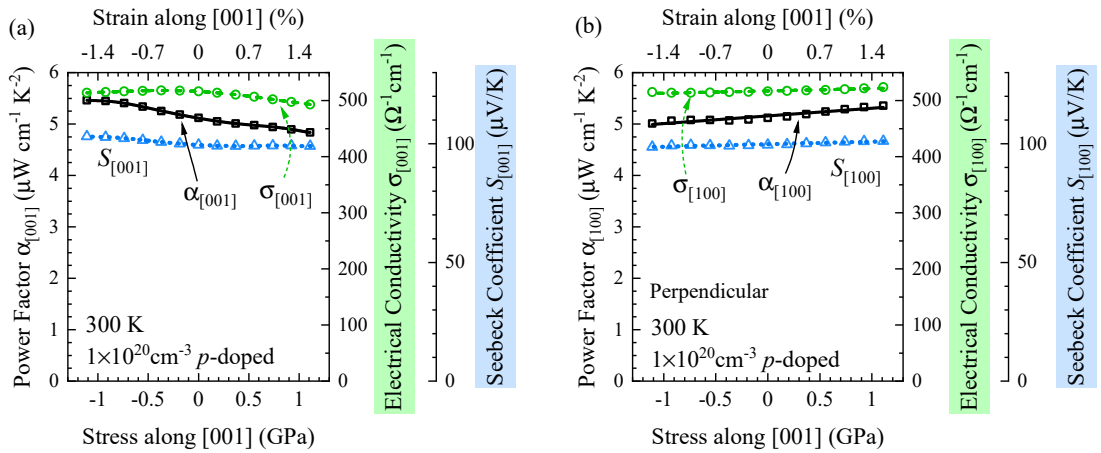

Figure 6.34 *Transport properties for $1 \times 10^{20}\,cm^{-3}$ p-doped Mg_2Sn under uniaxial [001] stress at 300 K (a) along [001], and (b) perpendicular to [001]. For this combination of doping concentration and temperature, Mg_2Sn is in the saturated regime (Fig. 6.27).*

Intrinsic Regime

In the intrinsic regime, significant changes to the conduction band structure under [001] stress affect the transport properties of both *p*- and *n*-doped Mg_2Sn. Figure 6.35(a) shows that, in the intrinsic regime, increasing compressive [001] stress can greatly improve the power factor along [001] of *p*-doped Mg_2Sn. Increasing compressive stress increases the Seebeck coefficient along [001], due to the reducing mobility of the conduction-band electrons relative to valence-band holes. This leads to an approximately 3-fold increase in the power factor with just 0.5 GPa of compressive stress. The power factor along [001] of *p*-doped Mg_2Sn in the intrinsic regime greatly increases with increasing compressive [001] stress.

The trend in the power factor of *n*-doped Mg_2Sn under stress depends on whether or not the intrinsic carrier concentration significantly exceeds the *n*-doping concentration. This is because there are two competing effects that cause tensile stress to change the Seebeck coefficient:

(i) The reduction in the band gap of Mg_2Sn under increasing tensile stress significantly increases the intrinsic carrier concentration. As the intrinsic carrier concentration increases, the Seebeck coefficient tends towards the value it would be for a purely undoped sample. For example, the Seebeck coefficient of $-1 \times 10^{18}\,cm^{-3}$ and $-1 \times 10^{19}\,cm^{-3}$ *n*-doped Mg_2Sn are very different at 200 K, where the *n*-doping concentration dominates, but their Seebeck coefficients are approximately equal at 600 K, where the intrinsic carrier concentration is much

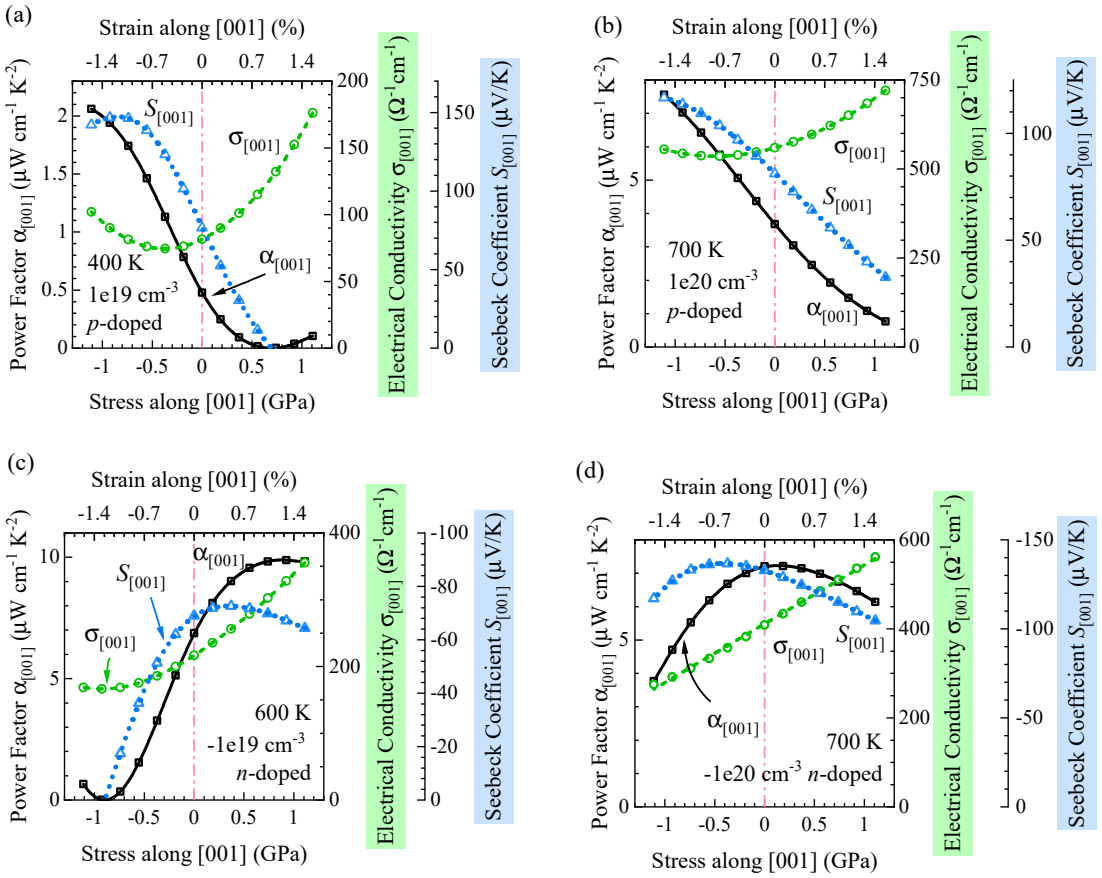

Figure 6.35 *Transport properties along [001] for Mg_2Sn in the intrinsic regime under uniaxial [001] stress. (a) 1×10^{19} cm^{-3} p-doped Mg_2Sn at 400 K; (b) 1×10^{20} cm^{-3} p-doped Mg_2Sn at 700 K; (c) -1×10^{19} cm^{-3} n-doped Mg_2Sn at 600 K; (d) -1×10^{20} cm^{-3} n-doped Mg_2Sn at 700 K.*

greater. Figure 6.36 illustrates this concept. Below 300 K, where the doping concentration dominates and all samples are firmly in the saturated regime, the Seebeck coefficient for each different doping concentration is drastically different. In contrast, at 600 K, where the intrinsic carrier concentration dominates, all samples have a very similar Seebeck coefficient — the same value as for undoped Mg_2Sn.

Increases to the intrinsic carrier concentration, caused by closing the band gap under stress, tend the Seebeck coefficient towards the value for undoped Mg_2Sn. This effect was not particularly significant for Mg_2Si, as the change in the band gap of Mg_2Si under stress was small compared to the large original gap. This is not the case for Mg_2Sn, for which the band gap significantly narrows under [001] stress (Fig. 6.30).

(ii) The increase, under tensile stress, of conduction-band mobility along [001]

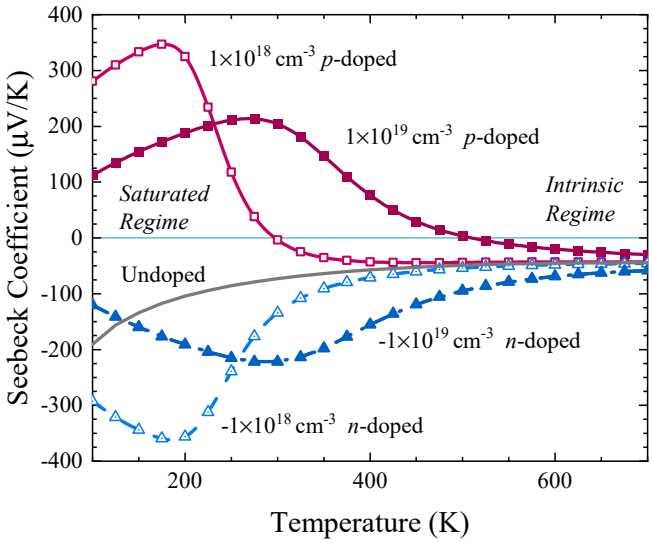

Figure 6.36 *The Seebeck coefficient of unstressed Mg_2Sn vs temperature for a variety of doping concentrations.*

relative to valence-band mobility acts to increase the Seebeck coefficient. This simultaneous-valley-transform effect is most significant when the intrinsic carrier concentration is large compared to the doping concentration.

If the intrinsic carrier concentration is similar to the n-doping concentration, effect (i) causes the Seebeck coefficient to decrease with increasing tensile stress. If the intrinsic carrier concentration is already much greater than the n-doping concentration, then the simulateneous-valley-transform effect causes the Seebeck coefficient to greatly increase with increasing tensile stress.

Figures 6.35(c) and (d) illustrate this notion. In both cases, the intrinsic carrier concentration n_{int} is significant compared to the doping concentration n_{dop} (Fig. 6.27), but to different extents. For the case shown in Fig. 6.35(c) ($-1 \times 10^{19}\,\text{cm}^{-3}$ n-doped Mg_2Sn at 600 K), n_{int} is approximately 6 times greater than n_{dop}. For this combination of temperature and doping concentration, the transport properties of Mg_2Sn are dominated by intrinsic carriers. As such, the effects of simultaneous-valley-transform is significant, which causes the Seebeck coefficient along [001] to slightly increase with increasing tensile stress: leading to a greatly improved power factor along [001].

In contrast, in the case shown in Fig. 6.35(d) ($-1 \times 10^{20}\,\text{cm}^{-3}$ n-doped Mg_2Sn at 700 K), n_{int} is approximately half n_{dop}: Mg_2Sn is close to the border between the intrinsic and saturated regimes. In this case, effect (i) is predominant. The narrowing band gap under increasing tensile stress causes the Seebeck coefficient to decrease, and thus the greatest power factor is for unstressed Mg_2Sn.

For n-doped Mg_2Sn, the greatest power factor is for unstressed Mg_2Sn, unless n_{int} was much greater than n_{dop} in which case increasing tensile stress improves the power factor along [001].

Summary

For n-doped Mg_2Sn in the saturated regime, the electrical conductivity along [001] increases with increasing tensile [001] stress, and the Seebeck coefficient decreases. These trends are consistent with those of n-doped Mg_2Si. For low and intermediate doping concentrations, the greatest power factor is for Mg_2Sn with near-zero stress. For very high doping concentrations, 10^{20} and above, the power factor along [001] can be improved under increasing compressive [001] stress, due to convergence of the upper and lower conduction bands at X.

For p-doped Mg_2Sn in the saturated regime, the transport properties remain approximately constant under uniaxial [001] stress. Small improvement in the power factor along [001] can be found under compressive stress. However, in the intrinsic regime, the power factor along [001] of p-doped Mg_2Sn can be greatly improved by increasing compressive [001] stress.

For n-doped Mg_2Sn, if the intrinsic carrier concentration greatly exceeds the doping concentration, then the power factor along [001] can be greatly increased by increasing tensile [001] stress. However, if the doping concentration and intrinsic carrier concentration are similar, then the greatest power factor is for unstressed Mg_2Sn.

6.2.7 Uniaxial Stress along [111]

n-type Mg_2Sn in the saturated regime

Uniaxial stress along [111] cannot, by symmetry, split the degeneracy of the X-point conduction-band valleys. However, as was the case for Mg_2Si, it does change the shape of the valleys. Figure 6.37(a) shows how the conduction-band valleys of Mg_2Sn are reshaped under stress. It is worth noting how the changes are qualitatively similar to those seen in Mg_2Si [Fig. 6.10(a)]. For both Mg_2Sn and Mg_2Si, increasing tensile [111] stress increased the gradient along FB–M_2 of the lower conduction band, which runs roughly parallel to [111], and reduces the gradient along FB–Q, which runs perpendicularly. Thus, tensile [111] stress increases the mobility along [111] of conduction-band electrons. Furthermore, increasing tensile stress reduces the band gap, increasing the intrinsic carrier concentration. As a result of these two effects, the conductivity along [111] of n-doped Mg_2Sn increases with increasing tensile stress.

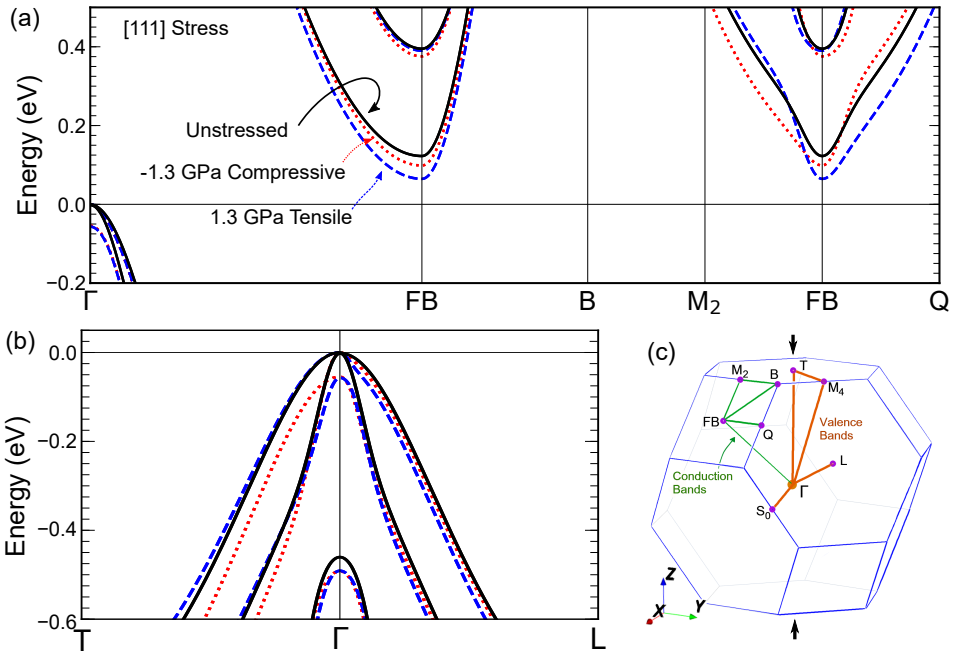

Figure 6.37 *Calculated electronic band structure of Mg_2Sn under uniaxial [111] stress. (a) Conduction band edges (b) Valence band edges (c) Diagram of the Brillouin zone detailing special points*[130].

Figures 6.39(a) and (b) quantify this notion for medium and heavily n-doped Mg_2Sn, respectively. Increasing uniaxial tensile [111] stress greatly increases the conductivity along [111], but keeps the Seebeck coefficient approximately

constant. As a result, 0.5 GPa of tensile stress (equivalent to a strain of ∼0.6 %) increases the power factor along [111] by approximately 20 % — an excellent improvement.

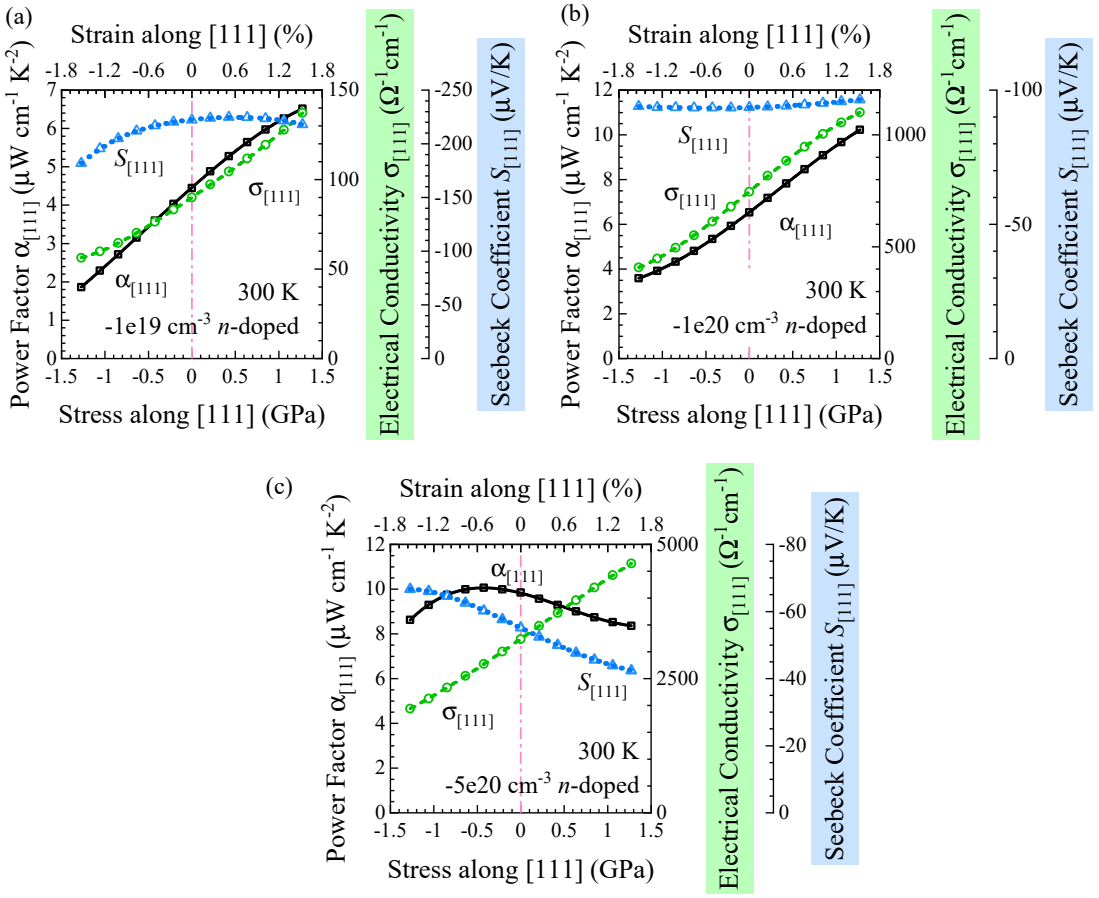

Figure 6.38 *Transport properties along [111] against uniaxial [111] stress for Mg_2Sn with an n-doping concentration of (a) -1×10^{19} cm^{-3}, (b) -1×10^{20} cm^{-3}, and (c) -5×10^{20} cm^{-3}, at 300 K. All three of these cases are in, or bordering, the saturated regime.*

However, increasing tensile stress diverges the upper and lower conduction bands (Fig. 6.37). At low and intermediate doping concentrations, this divergence has little effect because the energy difference between the chemical potential and the upper conduction band is much greater than k_BT. However, if the n-doping concentration is very high, $-5 \times 10^{20}\,\mathrm{cm}^{-3}$ or above, divergence of the two conduction bands under stress causes a decrease the in the Seebeck coefficient. Figure 6.39(c) shows this effect for the very heavily n-doped case of $-5 \times 10^{20}\,\mathrm{cm}^{-3}$ at 300 K. In this case, the upper conduction band is well within $5k_BT$ of the chemical potential (Fig. 6.29). As a result, divergence of the upper and lower conduction bands under increasing tensile stress reduces the Seebeck coefficient significantly. Figure 6.39(c) shows that, for very heavily

n-doped Mg_2Sn ($-5 \times 10^{20}\,cm^{-3}$ and above), increasing tensile stress actually decreases the power factor along [111].

p-type Mg_2Sn in the saturated regime

Figure 6.37(b) shows how the valence bands of Mg_2Sn change under uniaxial [111] stress. Increasing compressive [111] stress increases the curvature of the first valence band along Γ–T, parallel to [111], and also increases the gradient of the second valence band along Γ–T. This increases the mobility of valence-band holes along [111]. However, divergence of the first and second valence bands reduces the Seebeck coefficient.

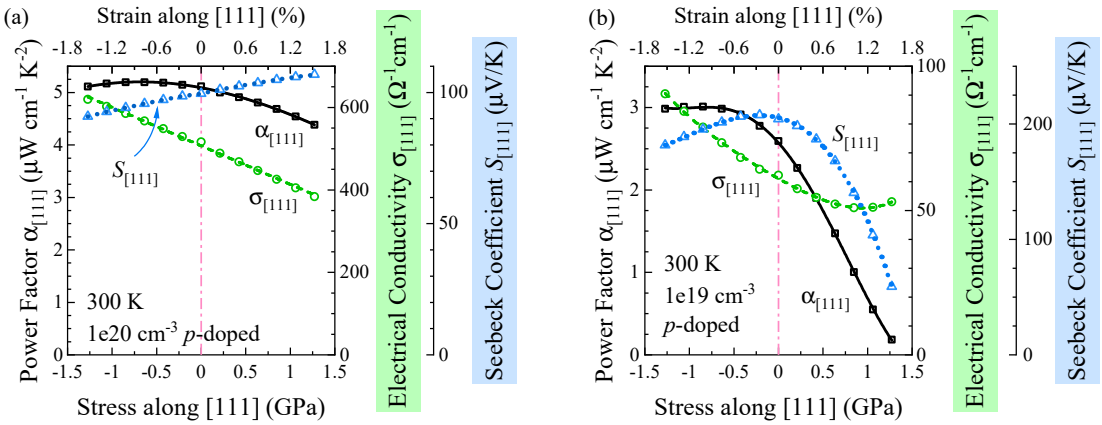

Figure 6.39 *Transport properties along [111] against uniaxial [111] stress for (a) $1 \times 10^{20}\,cm^{-3}$ and (b) $1 \times 10^{19}\,cm^{-3}$ p-doped Mg_2Sn at 300 K. Symbols are calculated values, lines are guides to the eye.*

Figure 6.39(a) quantifies this notion for $1 \times 10^{20}\,cm^{-3}$ p-doped Mg_2Sn. Increasing compressive [111] stress increases the conductivity along [111], and concomitantly reduces the Seebeck coefficient. Across all p-doping concentrations where the doping concentration is dominant, the power factor along [111] remains similar, or decreases, under stress. However, if Mg_2Sn is in or bordering the intrinsic regime, increasing compressive stress does increase the power factor along [111]. Mg_2Sn with a p-doping concentration of $1 \times 10^{19}\,cm^{-3}$ at 300 K is one such example. Figure 6.39(b) shows how, for cases bordering the intrinsic and saturated regimes, the power factor along [111] increases with increasing compressive stress.

Mg_2Sn in the intrinsic regime

In the intrinsic regime, simultaneous valley transform under uniaxial [111] stress leads to a concomitant increase of the electrical conductivity and the Seebeck coefficient. For p-doped Mg_2Sn in the intrinsic regime, increasing compressive [111] stress will increase the mobility along [111] of valence-band holes, and reduce that of conduction-band electrons. Increasing the mobility of the valence band relative to the conduction band mobility leads to a large increase in the Seebeck coefficient along [111].

Figure 6.40(a) quantifies this for $1 \times 10^{20}\,\mathrm{cm}^{-3}$ p-doped Mg_2Sn at 800 K. For this case, the intrinsic carrier concentration is approximately equal to the doping concentration [Fig. 6.27(b)]. Increasing compressive stress greatly increases the Seebeck coefficient. The conductivity along [111] decreases slightly with increasing compressive [111] stress, due to the decrease in mobility of the conduction-band electrons. Despite the small decrease in conductivity, there is a large improvement in the power factor along [111]: 0.5 GPa of compressive stress approximately doubles the power factor.

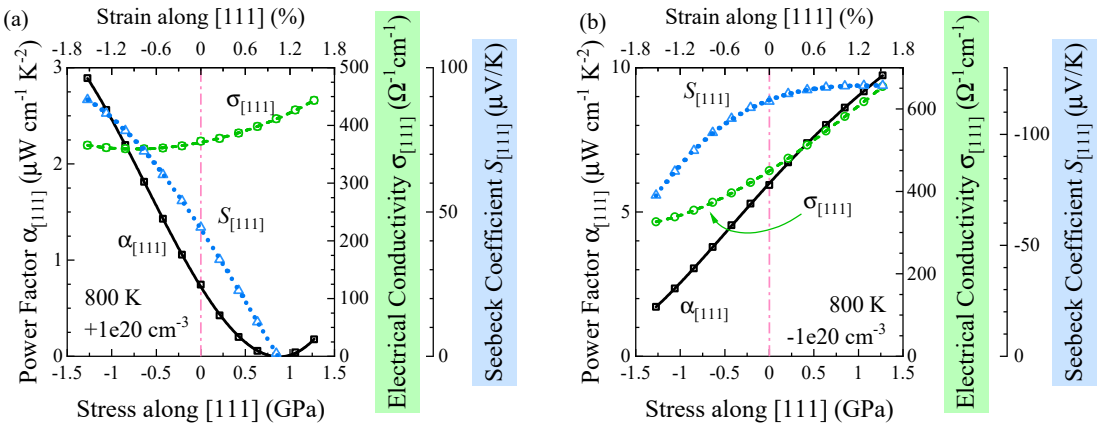

Figure 6.40 *Transport properties along [111] against uniaxial [111] stress for (a) $1 \times 10^{20}\,cm^{-3}$ p-doped and (b) $-1 \times 10^{20}\,cm^{-3}$ n-doped Mg_2Sn at 800 K. Symbols are calculated values, lines are guides to the eye. Both of these cases are in the intrinsic regime.*

For n-doped Mg_2Sn, increasing tensile stress concomitantly increases both the electrical conductivity along [111], and the Seebeck coefficient. This increases the power factor along [111]: ∼0.5 GPa of tensile stress increases the power factor by approximately 25 %. Overall, in the intrinsic regime, increasing tensile (compressive) [111] stress increases the power factor along [111] of n-doped (p-doped) Mg_2Sn.

Summary

For low, intermediate, and high n-doping concentrations when Mg_2Sn in the saturated regime, increasing tensile stress along [111] increases the power factor along [111]. However, if the n-doping concentration is very high ($-5 \times 10^{20}\,\mathrm{cm}^{-3}$ and above), then the power factor remains similar or decreases under increasing tensile stress.

For p-doped Mg_2Sn in the saturated regime, the power factor along [111] increases under increasing compressive [111] stress only if intrinsic carrier concentration is non-negligible (5% or so). Otherwise, the power factor remains similar or decreases under compressive [111] stress. In other words, there is little benefit to the power factor of p-type Mg_2Sn unless it is close to, or in, the intrinsic regime.

Finally, if the intrinsic carrier concentration dominates, then increasing compressive (tensile) [111] stress can greatly increase the power factor along [111] of p-type (n-type) Mg_2Sn.

6.2.8 Uniaxial Stress along [110]

n-type Mg_2Sn in the saturated regime

Uniaxial stress along [110] changes the conduction-band structure of Mg_2Sn in a manner qualitatively similar to that of Mg_2Si. Figure 6.41 shows how increasing compressive stress increases the gradient of the lower conduction band along X–U_0, perpendicular to the applied stress, and reduces the gradient along X–F_2, parallel to [110]. Conversely, increasing tensile [110] stress increases the gradient along X–F_2, and reduces the gradient along X–U_0. These changes are qualitatively similar to those of Mg_2Si under [110] stress (Fig. 6.16). The primary difference is that increasing tensile stress along [110] significantly reduces the band gap of Mg_2Sn.

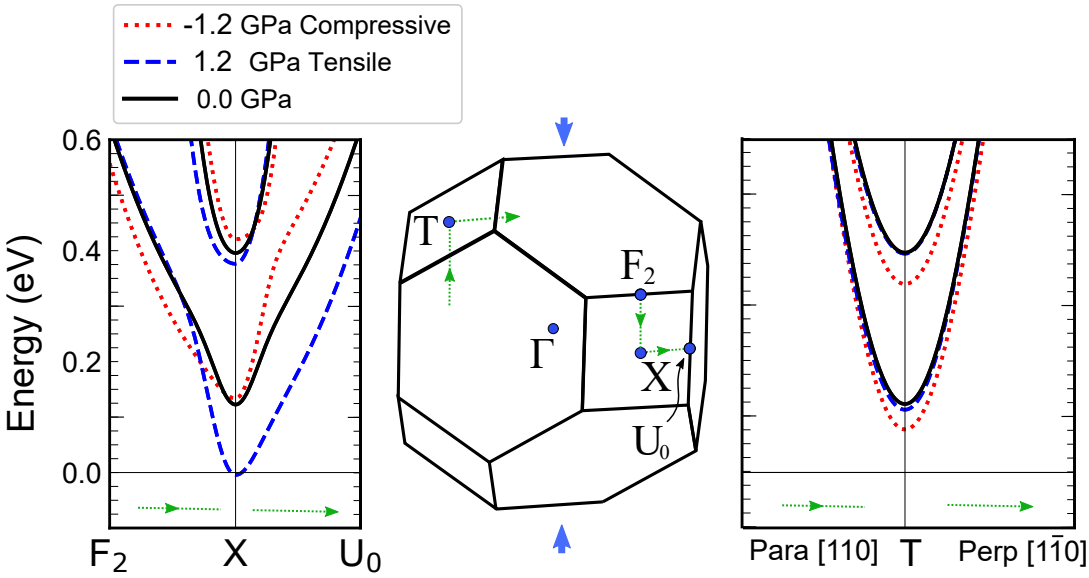

Figure 6.41 *Conduction-band valleys of Mg_2Sn under −1.7 GPa compressive uniaxial stress along [110] (red-dotted line), 1.7 GPa tensile stress (blue-dashed line), and zero stress (black-solid line). 1.7 GPa is equivalent to a strain of ∼1.5 %. (left) Conduction-band valley at X; (centre) diagram of selected special points in the Brillouin zone of [110] stressed Mg_2Sn, with labels taken from the Bilbao Crystallographic Server[130]; (right) conduction-band valley at T perpendicular and parallel to [110]. The left and right figures are to the same scale. The energy of the valence band maximum is set to 0 eV.*

Because the change in the conduction-bands under stress is similar for both Mg_2Sn and Mg_2Si, the change in their respective transport properties are also qualitatively similar. Increasing tensile stress increases the conductivity along

[110] of n-type Mg_2Sn, due partly because the mobility along [110] of the X-point carrier pocket increases, and partly because conduction-band electrons are transferred from the low-[110]-mobility T-point valleys to the high-[110]-mobility X-point valley.

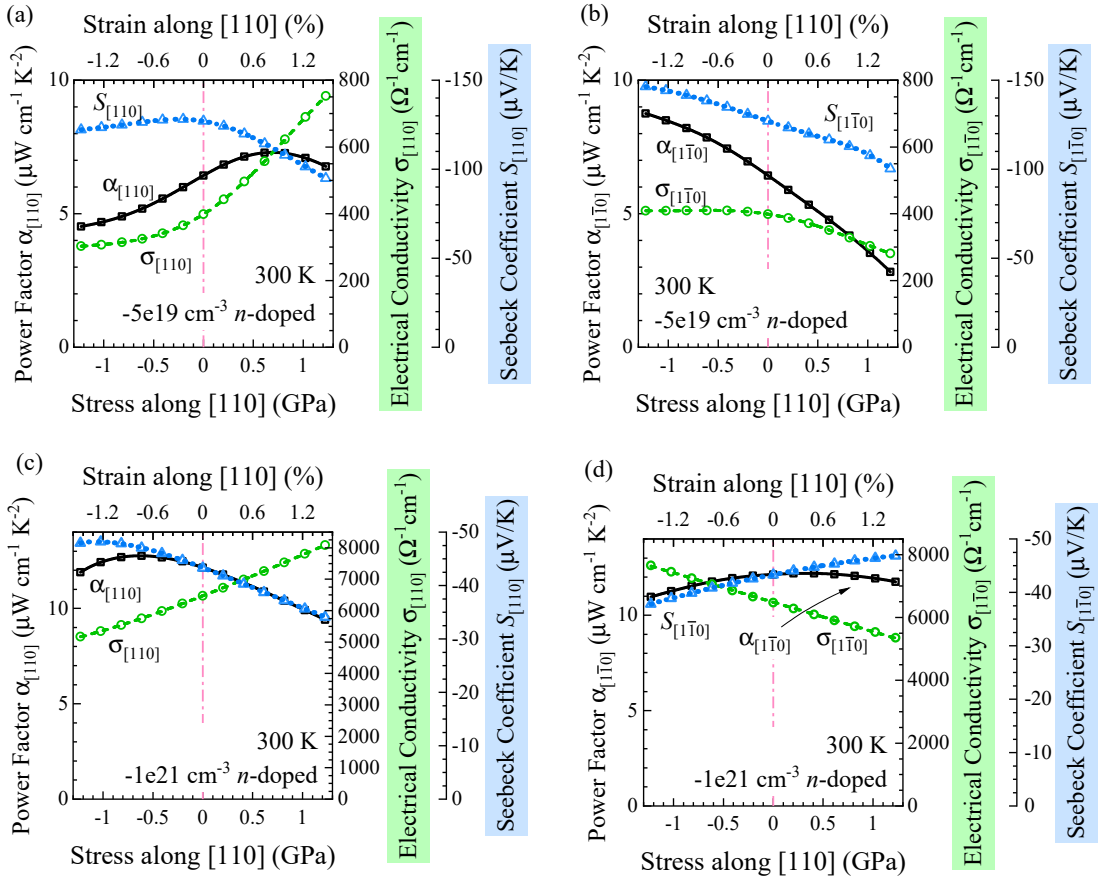

Figure 6.42 *Calculated electrical-transport properties of n-doped Mg_2Sn, in the saturated regime, at 300 K against uniaxial [110] stress. (a) -5×10^{19} cm^{-3}, transport properties along [110]; (b) -5×10^{19} cm^{-3}, transport properties along [1$\bar{1}$0], perpendicular to the applied stress; (c) -1×10^{21} cm^{-3}, transport properties along [110]; (d) -1×10^{21} cm^{-3}, transport properties along [1$\bar{1}$0], perpendicular to the applied stress. Symbols are calculated values, lines are guides to the eye.*

Under tensile stress, intervalley transfer reduces the Seebeck coefficient along [110]. The reduction in the number of carrier pockets contributes to this, but the large reduction in the band gap is also a factor. Reducing the band gap increases the intrinsic carrier concentration, which reduces the Seebeck coefficient for cases that are bordering the saturated and intrinsic regimes. Of course, this second effect (increasing the intrinsic carrier concentration), is not significant if the intrinsic carrier concentration is negligible compared to the doping concentration.

Combined, these effects cause the Seebeck coefficient to reduce with increasing tensile stress.

Figure 6.42(a) quantifies this notion for $-5 \times 10^{19}\,\mathrm{cm}^{-3}$ n-doped Mg_2Sn at 300 K, a case firmly in the saturated regime. The conductivity along [110] increases with increasing tensile stress, and the Seebeck coefficient concomitantly decreases. At this doping concentration, increasing tensile stress slightly increased the power factor of along [110] before reaching a maximum at ∼0.5 GPa, after which it decreases.

Increasing compressive stress along [110] cases a reshaping of the X-point valley (Fig. 6.41). The gradient along X–U_0 of the lower conduction band increases with increasing compressive stress, and the curvature along X–F_2 decreases. As a result, the mobility along $[1\bar{1}0]$, perpendicular to [110], of electrons in the X-point valley will increase with increasing compressive stress. By increasing the mobility along $[1\bar{1}0]$ of the X-point valley, but maintaining a high rate of change of the density of states (because the curvature along [110] decreases), the Seebeck coefficient along $[1\bar{1}0]$ increases with increasing compressive stress. Figure 6.42(b) quantifies this notion for $-5 \times 10^{19}\,\mathrm{cm}^{-3}$ n-doped Mg_2Sn at 300 K. In this case, the conductivity along $[1\bar{1}0]$ is approximately constant with increasing compressive stress, but the Seebeck coefficient increases. As a result, the power factor along $[1\bar{1}0]$ increases significantly.

For most combinations of doping concentration and temperature considered for which Mg_2Sn is in the saturated regime, increasing compressive stress increased the Seebeck coefficient along $[1\bar{1}0]$ — increasing the power factor along $[1\bar{1}0]$. A notable exception was the highest doping concentration considered: $-1 \times 10^{21}\,\mathrm{cm}^{-3}$ [Fig. 6.42(d)]. In this case, the Seebeck coefficient along $[1\bar{1}0]$ decreases with increasing compressive stress. This is likely due to the divergence of the upper and lower conduction bands at X (Fig. 6.41). In this case, the largest power factor is for unstressed Mg_2Sn.

Uniaxial stress along [110] also has an affect on the transport properties along [001]. Figure 6.43 shows how the band edges of Mg_2Sn change with stress along [110]. Increasing compressive stress clearly reduces the lower-conduction-band minimum at T, relative to the minimum at X. This causes conduction-band electrons to be transferred from the X-point valley to the T-point valleys. The T-point valleys have greater mobility along [001], as shown by comparing the gradient of the lower conduction band along X–Γ, to the gradient along T–W.

Figure 6.47 shows how this affects transport properties along [001] of $-5 \times 10^{19}\,\mathrm{cm}^{-3}$

n-doped Mg_2Sn. Intervalley transfer under compressive stress increases the conductivity along [001]. Concomitantly, the Seebeck coefficient along [001] is reduced. Overall, the power factor along [001] remains approximately constant under compressive [110] stress.

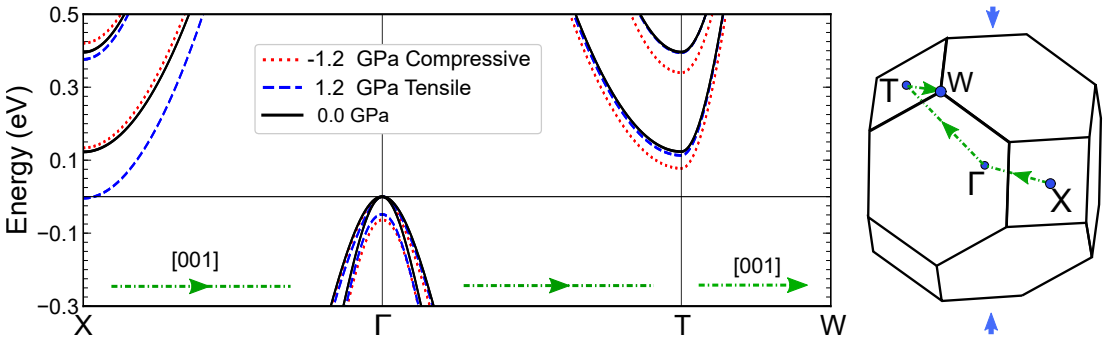

Figure 6.43 *Calculated bandstructure of Mg_2Sn under uniaxial [110] stress.*

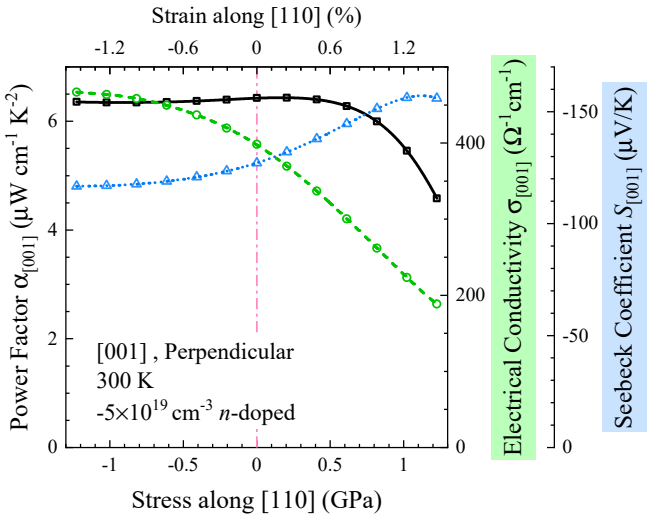

Figure 6.44 *Calculated electrical-transport properties along [001] of $-5 \times 10^{19}\,cm^{-3}$ n-doped Mg_2Sn at 300 K against uniaxial [110] stress. Symbols are calculated values, lines are guides to the eye.*

p-type Mg_2Sn in the saturated regime

Figure 6.45 shows how the valence bands of Mg_2Sn change under uniaxial [110] stress. Under compressive stress, there is an increase in curvature along Γ–Σ_0 of the first valence band. This increases the mobility along [110] of valence band holes. However, there is also a divergence between the first and second valence bands. In the saturated regime, this divergence acts to decrease the Seebeck coefficient along [110].

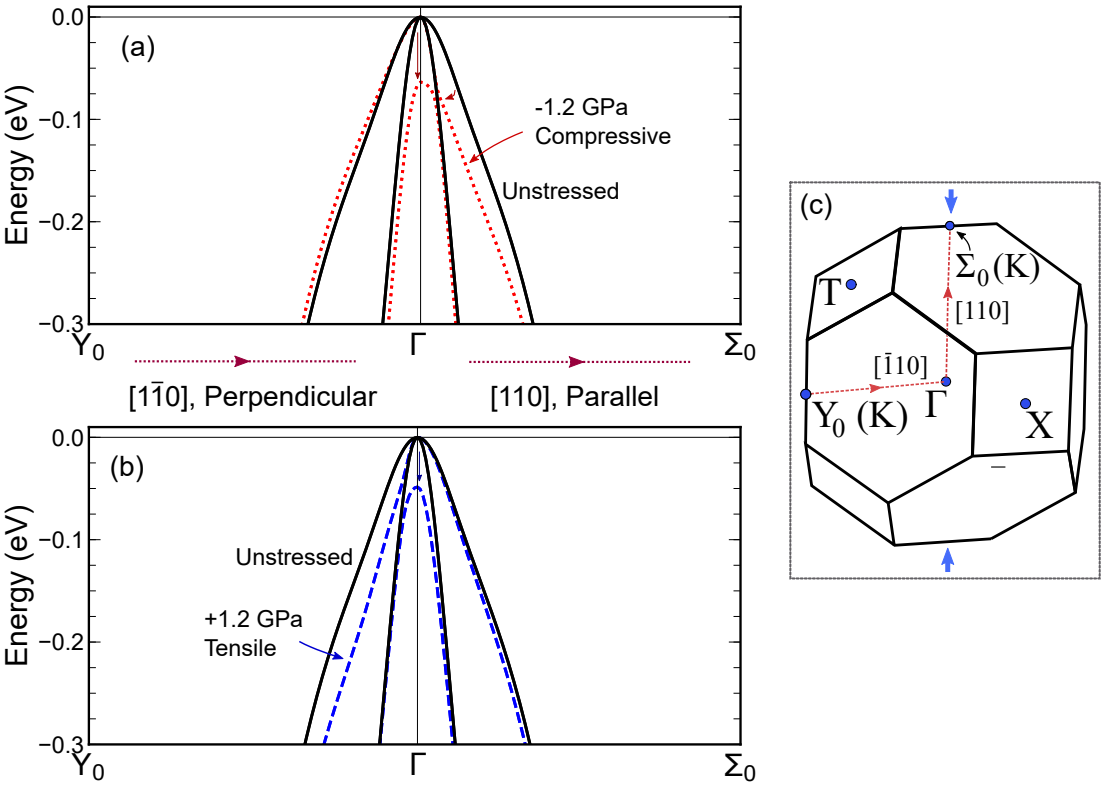

Figure 6.45 *Calculated bandstructure of Mg_2Sn under (a) compressive and (b) tensile uniaxial [110] stress. (c) diagram of selected special points in the Brillouin zone of [110] stressed Mg_2Sn, with labels taken from the Bilbao Crystallographic Server*[130]

Figure 6.46(a) quantifies this notion for $1 \times 10^{20}\,\mathrm{cm}^{-3}$ *p*-doped Mg_2Sn at 300 K. For this combination of doping concentration and temperature, Mg_2Sn is in the saturated regime. As such, increasing compressive [110] stress increases the conductivity, but concomitantly reduces the Seebeck coefficient. As a result, there is a very small increase in the power factor along [110] ($\sim$3 % with -0.5 GPa of compressive stress).

Increasing tensile [110] stress increases the gradient along Γ–Y_0 of the first valence band [Fig. 6.45(b)]. This increases the mobility along [1$\bar{1}$0], perpendicular to the

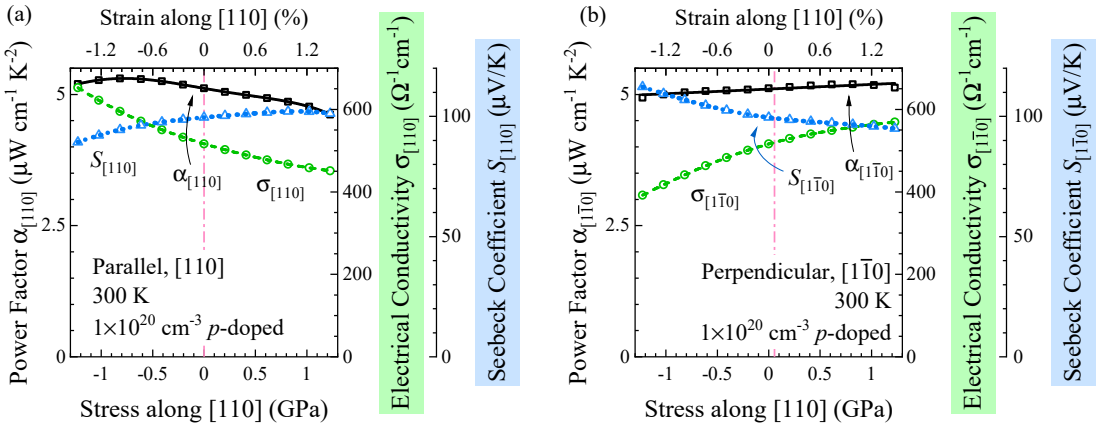

Figure 6.46 *Calculated transport properties of 1×10^{20} cm^{-3} p-doped Mg_2Sn at 300 K (a) along [110], and (b) along [1$\bar{1}$0], perpendicular to [110], against uniaxial [110] stress. Symbols are calculated values, lines are guides to the eye.*

applied [110] stress, of valence-band holes. As a result, increasing tensile [110] stress increases the conductivity along [1$\bar{1}$0] [Fig. 6.46(b)]. The Seebeck coefficient concomitantly decreases with increasing tensile stres, and the power factor very slighly increases.

Under [110] stress, the valence bandstructure of Mg_2Sn does not exhibit changes that would improve the transport properties along [001]. Fig. 6.43 shows that the primary change to the valence bandstructure which affects transport along [001] is the divergence of the first and second valence bands under both compressive and tensile stress. There is no clear change to the curvature or gradients of either valence band — only the energies of their maxima change. As a result, there is little change to the transport properties along [001] of p-doped Mg_2Sn in the saturated regime. Figure 6.47 quantifies this for 1×10^{20} cm^{-3} p-doped Mg_2Sn at 300 K. Both the conductivity and the Seebeck coefficient along [001] remain approximately with uniaxial [110] stress.

In general, for p-doped Mg_2Sn in the saturated regime, the power factors along [110], [1$\bar{1}$0], and [001] cannot be significantly improved by uniaxial stress along [110].

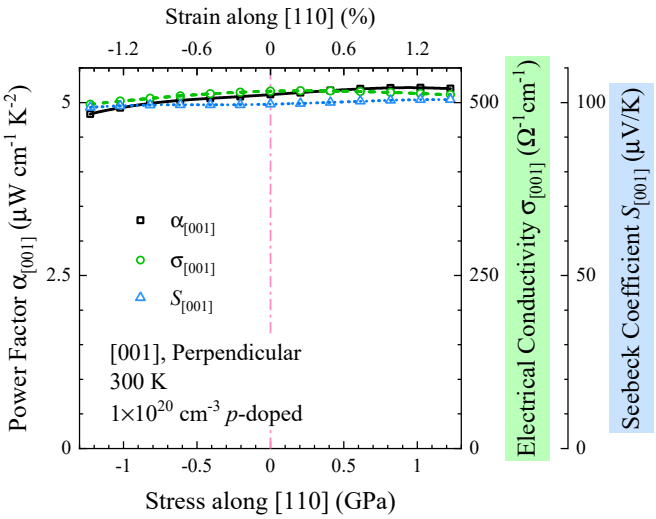

Figure 6.47 *Calculated electrical-transport properties along [001] of $1 \times 10^{20}\,cm^{-3}$ p-doped Mg_2Sn at 300 K against uniaxial [110] stress. Symbols are calculated values, lines are guides to the eye.*

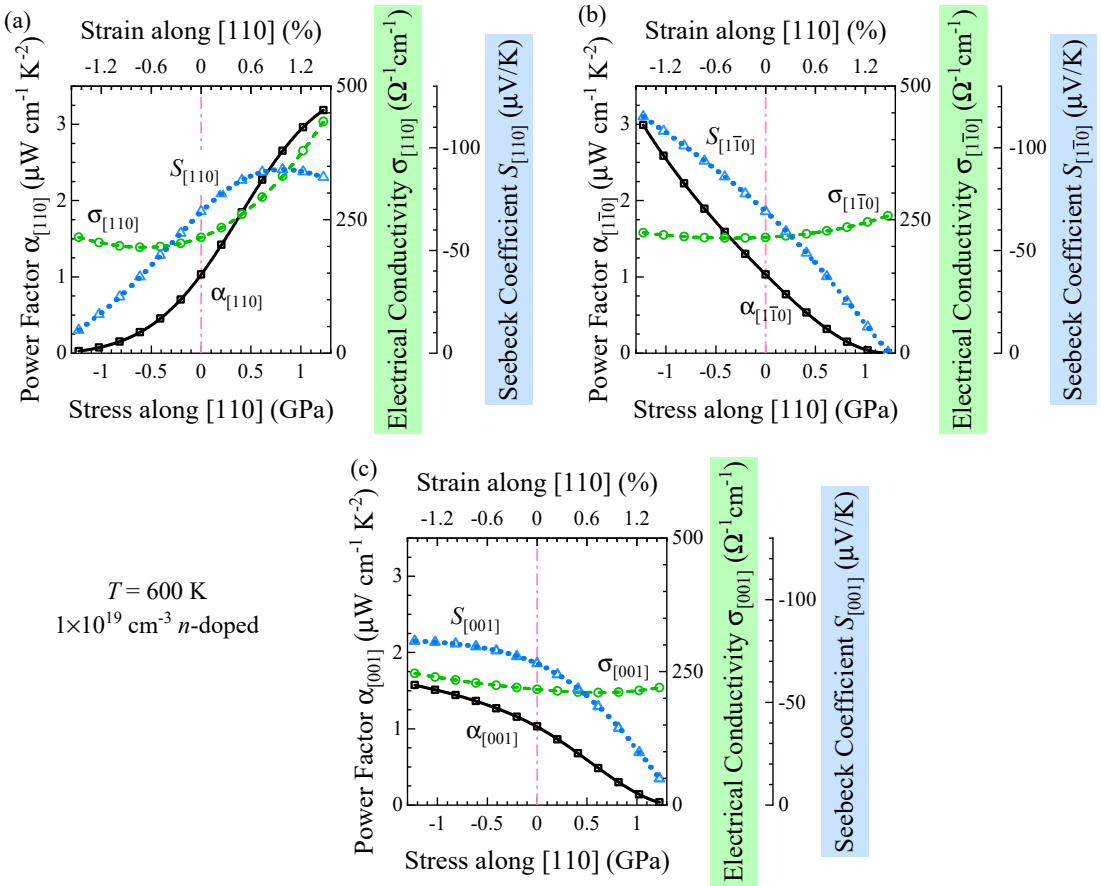

Figure 6.48 *Calculated electrical-transport properties against uniaxial [110] stress for $-1 \times 10^{19}\,cm^{-3}$ n-doped Mg_2Sn at 600 K. This case is in the intrinsic regime. Transport properties are (a) along [110], (b) along [1$\bar{1}$0], and (c) along [001]. Symbols are calculated values, lines are guides to the eye.*

Mg_2Sn in the intrinsic regime

In the intrinsic regime, the changes in the conduction and valence bands under [110] stress both contribute to the change in transport properties. For n-type Mg_2Sn in the saturated regime, increasing tensile [110] stress increases the conductivity along [110]. Conversely, increasing tensile stress reduces the conductivity along [110] for p-type Mg_2Sn in the saturated regime. Thus, in the intrinsic regime, increasing tensile (compressive) stress concomitantly increases both the conductivity and Seebeck coefficient along [110] for n-type (p-type) Mg_2Sn.

Figure 6.48(a) shows this effect for $-1 \times 10^{19}\,\mathrm{cm}^{-3}$ n-doped Mg_2Sn. The simultaneous-valley-transform effect causes both the Seebeck coefficient and electrical conductivity to concomitantly increase with increasing tensile stress. Thus, a huge improvement in the power factor along [110] can be achieved: 0.5 GPa of stress increases the power factor by a factor of 2.

Simultaneous-valley-transform effect also changes transport-properties perpendicular to [110]. Increasing compressive stress greatly increases the Seebeck coefficient perpendicular to [110], both along $[1\bar{1}0]$ and along [001]. This also leads to a large improvement in the power factor [Figs. 6.48(b) and 6.48(c)].

As expected, the power factor along (perpendicular to) [110], of p-type Mg_2Sn in the intrinsic regime, can also be improved by increasing compressive (tensile) [110] stress. Figure 6.49 illustrates this for $1 \times 10^{20}\,\mathrm{cm}^{-3}$ p-doped Mg_2Si at 800 K. It is worth noting that if the intrinsic carrier concentration far exceeds the p-doping concentration, then Mg_2Sn has a negative Seebeck coefficient, and is thus no longer p-type. However, if the intrinsic carrier concentration is significant, but not dominant, then trends such as those shown in Fig. 6.49 are observed.

Overall, increasing tensile (compressive) stress increases the power factor along [110] for n-type (p-type) Mg_2Sn in the intrinsic regime. Stress in the opposite direction increases the power factor perpendicular to [110].

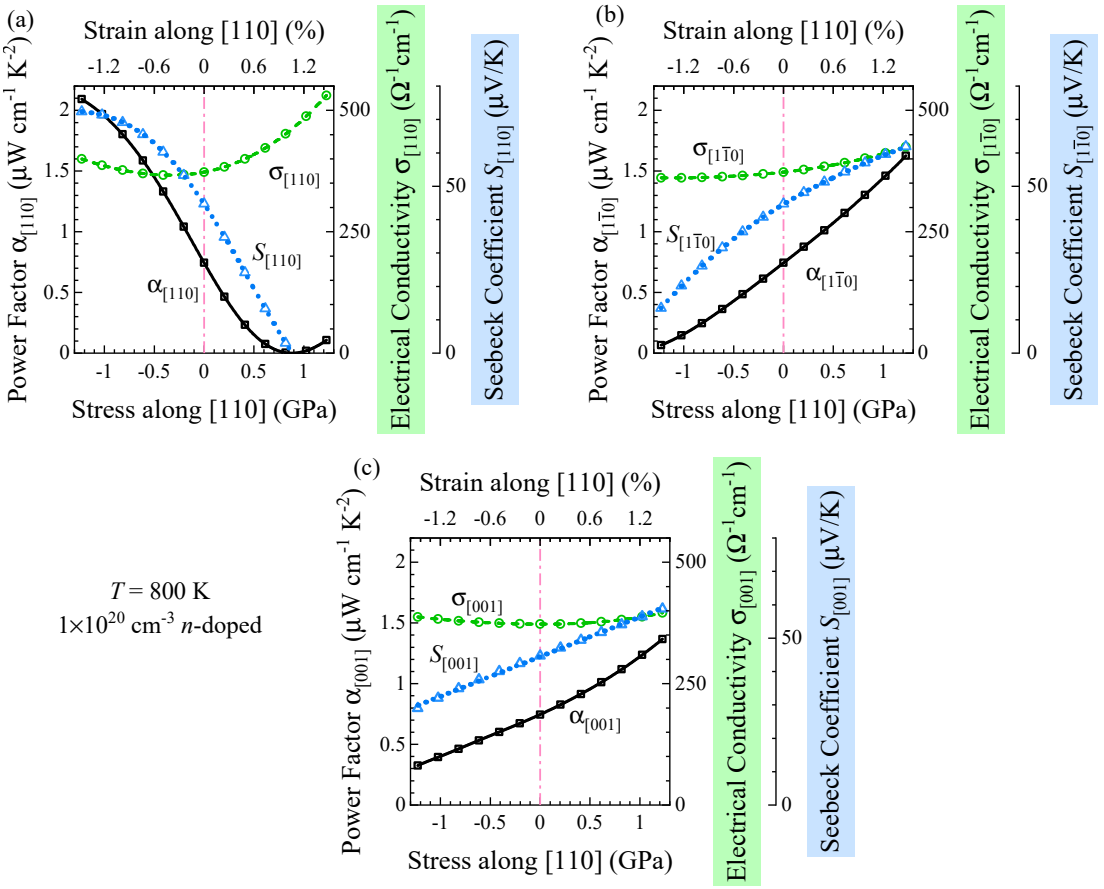

Figure 6.49 *Calculated electrical-transport properties against uniaxial [110] stress for 1×10^{20} cm^{-3} p-doped Mg_2Sn at 800 K. This case is in the intrinsic regime. Transport properties are (a) along [110], (b) along [1$\bar{1}$0], and (c) along [001]. Symbols are calculated values, lines are guides to the eye.*

Summary

For the majority of doping concentrations and temperatures considered, increasing tensile (compressive) uniaxial [110] stress increased the conductivity parallel (perpendicular to) [110] for n-type Mg_2Sn, and reduced the conductivity for p-type Mg_2Sn. In the saturated regime, the Seebeck coefficient generally concomitantly decreased. In the intrinsic regime, it increased.

Two notable exceptions are: (i) the transport properties along [001] for p-type Mg_2Sn in the saturated regime, which were approximately constant under stress, and (ii) n-doped Mg_2Sn with a carrier concentration of $\sim 5 \times 10^{19}$ cm^{-3} and below in the saturated regime, for which the conductivity along [1$\bar{1}$0] remained approximately constant under increasing comrpessive stress, and the Seebeck coefficient increased.

The key point is that, in general, the power factor of n-type (p-type) Mg_2Sn along [110] can be improved by applying either tensile (compressive) [110] stress. Crucially, the direction of stress is the same as that for improving the power factor of Mg_2Si. This indicates that $Mg_2Sn_{1-x}Si_x$ alloys can also be improved using uniaxial [110] stress.

6.3 Summary on investigations of Mg_2Si and Mg_2Sn

The electrical-transport properties of Mg_2Si and Mg_2Sn were each examined under uniaxial stress along [001], [111], and [110], respectively. Depending on the direction of stress, different mechanisms affected the transport properties. For the majority of combinations of n-doping concentration and temperature, for both Mg_2Si and Mg_2Sn, the trends in transport properties of an n-doped sample in the saturated regime are as follows:

(i) The conductivity parallel (perpendicular) to the direction of stress increases with increasing tensile (compressive) stress;

(ii) the Seebeck coefficient parallel (perpendicular) to the direction of stress decreases, or remains approximately constant, with increasing tensile (compressive) stress;

(iii) the power factor along (perpendicular to) the direction of stress increases with increasing tensile (compressive) stress. One exception was for Mg_2Sn at very high n-doping concentrations ($10^{20}\,cm^{-3}$ and above) under uniaxial [001] stress. In this case the power factor along [001] actually improves under compressive stress.

For p-doped Mg_2Si and Mg_2Sn in the saturated regime, there was little change in the transport properties under uniaxial stress along [001]. This was expected, as none of the valence bands have large anisotropic features oriented along [001]. For stress along [111] and [110], the trends are:

(i) the conductivity parallel (perpendicular to) the direction of stress increases with increasing compressive (tensile) stress;

(ii) the Seebeck coefficient parallel (perpendicular to) the direction of stress decreased, or stayed approximately constant, with increasing compressive (tensile) stress;

(iii) the thermoelectric power factor was generally greatest for unstressed Mg_2Si or Mg_2Sn, unless the p-doping concentration was low ($10^{18}\,cm^{-3}$), in which case the power factor along the direction of stress improved with increasing compressive stress.

In the intrinsic regime, the simultaneous transformation of both valence and conduction bands allows for large improvements in the power factor. If the

intrinsic carrier concentration is significant, then increasing compressive stress increases both the conductivity along the direction of stress, and the magnitude of the Seebeck coefficient, for p-type Mg_2Si or Mg_2Sn. This can lead to very large improvements in the power factor: improvements on the scale of 100 % per GPa of stress. Conversely, for n-type Mg_2Si or Mg_2Sn, increasing tensile stress concomitantly increases the conductivity and Seebeck coefficient along the direction of stress: again leading to large improvements of the power factor.

Importantly, large improvements in the power factor are possible under anisotropic stress. This is possible for both Mg_2Si and Mg_2Sn. Furthermore, both of these materials exhibit trends in their transport properties under stress which are qualitatively similar. This indicates that alloys of the form $Mg_2Sn_{1-x}Sn_x$, which are very common for thermoelectric devices, will likely exhibit these same trends under stress: also leading to large improvements in their power factors.

Chapter 7

Conclusions

Many different processes are applied to thermoelectric materials in order to improve their thermoelectric figure of merit, $ZT = \sigma S^2 T/\kappa$. Some of these processes (alloying, thin films, high-pressure growth, hot pressing) can significantly change the lattice parameters of the thermoelectric in question, locking in strains and stresses to the material. This is often done intentionally, in order to reduce the thermal conductivity κ. However, it is also important to understand how such strains and stresses can affect the electrical conductivity σ and the Seebeck coefficient S.

Previous experimental studies on lead telluride (PbTe) reported large increases in the thermoelectric power factor, $\alpha = \sigma S^2$, under increasing pressure on the scale of GPa[7–9]. Initially, this thesis set out to understand to what extent this improvement was due to fundamental changes in the bandstructure of bulk PbTe.

A thorough computational investigation was conducted, within the framework of density functional theory and Boltzmann transport theory, to examine the electron-transport properties of lead telluride under hydrostatic pressure and non-hydrostatic stress. Given the assumption of fixed doping concentration, increasing hydrostatic pressure did not increase the power factor of lead telluride. It is likely that the reported increases to the power factor are due to the doping concentration increasing with increasing pressure, possibly due to the introduction of defects in the sample which then acted as donors.

Although increasing hydrostatic pressure does not improve the power factor of PbTe, anisotropic stress can improve it. 1 GPa of stress along just one or two axes can increase the direction-dependent power factor by between 10 % and several hundreds of percent, depending on the doping concentration, temperature, and

direction of stress.

In general, increasing compressive (tensile) stress increases the power factor along the direction of stress, for p-type (n-type) PbTe. This improvement is not due to changes of the doping concentration, nor electron-scattering rate, both of which were assumed to be constant: it is perturbation of the bandstructure of PbTe under anisotropic stress that is responsible.

Several mechanisms were identified that help explain the trends in transport properties under anisotropic stress:

Intervalley transfer

Intervalley transfer is the redistribution of electrons/holes between different carrier valleys under anisotropic stress[16,71,72]. This effect occurs because PbTe has multiple valleys at the conduction and valence-band edges. Each valley is centred away from the Γ point, and charge carriers in each valley contribute towards electrical transport along any particular direction.

However, because each individual carrier-pocket has highly anisotropic transport properties, the contribution of each valley towards the conductivity along a particular crystal direction is not always equal. Depending on the crystal direction along which the electrical conductivity, or Seebeck coefficient, is measured, some valleys will have, on average, much higher mobility than the other valleys.

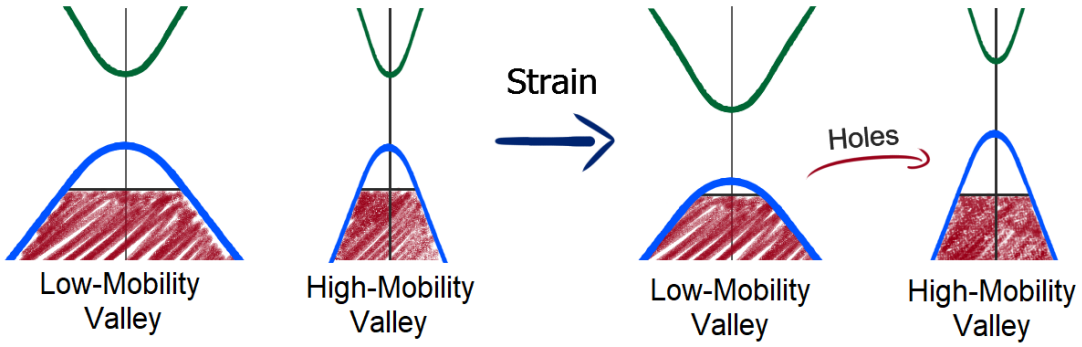

Stress which breaks the symmetry of these valleys causes electrons/holes to be redistributed between them. This can allow charge carriers to be transferred from valleys with a low mobility in a specific direction, into valleys with higher mobility: increasing the electrical conductivity along that direction.

In the saturated regime, where the doping concentration is dominant, the Seebeck coefficient generally decreased in the intervalley-transfer effect. This is because the different valleys are diverging in energy: reducing the number of valleys.

However, for many combinations of doping concentration and temperature, the power factor still increased overall.

Valley reshaping

An intervalley-transfer effect is a change in energy of distinct carrier-pockets, and the resulting redistribution of charge carriers between them. A valley-reshaping effect is the change in shape of the individual carrier pockets. This is distinct from a general increase in band curvature, like that seen in PbTe under hydrostatic stress; valley reshaping specifically implies that the gradient of the band edges are being changed more in one direction than others.

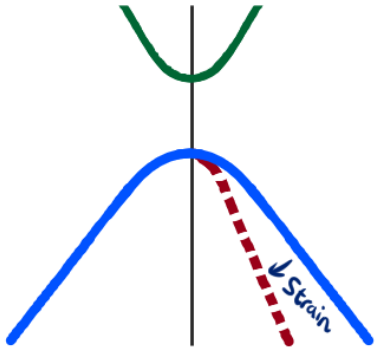

An indicator that this effect will happen under a specific direction of stress is the presence of large anisotropic features in the bandstructure near the band edges. For example, an energy isosurface of the valence band of PbTe shows a large connected structure just below the valence-band maximum (Fig. 7.1). Applying stress which breaks the symmetry of this structure changes the shape of the PbTe valence band — even near the valence-band maximum.

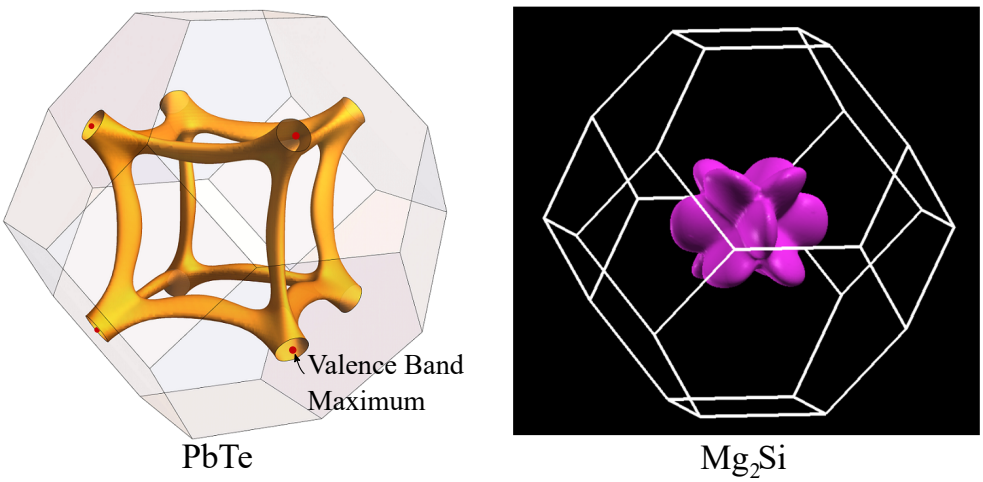

Figure 7.1 *Calculated energy isosurfaces for the valence band of PbTe (left) and Mg_2Si (right). The isosurface for PbTe is set 0.3 eV below the valence-band maximum, and the isosurface for Mg_2Si is set 0.2 eV below the valence-band maximum.*

Valley reshaping allows charge mobility to be increased along one direction, without a large reduction in the rate of change of the density of states. As a

result, anisotropic stress can change the conductivity along specific directions, and also maintain a large Seebeck coefficient.

Simultaneous Valley-Transform

If the intrinsic carrier concentration is significant compared to the doping concentration, the relative mobility of conduction-band electrons and valence-band holes is important. By applying stress which increases the relative mobility of electrons to holes, the Seebeck coefficient becomes more negative. Similarly, stress which increases the mobility of valence-band holes relative to conduction-band electrons will make the Seebeck coefficient more positive.

It was consistently found that if the intrinsic carrier concentration was significant, anisotropic stress could concomitantly increase both the electrical conductivity and the Seebeck coefficient. Under anisotropic stress, the simultaneous transformation of both valence and conduction bands can lead to large improvements in the thermoelectric power factor.

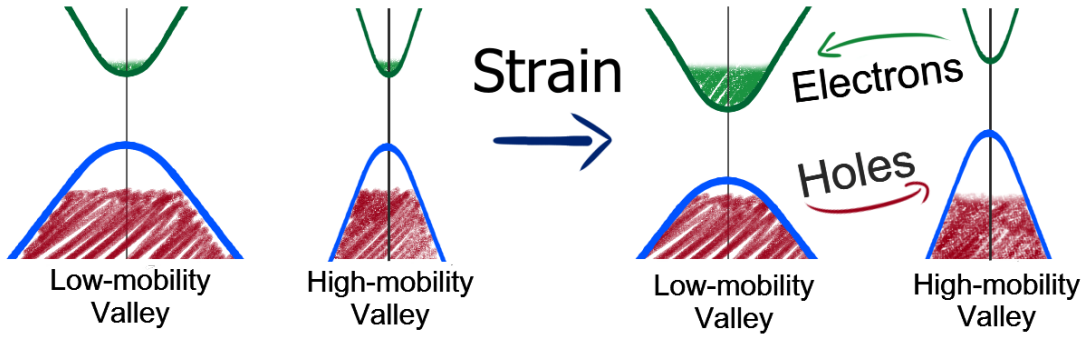

Understanding these mechanisms helped me to develop several *"rules of thumb"* for identifying new materials which can be improved by anisotropic stress:

(i) If the material has multiple valleys near the band edge, each away from Γ, and if each individual valley has anisotropic transport properties (e.g. low charge-carrier mobility along one direction, high mobility perpendicular to that) then the power factor along specific directions can potentially be increased by exploiting the intervalley-transfer effect.

(ii) If the material has large anisotropic features near the band edge (e.g. Fig. 7.1) then the a valley-reshaping effect may be induced.

(iii) If both valence and conduction bands have these features, then the simultaneous-valley-transform effect should enable the power factor to be greatly increased under anisotropic stress, if the intrinsic carrier concentration is

significant.

Guided by these rules, magnesium silicide and magnesium stannide were identified as thermoelectrics which can have their power factor improved by anisotropic stress. Indeed, uniaxial stress on the scale of 1 GPa can improve the power factor of Mg_2Si and Mg_2Sn by up to 200 %, depending on the doping concentration, temperature, and direction of stress. The changes in transport properties of Mg_2Si and Mg_2Sn could be explained in terms of the mechanisms described above.

This thesis shows that these rules of thumb can be used to identify thermoelectric materials which can have an increased power factor under anisotropic stress.

In particular, if the intrinsic carrier concentration is large compared to the doping concentration, then the increase in the power factor under stress can be very large — on the order of 100 % per GPa of stress. Thermoelectric materials often have low power factors at very high temperatures, due to the large intrinsic carrier concentration. Anisotropic stress could be a tool for increasing the efficiency of these thermoelectrics at high temperatures, thereby increasing the temperature range over which they can operate efficiently.

The mechanisms articulated in this thesis can help explain how anisotropic stress affects the electrical transport properties of a thermoelectric. Furthermore, this work shows that anisotropic stress is a promising tool for improving the direction-dependent power factor of thermoelectric materials.

Appendix A

Appendices

A.1 Some References I found Helpful

A.1.1 For the Theory behind Density Functional Theory

- CECAM Theory behind Density Functional Theory lecture series, available on youtube: https://www.youtube.com/channel/UCfLssAro7SMxgaeKTNFFeeA/videos
- Density Functional Theory: An overview [85].
- An Introduction to Density Functional Theory, by N.M. Harrison: https://www.imperial.ac.uk/media/imperial-college/research-centres-and-groups/computational-materials-science/teaching/DFT_NATO.pdf
- Quantum Mechanics of the Electron Gas: https://www.tcm.phy.cam.ac.uk/~pdh1001/thesis/node16.html
- *Electronic Structure: Basic Theory and Practical Methods* [188]
- *The Born-Oppenheimer Approximation*: http://vergil.chemistry.gatech.edu/notes/bo/bo.pdf [189]
- *Plane-waves, Pseudopotentials, and the LAPW method*, Singh, David J. and Nordstrom, Lars (2005) [190]
- *On the Nature of Self-Consistency in Density Functional Theory*, Nick Woods (2018) [191]

A.1.2 Thermoelectric Transport Theory

- *Electrons and Phonons: the theory of transport phenomenon in solids*, Ziman (1960)[16]
- *Solid State Physics*, Ashcroft & Mermin (1976)[14]
- *The Best Thermoelectric*, Mahan & Sofo (1996)[20]
- *Introduction to Solid State Physics*, Kittel (2004)[24]

A.1.3 Elastic Constants

- *Young's modulus surface and Poisson's ratio curve for cubic metals*, Zhang *et al.* (2007)[166]
- *The Directional Dependence of Elastic Stiffness and Compliance Shear Coefficients and Shear Moduli in Cubic Materials*, Knowles & Howie (2015)[167]

A.2 Implementation of density functional theory: Wien2k

An earlier section covered the foundational pillars common to most density-functional-theory implementations. This appendix summarizes some concepts used by the specific implementation of density functional theory used in this thesis: the Wien2k code. A more comprehensive overview of this code was published by the creators of the Wien2k code in 2020 [192].

A.2.1 The Augmented Plane Wave (APW) method

To solve the Kohn-Sham equations computationally, a basis must be chosen in which to expand the orbitals. However, in a real material, different regions will be better treated using different basis choices. Regions near the atom have a very high rate of change of the density, and the electron wavefunctions are usually best described using functions like the hydrogen orbitals. Regions far away from the atoms tend to have much more slowly varying electron density, and so the wavefunctions in these regions tend to be better expanded using plane-waves. The *augmented plane wave* method (APW) attempts to find the best of both worlds.

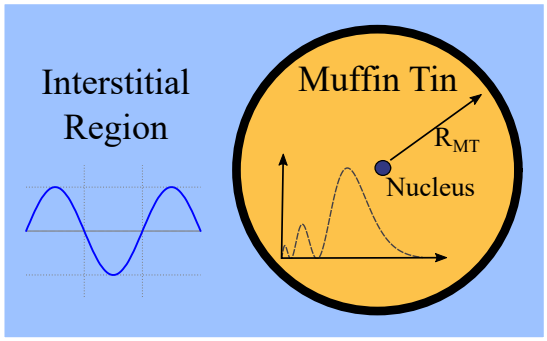

The APW method segments space by defining *"Muffin Tins"*: spherical regions of space centred on the atomic nuclei. Each Kohn-Sham orbital $\psi_{\vec{k}}$ is expanded using hydrogen-like functions as a basis set *within* a muffin tin T, and a basis of plane waves in the interstitial region between muffin tins:

$$\psi_{\vec{k}}^{\mathrm{APW}}(\vec{r}) = \begin{cases} \sum_{\vec{K}} \sum_{l,m} A_{\vec{k}+\vec{K}}^{T,lm} u_{Tl}\big(r, E_{T,l}\big)\, Y_{lm}(\vec{r}) & \vec{r} \in \text{Muffin Tin } T, \\ \frac{1}{\Omega}\left(\sum_{\vec{K}} e^{i\vec{K}\cdot\vec{r}}\right) \times e^{i\vec{k}\cdot\vec{r}} & \vec{r} \notin \text{Muffin Tin}, \end{cases} \tag{A.1}$$

where T indexs the different muffin tins within the material; Y_{lm} is the spherical harmonic function for angular quantum numbers l and m; u_{Tl} is a radial

wavefunction defined for a specific muffin tin T, angular momentum l, and energy $E_{T,l}$; Ω is just a constant used to normalize the plane-wave part; $\{K\}$ is the set of reciprocal lattice vectors; and $A^{T,lm}_{\vec{k}+\vec{K}}$ is a coefficient chosen so that the parts of the basis function inside and outside the muffin tin forms a continuous *augmented plane wave*.

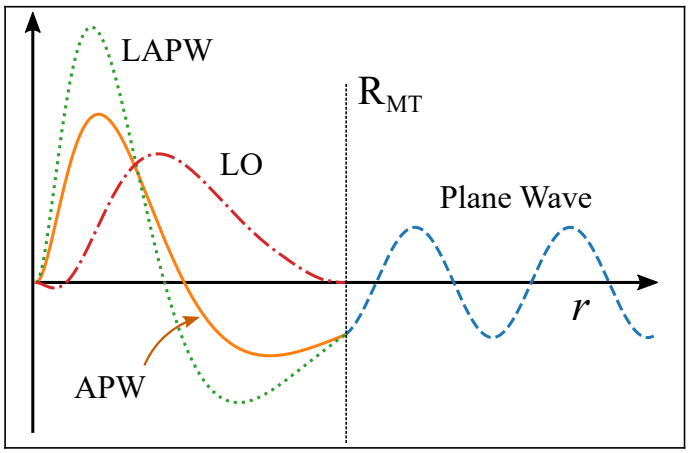

Figure A.1 *Illustration of augmented-plane-wave (APW), linearized-augment-plane-wave (LAPW), and local orbital (LO) basis functions. Outside the muffin tin radius (R_{MT}) the waveform is a plane-wave. The y-axis is arbitrary, and the basis functions have not been normalized to ease visualization.*

Both parts of the augmented plane wave involve sums over reciprocal lattice vectors $\vec{K}$. Including more and more lattice vectors $\vec{K}$ in these sums is akin to including more and more basis-vectors in an expansion of the augmented plane wave. This improves the accuracy of the calculation — at the expense of computational time. Wien2k has a parameter, the dimensionless *RKmax*, which is the radius of the muffin tin R_{MT} multiplied by the largest $\vec{K}$ used in the augmented-plane-wave expansions[192]. When conducting a calculation using Wien2k, it is important to first *converge* RKmax by performing multiple calculations with different values of RKmax, then choosing an RKmax above which the quantities of interest do not significantly change. These *convergence tests* will be elaborated in a later section.

A.2.2 Local Orbitals

In addition to augmented-plane-waves, local orbitals (LOs) are added to the basis functions. Although the augmented-plane-waves technically form a complete basis set, the addition of LOs reduces the total number of basis functions needed to accurately compute the Kohn-Sham orbitals, speeding up computation.

These local orbitals have a shape that looks like a linear combination of augmented plane waves — except that there is no plane wave outside the muffin-tin; hence the adjective *"local"*.

$$\phi_{l,m}^{\mathrm{LO}}(\vec{r}) = \begin{cases} \Big[A^{T,lm} u_{Tl}\big(r, E_{T,l}\big) + ... \\ \qquad B^{T,lm} \dot{u}_{Tl}\big(r, E_{T,l}\big) + ... \\ \qquad\qquad C^{T,lm} \tilde{u}_{Tl}\Big(r, E'_{T,l}\Big) \Big] Y_{lm}(\vec{r}) & \vec{r} \in \text{Muffin Tin } T, \\ 0 & \vec{r} \notin \text{Muffin Tin}, \end{cases} \tag{A.2}$$

where $\dot{u}$ is the first energy derivative of u, and $\tilde{u}$ is a different radial function calculated at a different energy E'. In this case, coefficients A, B, and C are determined by the requirements that ϕ^{LO} should be normalized, and have zero value and zero derivative at the boundary of the muffin tin ($\mathrm{R_{MT}}$)[192].

There is a class of local orbitals known as *relativistic* local orbitals (RLOs)[105]. These orbitals have the same constraints as ordinary local-orbitals, but are useful because they are non-zero at the nucleus $r = 0$. The shape of these orbitals is based on relativistic corrections to the hydrogen orbitals. They are particularly useful when computing materials have large spin-orbit coupling, for example, materials with lead atoms. Indeed, Larson (2003)[106] showed how the addition of RLOs was necessary to accurately compute the valence bandstructure of bismuth telluride.

A.2.3 The LAPW method

The linearized augmented plane wave (LAPW) method is similar to the APW method in most respects. A linearized augmented plane wave appears almost identical to an augmented-plane-waves, but with one additional term for the part of the basis function within the muffin tins:

$$\psi_{\vec{k}}^{\mathrm{LAPW}}(\vec{r}) = \begin{cases} \sum_{\vec{K}} \sum_{l,m} \Big[A_{\vec{k}+\vec{K}}^{T,lm} u_{Tl}\big(r, E_{T,l}\big) + ... \\ \qquad\qquad B_{\vec{k}+\vec{K}}^{T,lm} \dot{u}_{Tl}\big(r, E_{T,l}\big) \Big] Y_{lm}(\vec{r}) & \vec{r} \in \text{Muffin Tin } T, \\ \frac{1}{\Omega} \left(\sum_{\vec{K}} e^{i\vec{K}\cdot\vec{r}} \right) \times e^{i\vec{k}\cdot\vec{r}} & \vec{r} \notin \text{Muffin Tin}, \end{cases} \tag{A.3}$$

where $\dot{u}$ is the first energy derivative of u. The coefficients A and B are chosen so that the linearized augmented plane wave is continuous and first-order differentiable. By default Wien2k uses a LAPW basis for most orbitals. A small number are computed using an APW basis — usually the valence orbitals involved in chemical bonding (s,p,d) — and a small number of local orbitals are added to the basis set.

A.3 Calculation parameters

A.3.1 PbTe Calculations

Main parameters

Parameter	Stress Calculations	Transport Calculations
xc-potential	PBEsol	TB-mBJ, parameterization #2[100]
RKmax	9	7.5
k-points self-consistent	$20 \times 20 \times 20$	$28 \times 28 \times 28$
k-points non-self-consistent	N/A	$56 \times 56 \times 56$
$l$max	10	10
EMAX	5 Ry	5 Ry
GMax	$12\,{a_0}^{-1}$	$12\,{a_0}^{-1}$
Muffin Tin Radii R_{MT}	$2.5\,a_0$ for Pb & Te	$2.5\,a_0$ for Pb & Te

Local Orbital Energies

Local orbital energies are set in the `case.in1` file. Probably the easiest way to document these energies is to simply include a copy of this file. `case.in1`:

```
WFFIL  EF=.38294624266666666642   (WFFIL, WFPRI, ENFIL, SUPWF)
  7.50     10   4   ELPA pxq hm (R-MT*K-MAX,MAX L IN WF,V-NMT,lib,gridshape,hm/lm)
  0.30    4  0      (GLOBAL E-PARAMETER WITH n OTHER CHOICES, global APW/LAPW)
 2    0.75     0.0000 CONT 1
 2   -0.8530   0.0010 CONT 1
 0   -0.1269   0.0000 CONT 1
 1    0.1904   0.0000 CONT 1
  0.30    5  0      (GLOBAL E-PARAMETER WITH n OTHER CHOICES, global APW/LAPW)
 2    0.1377   0.0000 CONT 1
 2   -2.2920   0.0010 CONT 1
 0    1.00     0.0000 CONT 1
 0   -0.4461   0.0010 CONT 1
 1    0.2130   0.0000 CONT 1
K-VECTORS FROM UNIT:4   -8.5       5.0    32   emin / de (emax=Ef+de) / nband
```

With the lead atom LOs listed first, and the tellurium atom's second. The lead atoms relativistic local orbital is set in the `case.inso` file, included below:

```
WFFIL
4  0  0                 llmax,ipr,kpot
-10  1.9                Emin, Emax
    0 0 1                           h,k,l (direction of magnetization)
 1                       number of atoms with RLO
1 0.1904 0.0000 CONT              atom-number, E-param for RLO
0 0      number of atoms without SO, atomnumbers
```

A.3.2 Mg_2X Calculations

Wien2k Calculations.

Parameter	Mg_2Si calculations	Mg_2Sn calculations
xc-potential	TB-mBJ, parameterization #1	TB-mBJ, parameterization #1
RKmax	7.0	8.0
k-points self-consistent	$14 \times 14 \times 14$	$14 \times 14 \times 14$
k-points non-self-consistent	$50 \times 50 \times 50$	$50 \times 50 \times 50$
$l$max	10	10
EMAX	5 Ry	5 Ry
GMax	$12\,{a_0}^{-1}$	$12\,{a_0}^{-1}$
Muffin Tin Radii R_{MT}	2.39 for Si; 2.5 for Mg	2.5 for Sn and Mg

Local Orbital energies did not need to be altered. The defaults were used.

BoltzTraP2 Calculations

The number of interpolated k-points m for every input k-point was set to 3. The number of bins used in the histogram of states as a function of energy was increased above 10,000.

Elastic Constants

In order to apply strains commensurate with uniaxial stress, I needed to calculate the direction-dependent Poisson's ratio of Mg_2Si and Mg_2Sn from their experimental elastic constants. To do this, equations are needed relating elastic constants to the Poisson's ratio. Two equations were found in Baughman *et al.*[165], which relate the Poisson's ratio for a strain along [110] to relaxations along $[1\bar{1}0]$ and [001]. By rearranging these equations, the elastic constants could be related to the required Poisson's ratios.

I use the following notation:

$$\nu_{\hat{x}}^{\hat{y}} = -\frac{\Delta\epsilon_{\hat{y}}}{\Delta\epsilon_{\hat{x}}}, \tag{A.4}$$

where $\Delta\epsilon_{\hat{i}}$ is the strain along the $\hat{i}$ direction.

Table A.1 *Experimentally measured elastic constants and lattice parameters from literature[162,163,168,169], followed by Poisson's ratios and Young's moduli I derived.*

Property	Mg_2Si	Mg_2Sn
a_0 (Å)	6.521 [168]	6.765 [169]
$a_0(T)$ (Å)	6.3272 + 6.5e-5T + 4.0e-8T^2 [144]	6.7323 + 8.5e-5T + 3.8e-8T^2 [144]
C_{11} (GPa)	121 [162]	82.4 [163]
C_{12} (GPa)	22 [162]	20.8 [163]
C_{44} (GPa)	46.4 [162]	36.6 [163]
B_0 (GPa)	55	41
S_{11} (GPa^{-1})	0.00875	0.0135
S_{12} (GPa^{-1})	-0.0013468	-0.00272
S_{44} (GPa^{-1})	0.02155	0.0273
$\nu_{[001]}^{[100]} = \nu_{[001]}^{[010]}$	0.154	0.202
$\nu_{[111]}^{[110]} = \nu_{[111]}^{[112]}$	0.171	0.158
$\nu_{[110]}^{[110]}$	0.185	0.118
$\nu_{[110]}^{[001]}$	0.148	0.223
$Y_{[001]}$ (GPa)	114	74.0
$Y_{[111]}$ (GPa)	109	84.8
$Y_{[110]}$ (GPa)	110	81.8

A.4 Equations relating Elastic Properties

This is a short list of some useful formula for relating elastic constants to elastic compliances, Poisson's ratios, and Young's moduli. Equations taken from Zhang

et al.[166], Ballato[164], Knowles & Howie[167], and Baughman *et al.*[165].

Elastic Compliance

The elastic compliance tensor of a cubic material has the same form as the elastic constants tensor. Indeed, they are inverse tensors of each other. The elastic compliances S_{ij} and elastic constants C_{ij} are related to each other by:

$$S_{11} = \frac{C_{11} + C_{12}}{(C_{11} - C_{12})(C_{11} + 2C_{12})}, \tag{A.5}$$

$$S_{12} = \frac{-C_{12}}{(C_{11} - C_{12})(C_{11} + 2C_{12})}, \tag{A.6}$$

$$S_{44} = \frac{1}{C_{44}}. \tag{A.7}$$

The inverse equations are obtained simply by switching each C_{ij} with its counterpart S_{ij}.

Young's Modulus

The Young's modulus $Y_{[hkl]}$ for a cubic material being strained perpendicular to the plane given by Miller index $[hkl]$ is given in terms of the elastic compliance coefficients S_{11}, S_{12}, and S_{44} as:

$$Y_{[hkl]} = \frac{1}{S_{11} - 2\left(S_{11} - S_{12} - \frac{1}{2}S_{44}\right)\Gamma}, \tag{A.8}$$

$$\text{where} \qquad \Gamma = \frac{(hk)^2 + (hl)^2 + (kl)^2}{\left(h^2 + k^2 + l^2\right)^2}. \tag{A.9}$$

Poisson's Ratio

The Poisson's ratio for principal strain normal to the plane given by Miller index $[hkl]$ is direction dependent. For example, uniaxial stress along [110] induces a different strain along $[1\bar{1}0]$ than along [001]. For notation, the Poisson's ratio $\nu_{[hkl]}^{[\alpha\beta\gamma]}$ is given by

$$\nu_{[hkl]}^{[\alpha\beta\gamma]} = -\frac{\Delta\epsilon_{[\alpha\beta\gamma]}}{\Delta\epsilon_{[hkl]}}, \tag{A.10}$$

where $\Delta\epsilon_{[hkl]}$ and $\Delta\epsilon_{[\alpha\beta\gamma]}$ is the strain perpendicular to the plane given by the Miller indices $[hkl]$ and $[\alpha\beta\gamma]$, respectively, The plane given by $[\alpha\beta\gamma]$ is assumed

to be perpendicular to $[hkl]$.

This Poisson's ratio $\nu_{[hkl]}^{[\alpha\beta\gamma]}$ can be calculated using the elastic compliance coefficients S_{11}, S_{12}, and S_{44} [166]. It depends on the angle θ between the normal to the $[\alpha\beta\gamma]$ plane and the normal to a reference plane $[hlkl-(h^2+k^2)]$:

$$\theta = \arccos\left[\frac{\alpha hl + \beta kl - \gamma\left(h^2+k^2\right)}{\left(\alpha^2+\beta^2+\gamma^2\right)\left(h^2l^2+k^2l^2+\left(h^2+k^2\right)^2\right)}\right]. \tag{A.11}$$

The Poisson's ratio is given by:

$$\begin{aligned}\nu_{[hkl]}^{[\alpha\beta\gamma]} = \Bigg\{ S_{12} + \frac{S_{11}-S_{12}-\frac{1}{2}S_{44}}{h^2+k^2+l^2} \times \Bigg[&\left(\frac{h^2 l}{\sqrt{h^2+k^2}\sqrt{h^2+k^2+l^2}}\cos\theta - \frac{hk}{\sqrt{h^2+k^2}}\sin\theta\right)^2 \ldots \\ &+ \left(\frac{k^2 l}{\sqrt{h^2+k^2}\sqrt{h^2+k^2+l^2}}\cos\theta + \frac{hk}{\sqrt{h^2+k^2}}\sin\theta\right)^2 \ldots \\ &+ \left(\frac{l\sqrt{h^2+k^2}}{\sqrt{h^2+k^2+l^2}}\cos\theta\right)^2 \Bigg] \Bigg\} \Bigg/ \ldots \\ &\left[-S_{11} + (2S_11 - 2S_{12} - S_{44}) \times \frac{h^2k^2+h^2l^2+k^2l^2}{\left(h^2+k^2+l^2\right)^2}\right].\end{aligned} \tag{A.12}$$

Again, the plane $[\alpha\beta\gamma]$ is assumed to be perpendicular to $[hkl]$. Importantly, this equation assumes the indices $[hkl]$ are in descending order, e.g. [100] rather than [001].

A.5 The Kane Model

The Kane model is given by an equation of the form,

$$E(\Delta\boldsymbol{k}) = E_0 \pm \left(E_\alpha - \sqrt{E_\alpha^2 + \sum_i \left(\boldsymbol{P}_i \cdot \Delta\boldsymbol{k}\right)^2}\right), \tag{A.13}$$

where $\Delta\boldsymbol{k}$ is the distance in k-space from the band extremum, E_0 is the energy of the band edge, E_α is a parameter which defines the energy scale over which the Kane-model appears parabolic, and $\boldsymbol{P}_i$ describe the orientation of the bandstructure and its gradient at large $\Delta\boldsymbol{k}$. Technically the Kane-model relates E_α and $\boldsymbol{P}_i$ to the band gap, however, for the purpose of fitting the bandstructure

they can be treated like free parameters.

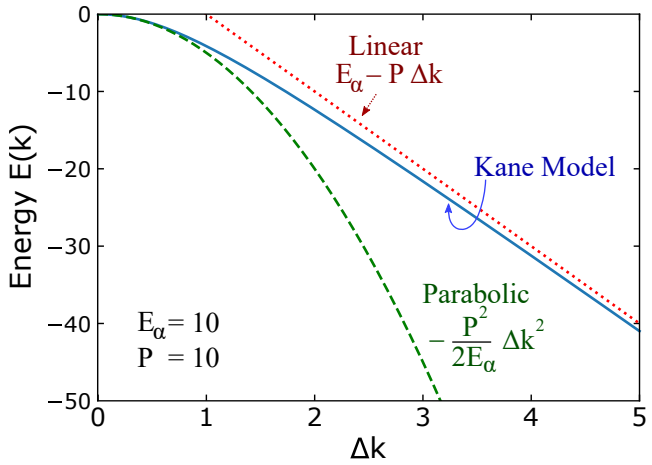

Figure A.2 *A Kane-type dispersion for arbitrarily chosen parameters (Eq. 2.66).*

Figure A.2 plots the general shape of this bandstructure for arbitrarily chosen E_α and P. As $E_\alpha \to \infty$ the Kane-model tends towards a parabolic band. When $\Delta\boldsymbol{k} \gg E_\alpha$ the bandstructure is linear, with a gradient given by P. In three dimensions, the vectors $\boldsymbol{P}_1, \boldsymbol{P}_2, \boldsymbol{P}_3$ describe the orientation of the bandstructure. They are mutually-orthogonal, each with dimensions of energy × length, and oriented along the major axes of the band edges. Often people will describe a Kane-model which cross-sections that are ellipses of revolution[32] — in which case $\boldsymbol{P}_1$ would be along the major axis $\boldsymbol{P}_{||}$, and $\boldsymbol{P}_2 = \boldsymbol{P}_3 = \boldsymbol{P}_\perp$.

Rearranging the Kane Model

Normally the Kane model is written in terms of the effective mass. Here I show how it can be rearranged to the form shown in equation A.13. I start with the normal expression for the Kane model, as shown in Cao *et al.*[32]:

$$E(1+\gamma E) = \frac{\hbar^2}{2}\left(\frac{k_{||}^2}{m_{||}^*} + \frac{k_\perp^2}{m_\perp^*}\right), \tag{A.14}$$

where they call γ the *nonparabolicity* parameter, with dimensions 1/energy. For simplicity I will first define $E_\alpha := 1/2\gamma$, since we will always consider a non-parabolic band, and this way E_α has the intuitive dimensions of energy. For

brevity I shall also wrap up the right hand side as C:

$$E\left(1+\frac{1}{2E_\alpha}E\right)=C, \tag{A.15}$$

$$\frac{1}{2E_\alpha}E^2+E-C=0, \tag{A.16}$$

$$E^2+2E_\alpha E-2E_\alpha C=0, \tag{A.17}$$

$$E=\frac{1}{2}\left(-2E_\alpha\pm\sqrt{4E_\alpha^2+8E_\alpha C}\right), \tag{A.18}$$

$$=-E_\alpha\pm\sqrt{E_\alpha^2+2E_\alpha C}. \tag{A.19}$$

Now let,

$$C:=\frac{1}{2E_\alpha}\left(\boldsymbol{P_1}\cdot\boldsymbol{k}\right)^2\left(\boldsymbol{P_2}\cdot\boldsymbol{k}\right)^2\left(\boldsymbol{P_3}\cdot\boldsymbol{k}\right)^2=\frac{1}{2E_\alpha}\sum_i\left(\boldsymbol{P_i}\cdot\boldsymbol{k}\right)^2. \tag{A.20}$$

If we recenter so when the distance of $\boldsymbol{k}$ from the band extremum $\Delta\boldsymbol{k}=0$, the energy $E=0$:

$$E=\pm\left(E_\alpha-\sqrt{E_\alpha^2+\sum_i\left(\boldsymbol{P}_i\cdot\boldsymbol{\Delta k}\right)^2}\right), \tag{A.21}$$

With the equation in this form, E_α is a parameter which defines the energy scale over which the Kane-model appears parabolic. As $E_\alpha\to\infty$, the Kane-model tends towards a parabolic band. P_1, P_2, P_3 are three orthogonal vectors, each with dimensions of energy $\times$ length, oriented along the major axes of the band. Often people will describe a Kane-model which cross-sections that are ellipses of revolution — in which case P_1 would be along the major axis $P_{||}$, and $P_2=P_3=P_\perp$. The P vectors parameterize the energy gradient of the bandstructure at large $\boldsymbol{k}$:

$$E\to\pm\left(E_\alpha-\sum_i\boldsymbol{P}_i\cdot\boldsymbol{\Delta k}\right),\quad\text{as}\quad|\Delta\boldsymbol{k}|\to\infty. \tag{A.22}$$

A.6 Problem of using PBEsol for transport calculations

PBEsol calculates the pressure dependence of the bandgap as positive, when in experiment it is found to be negative[49]. Furthermore, the PBEsol exchange

correlation potential has incorrect band ordering at the L-point for volumes around the calculated $V_{0,\mathrm{PBEsol}}$, a feature shared with the local-density-approximation[36]. Figure A.3 shows the bandstructure of unstressed PbTe as calculated by PBEsol, where the thickness of the lines is commensurate with the p-orbital character of the plotted bloch state. Figure A.3 shows a band-character inversion at the L-point - a characteristic of topological insulators. However, PbTe is not a topological insulator[193].

Figure A.3 also shows the Σ valence-band-maxima, about halfway between the Γ and K points, is far higher in energy than one would expect based on other calculations or experiments[36] [38] [194] [67] [66]. Both of these suggest that, while PBEsol is appropriate for estimating stress as a function of strain, it is inappropriate for calculating how the electron transport properties of PbTe.

At similar lattice parameters ($a_0 \approx 6.45\,\text{Å}$) the PBE-GGA exchange correlation potential also has a band inversion, and positive pressure dependence of the band gap. However, the PBE-GGA potential overestimates a_0 significantly ($a_{0,\mathrm{PBE}}$ ≈6.55–6.58 Å[195–197]). At volumes around $a_{0,\mathrm{PBE}}$ the pressure dependence of the band gap is negative, and there is no character inversion around the L-point. LDA, PBE, PBEsol, and the TB-mBJ functional all share a similar pattern. At very large volumes there is no band-character inversion at the L-point. The band gap closes under as the volume is reduced, eventually reaching zero with a dirac point. Under further compression the band gap begins to open again, this time with a character inversion at the L-point.

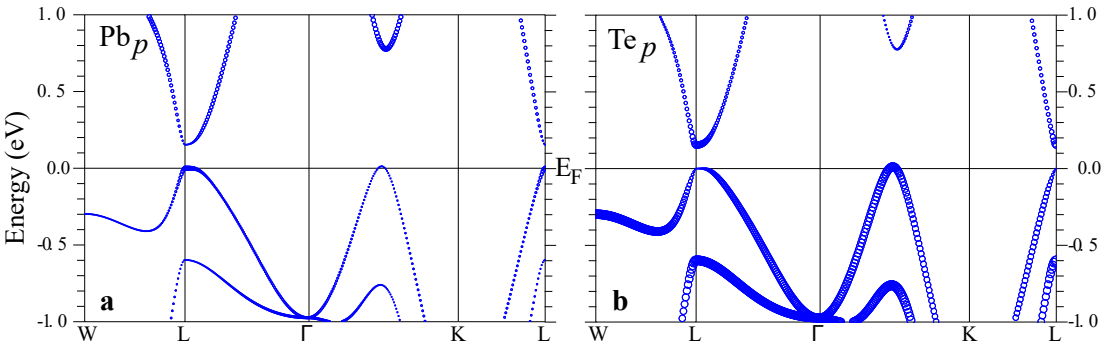

Figure A.3 *Band character of (a) Pb p-orbital and (b) Te p-orbital made using the PBEsol-GGA exchange correlation potential. Calculated with a lattice parameter $a = 6.439\,\text{Å}$.*

q

A.7 Tables of published data about PbTe

List of tables:

Table A.2 *Table of a_0 values*

Property	Value	Pressure	Temp	Exp/T	Notes	Reference
a	6.4879/454 Å	ambient	300K/0K	Exp	Calculated using an x-ray parameter and a different paper's thermal expansion coefficient.[114]	T & C.[48]
a	6.4611(3)Å	ambient	room	Exp	Neutron diffraction. 2003	[127]
a	6.431 Å	ambient	0K	Exp/T	Made using thermal expansion data from[114] and applying to a from[127]	[114,127] & me.
a	6.4541(9) Å	ambient	298 K	Exp	Does not quite fit with my predicted a_0 using thermal expansion data (above). I predict a_{298K} = 6.464, $a_{120K} \approx 6.44$Å	1987[128]
a	6.4384(4) Å	ambient	120K	Exp		1987[128]
a	6.573 Å	ambient	0K (DFT)	T	VASP-PAW, PBE-GGA, no SO coupling, BM EoS	2014[198]
a	6.58 Å	ambient	0K*	T	PBE-GGA+SO FP-LAPW method, Wien2k	2010[196]
a	$6.422 + (0.9545\text{x}10^{-4})T + (2.615\text{x}10^{-8})T^2$ Å	-	-	E		2013[45]
a	6.4534 Å	ambient	0K	T	My calculation. PBEsol+SO, no RLO.	

Table A.3 *Table of elastic constants and thermal expansion coefficients*

Property	Value	Pressure	Temp	Exp/T	Notes	Reference
B_0	45.63 GPa	ambient	0 K	Exp	extrapolated from 4.2 K	1968[114]
B_0	41.13 GPa	ambient	303 K	Exp		1968[114]
B_0	39.8/41.1 GPa	ambient	300/303 K	Exp		1983[199]
B_0, B'	39.1 GPa, 4.00	ambient	0K*	T	VASP-PAW, PBE-GGA, no SO coupling, BM EoS	2014[198]
B_0, B'	38.5 GPa, 4.50	ambient	0K*	T	PBE-GGA+SO FP-LAPW method, Wien2k	2010[196]
B_0, B'	39.95 GPa, 4.32	ambient	0K*	T	PBE-GGA Wien2k, no SO mentioned.	2011[200]
B_0	45.6 GPa	ambient	0K*	T	Calculated using phonons as well	[197]
α	1.98/2.04 ($10^{-5}K^{-1}$)	ambient	300/303 K	Exp		1983[199]
E_g	0.19 meV	ambient	0K	Exp	Extrapolated	[199]
E_g	0.19 meV	ambient	4.2K	Exp		[201]
$\partial E_g/\partial P\|_T$	-74 meV/GPa	ambient	295K	Exp		[49]
B_0	43.70 GPa	ambient	0K	T	My calculation. PBEsol+SO, no RLO	

Table A.4 *Band Gap data*

Property	Value	T	Exp/T	Notes	Reference
dE_g/dT	+4.5 x 10^{-4} eV/K	average from 90-295 K	Exp	-	[49]
dE_g/dP	-7.4 x 10^{-3} eV/kbar	295K	Exp	-	[49]
dE_g/dP	$-7 \rightarrow -9$ meV / GPa	Unclear. Presumably room temp.	Exp.	Hall and elec. resist vs T.	[59]
$\partial E_g/\partial T\|_V$	+2.8 x 10^{-4} eV/K	estimate	Exp	estimated using above results	[49]

Table A.5 *Miscellaneous data*

Property	Value	T	Exp/T	Notes	Reference
ν from $\mu \propto T^{-\nu}$	$1.2 \rightarrow 2.5$	up to room temp	Exp	Mobility vs T up to 300 K. Large value for low doping.	[59]

A.8 Table of Published Data about Mg_2X

A.8.1 Band Gap of Mg_2Si

Table A.6 *Band Gap, and Band Gap gradients for Mg_2Si.*

Band Gap (eV)	Method	Notes	Ref.
0.77	absorption, calculated from dielectric function	Room temp, polycrystal thin film layers	[202]
0.74	absorption	Thin films, room temp	[203]
0.78 ± 0.05	hall coefficient temperature curve	Single crystal, 0 K extrapolation from 70 K	[178]
0.74 - 0.66	optical absorption	bulk single crystal. 0.74 at 4 K, 0.66 at 300 K.	[204]
0.69 - 0.61	optical absorption	4 - 300 K. Cleaved single crystals.	[171]
0.60-0.78		Citing a variety of other papers	[205]
Gap Gradient	**Method**	**Notes**	**Ref.**
$\frac{\partial G}{\partial T} = -5 \times 10^{-4}$ eV/K	Infrared Absorption with T	Only gradients reported.	[206]
$\frac{\partial G}{\partial P} = 0 \pm 5$ meV / GPa	Absorption edge with P	Only gradients reported	[153]

Bibliography

[1] L. Anatychuk, Journal of Thermoelectricity , 5 (2004).

[2] D. Beretta, N. Neophytou, J. M. Hodges, M. G. Kanatzidis, D. Narducci, M. Martin-Gonzalez, M. Beekman, B. Balke, G. Cerretti, W. Tremel, A. Zevalkink, A. I. Hofmann, C. Müller, B. Dörling, M. Campoy-Quiles, and M. Caironi, *Thermoelectrics: From history, a window to the future*, Materials Science and Engineering: R: Reports **138**, 100501 (2019).

[3] Seebeck's Couples, https://www.chemistryworld.com/opinion/seebecks-couples/4012173.article, accessed: 01/02/2021.

[4] T. J. Seebeck, *Ueber den Magnetismus der galvanischen Kette.* (1822).

[5] T. M. of RetroTechnology, Thermo-Electric Generators, http://www.douglas-self.com/MUSEUM/POWER/thermoelectric/thermoelectric.htm#clam, accessed: 01/02/2021.

[6] NASA, NASA: Radioisotope Power Systems, https://rps.nasa.gov/power-and-thermal-systems/legacy-power-systems/, accessed: 02/02/2021.

[7] S. V. Ovsyannikov and V. V. Shchennikov, *Pressure-tuned colossal improvement of thermoelectric efficiency of PbTe*, Applied Physics Letters **90**, 122103 (2007).

[8] J. Baker, R. Kumar, C. Park, C. Kenney-Benson, A. Cornelius, and N. Velisavljevic, *High-pressure Seebeck coefficients and thermoelectric behaviors of Bi and PbTe measured using a Paris-Edinburgh cell*, Journal of Synchrotron Radiation **23**, 1368 (2016).

[9] M. K. Jacobsen, R. S. Kumar, and A. L. Cornelius, *Transport Properties of Ni and PbTe Under Pressure*, Journal of Electronic Materials **41**, 633 (2012).

[10] Y. Amagai, T. Shimazaki, K. Okawa, H. Fujiki, T. Kawae, and N.-H. Kaneko, *Precise measurement of absolute Seebeck coefficient from Thomson effect using AC-DC technique*, AIP Advances **9**, 065312 (2019).

[11] H. S. Kim, W. Liu, G. Chen, C.-W. Chu, and Z. Ren, *Relationship between thermoelectric figure of merit and energy conversion efficiency*, Proceedings of the National Academy of Sciences **112**, 8205 (2015).

[12] G. J. Snyder and A. H. Snyder, *Figure of merit ZT of a thermoelectric device defined from materials properties*, Energy & Environmental Science **10**, 2280 (2017).

[13] G. J. Snyder and A. H. Snyder, Tool for calculating thermoelectric device efficiency, `http://thermoelectrics.matsci.northwestern.edu/thermoelectrics/ztcalc.html`, accessed: October 2019.

[14] N. W. Ashcroft and N. Mermin, *Solid State Physics* (Brooks/Cole, Cenage Learning, 1976).

[15] J. Ziman, *Principles of the Theory of Solids* (Cambridge University Press, 1972).

[16] J. Ziman, *Electrons and Phonons. The theory of transport phenomena in solids* (Oxford University Press, 1960).

[17] G. D. Mahan, *Many-particle physics*, third edition ed. (New York ; Kluwer Academic/Plenum Publishers, 2000).

[18] J. M. Luttinger, *Theory of Thermal Transport Coefficients*, Physical Review **135**, A1505 (1964).

[19] F. G. Eich, M. Di Ventra, and G. Vignale, *Density-Functional Theory of Thermoelectric Phenomena*, Physical Review Letters **112**, 196401 (2014).

[20] G. D. Mahan and J. O. Sofo, *The best thermoelectric*, Proceedings of the National Academy of Sciences of the United States of America **93**, 7436 (1996).

[21] G. J. Snyder and E. S. Toberer, *Complex Thermoelectric Materials*, Nature Materials **7**, 105 (2008).

[22] X. Chen, D. Parker, and D. J. Singh, *Importance of non-parabolic band effects in the thermoelectric properties of semiconductors.*, Scientific Reports **3**, 3168 (2013).

[23] X. Zhang and L.-D. Zhao, *Thermoelectric materials: Energy conversion between heat and electricity*, Journal of Materiomics **1**, 92 (2015).

[24] C. Kittel, *Introduction to solid state physics*, 8th ed. (Wiley, 2004).

[25] E. Gamarekian, First Atom Battery Developed by U.S. (1959), copyright - Copyright The Washington Post Company Jan 17, 1959; Last updated - 2010-07-17.

[26] O. M. Løvvik, K. Berland, F. Remonato, E. Sagvolden, and E. Flage-Larsen, *Screening thermoelectric materials with ab initio atomistic modelling and machine learning techniques*, 17th European Conference on Thermoelectrics (2019).

[27] C. M. Jaworski, M. D. Nielsen, H. Wang, S. N. Girard, W. Cai, W. D. Porter, M. G. Kanatzidis, and J. P. Heremans, *Valence-band structure of highly efficient p-type thermoelectric PbTe-PbS alloys*, Physical Review B **87**, 045203 (2013).

[28] Z. Ye, S. Cui, T. Shu, S. Ma, Y. Liu, Z. Sun, J.-W. Luo, and H. Wu, *Electronic band structure of epitaxial PbTe (111) thin films observed by angle-resolved photoemission spectroscopy*, Physical Review B **95**, 165203 (2017).

[29] Y. Pei, Z. M. Gibbs, A. Gloskovskii, B. Balke, W. G. Zeier, and G. J. Snyder, *Optimum Carrier Concentration in n-Type PbTe Thermoelectrics*, Advanced Energy Materials **4**, 1400486 (2014).

[30] J. P. Heremans, B. Wiendlocha, and A. M. Chamoire, *Resonant levels in bulk thermoelectric semiconductors*, Energy & Environmental Science **5**, 5510 (2012).

[31] Y. Pei, H. Wang, and G. J. Snyder, *Band Engineering of Thermoelectric Materials*, Advanced Materials **24**, 6125 (2012).

[32] J. Cao, J. D. Querales-Flores, A. R. Murphy, S. Fahy, and I. Savić, *Dominant electron-phonon scattering mechanisms in n-type PbTe from first principles*, Physical Review B **98**, 205202 (2018).

[33] P. Walmsley, D. M. Abrams, J. Straquadine, M. K. Chan, R. D. McDonald, P. Giraldo-Gallo, and I. R. Fisher, *Sharp increase in the density of states in PbTe upon approaching a saddle point in the band structure*, Physical Review B **99**, 035105 (2019).

[34] P. Y. Yu and M. Cardona, Electronic Band Structures, in *Fundamentals of Semiconductors: Physics and Materials Properties* (Springer Berlin Heidelberg, Berlin, Heidelberg, 1996) pp. 17–105.

[35] P. Giraldo-Gallo, B. Sangiorgio, P. Walmsley, H. J. Silverstein, M. Fechner, S. C. Riggs, T. H. Geballe, N. A. Spaldin, and I. R. Fisher, *Fermi surface evolution of Na-doped PbTe studied through density functional theory calculations and Shubnikov–de Haas measurements*, Physical Review B **94**, 195141 (2016).

[36] A. Svane, N. E. Christensen, M. Cardona, A. N. Chantis, M. van Schilfgaarde, and T. Kotani, *Quasiparticle self-consistent GW calculations for PbS, PbSe, and PbTe: Band structure and pressure coefficients*, Physical Review B **81**, 245120 (2010).

[37] D. J. Singh, *Doping-dependent thermopower of PbTe from Boltzmann transport calculations*, Physical Review B **81**, 195217 (2010).

[38] D. Parker, X. Chen, and D. J. Singh, *High Three-Dimensional Thermoelectric Performance from Low-Dimensional Bands*, Physical Review Letters **110**, 146601 (2013).

[39] R. Tauber, A. Machonis, and I. Cadoff, *Thermal and optical energy gaps in PbTe*, Journal of Applied Physics **37**, 4855 (1966).

[40] R. S. Allgaier, *New Method for Computing the Weak-Field Hall Coefficient*, Physical Review **165**, 775 (1968).

[41] Crocker, A. J. and Rogers, L. M., *Valence band structure OF PbTe*, J. Phys. Colloques **29**, C4 (1968).

[42] Y. Xiao, H. Wu, J. Cui, D. Wang, L. Fu, Y. Zhang, Y. Chen, J. He, S. J. Pennycook, and L.-D. Zhao, *Realizing high performance n-type PbTe by synergistically optimizing effective mass and carrier mobility and suppressing bipolar thermal conductivity*, Energy & Environmental Science **11**, 2486 (2018).

[43] A. F. Gibson, *The Absorption Spectra of Single Crystals of Lead Sulphide, Selenide and Telluride*, Proceedings of the Physical Society. Section B **65**, 378 (1952).

[44] W. Scanlon, *Recent advances in the optical and electronic properties of PbS, PbSe, PbTe and their alloys*, Journal of Physics and Chemistry of Solids **8**, 423 (1959).

[45] Z. M. Gibbs, H. Kim, H. Wang, R. L. White, F. Drymiotis, M. Kaviany, and G. J. Snyder, *Temperature dependent band gap in PbX (X=S, Se, Te)*, Applied Physics Letters **103**, 262109 (2013).

[46] M. Baleva, T. Georgiev, and G. Lashkarev, *On the temperature dependence of the energy gap in PbSe and PbTe*, Journal of Physics: Condensed Matter **2**, 2935 (1990).

[47] N. Piccioli, J. M. Besson, and M. Balkanski, *Optical constants and band gap of PbTe from thin film studies between 25 and* 300^oK, Journal of Physics and Chemistry of Solids **35**, 971 (1974).

[48] Y. W. Tsang and M. L. Cohen, *Band ordering in PbTe*, Solid State Communications **9**, 261 (1971).

[49] V. Prakash, *The optical absorption edge in the lead salts and its variation with temperature and pressure*, Ph.D. thesis, Harvard Univ Cambridge Mass Div Of Engineering and Applied Physics (1967).

[50] A. A. Averkin and P. G. Dermezshi, *Effect of pressure on the electric properties of PBTE*, Soviet Physics-Solid State **8**, 79 (1966).

[51] J. D. Querales-Flores, J. Cao, S. Fahy, and I. Savić, *Temperature effects on the electronic band structure of PbTe from first principles*, Physical Review Materials **3**, 055405 (2019).

[52] H. Sitter, K. Lischka, and H. Heinrich, *Structure of the second valence band in PbTe*, Physical Review B **16**, 680 (1977).

[53] H. Kim and M. Kaviany, *Effect of thermal disorder on high figure of merit in PbTe*, Physical Review B **86**, 045213 (2012).

[54] M. Lach-hab, D. A. Papaconstantopoulos, and M. J. Mehl, *Electronic structure calculations of lead chalcogenides PbS, PbSe, PbTe*, Journal of Physics and Chemistry of Solids **63**, 833 (2002).

[55] B. Sangiorgio, E. S. Bozin, C. D. Malliakas, M. Fechner, A. Simonov, M. G. Kanatzidis, S. J. L. Billinge, N. A. Spaldin, and T. Weber, *Correlated local dipoles in PbTe*, Physical Review Materials **2**, 085402 (2018).

[56] B. Rashid, M. Hilal, S. H. Khan, and A. Khan, *First principles study of the spin–orbit interaction effect on the opto-electric properties of lead telluride*, Materials Science in Semiconductor Processing **41**, 83 (2016).

[57] R. D'Souza, J. Cao, J. D. Querales-Flores, S. Fahy, and I. Savić, *Electron-phonon scattering and thermoelectric transport in p-type PbTe from first principles*, Physical Review B **102**, 115204 (2020).

[58] J. Cao, J. Querales-Flores, S. Fahy, and I. Savić, *Thermally induced band gap increase and high thermoelectric figure of merit of n-type PbTe*, Materials Today Physics **12**, 100172 (2020).

[59] Y. Ravich, B. A. Efimova, and I. Smirnov, *Semiconducting Lead Chalcogenides* (Springer, Boston, MA, 1970).

[60] P. J. Stiles, E. Burstein, and D. N. Langenberg, *de Haas-van Alphen Effect in p-Type PbTe and n-Type PbS*, Journal of Applied Physics **32**, 2174 (1961).

[61] K. F. Cuff, M. R. Ellett, and C. D. Kuglin, *Oscillatory Magnetoresistance in the Conduction Band of PbTe*, Journal of Applied Physics **32**, 2179 (1961).

[62] R. S. Allgaier, *Valence Bands in Lead Telluride*, Journal of Applied Physics **32**, 2185 (1961).

[63] R. H. Rediker and A. R. Calawa, *Magnetotunneling in Lead Telluride*, Journal of Applied Physics **32**, 2189 (1961).

[64] R. S. Allgaier and B. B. Houston, *Hall Coefficient Behavior and the Second Valence Band in Lead Telluride*, Journal of Applied Physics **37**, 302 (1966).

[65] A. J. Crocker and L. M. Rogers, *Interpretation of the Hall coefficient, electrical resistivity and Seebeck coefficient of p-type lead telluride*, British Journal of Applied Physics **18**, 563 (1967).

[66] J. Androulakis, I. Todorov, D.-Y. Chung, S. Ballikaya, G. Wang, C. Uher, and M. Kanatzidis, *Thermoelectric enhancement in PbTe with K or Na codoping from tuning the interaction of the light- and heavy-hole valence bands*, Physical Review B **82**, 115209 (2010).

[67] Y. Pei, A. LaLonde, S. Iwanaga, and G. J. Snyder, *High thermoelectric figure of merit in heavy hole dominated PbTe*, Energy & Environmental Science **4**, 2085 (2011).

[68] M. Hong, Z.-G. Chen, Y. Pei, L. Yang, and J. Zou, *Limit of zT enhancement in rocksalt structured chalcogenides by band convergence*, Physical Review B **94**, 161201 (2016).

[69] Y. Pei, X. Shi, A. LaLonde, H. Wang, L. Chen, and G. J. Snyder, *Convergence of electronic bands for high performance bulk thermoelectrics*, Nature **473**, 66 (2011).

[70] A. Ishida, H. T. X. Thao, S. Nakashima, H. Yamamoto, and M. Ishikiriyama, *Thermoelectric properties of PbTe films and PbTe-based superlattices*, Materials Today: Proceedings **5**, 10187 (2018), 14th European Conference on Thermoelectrics.

[71] J. R. Burke, *Piezoresistance Effect in p-Type PbTe*, Physical Review **160**, 636 (1967).

[72] C. Herring, *Transport Properties of a Many-Valley Semiconductor*, Bell System Technical Journal **34**, 237 (1955).

[73] A. Schmitz, C. Stiewe, K. Zabrocki, J. de Boor, K. Mull, and E. Müller, *Current assisted sintering of PbTe — Effects on thermoelectric and mechanical properties*, Materials Research Bulletin **86**, 159 (2017).

[74] Y. Gelbstein, G. Gotesman, Y. Lishzinker, Z. Dashevsky, and M. Dariel, *Mechanical properties of PbTe-based thermoelectric semiconductors*, Scripta Materialia **58**, 251 (2007).

[75] J. E. Ni, E. D. Case, K. N. Khabir, R. C. Stewart, C.-I. Wu, T. P. Hogan, E. J. Timm, S. N. Girard, and M. G. Kanatzidis, *Room temperature Young's modulus, shear modulus, Poisson's ratio and hardness of PbTe–PbS thermoelectric materials*, Materials Science and Engineering: B **170**, 58 (2010).

[76] F. Ren, E. D. Case, J. R. Sootsman, M. G. Kanatzidis, H. Kong, C. Uher, E. Lara-Curzio, and R. M. Trejo, *The high-temperature elastic moduli of polycrystalline PbTe measured by resonant ultrasound spectroscopy*, Acta Materialia **56**, 5954 (2008).

[77] Y. Katsura, M. Kumagai, T. Kodani, M. Kaneshige, Y. Ando, S. Gunji, Y. Imai, H. Ouchi, K. Tobita, K. Kimura, and K. Tsuda, *Data-driven analysis of electron relaxation times in PbTe-type thermoelectric materials*, Science and Technology of Advanced Materials **20**, 511 (2019).

[78] Q. Song, T.-H. Liu, J. Zhou, Z. Ding, and G. Chen, *Ab initio study of electron mean free paths and thermoelectric properties of lead telluride*, Materials Today Physics **2**, 69 (2017).

[79] T. Gunst, T. Markussen, K. Stokbro, and M. Brandbyge, *First-principles method for electron-phonon coupling and electron mobility: Applications to two-dimensional materials*, Physical Review B **93**, 035414 (2016).

[80] V. V. Shchennikov and S. V. Ovsyannikov, *Thermoelectric power, magnetoresistance of lead chalcogenides in the region of phase transitions under pressure*, Solid State Communications **126**, 373 (2003).

[81] R. S. Allgaier and W. W. Scanlon, *Mobility of Electrons and Holes in PbS, PbSe, and PbTe between Room Temperature and 4.2°K*, Physical Review **111**, 1029 (1958).

[82] K. Kishimoto and T. Koyanagi, *Preparation of sintered degenerate n-type PbTe with a small grain size and its thermoelectric properties*, Journal of Applied Physics **92**, 2544 (2002).

[83] H. Fan, T. Su, H. Li, Y. Zheng, S. Li, M. Hu, H. Ma, and X. Jia, *High temperature thermoelectric properties of PbTe prepared by high pressure method*, Materials Science-Poland **33**, 152 (2015).

[84] R. M. Murphy, E. D. Murray, S. Fahy, and I. Savić, *Broadband phonon scattering in PbTe-based materials driven near ferroelectric phase transition by strain or alloying*, Physical Review B **93**, 104304 (2016).

[85] S. Kurth, M. Marques, and E. Gross, in *Encyclopedia of Condensed Matter Physics*, edited by F. Bassani, G. L. Liedl, and P. Wyder (Elsevier, Oxford, 2005) pp. 395–402.

[86] E. Schrödinger, *An Undulatory Theory of the Mechanics of Atoms and Molecules*, Physical Review **28**, 1049 (1926).

[87] M. Born and R. Oppenheimer, *Zur Quantentheorie der Molekeln.*, Ann. Phys. (Leipzig) **84**, 457 (1927).

[88] B. T. Sutcliffe and R. G. Woolley, *On the quantum theory of molecules*, The Journal of Chemical Physics **137**, 22A544 (2012).

[89] T. Jecko, *On the mathematical treatment of the Born-Oppenheimer approximation*, Journal of Mathematical Physics **55**, 053504 (2014).

[90] H. Akbas and O. T. Turgut, *Born-Oppenheimer approximation for a singular system*, Journal of Mathematical Physics **59**, 012107 (2018).

[91] P. Hohenberg and W. Kohn, *Inhomogeneous Electron Gas*, Physical Review **136**, B864 (1964).

[92] C. E. Shannon, *Prediction and Entropy of Printed English*, Bell System Technical Journal **30**, 50 (1951).

[93] F. G. Guerrero, *A New Look at the Classical Entropy of Written English*, CoRR **abs/0911.2284** (2009).

[94] M. D. Segall, P. J. D. Lindan, M. J. Probert, C. J. Pickard, P. J. Hasnip, S. J. Clark, and M. C. Payne, *First-principles simulation: ideas, illustrations and the CASTEP code*, Journal of Physics: Condensed Matter **14**, 2717 (2002).

[95] W. Kohn and L. J. Sham, *Self-Consistent Equations Including Exchange and Correlation Effects*, Physical Review **140**, A1133 (1965).

[96] CECAM, Teaching the Theory in Density Functional Theory Lecture Series (2017).

[97] J. P. Perdew, A. Ruzsinszky, G. I. Csonka, O. A. Vydrov, G. E. Scuseria, L. A. Constantin, X. Zhou, and K. Burke, *Restoring the Density-Gradient Expansion for Exchange in Solids and Surfaces*, Physical Review Letters **100**, 136406 (2008).

[98] F. Tran and P. Blaha, *Accurate Band Gaps of Semiconductors and Insulators with a Semilocal Exchange-Correlation Potential*, Physical Review Letters **102**, 226401 (2009).

[99] J. P. Perdew, K. Burke, and M. Ernzerhof, *Generalized Gradient Approximation Made Simple*, Physical Review Letters **77**, 3865 (1996).

[100] D. Koller, F. Tran, and P. Blaha, *Improving the modified Becke-Johnson exchange potential*, Physical Review B **85**, 155109 (2012).

[101] D. Koller, F. Tran, and P. Blaha, *Merits and limits of the modified Becke-Johnson exchange potential*, Physical Review B **83**, 195134 (2011).

[102] P. Blaha, Wien2k Mailing List, https://www.mail-archive.com/wien@zeus.theochem.tuwien.ac.at/msg04052.html, accessed: 15/02/2021.

[103] L. O. Wagner, E. M. Stoudenmire, K. Burke, and S. R. White, *Guaranteed Convergence of the Kohn-Sham Equations*, Physical Review Letters **111**, 093003 (2013).

[104] P. Blaha, K. Schwarz, G. K. Madsen, D. Kvasnicka, and J. Luitz, *Computer code WIEN2K*, Vienna University of Technology (2001).

[105] J. Kuneš, P. Novák, R. Schmid, P. Blaha, and K. Schwarz, *Electronic structure of fcc Th: Spin-orbit calculation with* $6p_{1/2}$ *local orbital extension*, Physical Review B **64**, 153102 (2001).

[106] P. Larson, *Effect of* $p_{1/2}$ *corrections in the electronic structure of* Bi_2Te_3 *compounds*, Physical Review B **68**, 155121 (2003).

[107] P. Blaha, K. Schwarz, G. K. H. Madsen, D. Kvasnicka, and J. Luitz, Wien2k User Guide, https://euler.phys.cmu.edu/cluster/WIEN2k/usersguide.html, accessed: 16/02/21.

[108] G. K. Madsen and D. J. Singh, *BoltzTraP. A code for calculating band-structure dependent quantities*, Computer Physics Communications **175**, 67 (2006).

[109] G. K. Madsen, J. Carrete, and M. J. Verstraete, *BoltzTraP2, a program for interpolating band structures and calculating semi-classical transport coefficients*, Computer Physics Communications **231**, 140 (2018).

[110] W. W. Schulz, P. B. Allen, and N. Trivedi, *Hall coefficient of cubic metals*, Physical Review B **45**, 10886 (1992).

[111] T. C. Harman, D. L. Spears, and M. J. Manfra, *High thermoelectric figures of merit in PbTe quantum wells*, Journal of Electronic Materials **25**, 1121 (1996).

[112] Y. Pei, A. D. LaLonde, H. Wang, and G. J. Snyder, *Low effective mass leading to high thermoelectric performance*, Energy & Environmental Science **5**, 7963 (2012).

[113] Y. Pei, H. Wang, Z. M. Gibbs, A. D. LaLonde, and G. J. Snyder, *Thermopower enhancement in Pb1- xMnxTe alloys and its effect on thermoelectric efficiency*, NPG Asia Materials **4**, e28 (2012).

[114] B. Houston, R. E. Strakna, and H. S. Belson, *Elastic Constants, Thermal Expansion, and Debye Temperature of Lead Telluride*, Journal of Applied Physics **39**, 3913 (1968).

[115] D. H. Parkinson and J. E. Quarrington, *The Molar Heats of Lead Sulphide, Selenide and Telluride in the Temperature Range 20 K to 260 K*, Proceedings of the Physical Society. Section A **67**, 569 (1954).

[116] R. W. Godby, M. Schlüter, and L. J. Sham, *Self-energy operators and exchange-correlation potentials in semiconductors*, Physical Review B **37**, 10159 (1988).

[117] V. Fiorentini and A. Baldereschi, *Dielectric scaling of the self-energy scissor operator in semiconductors and insulators*, Physical Review B **51**, 17196 (1995).

[118] R. S. Allgaier, *Weak-Field Magnetoresistance in p-Type Lead Telluride at Room Temperature and 77°K*, Physical Review **119**, 554 (1960).

[119] K. Cuff, M. Ellett, C. Kuglin, and L. Williams, *Physics of Semiconductors: Proceedings of the Seventh International Conference, Paris, 1964*, Proceedings of the Seventh International Conference (1964).

[120] G. Martinez, M. Schlüter, and M. L. Cohen, *Electronic structure of PbSe and PbTe. I. Band structures, densities of states, and effective masses*, Physical Review B **11**, 651 (1975).

[121] S.-Y. Yang, *Electrical behavior of lead telluride at elevated temperature*, Ph.D. thesis, Marquette University (1990), copyright - Database copyright ProQuest LLC; ProQuest does not claim copyright in the individual underlying works; Last updated - 2016-05-14.

[122] J. Martin, L. Wang, L. Chen, and G. S. Nolas, *Enhanced Seebeck coefficient through energy-barrier scattering in PbTe nanocomposites*, Physical Review B **79**, 115311 (2009).

[123] J. P. Heremans, V. Jovovic, E. S. Toberer, A. Saramat, K. Kurosaki, A. Charoenphakdee, S. Yamanaka, and G. J. Snyder, *Enhancement of Thermoelectric Efficiency in PbTe by Distortion of the Electronic Density of States*, Science **321**, 554 (2008).

[124] W. W. Scanlon, *Precipitation of Te and Pb in PbTe Crystals*, Physical Review **126**, 509 (1962).

[125] C. M. Jaworski, B. Wiendlocha, V. Jovovic, and J. P. Heremans, *Combining alloy scattering of phonons and resonant electronic levels to reach a high thermoelectric figure of merit in PbTeSe and PbTeS alloys*, Energy & Environmental Science **4**, 4155 (2011).

[126] Y. Takagiwa, Y. Pei, G. Pomrehn, and G. J. Snyder, *Dopants effect on the band structure of PbTe thermoelectric material*, Applied Physics Letters **101**, 092102 (2012).

[127] N. Bouad, L. Chapon, R.-M. Marin-Ayral, F. Bouree-Vigneron, and J.-C. Tedenac, *Neutron powder diffraction study of strain and crystallite size in mechanically alloyed PbTe*, Journal of Solid State Chemistry France **173**, 189 (2003).

[128] Y. Noda, K. Masumoto, S. Ohba, Y. Saito, K. Toriumi, Y. Iwata, and I. Shibuya, *Temperature dependence of atomic thermal parameters of lead chalcogenides, PbS, PbSe and PbTe*, Acta Crystallographica Section C **43**, 1443 (1987).

[129] G. Rousse, S. Klotz, A. M. Saitta, J. Rodriguez-Carvajal, M. I. McMahon, B. Couzinet, and M. Mezouar, *Structure of the intermediate phase of PbTe at high pressure*, Physical Review B **71**, 224116 (2005).

[130] M. I. Aroyo, D. Orobengoa, G. de la Flor, E. S. Tasci, J. M. Perez-Mato, and H. Wondratschek, *Brillouin-zone database on the Bilbao Crystallographic Server*, Acta Crystallographica Section A **70**, 126 (2014).

[131] Y. Tang, Z. M. Gibbs, L. A. Agapito, G. Li, H.-S. Kim, M. B. Nardelli, S. Curtarolo, and G. J. Snyder, *Convergence of multi-valley bands as the electronic origin of high thermoelectric performance in CoSb3 skutterudites*, Nature Materials **14**, 1223 (2015).

[132] H. J. Goldsmid, *Introduction to Thermoelectricity*, 2nd ed., Springer Series in Materials Science, 121 (Springer Berlin Heidelberg : Imprint: Springer, Berlin, Heidelberg, 2016).

[133] R. S. Allgaier, *History of narrow-gap semiconductors and semimetals, 1945-65*, Semiconductor Science and Technology **5**, S326 (1990).

[134] W. Klemm and H. Westlinning, *Untersuchungen über die Verbindungen des Magnesiums mit den Elementen der IV b-Gruppe*, Zeitschrift für anorganische und allgemeine Chemie **245**, 365 (1941).

[135] K. Koumoto and T. Mori, *Thermoelectric Nanomaterials* (Springer, Berlin, Heidelberg, 2013).

[136] V. Zaitsev, M. Fedorov, I. Eremin, E. Gurieva, and D. Rowe, *Thermoelectrics Handbook: Macro to Nano* (CRC Press, Taylor & Francis Group, 2006).

[137] Y. R. Jin, Z. Z. Feng, L. Y. Ye, Y. L. Yan, and Y. X. Wang, *Mg_2Sn: a potential mid-temperature thermoelectric material*, Royal Society of Chemistry Advances **6**, 48728 (2016).

[138] G. Tan, L.-D. Zhao, and M. G. Kanatzidis, *Rationally Designing High-Performance Bulk Thermoelectric Materials*, Chemical Reviews **116**, 12123 (2016), pMID: 27580481.

[139] G. Li, H. Gill, and R. Varin, *Magnesium silicide intermetallic alloys*, Metallurgical Transactions A **24**, 2383 (1993).

[140] W. Lawson, S. Nielsen, E. Putley, and V. Roberts, *The preparation, electrical and optical properties of Mg_2Sn.*, Electronics **1**, 203 (1955).

[141] Fitriani, R. Ovik, B. Long, M. Barma, M. Riaz, M. Sabri, S. Said, and R. Saidur, *A review on nanostructures of high-temperature thermoelectric materials for waste heat recovery*, Renewable and Sustainable Energy Reviews **64**, 635 (2016).

[142] S. LeBlanc, S. K. Yee, M. L. Scullin, C. Dames, and K. E. Goodson, *Material and manufacturing cost considerations for thermoelectrics*, Renewable and Sustainable Energy Reviews **32**, 313 (2014).

[143] W. Liu, X. Tan, K. Yin, H. Liu, X. Tang, J. Shi, Q. Zhang, and C. Uher, *Convergence of Conduction Bands as a Means of Enhancing Thermoelectric Performance of n-Type* $Mg_2Si_{1-x}Sn_x$ *Solid Solutions*, Physical Review Letters **108**, 166601 (2012).

[144] H. Kasai, L. Song, H. L. Andersen, H. Yin, and B. B. Iversen, *Multi-temperature structure of thermoelectric* Mg_2Si *and* Mg_2Sn, Acta Crystallographica Section B **73**, 1158 (2017).

[145] H. Balout, P. Boulet, and M.-C. Record, *Electronic and transport properties of* Mg_2Si *under isotropic strains*, Intermetallics **50**, 8 (2014).

[146] S.-D. Guo and J.-L. Wang, *Pressure enhanced thermoelectric properties in* Mg_2Sn, Royal Society of Chemistry Advances **6**, 31272 (2016).

[147] H. Balout, P. Boulet, and M.-C. Record, *Effect of Biaxial Strain on Electronic and Thermoelectric Properties of* Mg_2Si, Journal of Electronic Materials **42**, 3458 (2013).

[148] H. Balout, P. Boulet, and M.-C. Record, *Computational Investigation of the Electronic and Thermoelectric Properties of Strained Bulk* Mg_2Si, Journal of Electronic Materials **43**, 3801 (2014).

[149] H. Balout, P. Boulet, and M.-C. Record, *Calculations of thermoelectric properties:* Mg_2Si *under uniaxial [110] strains versus (110)-oriented thin film*, The European Physical Journal B **88**, 209 (2015).

[150] C. Kittel, *Introduction to solid state physics*, 8th ed. (Wiley, 2004).

[151] J. Hao, B. Zou, P. Zhu, C. Gao, Y. Li, D. Liu, K. Wang, W. Lei, Q. Cui, and G. Zou, *In situ X-ray observation of phase transitions in* Mg_2Si *under high pressure*, Solid State Communications **149**, 689 (2009).

[152] N. V. Morozova, S. V. Ovsyannikov, I. V. Korobeinikov, A. E. Karkin, K.-i. Takarabe, Y. Mori, S. Nakamura, and V. V. Shchennikov, *Significant enhancement of thermoelectric properties and metallization of Al-doped* Mg_2Si *under pressure*, Journal of Applied Physics **115**, 213705 (2014).

[153] A. Stella, A. D. Brothers, R. H. Hopkins, and D. W. Lynch, *Pressure Coefficient of the Band Gap in* Mg_2Si*, Mg2Ge, and* Mg_2Sn, Physica Status Solidi (b) **23**, 697 (1967).

[154] F. Kalarasse and B. Bennecer, *Electronic and optical properties of the antifluorite semiconductors Be2C and Mg2X (X=C, Si, Ge) under hydrostatic pressure*, Journal of Physics and Chemistry of Solids **69**, 1775 (2008).

[155] F. Yu, J.-X. Sun, W. Yang, R.-G. Tian, and G.-F. Ji, *A study of the phase transitions, electronic structures and optical properties of* Mg_2Si *under high pressure*, Solid State Communications **150**, 620 (2010).

[156] P. Cannon and E. T. Conlin, *Magnesium Compounds: New Dense Phases*, Science **145**, 487 (1964).

[157] T. Dyuzheva, S. Kabalkina, and L. Vereshchagin, *Polymorphism of Mg_2Sn at high temperatures and pressures*, Sov. Phys. Crystallogr. **17**, 705 (1973).

[158] T. Dyuzheva, N. Bendeliani, L. Dzhavadov, T. Kolobyanina, and N. Nikolaev, *Crystal growth of the high-pressure phase of Mg_2Sn*, Journal of Alloys and Compounds **223**, 74 (1995).

[159] Y. Liu, W.-C. Hu, D.-J. Li, X.-Q. Zeng, and C.-S. Xu, *Predictions of the structural, electronic and thermodynamic properties of the anti-fluorite-type Mg_2Sn under pressure from first principles*, Physica Scripta **88**, 045302 (2013).

[160] F. Yu, J.-X. Sun, and T.-H. Chen, *High-pressure phase transitions of Mg2Ge and Mg_2Sn: First-principles calculations*, Physica B: Condensed Matter **406**, 1789 (2011).

[161] S.-D. Guo, *Pressure-induced semiconductor-to-metal transition in Mg_2Sn with the modified Becke-Johnson potential*, EPL (Europhysics Letters) **109**, 57002 (2015).

[162] W. Whitten, P. Chung, and G. Danielson, *Elastic constants and lattice vibration frequencies of Mg_2Si*, Journal of Physics and Chemistry of Solids **26**, 49 (1965).

[163] L. Davis, W. Whitten, and G. Danielson, *Elastic constants and calculated lattice vibration frequencies of Mg_2Sn*, Journal of Physics and Chemistry of Solids **28**, 439 (1967).

[164] A. Ballato, Poisson's ratio for cubic crystals, `https://apps.dtic.mil/dtic/tr/fulltext/u2/a293549.pdf` (1995), no. ARL-TR-425. ARMY RESEARCH LAB FORT MONMOUTH NJ.

[165] R. H. Baughman, J. M. Shacklette, A. A. Zakhidov, and S. Stafström, *Negative Poisson's ratios as a common feature of cubic metals*, Nature **392**, 362 (1998).

[166] J.-M. Zhang, Y. Zhang, K.-W. Xu, and V. Ji, *Young's modulus surface and Poisson's ratio curve for cubic metals*, Journal of Physics and Chemistry of Solids **68**, 503 (2007).

[167] K. M. Knowles and P. R. Howie, *The Directional Dependence of Elastic Stiffness and Compliance Shear Coefficients and Shear Moduli in Cubic Materials*, Journal of Elasticity **120**, 87 (2015).

[168] M. Kubouchi, K. Hayashi, and Y. Miyazaki, *Quantitative analysis of interstitial Mg in Mg_2Si studied by single crystal X-ray diffraction*, Journal of Alloys and Compounds **617**, 389 (2014).

[169] J. L. Corkill and M. L. Cohen, *Structural, bonding, and electronic properties of IIA-IV antifluorite compounds*, Physical Review B **48**, 17138 (1993).

[170] K. Kutorasinski, B. Wiendlocha, J. Tobola, and S. Kaprzyk, *Importance of relativistic effects in electronic structure and thermopower calculations for Mg_2Si, Mg_2Ge, and Mg_2Sn*, Physical Review B **89**, 115205 (2014).

[171] H. Udono, H. Tajima, M. Uchikoshi, and M. Itakura, *Crystal growth and characterization of Mg_2Si for IR-detectors and thermoelectric applications*, Japanese Journal of Applied Physics **54**, 07JB06 (2015).

[172] H. G. Lipson and A. Kahan, *Infrared Absorption of Magnesium Stannide*, Physical Review **133**, A800 (1964).

[173] J. Tani and H. Kido, *Thermoelectric properties of Bi-doped Mg_2Si semiconductors*, Physica B: Condensed Matter **364**, 218 (2005).

[174] J. Tani and H. Kido, *Thermoelectric properties of Sb-doped Mg_2Si semiconductors*, Intermetallics **15**, 1202 (2007).

[175] J. ichi Tani and H. Kido, *Thermoelectric Properties of P-doped Mg_2Si Semiconductors*, Japanese Journal of Applied Physics **46**, 3309 (2007).

[176] J. Tani and H. Kido, *First-principles and experimental studies of impurity doping into Mg_2Si*, Intermetallics **16**, 418 (2008).

[177] M. Akasaka, T. Iida, A. Matsumoto, K. Yamanaka, Y. Takanashi, T. Imai, and N. Hamada, *The thermoelectric properties of bulk crystalline n- and p-type Mg_2Si prepared by the vertical Bridgman method*, Journal of Applied Physics **104**, 013703 (2008).

[178] R. G. Morris, R. D. Redin, and G. C. Danielson, *Semiconducting Properties of* Mg_2Si *Single Crystals*, Physical Review **109**, 1909 (1958).

[179] H. Ihou-Mouko, C. Mercier, J. Tobola, G. Pont, and H. Scherrer, *Thermoelectric properties and electronic structure of p-type Mg_2Si and $Mg_2Si0.6Ge0.4$ compounds doped with Ga*, Journal of Alloys and Compounds **509**, 6503 (2011).

[180] A. Kolezynski, P. Nieroda, and K. T. Wojciechowski, *Li doped Mg_2Si p-type thermoelectric material: Theoretical and experimental study*, Computational Materials Science **100**, 84 (2015), 13th International Symposium on Novel and Nano Materials: ISNNM-2014.

[181] S. Kim, B. Wiendlocha, H. Jin, J. Tobola, and J. P. Heremans, *Electronic structure and thermoelectric properties of p-type Ag-doped Mg_2Sn and $Mg_2Sn_{1-x}Si_x$ ($x = 0.05, 0.1$).*, Journal of Applied Physics **116**, 153706 (2014).

[182] J.-i. Tani, T. Shinagawa, and M. Chigane, *Thermoelectric Properties of Impurity-Doped Mg_2Sn*, Journal of Electronic Materials **48**, 3330 (2019).

[183] S.-M. Choi, T. H. An, W.-S. Seo, and C. Park, *Doping Effects on Thermoelectric Properties in the Mg_2Sn System*, Journal of Electronic Materials **41**, 1071 (2012).

[184] J. Mao, Y. Wang, B. Ge, Q. Jie, Z. Liu, U. Saparamadu, W. Liu, and Z. Ren, *Thermoelectric performance enhancement of Mg_2Sn based solid solutions by band convergence and phonon scattering via Pb and Si/Ge substitution for Sn*, Physical Chemistry Chemical Physics **18**, 20726 (2016).

[185] W. Saito, K. Hayashi, J. Dong, J.-F. Li, and Y. Miyazaki, *Control of the Thermoelectric Properties of Mg_2Sn Single Crystals via Point-Defect Engineering*, Scientific Reports **10** (2020).

[186] N. Savvides and H. Y. Chen, *Thermal Conductivity and Other Transport Properties of Mg_2Sn:Ag*, Journal of Electronic Materials **39**, 2136 (2010).

[187] L. D. Crossman and G. C. Danielson, *Piezoresistance of n-Type Magnesium Stannide*, Physical Review **171**, 867 (1968).

[188] R. M. Martin, *Electronic Structure: Basic Theory and Practical Methods* (Cambridge University Press, 2004).

[189] C. D. Sherrill, *The Born-Oppenheimer Approximation* (Georgie Institute of Technology, 2005).

[190] D. J. Singh and L. Nordstrom, *Planewaves, Pseudopotentials, and the LAPW Method*, 2nd ed. (Springer US, 2005).

[191] N. Woods, *On the Nature of Self-Consistency in Density Functional Theory*, Ph.D. thesis, The University of Cambridge (2018).

[192] P. Blaha, K. Schwarz, F. Tran, R. Laskowski, G. K. H. Madsen, and L. D. Marks, *WIEN2k: An APW+lo program for calculating the properties of solids*, The Journal of Chemical Physics **152**, 074101 (2020).

[193] P. Dziawa, B. J. Kowalski, K. Dybko, R. Buczko, A. Szczerbakow, M. Szot, E. Łusakowska, T. Balasubramanian, B. M. Wojek, M. H. Berntsen, O. Tjernberg, and T. Story, *Topological crystalline insulator states in $Pb_{1-x}Sn_xSe$*, Nature Materials **11**, 1023 (2012).

[194] Y. Gelbstein, Z. Dashevsky, and M. P. Dariel, *The search for mechanically stable PbTe based thermoelectric materials*, Journal of Applied Physics **104**, 033702 (2008).

[195] Y. Zhang, X. Ke, C. Chen, J. Yang, and P. R. C. Kent, *Thermodynamic properties of PbTe, PbSe, and PbS: First-principles study*, Physical Review B **80**, 024304 (2009).

[196] L. Xu, Y. Zheng, and J.-C. Zheng, *Thermoelectric transport properties of PbTe under pressure*, Physical Review B **82**, 195102 (2010).

[197] J. M. Skelton, S. C. Parker, A. Togo, I. Tanaka, and A. Walsh, *Thermal physics of the lead chalcogenides PbS, PbSe, and PbTe from first principles*, Physical Review B **89**, 205203 (2014).

[198] J. E. Petersen, L. M. Scolfaro, and T. H. Myers, *Elastic and mechanical properties of intrinsic and doped PbSe and PbTe studied by first-principles*, Materials Chemistry and Physics **146**, 472 (2014).

[199] B. S. G. Nimtz, *Narrow-gap Semiconductors*, 7th ed. (Springer, 1985).

[200] Y. Bencherif, A. Boukra, A. Zaoui, and M. Ferhat, *High-pressure phases of lead chalcogenides*, Materials Chemistry and Physics **126**, 707 (2011).

[201] R. Dalven, *A review of the semiconductor properties of PbTe, PbSe, PbS and PbO*, Infrared Physics **9**, 141 (1969).

[202] T. Kato, Y. Sago, and H. Fujiwara, *Optoelectronic properties of Mg_2Si semiconducting layers with high absorption coefficients*, Journal of Applied Physics **110**, 063723 (2011).

[203] J. E. Mahan, A. Vantomme, G. Langouche, and J. P. Becker, *Semiconducting* Mg_2Si *thin films prepared by molecular-beam epitaxy*, Physical Review B **54**, 16965 (1996).

[204] D. Tamura, R. Nagai, K. Sugimoto, H. Udono, I. Kikuma, H. Tajima, and I. J. Ohsugi, *Melt growth and characterization of Mg_2Si bulk crystals*, Thin Solid Films **515**, 8272 (2007), aPAC-SILICIDE 2006.

[205] O. Madelung, U. Rössler, and M. Schulz, eds., Magnesium silicide (Mg_2Si) band structure, energy gap, in *Non-Tetrahedrally Bonded Elements and Binary Compounds I* (Springer Berlin Heidelberg, Berlin, Heidelberg, 1998) pp. 1–7.

[206] P. Koenig, D. Lynch, and G. Danielson, *Infrared absorption in magnesium silicide and magnesium germanide*, Journal of Physics and Chemistry of Solids **20**, 122 (1961).